UiT
THE ARCTIC UNIVERSITY OF NORWAY

Faculty of Science and Technology

Department of Geosciences

Distribution and quantification of gas hydrates and free gas in marine sediments of Vestnesa Ridge, offshore W-Svalbard

—

Sunny Singhroha

A dissertation for the degree of Philosophiae Doctor – April 2019

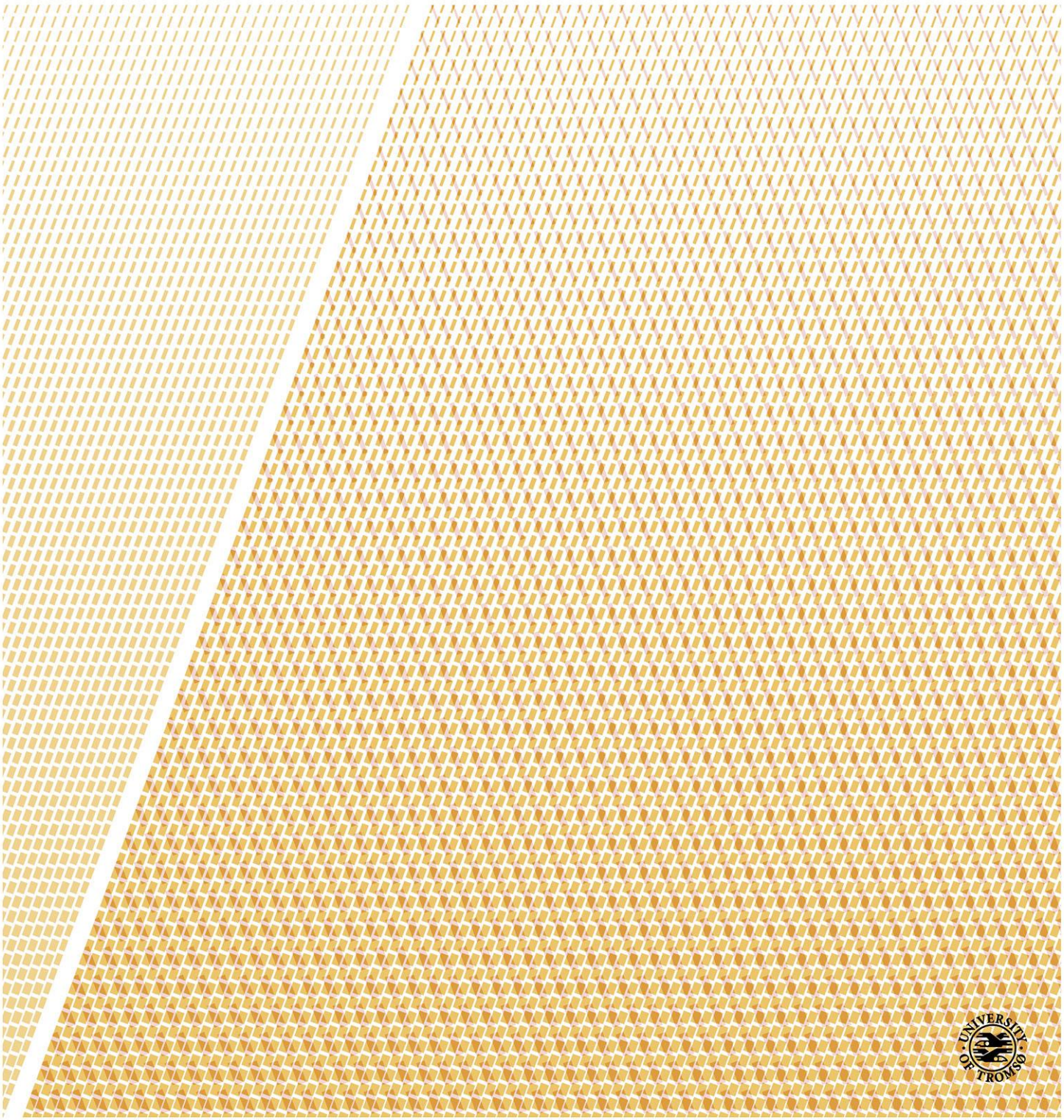

Distribution and quantification of gas hydrates and free gas in marine sediments of Vestnesa Ridge, offshore W-Svalbard

Sunny Singhroha

A

Dissertation for the Degree of

Philosophiae Doctor

FACULTY OF SCIENCE AND TECHNOLOGY

DEPARTMENT OF GEOSCIENCES

April 2019

Dedicated to my parents

Dr. Chand Ram & Smt. Santosh Devi

Preface

A large amount of methane (>500 Gt of Carbon) is globally locked in low-temperature and high-pressure natural environments in the form of gas hydrates. Gas hydrates occur within sediments on the western Svalbard continental margin and the Vestnesa Ridge, a large sediment drift that extends in the west-northwest direction from the margin towards the mid-ocean ridge. The distribution of gas hydrates in the Vestnesa Ridge is primarily mapped through the presence of BSR in the seismic data. A BSR indicates the transition from gas hydrate-bearing sediments to those containing gas at the base of the gas hydrate stability zone (GHSZ) and gives little or no information about the distribution of gas hydrates within the GHSZ. Geophysical studies can help in delineating the gas hydrate distribution along the Vestnesa Ridge. Geophysical surveys that measure physical properties can distinguish gas hydrates from the background sediment matrix. Intrinsic properties of a medium i.e. P- and S-wave seismic velocities and seismic attenuation changes in hydrate-saturated marine sediments with changes in hydrate saturation and morphology. For remote large-scale gas hydrate exploration, gas hydrate distribution is primarily mapped using seismic velocity analysis. In this doctoral work, I explore the potential application of detailed seismic velocity (travel time inversion, full waveform inversion, and azimuthal velocity modelling) and seismic attenuation analysis to study the distribution of gas hydrates in the eastern segment of the Vestnesa Ridge that is characterized by many active seepages of gas from pockmarks at the seafloor.

The present study titled “Distribution and quantification of gas hydrates and free gas in marine sediments of Vestnesa Ridge, offshore W-Svalbard” has been submitted at the University of Tromsø – The Arctic University of Norway as a PhD dissertation in partial fulfillment of the requirements for the PhD degree. The research work for this thesis has been carried out from January 2015 to April 2019 in the Center for Arctic Gas Hydrates, Environment and Climate (CAGE) at the Department of Geosciences, University of Tromsø. This research work has been funded by the University of Tromsø – The Arctic University of Norway as a part of its contribution towards CAGE.

During the course of my PhD, I was a part of six research cruises onboard R/V Helmer Hanssen. I used OBS data acquired during some of these cruises in this thesis to study Vestnesa gas hydrate system. Apart from obligatory courses, I participated in two geological field trip courses in Italy in 2015 and 2016. I also contributed in the departmental work, mainly in the form of

teaching and conducting exercises for different courses, which accounted for 25% of my time in the PhD tenure.

This doctoral thesis includes an introduction and three articles. Some of the results in this thesis have also been presented during various international conferences and meetings. I have also contributed to an additional article, which is not included in this thesis. The three scientific articles presented in this thesis are as follows:

Article I

Singhroha, S., Bünz, S., Plaza-Faverola, A., & Chand, S. (2016). Gas hydrate and free gas detection using seismic quality factor estimates from high-resolution P-Cable 3D seismic data. Interpretation (Tulsa), 1, SA39-SA54. Doi: 10.1190/INT-2015-0023.1

Article II

Singhroha S., Chand, S., & Bünz, S. (2019). Constraints on gas hydrate distribution and morphology in Vestnesa Ridge, W-Svalbard margin using multicomponent ocean-bottom seismic data. Journal of Geophysical Research – Solid Earth. Doi: 10.1029/2018JB016574

Article III

Singhroha, S., Bünz, S., Plaza-Faverola, A., & Chand, S. Structural control on the distribution of gas hydrates in the Vestnesa Ridge. Submitted to the Journal of Geophysical Research – Solid Earth.

Additional contribution

Song, S., Tinivella, U., Giustiniani, M., Singhroha, S., Bünz, S., & Cassiani, G. (2018). OBS Data Analysis to Quantify Gas Hydrate and Free Gas in the South Shetland Margin (Antarctica). Energies, 11(12), 3290.

List of supervisors

Prof. Stefan Bünz

CAGE – Centre for Arctic Gas Hydrates, Environment and Climate,
Department of Geosciences,
UiT – The Arctic University of Norway, Tromsø, Norway

Dr. Andreia Plaza-Faverola

CAGE – Centre for Arctic Gas Hydrates, Environment and Climate,
Department of Geosciences,
UiT – The Arctic University of Norway, Tromsø, Norway

Dr. Shyam Chand

Geological Survey of Norway (NGU), Trondheim, Norway

CAGE – Centre for Arctic Gas Hydrates, Environment and Climate,
Department of Geosciences,
UiT – The Arctic University of Norway, Tromsø, Norway

Acknowledgement

My interest in research grew while I was working on my master's thesis with Dr. Pawan Dewangan in the gas hydrate group in the National Institute of Oceanography (NIO), Goa. I admired his passion for geophysics and his energy and enthusiasm in the research acted as a spur for me to pursue the path of scientific research.

My four years of the PhD journey in the Centre for Arctic Gas hydrates, Environment and Climate (CAGE) has been an exclusive learning experience. This journey demands plenty of help and guidance from experts. First of all, I would like to acknowledge that this PhD thesis is a result of continuous support and mentorship by Prof. Stefan Bünz. It has been a wonderful experience to work under his esteemed guidance. He is my main supervisor and this thesis would not have been possible without him. I want to thank him for reposing his faith in me by selecting me for the PhD position and at every step during the PhD. He has actively supervised my research work, ideas and plans throughout my PhD tenure. He has provided constant inspiration, inducement and encouragement to me. He has always been very calm, kind and helpful.

In addition to supervision from my main supervisor, I was co-supervised by Dr. Andreia Plaza-Faverola and Dr. Shyam Chand. They helped me in different stages of my PhD and they were involved in significant parts of my PhD journey. We had great scientific discussions and these discussions considerably improved my scientific understanding about the topic.

I would also like to thank the funding institutions that provided me funds to carry out my PhD research work. This work is funded by the University of Tromsø and partly supported by the Research Council of Norway through its Centres of Excellence funding scheme, project no. 223259. Apart from my stay in the University of Tromsø, I also worked in the Geological Survey of Norway (NGU) and University of Edinburgh for approximately 4 months in both the places. Special thanks to Dr. Shyam Chand and Dr. Mark Chapman for helping me during this period.

In this PhD thesis, I have used the data that has been acquired during various research cruises on R/V Helmer Hanssen. I thank the crew of the R/V Helmer Hanssen and those who contributed to the OBS and P-Cable seismic data acquisition. I would like to give special thanks to Dr. Sunil Vadakkepuliyambatta for his help in OBS data acquisition.

I would also like to thank my several friends who made these four years exciting and with whom I spent wonderful weekend evenings. Special thanks to Vikram, Ankit, Arpit, Rajwinder, Mukesh, Nishant, Espen, Arunima, Jared, Magnus, Wei Li, Haoyi, Siri, Sandra, Kärt, Sunil, Henry, Kate, Malin, Pavel and Alexey. Special thanks to others also whose name I have not mentioned.

Lastly, I am grateful to my beloved family members with special thanks to Roopam Bamal, my wife, for their endless support and encouragement to pursue PhD studies.

Table of Contents

Preface iv
Acknowledgement vii
List of illustrations xi
List of acronyms xii
1. Scope of the thesis 1
2. Gas hydrates 3
3. Occurrence of natural gas hydrates 5
4. Properties of gas hydrates 9
4.1. P- and S-wave Seismic velocities 9
4.2. Seismic attenuation 10
4.3. Electrical resistivity 11
5. Exploration techniques for gas hydrates 13
6. Study area 15
6.1. Structural evolution of the study area 15
6.1.1. Faults 17
6.2. Stratigraphic evolution of study area 17
6.3. Vestnesa Ridge 18
6.4. Gas hydrate system in the Vestnesa Ridge 19
7. Data and methods 20
7.1. Data acquisition 20
7.1.1. High resolution P-Cable 3D Seismic data 20
7.1.2. Ocean bottom seismic experiments 20
7.2. Methods 21
7.2.1. Seismic Q analysis 21
7.2.2. Seismic velocity analysis 22
7.2.3. SCA/DEM modelling 23
8. Articles 24
8.1. Article 1 24
8.2. Article 2 25
8.3. Article 3 26
9. Synthesis and outlook 27
9.1. Synthesis 27
9.2. Outlook 29
Future research 29

10. References 31

Articles 1-3

List of illustrations

Figure 1. Schematic description of the variation of phase boundaries of gas hydrate stability with depth due to variation in pressure temperature conditions (modified from Ruppel et al., 2007).

Figure 2. Schematic description of end member gas hydrate morphologies (pore-filling (a), grain coating (b), cementing (c), inclusion/matrix frame (d), fracture/fault filling (e) and massive/nodular gas hydrate deposits).

Figure 3. Schematic description of the variation in P- and S-wave velocities with gas hydrate saturation and morphology (modified from Mahabadi et al., 2019 and Dai et al., 2012).

Figure 4. Schematic description of the variation of electrical conductivity with gas hydrate saturation and morphology (modified from Dai et al., 2012).

Figure 5. Bathymetry map of the study area. Green rectangle shows the area in which 3D seismic data is acquired. Blue dots show the location of OBS stations. Black lines show the acquisition lines used for some OBS stations. Circles around two OBS stations show the circular tracks on which azimuthal seismic data is acquired for two OBS stations.

List of acronyms

GHSZ	Gas hydrate stability zone
K	Bulk modulus
μ	Shear modulus
Vp	P-wave velocity
Vs	S-wave velocity
Q	Quality Factor
OBS	Ocean bottom seismic/Ocean bottom seismometer
VSP	Vertical seismic profile
BSR	Bottom simulating reflector/Bottom simulating reflection
PP	Incident P-wave reflected as P-wave
PS	Incident P-wave reflected as S-wave (converted S-wave)
CSEM	Controlled source electromagnetic
NMR	Nuclear magnetic response
FWI	Full waveform inversion
SCA	Self-consistent approximation
DEM	Differential effective medium
NMO	Normal moveout
SR	Spectral ratio
P	Primary (compressional) seismic body wave
S	Secondary (Shear) wave
1D	one-dimensional
2D	two-dimensional
3D	three-dimensional

1. Scope of the thesis

This doctoral thesis focuses on the gas hydrate system in the Vestnesa Ridge, western Svalbard margin. The gas hydrate system in this region is extensive and partly continuous; it covers the complete Vestnesa Ridge (Vogt et al., 1994; Eiken & Hinz, 1993, Posewang & Mienert, 1999, Vanneste et al., 2005; Hustoft et al., 2009; Bünz et al., 2012; Plaza-Faverola et al., 2015, 2017; Dumke et al., 2016; Bohrmann et al., 2016). It is important to study gas hydrates mainly due to their inherent resource potential, environmental impacts of gas hydrate dissociation and geohazard concerns (Sloan, 1998; Ruppel & Kessler, 2017). The presence of several active methane seepage sites in the eastern segment of the Vestnesa Ridge makes the study of this gas hydrate system more significant from the environmental point of view (Hustoft et al., 2009; Petersen et al., 2010; Bünz et al., 2012). Gas hydrate stability modelling corroborated with mapping bottom-simulating reflections (BSR) as a seismic indicator for the presence of gas hydrates helps in identifying the lateral extents of this gas hydrate system (Shipley et al., 1979; Bünz et al, 2012; Plaza-Faverola et al., 2017). However, the amount and the distribution of gas hydrates in sub-seabed sediments is still an unanswered question. The lack of knowledge of gas hydrate distribution and saturation models limits the accuracy of estimates of the amount of carbon stored in the Vestnesa Ridge gas hydrate system. Moreover, a better understanding of gas hydrate systems, especially in proximity to fluid flow features would improve the understanding of processes leading to fluid leakage through the hydrate stability zone (Plaza-Faverola et al., 2015; Plaza-Faverola & Keiding, 2019; Waghorn et al., 2018). The understanding of fluid leakage processes is crucial in addressing questions related to the amount and rate of methane seepage in the geological past and present. It is also important to study different factors that control gas hydrate distribution. Hence, high-resolution gas hydrate saturation models are prerequisite to study the spatial variability of gas hydrates within the gas hydrate stability zone (GHSZ) and to understand the link between gas hydrate distribution and methane seepage occurring at the seafloor.

Seismic velocities in a medium are sensitive to the presence of gas hydrates and seismic velocity modelling is normally used to develop gas hydrate saturation models (Dvorkin & Nur, 1993; Ecker et al., 1998; Dai et al., 2012; Singh et al., 1993; Chabert et al., 2011; Wang et al., 2018). The combined analysis of P- and S-waves provides better constrains on gas hydrate saturation estimates (Bünz et al., 2005; Kumar et al., 2007; Satyavani et al., 2016; Chabert et al., 2011; Song et al., 2018). Some advanced seismic velocity analysis techniques like full waveform inversion (FWI) allow us to estimate high-resolution velocity models and get information about

the fine-scale gas hydrate distribution (Singh et al., 1993; Pecher et al., 1996; Westbrook et al., 2008; Wang et al., 2018). Methods to develop gas hydrate saturation models from 2D or 3D seismic data in the absence of seismic velocity models are still in infancy (Rossi et al., 2007; Kim et al., 2015). These methods need to be developed further as per the need and the quality of the dataset available. The overall objectives of this doctoral thesis are as follows:

- Developing a reliable geophysical approach that can constrain the presence of gas hydrates and associated free gas in marine sediments in the absence of seismic velocity model.
- Understanding the spatial distribution and the amount of gas hydrates and free gas stored in sediments of Vestnesa Ridge through analysis of P- and S-wave velocities and rock physics modelling.
- Improving the current understanding about structural and stratigraphic controls on the distribution of gas hydrates in the Vestnesa Ridge.

2. Gas hydrates

At a certain low temperature and high-pressure condition, most low molecular weight gases (CH_4, C_2H_6, CO_2, N_2, O_2, etc.) in the presence of water freezes into an ice like crystalline solid known as gas hydrates (Sloan, 1998; Bishnoi & Natrajan, 1996). These hydrates have gases trapped inside the cages of hydrogen-bonded water molecules (Claussen, 1951). Artificially produced gas hydrates were first made in 1810 at a laboratory (Davy, 1810) and these remained a part of laboratory experiments for more than a century. In 1930s, gas hydrates came in highlight due to disruptions in the flow of natural gas because of the gas hydrate formation in gas pipelines (Hammerschmidt, 1934). Interest in gas hydrates rapidly grew in 1960s after the first discovery of natural occurrences of gas hydrates (Makogon, 1965). Some geological settings (for example, in continental margins and permafrost environments) host large deposits of gas hydrates (Kvenvolden & McMenamin, 1980). Naturally occurring gas hydrates are also referred to as methane hydrates in the literature, as it is mostly methane that is locked in naturally occurring gas hydrates.

In the past few decades, gas hydrates have gained a special attention and in the following section, I will highlight some key aspects that are driving gas hydrate research.

- Gas hydrates are a very large component of the global carbon budget and an important component of the global carbon cycle. These gas hydrate reservoirs act as big carbon repositories that store huge amount of carbon (~500-3,000 Gt of carbon) (Milkov, 2004; Ruppel & Kessler, 2017). Even with conservative estimates, the amount of carbon associated with gas hydrates is high or comparable to the entire carbon stock in the terrestrial biosphere (500-1,000 Gt of carbon). Any changes that can potentially unlock a small fraction of this carbon from gas hydrate reservoirs can affect earth's climate, environment and terrestrial ecosystem (Kennett et al., 2002; Hunter et al., 2013). Some environmentally sensitive areas, such as Arctic and permafrost environments, have large reservoirs of gas hydrates (Hunter et al., 2013; Kretschmer et al., 2015; Marín-Moreno et al., 2016; Ruppel & Kessler, 2017). The increase in global and ocean water temperature will affect the stability of gas hydrates in the Arctic over coming decades (Marín-Moreno et al., 2013, 2015, 2016; Vadakkepuliyambatta et al., 2017; Phrampus & Hornbach, 2012). The widespread presence of active methane seeps in the Arctic are hypothesized to be a result of the dissociation of gas hydrates (Westbrook et al., 2009; Sarkar et al., 2012; Bünz et al., 2012; Portnov et al., 2013; Berndt et al., 2014; Portnov et al., 2016). In addition, methane

gas has a very high greenhouse warming potential (~32 times more than carbon dioxide; Etminan et al., 2016).

- With an increase in the global energy demand, focus on the commercial exploitation of gas hydrates has grown (Boswell et al., 2015; Johnson & Max, 2006). Carbon emissions from methane is significantly less than from conventional fossil fuels. Some of the largest energy importing nations (USA, China, India, Japan, South Korea, etc.) have rich gas hydrate deposits in their continental margins and these nations see gas hydrates as a future energy resource that can meet energy demands of these nations for decades (Riedel et al., 2010). Japan and China have already carried out successful production tests of methane gas from gas hydrates (Konno et al., 2017; Li et al., 2018; Chen et al., 2018). However, there are many environmental concerns that require apt consideration before starting any large-scale commercial exploitation (Nagakubo et al., 2011).
- The presence of gas hydrates and free gas in marine sediments can pose a serious geohazard (Maslin et al., 2010). Gas hydrate dissociation decreases the stiffness of the matrix, potentially resulting in slope instability and marine landslides (Paull et al., 2007). There are also concerns of blowouts associated with drilling through gas hydrate systems (McConnell et al., 2012).
- The formation of gas hydrates in pipelines that bring oil and gas upwards, generates issues with flow assurance creating disruptions in the oil and gas production (Sloan et al., 2011). Normally, chemicals that inhibit the formation of gas hydrates are used to keep pipelines from clogging (Lund et al., 1996).

In order to understand gas hydrates' energy, climate change and geohazard potential, it is necessary to better understand occurrences of gas hydrates in different geological settings. Moreover, there is a large difference in the lower (455 Gt of carbon) and upper (74,400 Gt of carbon) estimates of the global gas hydrate inventory (Wallmann et al., 2012; Klauda & Sandler, 2005; Milkov, 2004; Buffett & Archer, 2004; Dickens & Forswall, 2009; Dawe & Thomas, 2007). Hence, there is a need to get more accurate estimates of the amount of gas hydrates stored in different geological settings.

3. Occurrence of natural gas hydrates

Availability of low molecular weight gas, water, low temperature and high-pressure are prerequisites for the formation of gas hydrates (Rempel & Buffet, 1997). In continental margins and permafrost environments, these prerequisites are fulfilled and gas hydrates lock large amounts of in-situ produced microbial methane (methane produced due to microbial biodegradation of organic matter) and thermogenic methane (methane produced at deeper depth due to thermal breakdown of organic matter) (Kvenvolden, 1993). The majority of natural gas hydrates occur in marine environments (~99%) and a small proportion of gas hydrates occur in permafrost environments (~1%) (Mclver, 1981; Ruppel, 2015). However, a significant amount of gas hydrates potentially stored in subglacial conditions is still unexplored (Wadham et al., 2012). In addition, there are a few inland locations like Baikal Lake (Khlystov et al., 2013), Qilian mountains (Lu et al., 2016), Tibetan plateau (Yang et al., 2010), etc. that host a minor fraction of the global gas hydrate inventory.

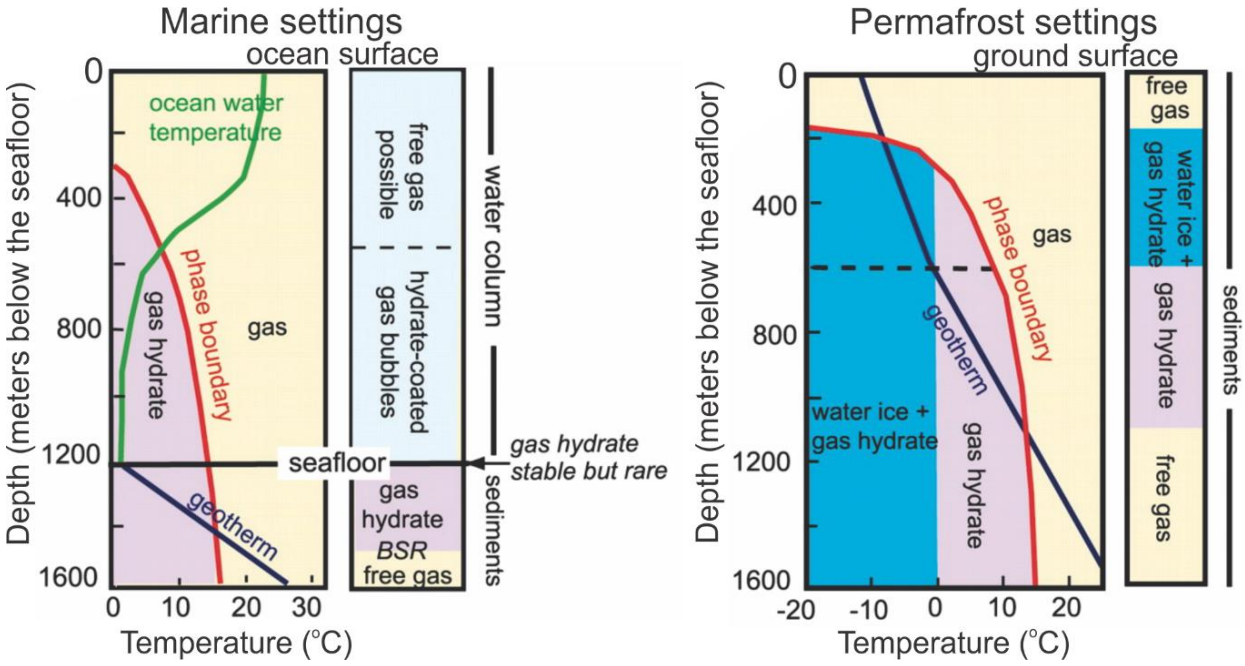

Figure 1. Schematic description of the variation of phase boundaries of gas hydrate stability with depth due to variations in pressure temperature conditions (modified from Ruppel et al., 2007).

In marine environments, gas hydrates are stable below ~500 m seafloor depth in temperate latitudes and below ~300 m seafloor depth at high Arctic latitudes, where bottom water temperature is colder (Ruppel & Kessler, 2017). In sub-seafloor sediments, the temperature increases with depth depending on the heat flow from below and the geothermal gradient at that

specific site (Macelloni et al., 2015). The requirements of low temperature and high-pressure for gas hydrate formation is therefore, met within a certain depth range below the seafloor (Figure 1). Below this depth, the increase in pressure is not able to compensate for the increase in temperature in sediments (Figure 1; Sloan, 1998). Here, gas hydrates are not stable and free gas often occur below the base of the gas hydrate stability zone (GHSZ) as the presence of gas hydrates in the sediments decreases the permeability and traps the free gas below (Figure 1). In permafrost settings, the pressure and temperature increases with depth (Figure 1). Due to freezing conditions, the ground temperature is very low and gas hydrate becomes stable after a certain depth due to the increase in overburden pressure. Gas hydrates in permafrost remain stable up to a depth after which temperature becomes too high to be compensated by the increase in pressure (Figure 1).

Gas hydrates can occur in sediments anywhere within the GHSZ. However, the distribution of gas hydrates within the GHSZ is generally very sporadic. This is because of the dependence of gas hydrate formation on the availability of hydrocarbon gas and pore water, salinity, permeability, porosity, etc. apart from the pressure and temperature requirements (Duan et al., 2011). All these factors depend on the regional and local geologic conditions of the study area. The amount of organic content in a sediment decides the amount of in situ methane production due to microbial and thermogenic processes (Waseda, 1998). In addition to biogenic methane, there can also be an influx of abiotic methane in some cases (Etiope & Lollar, 2013; Johnson et al., 2015). Structural and stratigraphic aspects of a geological setting control the fate of methane and other fluids. Faults and fractures give preferential migration pathways and largely control the upward migration of fluids (Jain & Juanes, 2009). Permeability and porosity within different formations induce stratigraphic control and regulate the upward and lateral migration of fluids (Nimblett & Ruppel, 2003; Dai et al., 2012). All these geological factors (permeability, porosity, faults, fractures, total organic content, salinity, heat flow, etc.) vary with geological settings and gas hydrates occur in a very wide range of sedimentary environments. Hence, it is useful to study the evolution of geological settings in a sedimentary basin in order to understand the evolution of a gas hydrate system (Collett, 2009; Max & Johnson, 2014). The lack of knowledge about the present- and paleo-geological conditions create limitations in understanding the present-day gas hydrate system. A detailed study of the sedimentary basin evolution in context with the gas hydrate system gives insights about causes behind variations in saturation and distribution of gas hydrates at small and large scales within a basin.

Gas hydrate distribution within sediments vary also at a microscopic scale (Ecker et al., 1998). Above discussed geological factors (permeability, porosity, availability of water, quantity of available methane, etc.) and some additional factors like the grain size of host sediments, capillary effects, etc. control the formation and microstructural distribution of gas hydrates in different geological environments (Duan et al., 2011; Jain & Juanes, 2009). Gas hydrates can occur in different morphologies within the GHSZ due to these factors. Gas hydrate morphologies are classified in different ways (Ecker et al., 1998; Dai et al., 2004; Sava & Hardage, 2006). Based on these studies, a detailed classification of common gas hydrate morphologies as illustrated in Figure 2 is as follows:

a) Pore-filling gas hydrates without any contact with host sediments
b) Pore-filling gas hydrates coating host sediments
c) Gas hydrate cementing host sediments
d) Gas hydrate as an inclusion/matrix grain
e) Gas hydrate filling in fractures/faults/veins
f) Layered/massive/nodular gas hydrate deposits

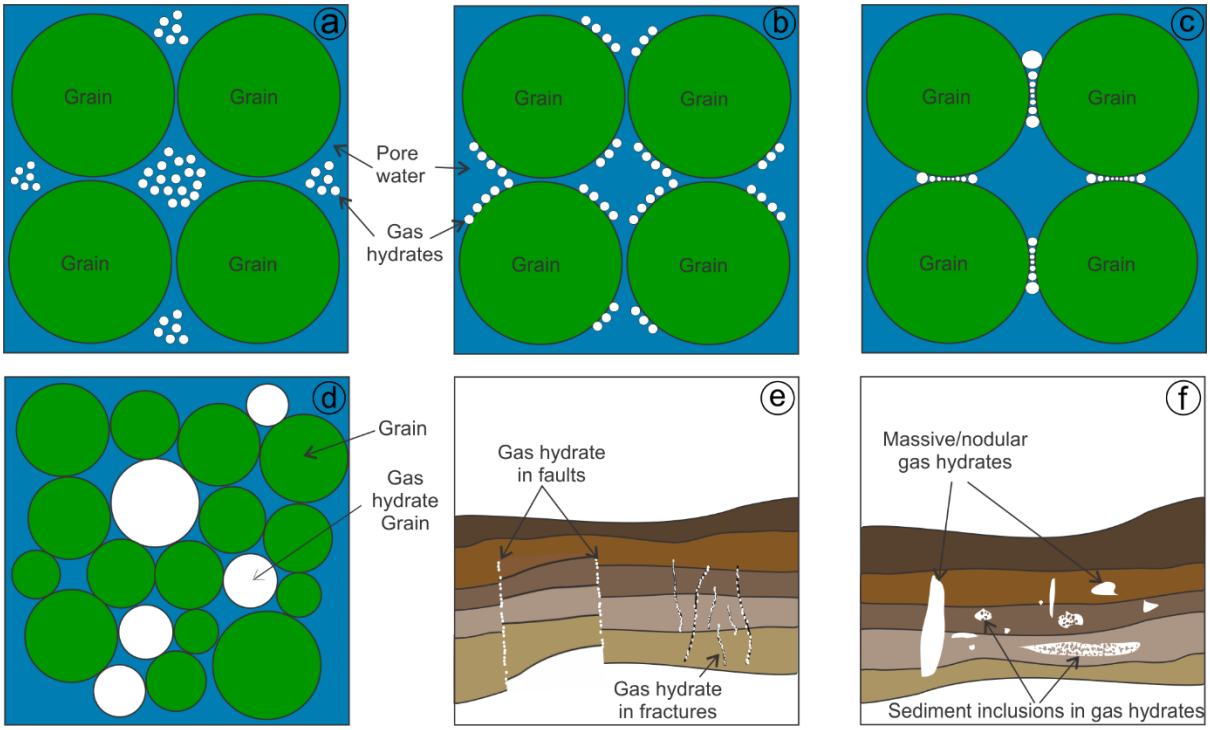

Figure 2. Schematic description of end member gas hydrate morphologies (pore-filling (a), grain coating (b), cementing (c), inclusion/matrix frame (d), fracture/fault filling (e) and massive/nodular gas hydrate deposits).

Naturally occurring gas hydrates are concoction of these several probable end member morphologies. Highly porous coarse-grained sedimentary environments favor the formation of pore-filling gas hydrates (Holland et al., 2018; Babu et al., 2013; Dai et al., 2012; Jain & Juanes, 2009). Gas hydrate saturation also affects the gas hydrate morphology (Sahoo et al., 2018). In highly porous sediments, gas hydrates at low saturations tend to occupy pore spaces (Figure 2a) whereas, hydrates at higher saturations tend to coat (Figure 2b), cement (Figure 2c) and even displace grains in the background matrix becoming a part of the matrix itself (Figure 2d) (Dai et al., 2012). Fine-grained sedimentary environments with low permeability restrict the flow of gas to pore spaces and thus, limit the presence of pore-filling gas hydrate deposits. Fractures and faults provide permeable pathways for the methane gas in the fine-grained sediments (Jain & Jaunes, 2009; Weinberger & Brown, 2006; Liu & Flemings, 2007). Hence, such sedimentary environments have predominant presence of gas hydrates in faults/fractures (Holland et al., 2018; Holland & Schultheiss, 2014) and the presence of massive/nodular gas hydrates (Figure 2e and 2f). Different fluids have different adhesion to different sediment grains due to the differences in surface tension forces/capillary effects (Jain & Juanes, 2009). The likelihood of the presence of gas hydrate coated sediment grains at low gas hydrate saturations thus also depend on capillary forces (Duan et al., 2011; Riestenberg et al., 2003; Daigle & Dugan, 2011; Kerkar et al., 2009, 2014). Several physical properties, especially elastic and resistive properties, of gas hydrate-bearing sediments depend on the nature of spatial relationship between gas hydrates and host sediments (i.e. gas hydrate morphology).

4. Properties of gas hydrates

4.1. P- and S-wave Seismic velocities

Seismic wave propagation velocities in a medium depend on the bulk and shear modulus of a medium (Sheriff & Geldart, 1995). Bulk modulus (K), a measure of compressive strength, is the resistance in an elastic medium to a uniform compression; and shear modulus (μ), a measure of shear strength, is the material's response to shear stress (Sheriff & Geldart, 1995). The compressive strength of a medium depends on grains and pore fluid properties whereas the shear strength depends on stiffness of a granular skeleton (Biot, 1956; Waite et al., 2009). The presence of gas hydrates increases the compressive and shear strengths of a medium depending on morphology (Dvorkin & Nur, 1993; Ecker et al., 1998; Priest et al., 2005; Priest et al., 2009; Dai et al., 2012). Gas hydrates support the granular skeleton of a matrix in cases where gas hydrates coat grains, cement grain contacts or occur as an inclusion/grain. In such cases, the presence of gas hydrates increase the shear strength of a medium whereas the increase in shear strength is negligible in cases where gas hydrates occupy the pore spaces exclusively (Ecker et al., 1998; Yun et al., 2005; Waite et al., 2009). Broad classification of gas hydrates morphology as pore filling (present within pore spaces of sediments) and load bearing (gas hydrates contributing to the granular skeleton of the composite) deposits is the most commonly used classification in the literature (Ecker et al., 1998). The increase in compressive strength is slightly higher for load bearing gas hydrate morphologies compared to the pore-filling gas hydrate morphologies (Dai et al., 2012). The presence of free gas as a pore fluid decreases the compressive strength of a medium and has a little effect on the shear strength of a medium, as displacement of pore water by gas does not alter granular skeleton (Domenico, 1977; Gei & Carcione; 2003).

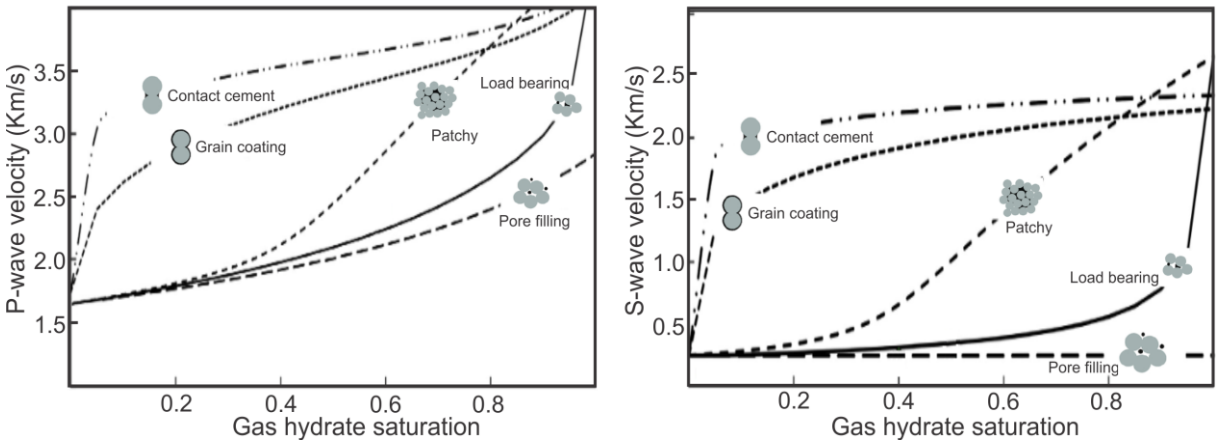

Figure 3. Schematic description of the variation in P- and S-wave velocities with gas hydrate saturation and morphology (modified from Mahabadi et al., 2019 and Dai et al., 2012).

P- and S-wave seismic velocities depend on the compressive and shear strength of a medium, respectively (Sheriff & Geldart, 1995). Gas hydrates have high bulk (K=7.9 GPa) and shear modulus (μ =3.3 GPa) compared to water that has low bulk modulus (K=2.17 GPa) and no shear strength (μ =0) (Best et al., 2013). Seismic velocity estimates from synthetic pure gas hydrate show high P- (3.65 km/s) and S-wave (1.89 km/s) velocities for pure hydrates (Waite et al., 2000). Replacement of pore water by gas hydrate increases the P-wave velocity (Figure 3; Lee, 2007; Lee et al., 2010). The S-wave velocity also increases due to the presence of gas hydrates and the amount of increase in the S-wave velocity depends on the contribution of gas hydrates to the granular skeleton of the composite (Figure 3). Thus, the P and S-wave velocity of gas hydrate-bearing sediments is a function of mineral composition, porosity, pore fluid, gas hydrate saturation, gas hydrate morphology, grain connectivity, degree of consolidation or lithification, etc. (Figure 3; Berryman, 1992; Jakobsen et al., 2000). All these factors can be included in a rock physics model to get a response from gas hydrate-bearing sediments to a seismic input (Chand et al., 2004). The presence of free gas within the GHSZ or below the GHSZ decreases the P-wave velocity and has a negligible effect on the S-wave velocity as gases do not shear (μ =0) and they have a very low bulk modulus (K=100-150 kPa).

4.2. Seismic attenuation

Seismic waves loose energy as they pass through a medium (Biot, 1956; Johnston et al., 1979). Geometrical spreading, scattering and intrinsic attenuation are three main reasons behind the loss of energy with propagation (Teng, 1968; Fu, 1947; O'Doherty & Anstey, 1971). Intrinsic attenuation accounts for the loss of energy due to conversion of elastic energy to heat energy in a medium (Mavko & Nur, 1979; Winkler et al., 1979). Higher frequencies decay at a rapid rate in a medium compared to lower frequencies (Knopoff; 1964; Johnston et al., 1979). Through the analysis of the differential decay of different frequencies, seismic quality factor (Q) can be estimated to quantify seismic attenuation in a medium (Bath, 1974; Raikes & White, 1984; Janssen et al., 1985; Quan & Harris, 1997; Zhang & Ulrych, 2002). Q is inverse of seismic attenuation and shows the medium's ability to allow seismic energy to propagate without decay. Q is an intrinsic property of a medium and it varies with a medium (Toksöz et al., 1979; Toksöz & Johnston, 1981). The existence of different fluids in a medium is often detected using Q analysis; for example, free gas in a medium considerably decreases the seismic Q (O'Connell & Budiansky, 1977; Murphy et al., 1986; O'Hara, 1989). Low Q anomalies is one of the indicators of the presence of hydrocarbons in the subsurface and Q analysis is a very useful

attribute used in oil and gas industry to detect the presence of hydrocarbons (Rapoport et al. 2004).

There is no uniform scientific consensus about the effect of the presence of gas hydrates on the Q value (Guerin et al., 1999; Chand et al., 2004; Priest et al., 2006; Rossi et al., 2007; Sain & Singh, 2011; Best et al., 2013; Dewangan et al., 2014). Studies that involve acquisition of remote data, i.e. without any proximal presence or direct contact of instruments with gas hydrate-saturated sediments (mainly 2D, 3D and ocean bottom seismic data), show high Q in gas hydrate-saturated sediments (Rossi et al., 2007; Sain & Singh, 2011; Best et al., 2013; Jaiswal et al., 2012; Dewangan et al., 2014; Singhroha et al., 2016). The observed results are supported by the argument that the presence of gas hydrate increases the stiffness of the matrix/granular skeleton and stiff materials often have high Q. However, most of the laboratory experiments and data acquired through vertical seismic profiling (VSP) or well logs show low Q in gas hydrate-saturated sediments (Guerin et al., 1999; Wood et al., 2000; Guerin & Goldberg, 2002, 2005; Matsushima, 2005; Pratt et al., 2005, 2006; Bellefleur et al., 2007; Best et al., 2013). The observed low Q values in gas hydrate-saturated sediments is supported by the fact that there can be a potential presence of squirt flows that attenuates the seismic energy leading to low Q values in a medium. However, the presence of small amounts of free gas in the GHSZ can also induce attenuation. A recent study (Sahoo et al., 2018) shows the presence of free gas under gas hydrate stability conditions due to unavailability of water. All the methods that involve drilling/coring disturbs the in-situ sediments and some hydrate can convert in free gas due to the heat produced while drilling/coring resulting in the observed low Q values. There have been very limited number of studies that explore potential changes in seismic Q due to changes in gas hydrate morphology (Best et al., 2013).

4.3. Electrical resistivity

Electrical conductivity, inverse of electrical resistivity, in a medium is primarily due to the presence of charged ions in fluids present within the pore spaces (Archie, 1942). Hence, the presence of connected pores and saline pore water are required for good electrical conductivity in a medium (Archie, 1942). The presence of gas hydrates or free gas in the pore spaces inhibits the natural flow of charged ions and thus the presence of gas hydrate-saturated marine sediments increases the resistivity (or reduces the conductivity) (Pearson et al., 1983; Cook, 2010). In addition, gas hydrate dissociation releases fresh pore water and decreases the salinity

of a medium and thus gas hydrate dissociation is often accompanied with an increase in electrical resistivity.

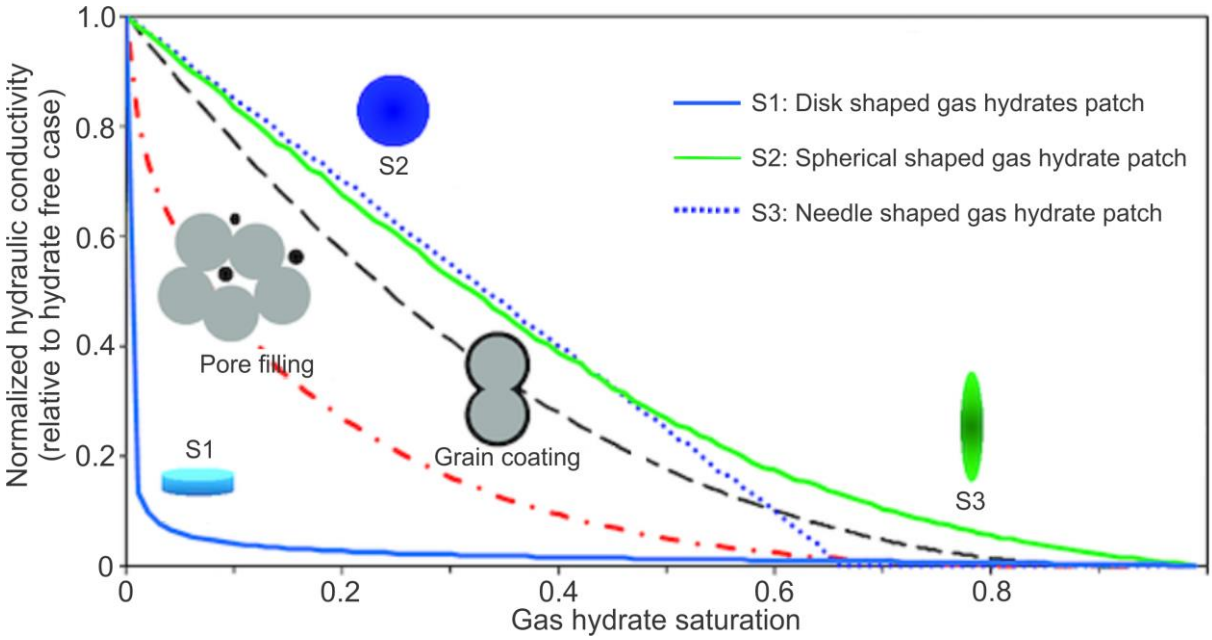

Figure 4. Schematic description of the variation of electrical conductivity with gas hydrate saturation and morphology (modified from Dai et al., 2012).

Pure gas hydrate is primarily an insulator (~5 order of magnitudes higher resistivity than seawater) and the conduction in gas hydrate-saturated marine sediments mainly takes place through networks parallel to gas hydrates (Pearson et al., 1983; Du Frane et al., 2015). Shallow sediments (~0-100 m) below the seafloor have high porosity and thus very low resistivity (~1 Ωm) and hence increases in resistivity due to the presence of gas hydrates are detectable even though resistivity anomalies are small (Collett & Ladd, 2000; Boswell et al., 2012; Riedel et al., 2005; Sun et al., 2012; Hsu et al., 2014). There is a large variation in the resistivity anomaly (~1-250 Ωm) measured in gas hydrate-saturated marine sediments (Figure 4; Schwalenberg et al., 2005, 2010, 2017; Constable et al., 2016; Boswell et al., 2012; Collett et al., 2012). This variation is due to the variation in gas hydrate saturation and morphology (Figure 4). Gas hydrate morphology has a big impact on the resistivity values (Figure 4; Spangenberg, 2001). Gas hydrates-filled faults and fractures (comparable to the S1 case in Figure 4) show higher resistivity for similar gas hydrate content in a given composite (Lee & Collett, 2009, 2012; Cook et al., 2010; Cook et al., 2012).

5. Exploration techniques for gas hydrates

As discussed in previous section, gas hydrates have several properties that make them distinct from background host sediments. Based on these differences in physical properties, different geophysical methods can be deployed for the remote or in-situ detection of gas hydrates. Different geophysical methods measure different physical properties and map the subsurface using differences in these physical properties. Since seismic and resistive properties of gas hydrates are distinct from background host sediments, geophysical exploration methods that measure these properties are often deployed to study the distribution of gas hydrates in the subsurface.

Seismic methods rely primarily upon differences in seismic velocity and seismic Q to detect the presence of gas hydrates. There is a sharp contrast in seismic velocity and density of pore fluids at the base of the GHSZ (Sloan, 1998). The presence of gas hydrates in the sediments above the base of the GHSZ increases the P-wave velocity and the presence of free gas in the sediments below the base of the GHSZ decreases the P-wave velocity (Shipley et al., 1979; Kvenvolden & McMenamin, 1980; Yuan et al., 1996). This change in the P-wave velocity creates a sharp impedance contrast at the base of the GHSZ resulting in a distinct bottom simulating reflection (BSR) due to a substantial reflection of seismic energy from the base of the GHSZ (Shipley et al., 1979). It is easy to identify a BSR in a seismic section as its polarity is reversed compared to the seafloor polarity and a BSR crosscuts geologic strata as it follows a trend parallel to the seafloor (due to the pressure and temperature controls on gas hydrate stability) (Shipley et al., 1979; Carson & Screaton, 1998). The presence of a BSR provides an indirect evidence for the presence of gas hydrates in marine sediments. However, a BSR gives little or no information about the distribution and amount of gas hydrates within the GHSZ. In addition, the absence of a BSR in a region that fulfills the requirements of the stability of gas hydrate does not rule out the possibility of the presence of gas hydrates as there might not be sufficient gas or gas hydrates at the base of the GHSZ to generate a detectable BSR. Gas hydrates may occur without any observable BSR (Holbrook et al., 1996).

Seismic velocity and seismic Q models within the GHSZ can help in mapping the distribution of gas hydrates (Madrussani et al., 2010; Bünz et al., 2005; Kumar et al., 2007; Rossi et al., 2007; Westbrook et al., 2008; Chabert et al., 2011; Wang et al., 2018; Song et al., 2018; Singhroha et al., 2016; Dewangan et al., 2014). The resolution of derived velocity models thus dictate the resolution of mapped gas hydrate deposits. The combined study of P- and S-wave

velocities potentially gives additional information about gas hydrate morphology and better constrains gas hydrate saturation estimates (Bünz et al., 2005; Chabert et al., 2011; Song et al., 2018). Analysis of seismic Q anomalies in the GHSZ further hints and limits regions where gas hydrates may be present within sediments (Rossi et al., 2007; Singhroha et al., 2016). Low seismic Q anomalies below the BSR due to the presence of free gas below the GHSZ are very useful and are a distinctive characteristic of the occurrence of free gas below the GHSZ (Rossi et al., 2007; Madrussani et al., 2010; Singhroha et al., 2016). Controlled source electromagnetics (CSEM) and resistivity well logs use the differences in the electrical resistivity in order to detect the presence of gas hydrates (Hyndman et al., 1999, Collett & Ladd, 2000, Malinverno et al., 2008).

These seismic and resistive properties can be studied remotely (using 2D and 3D marine seismic or CSEM) or in-situ (using pressure cores or well log data). Large-scale marine seismic and CSEM surveys are important to get a good idea about the regional distribution of gas hydrates. Information derived using pressure cores or well log data constrains and provide better estimates about the gas hydrate saturation and morphology at one location (Lee & Collett, 2006). Some additional well logs, like density porosity (DPHI), nuclear magnetic response (NMR), neutron porosity, temperature, caliper, etc. may also detect and quantify gas hydrates in sediments (Collett et al., 2011).

The selection of a geophysical exploration method in an area depends on the stage of gas hydrate exploration. The initial stage of gas hydrate exploration usually involves acquisition of 2D seismic data to map the potential presence of gas hydrate deposits by observing BSR. 3D seismic data give further information about the spatial distribution of BSR, fluid flow features and potential stratigraphic and structural settings that can play an important role in the evolution of gas hydrate deposits over time. Combined P- and S-wave velocity analysis, seismic Q and resistivity analysis constrains and quantifies gas hydrates within the GHSZ. At selected locations of interest as identified through this detailed analysis, well logs and pressure cores can provide very accurate details about gas hydrates. Thus, it is important to review earlier studies in an area and select the appropriate exploration method that can further advance the previous findings about the gas hydrate system keeping in mind available resources.

6. Study area

Gas hydrates widely occur in the Arctic. These hydrate deposits have gained a special attention lately, as these are potentially more sensitive to climate changes than deposits in other continental margins (Overpeck et al., 1997; Ruppel & Kessler, 2017). The North Atlantic Current brings relatively warm (>3-5°C) and saline water in the Arctic (Hansen & Østerhus, 2000). The Fram strait is the only deepwater gateway (~5.6 km depth in Molloy deep) between the Arctic and North Atlantic (Von Appen et al., 2015). This present study focusses on the gas hydrate system in the Vestnesa Ridge, a large contourite drift deposit in the Fram Strait (Figure 5). This section contains detailed discussion on the background geology of the study area.

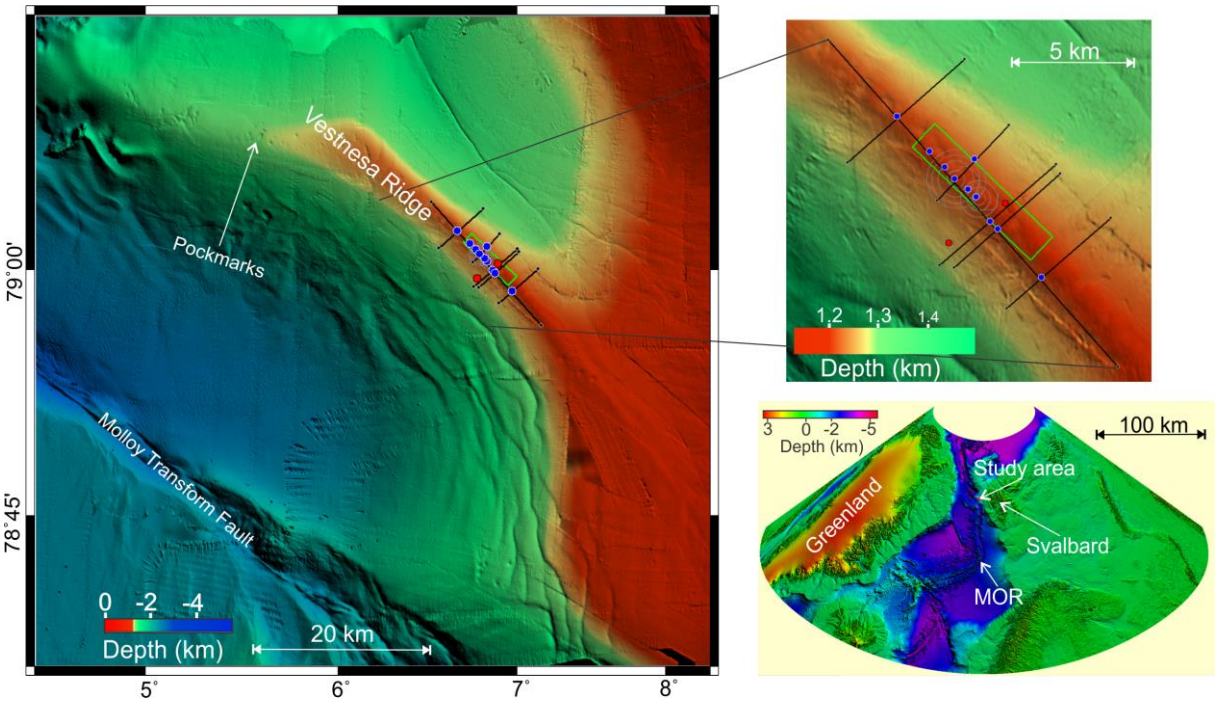

Figure 5. Bathymetry map of the study area. Green rectangle shows the area in which 3D seismic data is acquired. Blue dots show the location of OBS stations. Black lines show the acquisition lines used for some OBS stations. Circles around two OBS stations show the circular tracks on which azimuthal seismic data is acquired for two OBS stations.

6.1. Structural evolution of the study area

The evolution of Fram strait was preceded by the continental break up and sea-floor spreading in the early Eocene along Reykjanes, Aegir, and Mohns Ridges (Demenitskaya & Karasik, 1969; Talwani & Eldholm, 1977; Eldholm et al., 1987). Heat flow models suggested the first intrusion of magma around 60 mya at ≈78° N and the beginning of the formation of oceanic crust around 40-50 mya (Crane et al., 1988). The Fram strait started opening after the change in the plate movement (~33 ma) between Svalbard and Greenland from strike slip to oblique

divergence (Vogt, 1986; Myhre & Eldholm, 1988). High heat flow anomalies, potentially hinting at high magmatic activity, occurred around 14 mya to the west and around 13 mya to the east of the northern Knipovich Ridge and around 36 mya on the eastern flank of the southern Knipovich ridge (Crane et al., 1988).

The shearing along faults between Greenland and Svalbard resulted in the western Spitsbergen Orogeny (Harland et al. 1974, Steel et al. 1985). Increased sedimentary load turned the central Spitsbergen basin into a foreland basin. The Western Spitsbergen Orogeny stopped in early Oligocene and the spreading direction changed from the NNW-SSE to the NW-SE direction. This spreading axis later developed into the Spitsbergen Shear Zone. This created an asymmetric, ultra-slow and obliquely spreading ridge system in the region. Heat flow, seismic, and topographic data point towards asymmetric sea floor spreading across the Knipovich Ridge (Johnson et al., 1972; Vogt et al., 1982; Kovacs & Vogt, 1982; Nunns & Peacock, 1983; Nunns, 1983). The results also indicated that the rifting was and is currently occurring in the asymmetric pure shear or high angle simple shear mode centered on a system of faults adjacent to continental margins of Svalbard. Crane et al. (1991) tried asymmetric pure shear, asymmetric simple shear and Ridge jumping models to match the measured heat flow values. With the help of integration of paleomagnetic record in the Fram Strait with geomagnetic polarity time scale, Engen et al. (2008) reconstructed the pattern of seafloor spreading with time. Around 23 mya, rifting shifted further north along the Molloy Ridge. Around 10-15 mya, further continental break-up occurred leading to the formation of the Fram Strait. This entire process formed four separate sedimentary basins, separated by Knipovich, Molloy and Hovgård Ridges, which developed with the spreading of the Eurasian and the North American plates (Eiken & Hinz, 1993). These four sedimentary basins were as follows:

1. The western Svalbard (Spitsbergen) slope and rise east of the Knipovich Ridge
2. The Vestnesa depocentre east of the Molloy Ridge together with Yermak Plateau
3. The Greenland-Spitsbergen sill located between the Hovgård Ridge and the Molloy transform fault
4. The Boreas Basin

Engen et al. (2008) used gravity and magnetic data to study the basement and regional crustal structure. Since oceanic crust is heavier than continental crust, anomalies observed in gravity data give indication about the continental and oceanic crust thicknesses and the depth to basement in this region. Results from the gravity, magnetic and seismic data suggest that the sediment thickness in these basins mostly lies in the range of 1-3 km, but sediments are thicker

(maybe more than 6 km) in the west Svalbard margin (Engen et al., 2008; Sellevoll et al., 1991; Ritzmann et al., 2002, 2004; Ritzmann & Jokat, 2003).

6.1.1. Faults

Rifting at Molloy and Knipovich Ridges and shear motion along the Spitsbergen Transform Fault play a big role in the development of tectonic stresses in the region. Half grabens, typically with normal faulting and rift flank uplifts mainly on one side, occur in the west Svalbard margin (Amundsen et al., 2011). These half grabens comprise of thick sediment layers and bounding faults dipping towards the ridge axis with deep roots in the basement (Amundsen et al., 2011). Tectonic stresses create and decide the orientation of the fault (especially regional faults) and changes in tectonic stresses potentially activate or deactivate faults. Multiple-seepage events as observed in the western Svalbard margin can be due to active faulting and dilation of faults in the region (Plaza-Faverola et al., 2015; Plaza-Faverola & Keiding, 2019; Waghorn et al., 2018). Faults in this region can potentially act as fluid migration pathways bringing deep sourced warm fluids upwards (Madrussani et al., 2010; Waghorn et al., 2018). The evolution of deeper detachment faults over geologic time lead to the formation of folds in the Svyatogor Ridge and episodic releases of fluids through the seafloor in this area may be related to these deep large-scale basement faults (Waghorn et al., 2018). Faults at shallower depths in the GHSZ can also be potentially plugged with gas hydrates and can act as a seal (Madrussani et al., 2010; Goswami et al., 2017).

6.2. Stratigraphic evolution of study area

The stratigraphic evolution of the west Svalbard margin is mainly studied using reflection seismic data and results from different drilling programs in the study area. The presence of features like migrating sediment waves, contourite mounds and moats in the processed multichannel seismic profiles hint towards sedimentation under the influence of bottom-water contourite currents (Eiken & Hiz, 1993; Stein et al., 2005; Ottesen et al., 2005). Studies indicate that sediments beyond the shelf break in the Western Svalbard margin mainly consist of turbiditic, glaciomarine and hemipelagic sediments (Howe et al., 2008).

Eiken and Hinz (1993) have identified three seismic units (YP-1, YP-2 and YP-3) using multichannel seismic data on the southern Yermak Plateau and the Vestnesa Ridge that has more than 2 km of sediments. The YP-3 seismic unit is the youngest seismic unit and consists of Quaternary sediments with a prograding sediment depocenter at outer shelf and circular shaped depocenter in the Vestnesa Ridge area. This seismic unit becomes quite thin between

the two depocenters. The boundary between the YP-3 seismic unit and the YP-2 seismic unit occurs around ~2.7 Mya and represents the base of glacial deposits (Knies et al., 2009). The YP-2 seismic unit mainly consists of Pliocene to mid Miocene sediments and it downlaps to the west with westward thickening wedges. The boundary between the YP-2 seismic unit and the YP-1 seismic unit potentially marks the onset of strong deep-ocean circulation (Mattingsdal et al., 2014). The YP-1 seismic unit is the bottommost sequence with sub paralleling reflection pattern. Some typical contourite features like moats, mounds, wavy patterns etc. occur in the seismic units YP-2 and YP-3. Therefore, there is a strong influence of bottom water currents in the stratigraphic evolution of these seismic units.

There are two drill sites in the study area. Deep sea drilling program (DSDP) site 344 lies near the Knipovich Ridge and ocean drilling program (ODP) site 986 lies on the western Svalbard margin. The main objective of DSDP drilling operation was to obtain samples down to the basement and to determine the nature and age of sediments. Results from ODP site helps in documenting the geological development of the west Svalbard margin from the late Pliocene to the present. Sedimentological analysis in this site also helps in improving the understanding about the seismic stratigraphy and age of sediments. The seismic units mapped using multichannel seismic data are also correlated with the results obtained from DSDP and ODP drill sites to get a good estimate of depositional age and nature of these sedimentary packages (Forsberg et al., 1999; Eiken & Hinz, 1993). Sedimentation, mainly comprising of silty turbidites, is high (~105 cm/yr) from the mid Weischselian to the Last glacial maximum (Howe et al., 2008). Sedimentation rate is relatively slow (<10 cm/yr) during the last glacial maximum to the early Holocene with sediment core analysis (Howe et al., 2008) revealing the occurrence of muddy-silty contourites with abundant IRD (ice-rafted debris).

6.3. Vestnesa Ridge

Vestnesa Ridge is a sedimentary ridge formed as contourite drift deposit on the western Svalbard margin and northeast of the Molloy Transform at ~79° N in water depths of ~1200 m (eastern segment) to ~1500 m (western segment). This sediment drift bends from SE-NW direction to almost E-W direction in the north. Geothermal gradients along the Ridge are high (>80-120 °C km^{-1}) (Crane et al., 1991). Numerous pockmarks, typically associated with focused fluid flow, are present at the crest of the Vestnesa Ridge (Bünz et al., 2012). Several pockmarks in the eastern segment of Vestnesa Ridge are actively venting methane gas through the seafloor (Bünz et al., 2012). A large number of pockmarks in the western segment of Vestnesa Ridge (i.e. after the Ridge bends from SE-NW direction to almost E-W direction) are

inactive. Seepage of methane from some selected pockmarks in the Vestnesa Ridge makes it interesting to understand the dynamics of gas hydrates underneath and their link with the methane seepage.

6.4. Gas hydrate system in the Vestnesa Ridge

Sediments in the Vestnesa Ridge fulfill the temperature and pressure requirements for the stability of gas hydrates (Plaza-Faverola et al., 2017). A prominent BSR reflection is visible on the 2D and 3D marine seismic data acquired over the years (Eiken & Hinz, 1993, Posewang & Mienert, 1999, Vanneste et al., 2005; Bünz et al., 2012; Plaza-Faverola et al., 2015). Gas hydrates are also sampled directly from the Vestnesa ridge during the R/V Maria S. Merian cruise in 2016 (Bohrmann et al., 2016). Hence, the presence of gas hydrate system in the Vestnesa Ridge is well established.

This gas hydrate system is present in a unique geological setting of proximal ultra-slow spreading plates and a young (<20 mya) and hence, relatively hot oceanic crust. The presence of pockmarks in the crest area of the Vestnesa Ridge and the absence of pockmarks in the flanks of the Vestnesa Ridge suggest a strong topographical control on the migration of fluids (Vogt et al., 1994; Hustoft et al., 2009; Bünz et al., 2012). Gas hydrate-bearing sediments have low permeability and fluids can migrate below the base of the GHSZ and expel itself near the crest area (Bünz et al., 2012; Goswami et al., 2015). Pockmarks that are dormant now were active in the past (Consolaro et al., 2015; Sztybor & Rasmussen 2016; Panieri et al., 2017). Plaza-Faverola et al. (2015) suggested tectonic control on the seepage of methane gas through pockmarks. Changes in methane seepage from pockmarks with time and selective seepage of methane from the eastern segment of the Vestnesa Ridge (i.e. before it bends) suggest that tectonic stresses might control the opening and closing of faults. This makes a selected group of pockmarks active now and it changes with changes in tectonic stress direction with time (Plaza-Faverola et al., 2015).

There is a little knowledge about the regional distribution of gas hydrates within sediments of Vestnesa Ridge (Goswami et al., 2015). Therefore, it is important to acquire data in the Vestnesa Ridge and apply methods that can help us in studying the distribution of gas hydrates and various factors that control their distribution.

7. Data and methods

7.1. Data acquisition

We acquired different datasets over several years to study the gas hydrate system in the Vestnesa Ridge. This section briefly summarizes some important seismic data acquisition and processing parameters.

7.1.1. High resolution P-Cable 3D Seismic data

In 2013, we acquired a high-resolution (20-300 Hz) P-Cable 3D seismic dataset (survey area shown as green rectangle in Figure 5), with 14 25-m-long streamers towed parallel behind R/V Helmer Hanssen (Planke et al., 2009; Plaza-Faverola et al., 2015; Waage et al., 2019). Shots were fired using a mini GI gun (Sercel; 15⁄15 in^3, 170 bar firing pressure) at 6 s firing interval and recorded traces had a 3 s record length with 0.25 ms sampling interval. Streamers originally spaced at 12.5 m have effective spacing between 6 m and 10 m due to curvature in the cross cable. Each streamer had eight receiver groups with a group spacing of 3.125 m. The source receiver offset varies from 97 to 143 m generating a geometry that had a bin size of 6.25 × 6.25 m^2.

This dataset is used to analyze the spatial distribution of seismic Q in different layers in the GHSZ and the free gas zone. Further details about the dataset, seismic data processing steps, and seismic Q analysis are included in Article 1. This dataset is also used in article 2 and article 3 for seismic interpretation.

7.1.2. Ocean bottom seismic experiments

Several studies in the past have used multicomponent ocean bottom seismic (OBS) data to study gas hydrate reservoirs in different geological settings (Singh et al., 1993; Pecher et al., 1996; Andreassen et al., 2003; Bünz et al., 2005; Kumar et al., 2007; Chabert et al., 2011; Satyavani et al., 2016; Song et al., 2018; Wang et al., 2018). P- and S-wave velocity models can be estimated using OBS data and these seismic velocity models can be used for the estimation of gas hydrate saturation in sediments. Over several years (2012-2017), we acquired multicomponent ocean bottom seismic (OBS) data near the crest of the eastern segment of the Vestnesa Ridge, which is characterized by the presence of active methane venting pockmarks. Multicomponent OBS instruments record pressure waves and ground acceleration using hydrophone and seismometer attached with the OBS. A seismometer sits on the ocean seafloor and records seismic vibrations in three perpendicular components and the hydrophone records pressure waves in the water column. A mini GI gun (Sercel; 15⁄15 in^3) or GI gun (Sercel; 45⁄45

in^3) was fired at 6 s interval and a firing pressure of 170 bar to provide source energy for the experiments. Nine OBS stations lie on the southwestern side and one OBS station lies on the northeastern side of the Vestnesa Ridge (OBS stations shown as blue dots in Figure 5). Further details about the dataset and processing is discussed in Article 2.

Two OBS sites are selected to get azimuthal OBS data around them (shown with circular tracks in Figure 5). This azimuthal OBS data is used for the azimuthal seismic velocity analysis. This type of seismic velocity analysis gives information regarding small variations in seismic velocities with azimuth. Further details about the dataset and processing is included in Article 3.

7.2. Methods

We apply different methods and approaches to the acquired dataset to estimate different physical properties, mainly, seismic Q and seismic velocities. We have discussed in detail about different methodologies in the articles. In this section, I briefly summarize some of these methods.

7.2.1. Seismic Q analysis

There are different methods for estimating seismic Q in a medium. Some of the most commonly used methods are spectral ratio method (Bath, 1974), centroid frequency shift method (Quan & Harris, 1997), peak frequency shift method (Zhang & Ulrych, 2002), the match-technique method (Raikes & White, 1984) and spectrum-modeling method (Janssen et al., 1985). We have used the spectral ratio method and the centroid frequency shift method for the seismic Q analysis.

Spectral ratio method

A seismic signal changes as it propagates in a medium. The higher frequencies decay more rapidly as compared to the lower frequencies. To estimate the average Q between two different times using the spectral ratio method; we pick two wavelets that are representative of seismic signals at these two times. We calculate the ratio of amplitude spectrums, i.e. spectral ratio, for these two wavelets. The Seismic Q can be estimated from the slope of the changes in the spectral ratio with frequency (Bath, 1974).

Centroid frequency shift method

The centroid frequency of an amplitude spectrum moves towards lower frequencies, as higher frequencies in a seismic signal attenuate at a rapid rate compared to lower frequencies. The

seismic Q in a medium can be estimated from the changes in centroid frequencies with time (Quan & Harris, 1997).

7.2.2. Seismic velocity analysis

The selection of a method for the seismic velocity modeling depends on the type and the quality of a dataset. In a marine setting with a conventional 3D seismic dataset, a P-wave velocity model can be derived through the normal move-out (NMO) analysis of arrival times. For NMO analysis to be accurate, we roughly need the farthest offset comparable or more than the depth of the zone of interest (Sheriff & Geldart, 1995). It is not possible to estimate P-wave velocities using the P-Cable seismic data, as the maximum offset (~140 m) is far less than the seafloor depth (~1200 m) in the Vestnesa Ridge. In order to perform seismic velocity analysis in the Vestnesa Ridge, we deployed OBS stations at the seafloor and acquired wide-angle ocean bottom seismic (OBS) data. We estimate P-wave velocities from PP reflections (i.e. reflected P-waves) and S-wave velocities from PS reflections (i.e. converted waves).

Travel time inversion

We pick different reflection arrivals from the PP and PS components recorded in the multicomponent OBS data. We invert these picked travel times in a layer-stripping manner using Zelt and Smith (1992) based approach to estimate P- and S-wave velocity models. The RMS misfit between estimated travel times (i.e. travel times for the estimated velocity model) and picked travel times is minimum for derived velocity models.

Full waveform inversion (FWI)

The interval P-wave velocity models derived from the travel time inversion have low resolution (>15-20m). The full waveform inversion (FWI) of the OBS data can resolve these velocity models further. Using travel time inversion derived velocity model as an initial model, we apply a downward continuation based 1D FWI approach (Singh et al., 1993) to estimate a high-resolution seismic velocity model at a selected OBS station to get finer details about variations in seismic velocities in the GHSZ with a special focus near the base of the GHSZ.

Azimuthal velocity analysis

We use azimuthal OBS data to analyze variations in seismic velocities with azimuth. We develop an initial 3D velocity model from 3D seismic data and velocity models from OBS stations. Using the azimuthal OBS data, we pick travel times at different offsets in different azimuths. We inverted these picked travel times in a layer-stripping fashion in different

azimuths as 2D models using Zelt and Smith (1992) based travel time inversion approach to estimate azimuthal velocity models for different layers.

7.2.3. SCA/DEM modelling

Different rock physics models establish a relationship between the presence of gas hydrates and different physical properties like seismic velocities and seismic attenuation. The physical properties estimated from datasets can be used to estimate gas hydrate saturations using self-consistent approximation (SCA) – differential effective medium (DEM) theory (Willis, 1997; Nishizawa, 1982; Chand et al., 2004). Using this theory, gas hydrates can be added in a biconnected composite at any porosity and its effect on physical properties can be estimated. We use this approach to estimate gas hydrate and free gas saturations using seismic velocity models derived from OBS data.

8. Articles

8.1. Article 1

Singhroha, S., Bünz, S., Plaza-Faverola, A., & Chand, S. (2016). Gas hydrate and free gas detection using seismic quality factor estimates from high-resolution P-Cable 3D seismic data. Interpretation (Tulsa), 1, SA39-SA54.

The seismic quality factor, Q, is sensitive to the presence of pore fluids. In this article, we explore the potential of high-resolution P-Cable seismic data to detect the presence of gas hydrates. Broad bandwidth data is good for the accurate estimation of the seismic Q. The P-Cable seismic data is unique in terms of the seismic bandwidth that it provides (20-300 Hz). This gives us an opportunity to estimate the seismic Q for different layers within the GHSZ and the free gas zone. The 3D seismic data allows us to map the spatial variation in seismic Q within a layer for the entire seismic cube. This is one of the first such attempts in which seismic Q is estimated for all traces within a 3D seismic dataset. It provides us with an opportunity to link the spatial variation in seismic Q with potential changes in gas hydrate distribution. The spectral ratio method and the centroid frequency shift method are two well-known methods commonly used for the estimation of seismic Q. We have applied these two methods to estimate the seismic Q for all traces in a seismic cube. Seismic Q estimates derived from the spectral ratio method are more fluctuating whereas seismic Q estimates derived from the centroid frequency shift method are more stable. In layers above and below the BSR, we clearly observe spatial variations in seismic Q. These variations of the seismic Q are closely related with the structures observed in the time structural variance map in a layer close to the BSR. We find high and low seismic Q anomalies in a layer above and below the BSR, respectively. These seismic Q anomalies are spatially confined within faults as mapped in the time structure variance maps. We attribute these high and low seismic Q anomalies to the presence of gas hydrates and free gas, respectively. The close association of seismic Q anomalies and faults show the potential impact of faults on the distribution of fluids in the study area. The differences in the spatial availability of free gas as observed in a Q slice below the GHSZ may also explain the differences in observed methane venting from some of the pockmarks. Hence, this Q analysis using the high-resolution P-Cable 3D seismic data with a large bandwidth is a potential cost-effective technique to analyze fluid flow and the spatial distribution of gas hydrates and free gas in marine sediments.

8.2. Article 2

Singhroha S., Chand, S., & Bünz, S. (2019). Constraints on gas hydrate distribution and morphology in Vestnesa Ridge, W-Svalbard margin using multicomponent ocean-bottom seismic data. Journal of Geophysical Research – Solid Earth, in press

P- and S-wave seismic velocities in gas hydrate-saturated marine sediments vary with gas hydrate saturation and morphology. In this article, we try to estimate gas hydrate saturation and morphology from seismic velocities derived from the analysis of ocean bottom seismic (OBS) data. We acquire OBS data at 10 sites along the Vestnesa Ridge. We carefully pick OBS locations so that we can get a regional overview of the gas hydrate distribution. We evaluate the effect of faults and structures on the gas hydrate distribution and analyze these results in relation with results obtained from the seismic Q analysis. P-wave seismic velocities are estimated using hydrophone and vertical seismometer components and S-wave seismic velocities are estimated using horizontal seismometer components. We pick different reflection arrivals and invert these reflection arrival times to estimate seismic velocities in different layers within the GHSZ and the free gas zone below. The results show a high P-wave ($V_p \approx 1.73$-1.82 km/s) and S-wave velocity ($V_s > 0.35$ km/s) in a layer above the BSR and a distinctive low P-wave velocity ($V_p \approx 1.28$-1.53 km/s) in a layer below the BSR. We apply full waveform inversion (FWI) at one OBS station to get better information from a high-resolution seismic velocity model. Results derived from FWI show P-wave velocities up to ~1.95 km/s above the BSR. We attribute these anomalous increase and decrease in seismic velocities to the presence of gas hydrates and free gas in sediments, respectively. Using an SCA/DEM approach, we estimate gas hydrate and free gas saturations in sediments from seismic velocity models. Results from OBS data suggest gas hydrate saturation up to 10%-18% in a layer above the BSR and 1.5-4.1% free gas saturation in the free gas zone below the BSR. The combined analysis of P- and S-wave velocities along with results obtained from seismic Q analysis throw some light on possible gas hydrate morphologies at different sites. Gas hydrate morphology as well as gas hydrate and free gas saturations vary across faults and these variations seem to be a result of structural control of faults on the distribution of gas hydrates thus corroborating the findings of seismic Q analysis.

8.3. Article 3

Singhroha, S., Bünz, S., Plaza-Faverola, A., & Chand, S. Structural control on the distribution of gas hydrates in the Vestnesa Ridge. Submitted to the Journal of Geophysical Research – Solid Earth.

Gas hydrate distribution within sediments varies from macroscale to microscale. Using azimuthal ocean bottom seismic (OBS) data, this article analyzes the directional variation in gas hydrate saturation with azimuth and the potential preferential alignment of gas hydrates due to the structural features in the Vestnesa Ridge. Azimuthal OBS data is acquired by shooting seismic in circular tracks of different radii around an OBS site. P-wave seismic velocities are estimated in different azimuths around two OBS sites through travel time inversion of picked travel times sorted by the azimuth. We find increase and decrease in seismic velocities in different azimuths. These azimuthal variations in seismic velocities are closely linked with faults and structures as interpreted using time structure variance maps estimated at different depths. We find a match in azimuths of elevated seismic velocities with fault directions in the GHSZ. These elevated P-wave velocities hint towards the presence of gas hydrates in faults. We find similar type of correlation in the free gas zone where seismic velocities decrease particularly in azimuths corresponding to the faults. In addition to elevated seismic velocities along faults, we also find changes in seismic velocities in azimuths across the faults and elevated seismic velocities in a group of azimuths that lies between two faults. Hence, the directional variation in seismic velocities also seem to be controlled by the presence of discontinuities. Hence, we infer the compartmentalization and preferential alignment of gas hydrates and free gas with fault systems of the Vestnesa Ridge.

9. Synthesis and outlook

9.1. Synthesis

The detailed mapping of gas hydrate occurrences in the subsurface, i.e. the determination of gas hydrate saturation and morphology and changes in these properties at a small and a large scale, needs an integrated application of different geophysical surveys and methodologies. The regional distribution of gas hydrates is primarily mapped using seismic velocity analysis and there is a need to further develop additional tools/methods and technologies (discussed in detail in section 5).

Several attempts have been made in conventional limited bandwidth (~10-80 Hz) seismic data to use seismic Q analysis as a proxy to map hydrates (Rossi et al., 2007; Sain & Singh, 2011; Best et al., 2013; Jaiswal et al., 2012; Dewangan et al., 2014). However, the P-Cable seismic data used herein has a broad bandwidth (20-300 Hz) and is best suited to test the robustness of seismic Q as proxy to study hydrates. In Article 1, we demonstrate the suitability of seismic Q analysis on broad bandwidth data. Spatial variations in seismic Q are constrained by the presence of faults and these variations can be because of variations in pore fluids, i.e. gas hydrates and free gas, across the fault. Earlier findings from Madrussani et al. (2010) also point towards the impact of faults on the gas hydrate and free gas distribution at another site on the W-Svalbard continental margin. It is important to verify these conclusions, as there is no uniform scientific consensus about seismic Q properties of gas hydrate-bearing sediments (discussed in detail in section 4.2). Seismic velocity properties of gas hydrate-bearing sediments are relatively well-established (discussed in detail in section 4.1) and can verify findings and conclusions from seismic Q analysis.

In Article 2, we document differences in P-wave velocities (~0.08 km/s) and PS reflectivity across the fault, across which seismic Q varies. These findings are corroborative evidences for conclusions made from seismic Q analysis. However, we did not find any significant differences in S-wave velocities across the fault. Hence, changes in seismic properties across the fault, i.e. from a relatively higher P-wave velocity, seismic Q and lower PS reflectivity to a relatively lower P-wave velocity, seismic Q and higher PS reflectivity, without any significant changes in shear wave velocities, strongly hint towards differences in the gas hydrate morphology across the fault. Article 2 discusses different morphologies that can create such seismic velocity and seismic Q anomalies. The study conclusively tells about the role of faults in the gas hydrate distribution. In order to further understand the role of faults, it is important

to understand processes happening within the fault and the presence of gas hydrates in and near faults.

In Article 3, we attempt to see the presence of gas hydrates in faults and fractures and their variation in close proximity to faults by carefully deploying OBS stations proximal to faults as interpreted in the time-structure variance maps. We find elevated seismic velocities in the fault directions, which gives a strong evidence of gas hydrate-filled fault and fractures. These observations further confirm conclusions made in Article 1 and Article 2 and add new insights about the Vestnesa gas hydrate system.

It is important to analyze results from seismic velocity and seismic Q analysis along with electrical resistivity analysis in the Vestnesa Ridge. Goswami et al. (2015) estimate gas hydrate saturations near an active pockmark in the Vestnesa Ridge using resistivity data acquired through the CSEM survey. They also use P-wave velocity models from two OBS stations as shown with red dots in Figure 5. Gas hydrate saturations estimates from Goswami et al. (2015) differ significantly from gas hydrate saturation estimates from the combined P- and S-wave velocity analysis (in Article 2). We observe similar differences in different geological settings that have gas hydrate-filled fracture deposits (Cook, 2010). As observed in well logs from Gulf of Mexico and Krishna-Godavari basin, the electrical resistivity increases with little or no increase in seismic velocities in gas hydrate-filled fracture intervals (Cook, 2010).

Goswami et al. (2015) estimate gas hydrate saturations using Archie's equation assuming isotropic gas hydrate distribution. Archie's equation use Archie's parameters (i.e. a, m and n) and these parameters depend strongly on the gas hydrate morphology (Lee & Collect, 2012; Cook and Waite, 2018). Gas hydrate saturation estimates from velocity analysis are relatively less sensitive to the presence of gas hydrates in faults and fractures (Ghosh et al., 2010). Differences observed in gas hydrate saturation estimates from resistivity and seismic velocity data indicate the presence of gas hydrates in faults and fractures. Goswami et al. (2017) also suggests the possibility of the occurrence of gas hydrates in faults and fractures in gas chimneys of the Vestnesa Ridge.

It is essential to look at results and observations in three articles in a relation with the broader knowledge and understanding about the gas hydrate system in the Vestnesa Ridge. Plaza-Faverola et al. (2015) suggest the control of tectonic stresses on the seepage of methane through pockmarks. Methane seeps from SE-NW segment of the Vestnesa Ridge (Bünz et al., 2012). Tectonic stresses favor the opening of faults in the SE-NW segment of the Vestnesa Ridge and

they favor the closing of faults in E-W segment of the Vestnesa Ridge (Plaza-Faverola & Keiding, 2019). Hence, structural features controlled by tectonic stresses decide the fate of migration of fluids at a regional scale (~50-100 km) in the study area. Within the actively seeping SE-NW segment of the Vestnesa Ridge, Article 1 and Article 2 suggest the role of faults at a local scale (~1-10 km) in relation to the variation of gas hydrate and free gas saturations along the ridge. Article 3 confirms the presence of gas hydrates in faults and indicates the variation of fluids in different azimuths across the fault thus confirming the role of faults in the variation and migration of fluids at a small scale (~10-200 m). Hence, this thesis in relation with earlier studies shows that the presence and properties of structural features at different scales influence the distribution of fluids in near surface sediments.

9.2. Outlook

Combined analysis of seismic Q, P- and S-wave velocities and azimuthal velocity analysis gives good estimates of gas hydrate saturation and delineates different morphologies. This integrated application of different geophysical methods and approaches for the detailed study of the gas hydrate system in the Vestnesa Ridge can also be applied to other gas hydrate systems. Some of the methodologies/techniques used in this thesis are novel and applied for the first time for the delineation of gas hydrate system. The extensive seismic Q analysis on 3D seismic data using well-established spectral ratio and centroid frequency shift methods is first such attempt to use this intrinsic property this extensively (on the scale of 3D seismic data) to study the subsurface. Circular seismic data acquisition used in this thesis for the quantitative azimuthal seismic velocity analysis at a given site is among initial attempts to understand azimuthal variations in seismic velocities using the circular acquisition geometry. These approaches can be applied in the exploration of other resources in the subsurface. The results obtained from the well-established approaches used for the seismic velocity analysis (in Article 2) provides veracity to the results obtained from these two relatively new methodologies/techniques. Hence, this thesis provides useful advances in geophysical methods as well as significant improvement in our knowledge about the Vestnesa gas hydrate system.

Future research

There is a potential to further develop all these methods/techniques to get a better understanding of gas hydrate systems. A rock physics model that can incorporate interval seismic Q data to estimate gas hydrate saturations can give independent gas hydrate saturation estimates from the seismic Q analysis. The gas hydrate saturations derived from the joint inversion of seismic Q and seismic velocity models are likely to be more constrained than the gas hydrate saturation

derived from the seismic velocities only. There is also a potential to derive gas hydrate saturations from the azimuthal seismic velocity models, which can give a better quantitative understanding of the presence of gas hydrates and free gas within faults and fractures.

There is an inherent non-uniqueness in the geophysical solutions derived from datasets. For example, P-wave seismic velocity data and electrical resistivity data cannot differentiate between the presence of gas hydrates in fractures and the co-existence of free gas with gas hydrates i.e. the presence of small amount of free gas in co-existence with high gas hydrate saturations will mimic the small gas hydrate saturations in fractures. The presence of seismic Q data can differentiate between these two possibilities. Hence, different unknown variables inside a gas hydrate system i.e. gas hydrate saturation, gas hydrate morphology, free gas saturation in co-existence with gas hydrates and the presence of authigenic carbonates (with many physical properties similar to gas hydrates) can only be theoretically resolved by the joint analysis of results from seismic Q, P- and S-wave velocities and CSEM data. With the current scientific knowledge base and the scientific understanding of rock physics, it seems far-fetched to do a quantitative analysis from all these multiple datasets. This is especially difficult as these methods vary considerably in terms of resolution and reliability. However, any step in this direction will be fruitful.

10. References

Amundsen, I. M. H., Blinova, M., Hjelstuen, B. O., Mjelde, R., & Haflidason, H. (2011). The Cenozoic western Svalbard margin: sediment geometry and sedimentary processes in an area of ultraslow oceanic spreading. Marine Geophysical Research, 32(4), 441-453. doi:10.1007/s11001-011-9127-z

Andreassen, K., Berteussen, K. A., Sognnes, H., Henneberg, K., Langhammer, J., & Mienert, J. (2003). Multicomponent ocean bottom cable data in gas hydrate investigation offshore of Norway. Journal of Geophysical Research: Solid Earth, 108(B8). doi:10.1029/2002jb002245

Archie, G.E. (1942). The electrical resistivity log as an aid in determining some reservoir characteristics. Transactions of AIME 146, 54e63.

Babu, P., Yee, D., Linga, P., Palmer, A., Khoo, B. C., Tan, T. S., & Rangsunvigit, P. (2013). Morphology of Methane Hydrate Formation in Porous Media. Energy & Fuels, 27(6), 3364-3372. doi:10.1021/ef4004818

Bath, M. (1974). Spectral analysis in geophysics. Developments in Solid Earth Geophysics, Vol 7, Elsevier Science Publishing Co.

Bellefleur, G., Riedel, M., Brent, T., Wright, F., & Dallimore, S. R. (2007). Implication of seismic attenuation for gas hydrate resource characterization, Mallik, Mackenzie Delta, Canada. Journal of Geophysical Research: Solid Earth, 112(B10). doi:10.1029/2007jb004976

Berndt, C., Feseker, T., Treude, T., Krastel, S., Liebetrau, V., Niemann, H., . . . Steinle, L. (2014). Temporal Constraints on Hydrate-Controlled Methane Seepage off Svalbard. Science, 343(6168), 284-287. doi:10.1126/science.1246298

Berryman, J. G. (1992). Single-scattering approximations for coefficients in Biot's equations of poroelasticity. The Journal of the Acoustical Society of America, 91(2), 551-571. doi:10.1121/1.402518

Best, A. I., Priest, J. A., Clayton, C. R. I., & Rees, E. V. L. (2013). The effect of methane hydrate morphology and water saturation on seismic wave attenuation in sand under shallow sub-seafloor conditions. Earth and Planetary Science Letters, 368, 78-87. doi:https://doi.org/10.1016/j.epsl.2013.02.033

Biot, M. A. (1956). "Theory of propagation of elastic waves in a fluid-saturated porous solid. I. low-frequency range," J. Acoust. Soc. Am. 28, 168-178.

Bishnoi, P. R., & Natarajan, V. (1996). Formation and decomposition of gas hydrates. Fluid Phase Equilibria, 117(1), 168-177. doi:https://doi.org/10.1016/0378-3812(95)02950-8

Bohrmann, G., Ahrlich, F., Bergenthal, M., Bünz, S., Düßmann, R., Ferreira, Ch., . . . Yao H. (2016). R/V Maria S. Merian cruise report MSM57: Gas hydrate dynamics at the continental margin of Svalbard. Can be accessed at http://oceanrep.geomar.de/43676/1/00105895-1.pdf

Boswell, R., Frye, M., Shelander, D., Shedd, W., McConnell, D. R., & Cook A. (2012). Architecture of gas-hydrate-bearing sands from Walker Ridge 313, Green canyon 955, and Alaminos canyon 21: northern deepwater Gulf of Mexico. Marine and Petroleum Geology, 34 (1), 134-149.

Boswell, R., Shipp, C., Reichel, T., Shelander, D., Saeki, T., Frye, M., . . . McConnell, D. (2015). Prospecting for marine gas hydrate resources. Interpretation, 4(1), SA13-SA24. doi:10.1190/INT-2015-0036.1

Buffett, B., & Archer, D. E. (2004). Global inventory of methane clathrate: Sensitivity to changes in environmental conditions. Earth Planet. Sci. Lett., 227, 185–199. doi:10.1016/j.epsl.2004.09.005.

Bünz, S., Mienert, J., Vanneste, M., & Andreassen, K. (2005). Gas hydrates at the Storegga Slide: constraints from an analysis of multicomponent, wide-angle seismic data. Geophysics, 70(5), B19-B34.

Bünz, S., Polyanov, S., Vadakkepuliyambatta, S., Consolaro, C., & Mienert, J. (2012). Active gas venting through hydrate-bearing sediments on the Vestnesa Ridge, offshore W-Svalbard. Marine Geology, 332-334, 189-197. doi:https://doi.org/10.1016/j.margeo.2012.09.012

Carson, B., & Screaton, E. J. (1998). Fluid flow in accretionary prisms: Evidence for focused, time-variable discharge. Reviews of Geophysics, 36(3), 329-351. doi:10.1029/97rg03633

Chabert, A., Minshull, T. A., Westbrook, G. K., Berndt, C., Thatcher, K. E., & Sarkar, S. (2011). Characterization of a stratigraphically constrained gas hydrate system along the western continental margin of Svalbard from ocean bottom seismometer data. Journal of Geophysical Research: Solid Earth, 116(B12). doi:10.1029/2011jb008211

Chand, S., Minshull, T. A., Gei, D., & Carcione, J. M. (2004). Elastic velocity models for gas-hydrate-bearing sediments—a comparison. Geophysical Journal International, 159(2), 573-590. doi:10.1111/j.1365-246X.2004.02387.x

Chen, L., Feng, Y., Okajima, J., Komiya, A., & Maruyama, S. (2018). Production behavior and numerical analysis for 2017 methane hydrate extraction test of Shenhu, South China Sea. Journal of Natural Gas Science and Engineering, 53, 55-66. doi:https://doi.org/10.1016/j.jngse.2018.02.029

Claussen, W.F. (1951). Suggested structures of water in inert gas hydrates. Journal of Chemical Physics, v.19, p. 259-260.

Collett, T. S. (2009). Gas Hydrate Petroleum Systems in Marine and Arctic Permafrost Environments. In Unconventional Energy Resources: Making the Unconventional Conventional. T. Carr, T. D'Agostino, W. Ambrose, J. Pashin, & N. C. Rosen (Eds.), (Vol. 29, pp. 0): SEPM Society for Sedimentary Geology.

Collett, T. S., & Ladd J. (2000). Detection of gas hydrate with downhole logs and assessment of gas hydrate concentrations (saturations) and gas volumes on the Blake Ridge with electrical resistivity log data, in Proceedings of the Ocean Drilling Program. Scientific Results, vol. 164, pp. 179-191.

Collett, T.S., Lewis, R.E., Winters, W.F., Lee, M.W., Rose, K.K., & Boswell, R.M. (2011). Downhole well log and core montages from the Mount Elbert Gas Hydrate Stratigraphic Test Well, Alaska North Slope. Journal of Marine and Petroleum Geology v. 28, no. 2, p. 561-577.

Collett, T. S., Lee, M. W., Zyrianova, M. V., Mrozewski, S. A., Guerin, G., Cook, A. E., & Goldberg, D. S. (2012). Gulf of Mexico Gas Hydrate Joint Industry Project Leg II logging-while-drilling data acquisition and analysis. Marine and Petroleum Geology, 34(1), 41-61. doi:https://doi.org/10.1016/j.marpetgeo.2011.08.003

Consolaro, C., Rasmussen, T.L., Panieri, G., Mienert, J., Bünz, S., & Sztybor, K. (2015). Carbon isotope (δ13C) excursions suggest times of major methane release during the last 14 kyr in Fram Strait, the deep-water gateway to the Arctic. Clim. Past 11, 669–685. http://dx.doi.org/10.5194/cp-11-669-2015.

Constable, S., Kannberg P. K., & Weitemeyer K. (2016). Vulcan: A deep-towed CSEM receiver. Geochem. Geophys. Geosyst., 17 (3), 1042-1064.

Cook, A.E. (2010). Gas hydrate-filled fracture reservoirs on continental margins. PhD thesis, Columbia University.

Cook, A., Anderson, B. I., Malinverno, A., Mrozewski, S., & Goldberg, D. S. (2010). Electrical anisotropy due to gas hydrate-filled fractures. Geophysics 75 (6), F173-F185.

Cook, A. E., Anderson, B. I., Rasmus, J., Sun, K., Li, Q., Collett, T. S., & Goldberg, D. S. (2012). Electrical anisotropy of gas hydrate-bearing sand reservoirs in the Gulf of Mexico. Marine and Petroleum Geology, 34(1), 72-84. doi:https://doi.org/10.1016/j.marpetgeo.2011.09.003

Cook, A. E., & Waite, W. F. (2018). Archie's Saturation Exponent for Natural Gas Hydrate in Coarse-Grained Reservoirs. Journal of Geophysical Research: Solid Earth, 123(3), 2069-2089. doi:10.1002/2017jb015138

Crane, K., Sundvor, E., Buck, R., & Martinez, F. (1991). Rifting in the northern Norwegian-Greenland Sea: Thermal tests of asymmetric spreading. Journal of Geophysical Research: Solid Earth, 96(B9), 14529-14550. doi:10.1029/91jb01231

Crane, K., Sundvor, E., Foucher, J.-P., Hobart, M., Myhre, A. M., & LeDouaran, S. (1988). Thermal evolution of the western Svalbard margin. Marine Geophysical Researches, 9(2), 165-194. doi:10.1007/bf00369247

Dai, S., Santamarina, J. C., Waite, W. F., & Kneafsey, T. J. (2012). Hydrate morphology: Physical properties of sands with patchy hydrate saturation. Journal of Geophysical Research: Solid Earth, 117(B11). doi:10.1029/2012JB009667

Dai, J., Xu, H., Snyder, F., & Dutta, N. (2004). Detection and estimation of gas hydrates using rock physics and seismic inversion: Examples from the northern deepwater Gulf of Mexico. The Leading Edge, 23(1), 60-66. doi:10.1190/1.1645456

Daigle, H., & Dugan, B. (2011). Capillary controls on methane hydrate distribution and fracturing in advective systems. Geochemistry, Geophysics, Geosystems, 12(1). doi:10.1029/2010GC003392

Davy, H. (1810). The bakterian Lecture: On some of the combinations of oxymuriatic gas and oygene and on the chemical relations of these principles to inflammable bodies. Phil. Trans. R. Soc. Lond. , 101, 1-35.

Dawe, R. A., & Thomas, S. (2007). A large potential methane source – natural gas hydrates. Energy sources: Part A, 29, 217–229.

Demenitskaya, R. M., & Karasik, A. M. (1969). The active rift system of the Arctic Ocean. Tectonophysics 8(4-6): 345-351.

Dewangan, P., Mandal, R., Jaiswal, P., Ramprasad, T., & Sriram, G. (2014). Estimation of seismic attenuation of gas hydrate bearing sediments from multi-channel seismic data: A case study from Krishna–Godavari offshore basin. Marine and Petroleum Geology, 58, 356-367. doi:https://doi.org/10.1016/j.marpetgeo.2014.05.015

Dickens G. R., & Forswall, C. (2009). Methane Hydrates, Carbon Cycling, and Environmental Change. In: Gornitz V. (eds) Encyclopedia of Paleoclimatology and Ancient Environments. Encyclopedia of Earth Sciences Series. Springer, Dordrecht

Domenico, S. N. (1977). Elastic properties of unconsolidated porous sand reservoirs. Geophysics, 42, 1339–1368.

Du Frane, W. L., Stern, L. A., Constable, S., Weitemeyer, K. A., Smith, M. M., & Roberts, J. J. (2015). Electrical properties of methane hydrate + sediment mixtures. Journal of Geophysical Research: Solid Earth, 120(7), 4773-4783. doi:doi:10.1002/2015JB011940

Duan, Z., Li, D., Chen, Y., & Sun, R. (2011). The influence of temperature, pressure, salinity and capillary force on the formation of methane hydrate. Geoscience Frontiers, 2(2), 125-135. doi:https://doi.org/10.1016/j.gsf.2011.03.009

Dumke, I., Burwicz, E. B., Berndt, C., Klaeschen, D., Feseker, T., Geissler, W. H., & Sarkar, S. (2016). Gas hydrate distribution and hydrocarbon maturation north of the Knipovich Ridge, western Svalbard margin. Journal of Geophysical Research: Solid Earth, 121(3), 1405-1424. doi:10.1002/2015jb012083

Dvorkin, J., & Nur, A. (1993). Rock physics for characterization of gas hydrate, in Howell, D. G., Ed., The future of energy gases: U.S. Geol. Surv. Prof. Paper 1579, 293–298.

Ecker, C., Dvorkin, J., & Nur, A. (1998). Sediments with gas hydrates: Internal structure from seismic AVO. Geophysics, 63, 1659–1669. doi: 10.1190/1.1444462.

Eiken, O., & Hinz, K. (1993). Contourites in the Fram Strait. Sed. Geol., 82, 1–4.

Eldholm, O., Faleide, J. I., & Myhre A. M. (1987). Continent-ocean transition at the western Barents Sea/Svalbard continental margin. Geology, 15(12): 1118-1122.

Engen, Ø., Faleide, J.I., & Dyreng, T.K. (2008). Opening of the Fram Straigth gateway: A review of plate tectonic constraint. Tectonophysics, 450, 51-59.

Etiope, G., & Lollar, B. S. (2013). ABIOTIC METHANE ON EARTH. Reviews of Geophysics, 51(2), 276-299. doi:10.1002/rog.20011

Etminan, M., Myhre, G., Highwood, E. J., & Shine, K. P. (2016). Radiative forcing of carbon dioxide, methane, and nitrous oxide: A significant revision of the methane radiative forcing. Geophysical Research Letters, 43(24), 12,614-612,623. doi:10.1002/2016GL071930

Forsberg, C.F., Solheim, A., Elverhøi, A., Jansen, E., Channell, J. E. T., & Andersen, E.S. (1999). 17. The depositional environment of the western Svalbard margin during the late Pliocene and the Pleistocene: Sedimentary facies changes at Site 986. Proceedings of the Ocean Drilling Program: Scientific Results 162:233-246. doi:10.2973/odp.proc.sr.162.032.1999

Fu, C. Y. (1947). Studies on seismic waves III. Propogation of elastic waves in the neighborhood of a free boundary. Geophysics, 12(1), 57-71. doi:10.1190/1.1437297

Gei, D., & Carcione, J. M. (2003). Acoustic properties of sediments saturated with gas hydrate, free gas and water. Geophysical prospecting, 51(2), 141-158. doi:10.1046/j.1365-2478.2003.00359.x

Ghosh, R., K. Sain, and M. Ojha (2010). Effective medium modeling of gas hydrate-filled fractures using the sonic login the Krishna-Godavari basin, offshore eastern India. Journal of Geophysical Research, 115, B06101, doi:10.1029/2009JB006711.

Goswami, B. K., Weitemeyer, K. A., Bünz, S., Minshull, T. A., Westbrook, G. K., Ker, S., & Sinha, M. C. (2017). Variations in pockmark composition at the Vestnesa Ridge: Insights from marine controlled source electromagnetic and seismic data. Geochemistry, Geophysics, Geosystems, 18(3), 1111-1125. doi:10.1002/2016GC006700

Goswami, B. K., Weitemeyer, K. A., Minshull, T. A., Sinha, M. C., Westbrook, G. K., Chabert, A., . . . Ker, S. (2015). A joint electromagnetic and seismic study of an active pockmark within the hydrate stability field at the Vestnesa Ridge, West Svalbard margin. Journal of Geophysical Research: Solid Earth, 120(10), 6797-6822. doi:10.1002/2015JB012344

Guerin, G., & Goldberg, D. (2002). Sonic waveform attenuation in gas hydrate-bearing sediments from the Mallik 2L-38 research well, Mackenzie Delta, Canada. Journal of Geophysical Research, 107, 2088. doi: 10.1029/2001JB000556.

Guerin, G., & Goldberg, D. (2005). Modeling of acoustic wave dissipation in gas hydrate-bearing sediments. Geochemistry, Geophysics, Geosystems, 6, Q07010. doi: 10.1029/2005GC000918.

Guerin, G., Goldberg, D., & Meltser A. (1999). Characterization of in situ elastic properties of gas hydrate bearing sediments on the Blake Ridge. Journal of Geophysical Research, 104, 17781–17795. doi: 10.1029/1999JB900127.

Hammerschmidt, E. G. (1934). Formation of Gas Hydrates in Natural Gas Transmission Lines. Ind. Eng. Chem., 26, 851.

Hansen, B., & Østerhus, S. (2000). North Atlantic–Nordic Seas exchanges. Progress in Oceanography, 45(2), 109-208. doi:https://doi.org/10.1016/S0079-6611(99)00052-X

Harland, W.B., Cutbill, J.L., Friend, P.F., Gobbett, D.J., Holliday, D.W. Maton, P.I., Parker, J.R., & Wallis, R.H. (1974). The Billefjorden fault zone, Spitsbergen: The long history of a major tectonic lineament. Norsk Polarinstitutt, Oslo, No. 161.

Holbrook, W. S., Hoskins, H., Wood, W. T., Stephen, R. A., & Lizarralde, D. (1996). Methane Hydrate and Free Gas on the Blake Ridge from Vertical Seismic Profiling. Science, 273(5283), 1840-1843. doi:10.1126/science.273.5283.1840

Holland, M., & Schultheiss, P. (2014). Comparison of methane mass balance and X-ray computed tomographic methods for calculation of gas hydrate content of pressure cores. Marine and Petroleum Geology, 58, 168-177. doi:https://doi.org/10.1016/j.marpetgeo.2014.07.016

Holland, M. E., Schultheiss, P. J., & Roberts, J. A. (2018). Gas hydrate saturation and morphology from analysis of pressure cores acquired in the Bay of Bengal during expedition NGHP-02, offshore India. Marine and Petroleum Geology. doi:https://doi.org/10.1016/j.marpetgeo.2018.07.018

Howe, J. A., Shimmield, T. M., Harland, R., & Eyles, N. (2008). Late Quaternary contourites and glaciomarine sedimentation in the Fram Strait. Sedimentology, 55(1), 179-200. doi:10.1111/j.1365-3091.2007.00897.x

Hsu, S.-K., Chiang, C.-W., Evans, R. L., Chen, C.-S., Chiu, S.-D., Ma, Y.-F., . . . Wang, Y. (2014). Marine controlled source electromagnetic method used for the gas hydrate investigation in the offshore area of SW Taiwan. Journal of Asian Earth Sciences, 92, 224-232. doi:https://doi.org/10.1016/j.jseaes.2013.12.001

Hunter, S. J., Goldobin, D. S., Haywood, A. M., Ridgwell, A., & Rees, J. G. (2013). Sensitivity of the global submarine hydrate inventory to scenarios of future climate change. Earth and Planetary Science Letters, 367, 105-115. doi:https://doi.org/10.1016/j.epsl.2013.02.017

Hustoft, S., Bünz, S., Mienert, J., & Chand, S. (2009). Gas hydrate reservoir and active methane-venting province in sediments on <20 Ma young oceanic crust in the Fram Strait, offshore NW-Svalbard. Earth and Planetary Science Letters 284, 12–24.

Hyndman, R., Yuan, T., & Moran K. (1999). The concentration of deep sea gas hydrates from downhole electrical resistivity logs and laboratory data. Earth Planet. Sci. Lett., 172 (1), 167-177.

Jain, A. K., & Juanes, R. (2009). Preferential Mode of gas invasion in sediments: Grain-scale mechanistic model of coupled multiphase fluid flow and sediment mechanics. Journal of Geophysical Research: Solid Earth, 114(B8). doi:10.1029/2008JB006002

Jaiswal, P., Dewangan, P., Ramprasad, T., & Zelt C. (2012). Seismic characterization of hydrates in faulted, fine-grained sediments of Krishna-Godavari Basin: Full waveform inversion. Journal of Geophysical Research, 117, B10305. doi: 10.1029/2012JB009201.

Jakobsen, M., Hudson, J. A., Minshull, T. A., & Singh, S. C. (2000). Elastic properties of hydrate-bearing sediments using effective medium theory. Journal of Geophysical Research: Solid Earth, 105(B1), 561-577. doi:10.1029/1999jb900190

Jannsen, D., Voss, J., & Theilen, F. (1985). Comparison of methods to determine Q in shallow marine sediments from vertical reflection seismograms. Geophysical Prospecting, 33, 479-497, 1985.

Johnson, A. H., & Max, M. D. (2006). The path to commercial hydrate gas production. The Leading Edge, 25(5), 648-651. doi:10.1190/1.2202672

Johnston, D. H., Toksöz, M. N., & Timur, A. (1979). Attenuation of seismic waves in dry and saturated rocks: II. Mechanisms. Geophysics, 44, 691-711.

Johnson, J.E., Mienert, J., Plaza-Faverola, A., Vadakkepuliyambatta, S., Knies, J., Bünz, S., ... Ferré, B. (2015). Abiotic methane from ultraslow-spreading ridges can charge Arctic gas hydrates. Geology, 43(5), 371-374. https://doi.org/10.1130/G36440.1

Johnson, G. L., Southall, J. R., Young, P. W., & Vogt, P. R. (1972). Origin and structure of the Iceland Plateau and Kolbeinsey Ridge. Journal of Geophysical Research, 77(29), 5688-5696. doi:10.1029/JB077i029p05688

Kennett, J., Cannariato, K. G., Hendy, I. L., & Behl, R. J. (2002). Methane Hydrates in Quaternary Climate Change: the Clathrate Gun Hypothesis. AGU Books Board 216 pp. doi: 10.1029/054SP

Kerkar, P. B., Horvat, K., Jones, K. W., & Mahajan, D. (2014). Imaging methane hydrates growth dynamics in porous media using synchrotron X-ray computed microtomography. Geochemistry, Geophysics, Geosystems, 15(12), 4759-4768. doi:10.1002/2014gc005373

Kerkar, P., Jones, K. W., Kleinberg, R., Lindquist, W. B., Tomov, S., Feng, H., & Mahajan, D. (2009). Direct observations of three dimensional growth of hydrates hosted in porous media. Applied Physics Letters, 95(2), 024102. doi:10.1063/1.3120544

Khlystov, O., Batist, M. D., Shoji, H., Hachikubo, A., Nishio, S., Naudts, L., . . . Kalmychkov, G. (2013). Gas hydrate of Lake Baikal: Discovery and varieties. Journal of Asian Earth Sciences, 62, 162-166. doi:https://doi.org/10.1016/j.jseaes.2012.03.009

Kim, K. J., Yi, B. Y., Kang, N. K., & Yoo, D. G. (2015). Seismic Attribute Analysis of the Indicator for Gas Hydrate Occurrence in the Northwest Ulleung Basin, East Sea. Energy Procedia, 76, 463-469. doi:https://doi.org/10.1016/j.egypro.2015.07.882

Klauda, J. B., & Sandler, S. I. (2005). Global Distribution of Methane Hydrate in Ocean Sediment. Energy & Fuels, 19(2), 459-470. doi:10.1021/ef049798o

Knies, J., Matthiessen, J., Vogt, C., Laberg, J. S., Hjelstuen, B. O., Smelror, M., . . . Vorren, T. O. (2009). The Plio-Pleistocene glaciation of the Barents Sea–Svalbard region: a new model based on revised chronostratigraphy. Quaternary Science Reviews, 28(9), 812-829. doi:https://doi.org/10.1016/j.quascirev.2008.12.002

Knopoff, L. (1964). Q. Reviews of Geophysics, 2(4), 625-660. doi:10.1029/RG002i004p00625

Konno, Y., Fujii, T., Sato, A., Akamine, K., Naiki, M., Masuda, Y., Yamamoto K., Nagao, J. (2017). Key Findings of the World's First Offshore Methane Hydrate Production Test off the Coast of Japan: Toward Future Commercial Production. Energy & Fuels, 31(3), 2607-2616. doi:10.1021/acs.energyfuels.6b03143

Kovacs, L. C., & Vogt, P. R. (1982). Depth-to-magnetic source analysis of the Arctic Ocean region. Tectonophysics, 89(1), 255-294. doi:https://doi.org/10.1016/0040-1951(82)90041-5

Kretschmer, K., Biastoch, A., Rüpke, L., & Burwicz, E. (2015). Modeling the fate of methane hydrates under global warming. Global Biogeochemical Cycles, 29(5), 610-625. doi:10.1002/2014GB005011

Kumar, D., Sen, M. K., & Bangs, N. L. (2007). Gas hydrate concentration and characteristics within Hydrate Ridge inferred from multicomponent seismic reflection data. Journal of Geophysical Research: Solid Earth, 112(B12), B12306. doi:10.1029/2007JB004993.

Kvenvolden, K.A. (1993). Gas hydrates – geological perspective and global change. Reviews of Geophysics, 31 (2), pp. 173-187

Kvenvolden, K. A., & McMenamin, M. A. (1980). Hydrates of Natural Gas: A review of their Geologic Occurrence. U. S. Geological Survey Circular. 825. doi:10.3133/cir825

Lee, J. Y. (2007). Hydrate-bearing sediments: Formation and geophysical properties. Doctoral thesis, 226 pp, Ga. Inst. of Technol., Atlanta.

Lee, M. W., & Collett, T. S. (2006). Gas hydrate and free gas saturations estimated from velocity logs on Hydrate Ridge, offshore Oregon, USA. In Trehu, A.M., Bohrmann, G., Torres, M.E., and Colwell, F.S. (Eds.), Proc. ODP, Sci. Results, vol. 2004, 1-25 pp.

Lee, M. W., & Collett, T.S. (2009). Gas hydrate saturations estimated from fractured reservoir at Site NGHP-01-10, Krishna-Godavari Basin, India. Journal of Geophysical Research, 114, B07102. doi:10.1029/2008JB006237.

Lee, M. W., & Collett, T. S. (2012). Pore- and fracture-filling gas hydrate reservoirs in the Gulf of Mexico Gas Hydrate Joint Industry Project Leg II Green Canyon 955 H well. Marine and Petroleum Geology, Volume 34, Issue 1, 2012, Pages 62-71, ISSN 0264-8172. http://dx.doi.org/10.1016/j.marpetgeo.2011.08.002.

Lee, J. Y., Francisca, F. M., Santamarina, J. C., & Ruppel, C. (2010). Parametric study of the physical properties of hydrate-bearing sand, silt, and clay sediments: 2. Small-strain mechanical properties. Journal of Geophysical Research: Solid Earth, 115(B11). doi:10.1029/2009jb006670

Li J., Ye J., Qin X., Qiu H., Wu N., Lu H., Xie W., Lu J., Peng F., Xu Z., Lu C., Kuang Z., Wei J., Liang Q., Lu H., & Kou B. (2018). The first offshore natural gas hydrate production test in South China Sea. China Geology, 1 (1), 5-16. doi: 10.31035/cg2018003

Liu, X., & Flemings, P. B. (2007). Dynamic multiphase flow model of hydrate formation in marine sediments. J. Geophys. Res., 112, B03101. doi:10.1029/2005JB004227.

Lu, Z., Zhai, G., Zhu, Y., Zhang, Y., Li, Y., Wang, W., . . . Tan, P. (2016). Fault Control of Gas Hydrate Accumulation in Qilian Mountain Permafrost. International Journal of Offshore and Polar Engineering, 26(02), 199-205.

Lund, A., Urdahl, O., & Kirkhorn, S. S. (1996). Inhibition of gas hydrate formation by means of chemical additives—II. An evaluation of the screening method. Chemical Engineering Science, 51(13), 3449-3458. doi:https://doi.org/10.1016/0009-2509(95)00410-6

Macelloni, L., Lutken, C. B., Garg, S., Simonetti, A., D'Emidio, M., Wilson, R. M., . . . McGee, T. M. (2015). Heat-flow regimes and the hydrate stability zone of a transient, thermogenic, fault-controlled hydrate system (Woolsey Mound northern Gulf of Mexico). Marine and Petroleum Geology, 59, 491-504. doi:https://doi.org/10.1016/j.marpetgeo.2014.09.010

Madrussani, G., Rossi, G., & Camerlenghi, A. (2010). Gas hydrates, free gas distribution and fault pattern on the west Svalbard continental margin. Geophysical Journal International, 180(2), 666-684. doi:10.1111/j.1365-246X.2009.04425.x

Mahabadi, N., Dai, S., Seol, Y., & Jang, J. (2019). Impact of hydrate saturation on water permeability in hydrate-bearing sediments. Journal of Petroleum Science and Engineering, 174, 696-703. doi:https://doi.org/10.1016/j.petrol.2018.11.084

Makogon Y.F. (1965). A Gas Hydrate Formation in the Gas Saturated Layers under Low Temperature. Gas Industry, No.5, p 14-15.

Malinverno, A., Kastner, M., Torres, M. E., & Wortmann, U. G. (2008). Gas hydrate occurrence from pore water chlorinity and downhole logs in a transect across the northern Cascadia margin (Integrated Ocean Drilling Program Expedition 311). Journal of Geophysical Research: Solid Earth, 113(B8). doi:10.1029/2008jb005702

Marín-Moreno, H., Giustiniani, M., Tinivella, U. & Piñero, E. (2016). The challenges of quantifying the carbon stored in Arctic marine gas hydrate. Marine and Petroleum Geology, 71, 76-82. (doi:10.1016/j.marpetgeo.2015.11.014).

Marín-Moreno, H., Minshull, T. A., Westbrook, G. K., & Sinha, B. (2015). Estimates of future warming-induced methane emissions from hydrate offshore west Svalbard for a range of climate models. Geochemistry, Geophysics, Geosystems, 16(5), 1307-1323. doi:10.1002/2015gc005737

Marín-Moreno, H., Minshull, T. A., Westbrook, G. K., Sinha, B., & Sarkar, S. (2013). The response of methane hydrate beneath the seabed offshore Svalbard to ocean warming during the next three centuries. Geophysical Research Letters, 40(19), 5159-5163. doi:10.1002/grl.50985

Maslin, M., Owen, M., Betts, R., Day, S., Jones, T. D., & Ridgwell, A. (2010). Gas hydrates: past and future geohazard? Philosophical Transactions of the Royal Society A: Mathematical, Physical and Engineering Sciences, 368(1919), 2369-2393. doi:10.1098/rsta.2010.0065

Matsushima, J. (2005). Attenuation measurements from sonic waveform logs in methane hydrate-bearing sediments at the Nankai Trough exploratory well off Tokai, central Japan. Geophysical Research Letters, 32, 1–5. doi: 10.1029/2005GL023217.

Mattingsdal, R., Knies, J., Andreassen, K., Fabian, K., Husum, K., Grøsfjeld, K., & De Schepper, S. (2014). A new 6 Myr stratigraphic framework for the Atlantic–Arctic Gateway. Quaternary Science Reviews, 92, 170-178. doi:https://doi.org/10.1016/j.quascirev.2013.08.022

Mavko, G., & Nur, A. (1979). Wave attenuation in partially saturated rocks. Geophysics, 56, 1940-1949.

Max, M. D., & Johnson, A. H. (2014). Hydrate petroleum system approach to natural gas hydrate exploration. Petroleum Geoscience, 2012-2049. doi:10.1144/petgeo2012-049

McConnell, D. R., Zhang, Z., & Boswell, R. (2012). Review of progress in evaluating gas hydrate drilling hazards. Marine and Petroleum Geology, 34(1), 209-223. doi:https://doi.org/10.1016/j.marpetgeo.2012.02.010

McIver, R. D. (1981). Gas hydrates, in Long-Term Energy Resources, edited by R. F. Meyer and J. C. Olson, pp. 713–726 , Pitman, Boston, MA

Milkov, A. V. (2004). Global estimates of hydrate–bound gas in marine sediments: How much is really out there? Earth–science review, 66, 183–197.

Murphy, W. F., Winkler, K.W., & Kleinberg, R. L. (1986) Acoustic relaxation in sedimentary rocks: Dependence on grain contacts and fluid saturation. Geophysics, 51, 757–766. doi: 10.1190/1.1442128.

Myhre, A. M., & Eldholm, O. (1988). The Western Svalbard Margin (74°-80°N). Marine and Petroleum Geology 5, 134-156.

Nagakubo S., Arata N., Yabe I., Kobayashi H., & Yamamoto K. (2011). Environmental Impact Assessment Study on Japan's Methane Hydrate R&D Program. Fire in the ice, 4- 11.

Nimblett, J., & Ruppel, C. (2003). Permeability evolution during the formation of gas hydrates in marine sediments. J. Geophys. Res., 108(B9), 2420. doi:10.1029/2001JB001650.

Nishizawa, O. (1982). Seismic velocity anisotropy in a medium containing oriented cracks: transversely isotropic case. Jour. Phys. Earth, 30, 331–347.

Nunns, A. G., (1983). Plate tectonic evolution of the Greenland-Scotland Ridge and surrounding regions, in Structure and Development of the Greenland-Scotland Ridge, New Methods and Concepts, edited by Bott et al., pp. 11-30, Plenum, New York.

Nunns, A. G., & Peacock, J. H. (1983). Correlation, identification and inversion of magnetic anomalies in the Norway Basin. Earth Evol. Sci., 2, 130-138.

O'Connell, R. J., & Budiansky, B. (1977). Viscoelastic properties of fluid-saturated cracked solids: Journal of Geophysical Research, 82, 5719–5735. doi: 10.1029/ JB082i036p05719.

O'Doherty, R. F., & Anstey, N. A. (1971). Reflections on amplitude. Geophya. Prosp., v. 19, p 430-458.

O'Hara, S. G. (1989). Elastic-wave attenuation in fluid-saturated Berea sandstone. Geophysics, 54, 785–788. doi: 10.1190/1.1442707.

Ottesen, D., Dowdeswell, J.A., & Rise, L. (2005). Submarine landforms and the reconstruction of fast-flowing ice streams within a large quaternary ice sheet: the 2500-km-long Norwegian-Svalbard margin (57 degrees-80 degrees N). Geological Society of America Bulletin 117, 1033–1050.

Overpeck, J., Hughen, K., Hardy, D., Bradley, R., Case, R., Douglas, M., . . . Zielinski, G. (1997). Arctic Environmental Change of the Last Four Centuries. Science, 278(5341), 1251-1256. doi:10.1126/science.278.5341.1251

Panieri, G., Bünz, S., Fornari, D. J., Escartin, J., Serov, P., Jansson, P., . . . Gracias, N. (2017). An integrated view of the methane system in the pockmarks at Vestnesa Ridge, 79°N. Marine Geology, 390, 282-300. doi:https://doi.org/10.1016/j.margeo.2017.06.006

Paull, C. K., Ussler III, W., & Holbrook, W. S. (2007). Assessing methane release from the colossal Storegga submarine landslide. Geophysical Research Letters, 34(4). doi:10.1029/2006GL028331

Pearson, C. F., Halleck, P. M., McGuire, P. L., Hermes, R., & Mathews, M. (1983). Natural gas hydrate deposits: a review of in situ properties. The Journal of Physical Chemistry, 87(21), 4180-4185. doi:10.1021/j100244a041

Pecher, I. A., Minshull, T. A., Singh, S. C., & Huene R. V. (1996). Velocity structure of a bottom simulating reflector offshore Peru: Results from full waveform inversion. Earth and Planetary Science Letters, 139(3), 459-69.

Petersen, C. J., Bünz, S., Hustoft, S., Mienert, J., & Klaeschen, D. (2010). High-resolution P-Cable 3D seismic imaging of gas chimney structures in gas hydrated sediments of an Arctic sediment drift. Marine and Petroleum Geology, 27(9), 1981-1994. doi:10.1016/j.marpetgeo.2010.06.006

Phrampus, B. J., & Hornbach, M. J. (2012). Recent changes to the Gulf Stream causing widespread gas hydrate destabilization. Nature, 490, 527-530, 2012.

Planke, S., Eriksen, F.N., Berndt, C., Mienert, J., & Masson, D. (2009). Spotlight on technology: P-cable high-resolution seismic. Oceanography, 22, 85. doi: 10.5670/oceanog.2009.09.

Plaza-Faverola, A., Bünz, S., Johnson, J. E., Chand, S., Knies, J., Mienert, J., & Franek, P. (2015). Role of tectonic stress in seepage evolution along the gas hydrate-charged Vestnesa Ridge, Fram Strait. Geophysical Research Letters, 42(3), 733-742. doi:10.1002/2014GL062474

Plaza-Faverola, A., & Keiding, M. (2019). Correlation between tectonic stress regimes and methane seepage on the western Svalbard margin. Solid Earth, 10(1), 79-94. doi:10.5194/se-10-79-2019

Plaza-Faverola, A., Vadakkepuliyambatta, S., Hong, W. L., Mienert, J., Bünz, S., Chand, S., & Greinert, J. (2017). Bottom-simulating reflector dynamics at Arctic thermogenic gas provinces: An example from Vestnesa Ridge, offshore west Svalbard. Journal of Geophysical Research: Solid Earth, 122(6), 4089-4105. doi:10.1002/2016JB013761

Portnov, A., Smith, A. J., Mienert, J., Cherkashov, G., Rekant, P., Semenov, P., . . . Vanshtein, B. (2013). Offshore permafrost decay and massive seabed methane escape in water depths >20 m at the South Kara Sea shelf. Geophysical Research Letters, 40(15), 3962-3967. doi:10.1002/grl.50735

Portnov, A., Vadakkepuliyambatta, S., Mienert, J., & Hubbard, A. (2016). Ice-sheet-driven methane storage and release in the Arctic. Nature Communications, 7, 10314. doi:10.1038/ncomms10314

Posewang, J., & Mienert, J. (1999). High-resolution seismic studies of gas hydrates west of Svalbard. Geo-Marine Letters 19, 150–156.

Pratt, R. G., Hou, F., Bauer, K. & Weber, M. (2005). Waveform tomography images of velocity and inelastic attenuation from the Mallik 2002 crosshole seismic surveys, in S. R. Dallimore, and T. S. Collet, eds., Scientific results from the Mallik 2002 gas hydrate production research well program, Mackenzie Delta, Northwest Territories, Canada: Geological Survey of Canada, Bulletin, 1–14.

Priest, J. A., Best, A. I., & Clayton, C. R. I. (2005). A laboratory investigation into the seismic velocities of methane gas hydrate-bearing sand. J. Geophys. Res., 110, B04102. doi:10.1029/2004JB003259

Priest, J. A., Best, A. I., & Clayton, C. R. I. (2006). Attenuation of seismic waves in methane gas hydrate-bearing sand: Geophysical Journal International, 164, 149–159. doi: 10.1111/j.1365-246X.2005.02831.x.

Priest, J.A., Rees, E.V.L. & Clayton, C.R.I. (2009). Influence of gas hydrate morphology on the seismic velocities of sands. J. Geophys. Res. 114, B11205. doi:10.1029/2009JB006284.

Quan, Y., & Harris, J. M. (1997). Seismic attenuation tomography using the frequency shift method. Geophysics, 62, 895-905.

Raikes, S. A., & White, R. E. (1984). Measurements of earth attenuation from downhole and surface seismic recordings. Geophysical Prospecting, 32, 892-919.

Rapoport, M. B., Rapoport, L. I., & Ryjkov, V. I. (2004). Direct detection of oil and gas fields based on seismic inelasticity effect. The Leading Edge, 23, 276–278. doi: 10.1190/1.1690901.

Rempel, A. W., & Buffet, B. A. (1997). Formation and Accumulation of Gas Hydrate in Porous Media. Journal of Geophysical Research, 102, 151-164. doi: https://doi.org/10.1029/97JB00392

Riedel, M., Collett, T., & Hyndman R. (2005). Gas hydrate concentration estimates from chlorinity, electrical resistivity and seismic velocity. Geol. Surv. Can. Open-File Rep, 4934.

Riedel, M., Willoughby, E. C., & Chopra, S. (2010). Gas Hydrates — Geophysical Exploration Techniques and Methods. In Geophysical Characterization of Gas Hydrates, Society of Exploration Geophysicists (pp. 1-22).

Riestenberg, D., West, O., Lee, S., McCallum, S., & Phelps, T. J. (2003). Sediment surface effects on methane hydrate formation and dissociation. Marine Geology, 198(1), 181-190. doi:https://doi.org/10.1016/S0025-3227(03)00100-2

Ritzmann, O., & Jokat W. (2003). Crustal structure of northwestern Svalbard and the adjacent Yermak Plateau: Evidence for Oligocene simple shear rifting and non-volcanic break-up. Geophysical Journal International, 152, 139-159.

Ritzmann, O., Jokat, W., Czuba, W., Guterch, A., Mjelde, R., & Nishimura, Y. (2004). A deep seismic transect from Hovgård Ridge to northwestern Svalbard across the continental-ocean transition: A sheared margin study. Geophysical Journal International, 157(2), 683-702. doi:10.1111/j.1365-246X.2004.02204.x

Ritzmann, O., Jokat, W., Mjelde, R., & Shimamura, H. (2002). Crustal structure between Knipovich Ridge and the Van Mijenfjorden (Svalbard). Marine Geophysical Researches, 23, 379-401.

Rossi, G., Gei, D., Böhm, G., Madrussani, G., & Carcione, J. M. (2007). Attenuation tomography: An application to gas-hydrate and free-gas detection. Geophysical prospecting, 55(5), 655-669. doi:10.1111/j.1365-2478.2007.00646.x

Ruppel, C. (2007). Tapping methane hydrates for unconventional natural gas. Elements, 3(3), 193-199. doi: 10.2113/gselements.3.3.193.

Ruppel, C. (2015). Permafrost-associated gas hydrate: Is it really approximately 1 % of the global system? J. Chem. Eng. Data, 60 (2), 429–436. doi:10.1021/je500770m.

Ruppel, C. D., & Kessler, J. D. (2017). The interaction of climate change and methane hydrates. Reviews of Geophysics, 55(1), 126-168. doi:10.1002/2016RG000534

Sahoo, S. K., Marín-Moreno, H., North, L. J., Falcon-Suarez, I., Madhusudhan, B. N., Best, A. I., & Minshull, T. A. (2018). Presence and Consequences of Coexisting Methane Gas With Hydrate Under Two Phase Water-Hydrate Stability Conditions. Journal of Geophysical Research: Solid Earth, 123(5), 3377-3390. doi:10.1029/2018JB015598

Sain, K., & Singh, A. K. (2011). Seismic quality factors across a bottom simulating reflector in the Makran Accretionary Prism, Arabian Sea. Marine and Petroleum Geology, 28, 1838–1843. doi: 10.1016/j.marpetgeo.2011.03.013.

Sarkar, S., Berndt, C., Minshull, T. A., Westbrook, G. K., Klaeschen, D., Masson, D. G., . . . Thatcher, K. E. (2012). Seismic evidence for shallow gas-escape features associated with a retreating gas hydrate zone offshore west Svalbard. Journal of Geophysical Research: Solid Earth, 117(B9). doi:10.1029/2011jb009126

Satyavani, N., Sain, K., & Gupta, H. (2016). Ocean bottom seismometer data modeling to infer gas hydrate saturation in Krishna-Godavari (KG) basin. Journal of Natural Gas Science and Engineering, 33, 908-917.

Sava, D., & Hardage, B. A. (2006). Rock physics characterization of hydrate-bearing deepwater sediments. The Leading Edge, 25(5), 616-619. doi:10.1190/1.2202666

Schwalenberg, K., Haeckel, M., Poort, J., & Jegen M. (2010). Evaluation of gas hydrate deposits in an active seep area using marine controlled source electromagnetics: Results from Opouawe bank, Hikurangi Margin, New Zealand. Mar. Geol., 272 (1), 79-88.

Schwalenberg, K., Rippe, D., Koch, S., & Scholl, C. (2017). Marine-controlled source electromagnetic study of methane seeps and gas hydrates at Opouawe Bank, Hikurangi Margin, New Zealand. J. Geophys. Res., 122 (5), 3334-3350.

Schwalenberg, K., Willoughby, E., Mir, R., & Edwards, R. (2005). Marine gas hydrate electromagnetic signatures in Cascadia and their correlation with seismic blank zones. First Break, 23 (4), 57-63.

Sellevoll, M. A., Duda, S. J., Guterch, A., Pajchel, J., Perchuc, E., & Thyssen, F. (1991). Crustal structure in the Svalbard region from seismic measurements. Tectonophysics, 189(1), 55-71. doi:https://doi.org/10.1016/0040-1951(91)90487-D

Sheriff, R. E., & Geldart, L. P. (1995). Exploration seismology. Cambridge University Press.

Shipley, T. H., Houston, M. H., Buffler, R. T., Shaub, F. J., McMillen, K. J., Ladd, J. W., & Worzel, J. L. (1979). Seismic evidence for widespread possible gas hydrate horizons on Continental slopes and rises. AAPG Bulletin, 63, 2204–2213.

Singh, S.C., Minshull, T.A., & Spence, G.D. (1993). Velocity structure of a gas hydrate reflector. Science, 260, 204-207.

Singhroha, S., Bünz, S., Plaza-Faverola, A., & Chand, S. (2016). Gas hydrate and free gas detection using seismic quality factor estimates from high-resolution P-cable 3D seismic data. Interpretation, 4(1), SA39-SA54. doi:10.1190/INT-2015-0023.1

Singhroha S., Chand, S., & Bünz, S. (2019). Constraints on gas hydrate distribution and morphology in Vestnesa Ridge, W-Svalbard margin using multicomponent ocean-bottom seismic data. Journal of Geophysical Research – Solid Earth. Doi: 10.1029/2018JB016574

Sloan, E. D., Jr. (1998). Clathrate hydrates of natural gases, 2nd ed.: Marcel Dekker Inc.

Sloan, D., Koh, C., Sum, A. K., Ballard, A. L., Creek, J., Eaton, M., Lachance, J., McMullen, N., Palermo, T., Shoup, G., & Talley, L. (Eds.) (2011). Natural Gas Hydrates in Flow Assurance (pp. iv). Boston: Gulf Professional Publishing.

Song, S., Tinivella, U., Giustiniani, M., Singhroha, S., Bünz, S., & Cassiani, G. (2018). OBS Data Analysis to Quantify Gas Hydrate and Free Gas in the South Shetland Margin (Antarctica). Energies, 11, 3290. doi: 10.3390/en11123290

Spangenberg, E. (2001). Modeling of the influence of gas hydrate content on the electrical properties of porous sediments. Journal of Geophysical Research: Solid Earth, 106(B4), 6535-6548. doi:10.1029/2000jb900434

Steel, R., Gjelberg, J., Helland-Hansen, W., Kleinspehn, K., Nøttvedt, A., & RyeLarsen, M. (1985). The Tertiary strike-slip basins and orogene belt of Spitsbergen. In: Biddle, K., & Cristie-Blick, N. (eds.), Strike-slip Deformation, Basin Formation, and Sedimentation, Soc. Econ. Paleontol. Mineral., Spec. Publ. 37, 339-359.

Stein, R., Niessen, F., Schoster, F., Bahr, B., Gebhardt, C., Kukina, N., Lensch, N., Nam, S., Noffke, H., Penshorn, D., Puhr, A., Saraswat, R., Scha¨ fer, Chr., Schnieder, J., Thiede, J., Winkleman, D. and Yanina, Y. (2005). Marine geology. In: Scientific Cruise Report of the Arctic Expedition ARK-XX/3 of RV Polarstern in 2004: Fram Strait, Yermak Plateau and East Greenland Continental Margin (ed. R. Stein). Ber. Polarfors., 517, 41–95.

Sun, Y., Wu, S., Dong, D., Lüdmann, T., & Gong, Y. (2012). Gas hydrates associated with gas chimneys in fine-grained sediments of the northern South China Sea. Marine Geology, 311-314, 32-40. doi:https://doi.org/10.1016/j.margeo.2012.04.003

Sztybor, K., & Rasmussen, T. L. (2016). Diagenetic disturbances of marine sedimentary records from methane-influenced environments in the Fram Strait as indications of variation in seep intensity during the last 35,000 years. Boreas, 46, 212– 228. doi:http://dx.doi.org/10.1111/bor.12202.

Talwani, M., & Eldholm, O. (1977). Evolution of the Norwegian-Greenland Sea. Geological Society of America Bulletin 88(7), 969-999.

Teng, T.-L. (1968). Attenuation of body waves and the Q structure of the mantle. Journal of Geophysical Research, 73(6), 2195-2208. doi:10.1029/JB073i006p02195¨

Toksöz, M. N., & Johnston, D. H. (1981). Seismic wave attenuation. SEG, Geophysics Reprint Series.

Toksöz, M. N., Johnston, D. H. & Timur, A. (1979). Attenuation of seismic waves in dry and saturated rocks. I: Laboratory measurements. Geophysics, 44, 681–690. doi: 10.1190/1.1440969.

Vadakkepuliyambatta, S., Chand, S., & Bünz, S. (2017). The history and future trends of ocean warming-induced gas hydrate dissociation in the SW Barents Sea. Geophysical Research Letters, 44(2), 835-844. doi:10.1002/2016GL071841

Vanneste, M., Guidard, S., & Mienert, J. (2005). Bottom-simulating reflections and geothermal gradients across the western Svalbard margin. Terra Nova 17, 510–516.

Vogt, P. R. (1986). Geophysical and geochemical signatures and plate tectonics, in The Nordic Seas, edited by B. G. Hurdle, SpringerVerlag, New York.

Vogt, P. R., Crane, K., Sundvor, E., Max, M. D., & Pfirman, S. L. (1994). Methane-generated (?) pockmarks on young, thickly sedimented oceaniccrust in the Arctic: Vestnesa ridge, Fram strait. Geology, 22(3), 255–258.

Vogt, P. R., Kovacs, L. C., Bernero, C., & Srivastava, S. P. (1982). Asymmetric geophysical signatures in the Greenland-Norwegian and Southern Labrador Seas and the Eurasia Basin. Tectonophysics, 89(1), 95-160. doi:https://doi.org/10.1016/0040-1951(82)90036-1

von Appen, W.-J., Schauer, U., Somavilla, R., Bauerfeind, E., & Beszczynska-Möller, A. (2015). Exchange of warming deep waters across Fram Strait. Deep Sea Research Part I: Oceanographic Research Papers, 103, 86-100. doi:https://doi.org/10.1016/j.dsr.2015.06.003

Waage, M., Bünz, S., Landrø, M., Plaza-Faverola, A., & Waghorn, K. A. (2019). Repeatability of high-resolution 3D seismic data. Geophysics, 84(1), B75-B94. doi:10.1190/geo2018-0099.1

Wadham, J. L., Arndt, S., Tulaczyk, S., Stibal, M., Tranter, M., Telling, J., . . . Butler, C. E. H. (2012). Potential methane reservoirs beneath Antarctica. Nature, 488, 633. doi:10.1038/nature11374

Waghorn, K. A., Bünz, S., Plaza-Faverola, A., & Johnson, J. E. (2018). 3-D Seismic Investigation of a Gas Hydrate and Fluid Flow System on an Active Mid-Ocean Ridge; Svyatogor Ridge, Fram Strait. Geochemistry, Geophysics, Geosystems, 19(8), 2325-2341. doi:10.1029/2018gc007482

Waite, W.F., Helgerud, M. B., Nur, A., Pinkston, J., Stern, L. A., Kirby, S. H., & Durham, W. B., Holder, G. D., & Bishnoi P.R. (2000). First laboratory measurements of compressional and shear wave speeds through pure methane hydrate at in situ conditions, Gas Hydrates: Challenges for the Future Blackwell Publishing, Malden, MA, 912, 1003–1010.

Waite, W. F., Santamarina, J. C., Cortes, D. D., Dugan, B., Espinoza, D. N., Germaine, J., . . . Yun, T.-S. (2009). Physical properties of hydrate-bearing sediments. Reviews of Geophysics, 47(4). doi:10.1029/2008rg000279

Wallmann, K., Pinero, E., Burwicz, E., Haeckel, M., Hensen, C., Dale, A., & Ruepke, L. (2012). The Global Inventory of Methane Hydrate in Marine Sediments: A Theoretical Approach. Energies, 5(7), 2449.

Wang, J., Jaiswal, P., Haines, S. S., Hart, P. E., & Wu, S. (2018). Gas hydrate quantification using full-waveform inversion of sparse ocean-bottom seismic data: A case study from Green Canyon Block 955, Gulf of Mexico. Geophysics, 83(4), B167-B181. doi:10.1190/geo2017-0414.1

Waseda, A. (1998). Organic carbon content, bacterial methanogenesis, and accumulation processes of gas hydrates in marine sediments. GEOCHEMICAL JOURNAL, 32(3), 143-157. doi:10.2343/geochemj.32.143

Weinberger, J. L., & Brown, K. M. (2006). Fracture networks and hydrate distribution at Hydrate Ridge, Oregon. Earth and Planetary Science Letters, 245(1), 123-136. doi:https://doi.org/10.1016/j.epsl.2006.03.012

Westbrook, G. K., Chand, S., Rossi, G., Long, C., Bünz, S., Camerlenghi, A., . . . Zillmer, M. (2008). Estimation of gas hydrate concentration from multi-component seismic data at sites on the continental margins of NW Svalbard and the Storegga region of Norway. Marine and Petroleum Geology, 25(8), 744-758. doi:10.1016/j.marpetgeo.2008.02.003

Westbrook, G. K., Thatcher, K. E., Rohling, E. J., Piotrowski, A. M., Pälike, H., Osborne, A. H., . . . Aquilina, A. (2009). Escape of methane gas from the seabed along the West Spitsbergen continental margin. Geophysical Research Letters, 36(15). doi:10.1029/2009gl039191

Willis, J. R. (1977). Bounds and self-consistent estimates for the overall properties of anisotropic composites. Journal of the Mechanics and Physics of Solids, 25, 185–202.

Winkler, K., Nur, A., & Gladwin M. (1979). Friction and seismic attenuation in rocks. Nature, 277, 528-531.

Wood, W. T., Holbrook, W. S., & Hoskins, H. (2000). In situ measurements of P-wave attenuation in methane hydrate and gas bearing sediments on the Blake Ridge, in Paull, C. K., Matsumoto, R., Wallace, P. J., & Dillon W. P. (eds.), Proceedings of the Ocean Drilling Program, Scientific Results: Ocean Drilling Program, 265–272.

Yang, M., Nelson, F. E., Shiklomanov, N. I., Guo, D., & Wan, G. (2010). Permafrost degradation and its environmental effects on the Tibetan Plateau: A review of recent research. Earth-Science Reviews, 103(1), 31-44. doi:https://doi.org/10.1016/j.earscirev.2010.07.002

Yuan, T., Hyndman, R. D., Spence G. D., & Desmons B. (1996). Seismic velocity increase and deep-sea gas hydrate concentration above a bottom simulating reflector on the northern Cascadia continental slope. J. Geophys. Res., 101, 13,655–13,671.

Yun, T. S., Francisca, F. M., Santamarina, J. C., & Ruppel, C. (2005). Compressional and shear wave velocities in uncemented sediment containing gas hydrate. Geophysical Research Letters, 32(10). doi:10.1029/2005gl022607

Zelt, C.A., & Smith, R.B. (1992). Seismic travel-time inversion for 2-D crustal velocity structure. Geophys. J. Int., 108, 16-34.

Zhang, C. J., & Ulrych, T. J. (2002). Estimation of quality factors from CMP records. Geophysics, 67, 1542–1547.

Article I

Singhroha, S., Bünz, S., Plaza-Faverola, A., & Chand, S. (2016). Gas hydrate and free gas detection using seismic quality factor estimates from high-resolution P-cable 3D seismic data. Interpretation (Tulsa), 1, SA39-SA54. Doi: 10.1190/INT-2015-0023.1

Gas hydrate and free gas detection using seismic quality factor estimates from high-resolution P-cable 3D seismic data

Sunny Singhroha[1], Stefan Bünz[1], Andreia Plaza-Faverola[1], and Shyam Chand[2]

Abstract

We have estimated the seismic attenuation in gas hydrate and free-gas-bearing sediments from high-resolution P-cable 3D seismic data from the Vestnesa Ridge on the Arctic continental margin of Svalbard. P-cable data have a broad bandwidth (20–300 Hz), which is extremely advantageous in estimating seismic attenuation in a medium. The seismic quality factor (Q), the inverse of seismic attenuation, is estimated from the seismic data set using the centroid frequency shift and spectral ratio (SR) methods. The centroid frequency shift method establishes a relationship between the change in the centroid frequency of an amplitude spectrum and the Q value of a medium. The SR method estimates the Q value of a medium by studying the differential decay of different frequencies. The broad bandwidth and short offset characteristics of the P-cable data set are useful to continuously map the Q for different layers throughout the 3D seismic volume. The centroid frequency shift method is found to be relatively more stable than the SR method. Q values estimated using these two methods are in concordance with each other. The Q data document attenuation anomalies in the layers in the gas hydrate stability zone above the bottom-simulating reflection (BSR) and in the free gas zone below. Changes in the attenuation anomalies correlate with small-scale fault systems in the Vestnesa Ridge suggesting a strong structural control on the distribution of free gas and gas hydrates in the region. We argued that high and spatially limited Q anomalies in the layer above the BSR indicate the presence of gas hydrates in marine sediments in this setting. Hence, our workflow to analyze Q using high-resolution P-cable 3D seismic data with a large bandwidth could be a potential technique to detect and directly map the distribution of gas hydrates in marine sediments.

Introduction

Gas hydrates are crystalline ice-like structures normally formed at certain temperature and pressure conditions (Brooks et al., 1986). The temperature and pressure conditions required for gas hydrates formation are available in continental slope and permafrost environments (Sloan, 1998). The presence of marine gas hydrates in continental margins has been confirmed from different drilling activities (Collet et al., 1999; Collett and Ladd, 2000; Zhang et al., 2007; Riedel et al., 2010; Liu et al., 2012; Ryu et al., 2013). Seismic methods are commonly used to remotely identify gas hydrates in the marine sediments. The presence of gas hydrates in the sediments is often indicated in seismic data by a bottom-simulating reflection (BSR) (Shipley et al., 1979). It marks a sharp impedance contrast between hydrate-bearing and gas-charged sediments. The BSR occurs at the base of the hydrate stability zone, which is governed mostly by pressure and temperature conditions (Sloan, 1998). Due to this control, the BSR often mimics the seafloor; therefore, it cross cuts the sedimentary strata (Shipley et al., 1979). Because the presence of gas hydrates increases the velocities, the concentration of gas hydrates in sediments is usually estimated using seismic velocity models (Ecker et al., 1998; Lee and Collett, 2001; Gei and Carcione, 2003; Chand et al., 2004). The presence of gas hydrates in sediments has a pronounced effect on the amplitude and frequency characteristics of a seismic signal also (Guerin and Goldberg, 2002; Pratt et al., 2003; Chand and Minshull, 2004). Hydrates in sediments show contradicting amplitude characteristics in seismic sections such as amplitude blanking (Korenaga et al., 1997) and amplitude enhancements (Nouzé et al., 2004; Riedel et al., 2010; Yoo et al., 2013) at different geologic settings.

Seismic signal attenuates mainly due to extrinsic attenuation (due to factors such as spherical divergence, obliquity factor, scattering etc.) and intrinsic attenuation (due to conversion of vibration energy into heat energy) (Mavko et al., 1998). At seismic frequencies,

[1]UiT The Arctic University of Norway, CAGE — Centre for Arctic Gas Hydrate, Environment and Climate, Department of Geology, Tromsø, Norway. E-mail: sunny.singhroha@uit.no; stefan.buenz@uit.no; andreia.a.faverola@uit.no.

[2]UiT The Arctic University of Norway, CAGE — Centre for Arctic Gas Hydrate, Environment and Climate, Department of Geology, Tromsø, Norway and Geological Survey of Norway (NGU), Trondheim, Norway. E-mail: shyam.chand@ngu.no.

Manuscript received by the Editor 20 January 2015; revised manuscript received 9 June 2015; published online 23 September 2015. This paper appears in *Interpretation*, Vol. 4, No. 1 (February 2016); p. SA39–SA54, 11 FIGS.

http://dx.doi.org/10.1190/INT-2015-0023.1.

analysis on attenuation normally refers to intrinsic attenuation (Mavko et al., 1998), which can be studied through spectral analysis (Jacobson et al., 1981). Because gas hydrate increases the stiffness of the matrix (Jung et al., 2012) and P-wave velocity, it was normally assumed that the sediments saturated with gas hydrates will show lower attenuation (Wood et al., 2000). Unlike P-wave velocity, no unique trend of seismic attenuation in gas hydrates can be observed from the literature; thus, making attenuation characteristic of the gas hydrate bearing sediments a debatable topic (Guerin et al., 1999; Wood et al., 2000; Chand et al., 2004; Rossi et al., 2007; Sain et al., 2009; Sain and Singh, 2011; Jaiswal et al., 2012; Dewangan et al., 2014). Laboratory experiments in hydrate bearing sediments indicated increase of attenuation with hydrate saturation (Priest et al., 2006; Best et al., 2013), whereas attenuation estimates from field experiments on gas hydrates indicated contradicting results. For example, studies on well-log data (Guerin and Goldberg, 2002, 2005; Matsushima, 2005), vertical seismic profile (VSP) data (Pratt et al., 2005; Bellefleur et al., 2007), and on crosshole seismic data (Pratt et al., 2003; Bauer et al., 2005) indicated an increase in attenuation. Other studies, mainly on surface seismic data (Matsushima, 2006; Rossi et al., 2007; Dewangan et al., 2014) indicated a decrease in attenuation. The increase (Guerin and Goldberg, 2002; Gei and Carcione, 2003; Chand and Minshull, 2004; Lee and Collett, 2006) and decrease (Sain and Singh, 2011; Dewangan et al., 2014) in attenuation have been explained by using different rock-physics models depending on the assumed microstructure of the hydrate and also sediment-hydrate mixtures. Chand and Minshull (2004) suggest that the amount of attenuation not only changes with hydrate saturation but also with the frequency of the seismic signal.

The seismic quality factor (Q), the inverse of seismic attenuation, can be estimated from the seismic data set using different methods, which include the amplitude decay method (Badri and Mooney, 1987), the rise time method (Gladwin and Stacey, 1974), the centroid frequency shift method (Quan and Harris, 1997), wavelet modeling (Jannsen et al., 1985), the pulse broadening method (Hatherly, 1986), the spectral ratio (SR) method (Båth, 1982; Jannsen et al., 1985), and the inversion method (Amundsen and Mittet, 1994). Tonn (1991) compares 10 methods of attenuation estimation using VSP seismograms and concludes that no single method is suitable for all situations.

In the present study, we apply two different methods to investigate seismic attenuation in gas-hydrate- and free-gas-saturated sediments from the Vestnesa Ridge, a deepwater gas hydrate system located offshore west Svalbard (Figure 1). The quality (Q) factor has been estimated from P-cable seismic data using the SR method (Jannsen et al., 1985) and the centroid frequency shift method (Quan and Harris, 1997). The centroid frequency shift method establishes a relationship between the change in the centroid frequency of an amplitude spectrum and the Q value of a medium (Quan and Harris, 1997). On the contrary, the SR method estimates the Q value of a medium by studying the differential decay of different frequencies (Båth, 1982). Due to limitations of seismic bandwidth in conventional seismic data, it is almost impossible to map Q with high accuracy. Low signal-to-noise ratio (S/N), short bandwidth, source/receiver array directivity, and distinct raypaths in a common depth point (CDP) gather are the main problems encountered in Q analysis from conventional surface seismic data (Hustedt and Clark, 1999). But P-cable surface seismic data are essentially zero offset (offset varying from 97 to 143 m) in deep water and have broad bandwidth (20–300 Hz). Raypaths of different traces in a CDP gather of P-Cable data are ap-

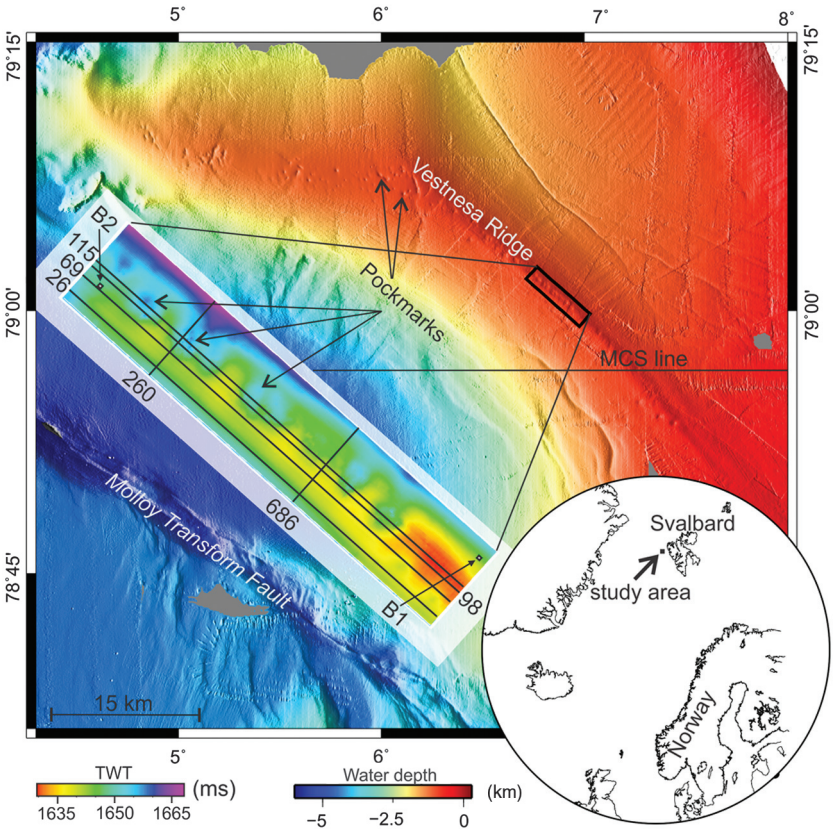

Figure 1. Bathymetry map showing the location of our study area at the Vestnesa Ridge, on the west Svalbard continental margin. The inset figure shows a seafloor time-structure map derived from the 3D seismic data. Key inlines and crosslines are indicated on this seafloor map. Two small boxes (B1 and B2) show the location of centroid frequency curves plotted in Figure 5. A velocity model was derived from the MCS line by Hustoft et al. (2009) (see also Figure 11d).

proximately similar at deep water depth because the offset is quite small. Stacked P-cable data have a high S/N, and the stacking process involves traces with almost similar raypaths. These characteristics of P-cable data match well with the characteristics of VSP data (Galperin, 1985) and make P-cable data suitable for subsurface Q analysis. Moreover, using P-cable 3D seismic data for estimating Q allows us to analyze the spatial distribution of Q, which can be integrated with 3D seismic interpretation. Thereby, we can link Q estimates with anomalies related to the presence of gas hydrate and free gas in the sediments.

Study area

Our study focuses on the active seeping segment of the Vestnesa Ridge, an approximately 100-km-long gas hydrate charged contourite drift developed over <20 Ma oceanic crust offshore west Svalbard (Figure 1) (Eiken and Hinz, 1993; Vogt et al., 1994; Bünz et al., 2012). The contourite drift is in close proximity to the Molloy and the Knipovich slow-spreading oceanic ridges, and it is located between the Molloy and the Spitsbergen transform faults (e.g., Ritzmann et al., 2004). The Vestnesa Ridge consists of three main stratigraphic sequences named according to their correlation with ocean drilling program sites at the Yermak Plateau (YP) (Eiken and Hinz, 1993): The oldest unit (YP1) is of Miocene age and consists dominantly of syn-rift deposits directly lying over the oceanic crust (Eiken and Hinz, 1993; Ritzmann et al., 2004); the middle sequence (YP2) consists of sediments deposited by migrating contour currents; and, finally, the youngest sequence (YP3), is dominated by margin-parallel contour currents and by glacigenic debris flow deposits (Howe et al., 2008).

A gas hydrate system and an associated free-gas zone exist along the Vestnesa Ridge (Hustoft et al., 2009; Petersen et al., 2010; Bünz et al., 2012; Plaza-Faverola et al., 2015). The system is restricted to the upper stratigraphic sequence (YP3) and has a series of gas chimneys and pockmarks associated along the full extent of the Vestnesa Ridge. However, only pockmarks located toward the easternmost part of the ridge (where our 3D seismic survey is located; Figure 1) are actively seeping gas presently (Bünz et al., 2012; Smith et al., 2014). Gas chimneys toward the westernmost part of the ridge seem inactive presently, but foraminiferal records indicated past activity approximately 8000 my ago (Consolaro et al., 2014).

Data

We used high-resolution P-cable (Planke et al., 2009; Petersen et al., 2010) 3D seismic data acquired in 2013 on board the *R/V Helmer Hanssen* (Plaza-Faverola et al., 2015). The system consists of 14 streamers towed parallel behind the ship. The 25-m-long streamers contain eight receiver groups each. The streamers are attached to a cross cable towed perpendicular to the vessel's streaming direction and spread by two large trawl doors. The spacing of streamers along the cross cable is 12.5 m. However, due to the curvature of the cross cable, the distance between the streamers varies between 6 and 10 m. The high-resolution P-cable system was used together with a Mini GI gun (Sercel; 15/15 in^3). The gun was fired at an interval of 6 s with a firing pressure of 170 bar. The source-receiver offset varies from 97 to 143 m. Traces have been recorded with a 3-s record length at a 0.25-ms sampling interval.

During seismic data processing, the utmost care has been taken to avoid all the steps that can potentially distort the amplitude spectrum within the main seismic bandwidth. The processing of the high-resolution 3D seismic data mainly included navigational correction, static and tidal correction, binning, band-pass filtering (10–20–300–350), and normal moveout (NMO) correction and stacking. NMO correction can potentially distort the amplitude spectrum due to NMO stretching. But for short-offset seismic data in deep water, this distortion will be too small and can be neglected. A 3D Stolt migration was applied using a constant velocity of 1500 m/s. The spatial resolution of the seismic data is quite high with a bin size of 6.25×6.25 m. The seismic data cover an area of approximately 14 km^2. The data have a broad frequency spectrum ranging from approximately 20 to 300 Hz (Figure 2a).

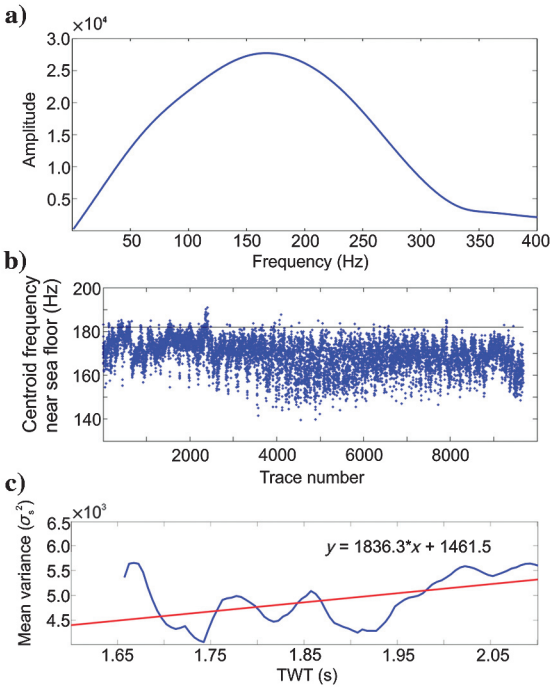

Figure 2. (a) Amplitude spectrum of the seismic signal near the seafloor. (b) Centroid frequency of the seismic signal in shallow sediments near the seafloor for different traces in seismic data. The black line shows the assumed centroid frequency at the seafloor. (c) The blue curve shows the mean variance of the amplitude spectrum (σ_s^2) at different arrival times. The red line shows the best fit line for changes of mean variance with two-way traveltime.

Methodology

Amplitude, frequency, and phase are three basic attributes of a seismic signal. Quantitative analysis of these attributes is done using different derivations and transforms. For example, quantitative estimation of the frequency attribute involves different time-frequency transforms. Reine et al. (2009) discuss the robustness of seismic attenuation measurements using different time-frequency transforms. In the present study, the short-time Fourier transform (Gabor, 1946) is used to transform a seismic signal into the frequency domain. The data converted to the frequency domain are used to study seismic attenuation. We use the centroid frequency shift (Quan and Harris, 1997) and the SR method (Jannsen et al., 1985) to estimate Q in gas-hydrate- and free-gas-saturated sediments.

Centroid frequency method

The centroid frequency of an amplitude spectrum (f_c) is defined as

$$f_c = \frac{\sum A(f) \times f}{\sum A(f)}, \tag{1}$$

where $A(f)$ corresponds to the amplitude of frequency (f) in an amplitude spectrum.

The centroid frequency of a signal gives us an idea about the energy level of a signal. Because the energy of a signal decreases as it propagates in the subsurface, the centroid frequency of an amplitude spectrum shifts toward lower values with further propagation into deeper layers. By plotting the centroid frequency for the entire seismic section, a broad overview about the subsurface seismic attenuation can be established. Quan and Harris (1997) propose a method to estimate Q using centroid frequency shift analysis. They consider the amplitude spectrum of the received signal $R(f)$ as a function of the incident wave $S(f)$ and the instrument/medium response $G(f)H(f)$:

$$R(f) = G(f)H(f)S(f). \tag{2}$$

Parameter $G(f)$ includes geometric spreading, instrument response, source/receiver coupling, radiation/transmission coefficients, and phase accumulation effects caused by propagation: $H(f)$ is a factor that takes into account the effect of intrinsic attenuation on a seismic signal. Because attenuation is proportional to frequency within the seismic bandwidth, response $H(f)$ can be written as (Johnston et al., 1979)

$$H(f) = \exp\left(-f \int_{\text{ray}} \alpha_0 \text{dl}\right), \tag{3}$$

where the integral is taken along the raypath, and α_0 is the attenuation coefficient defined by (Johnston et al., 1979)

$$\alpha_0 = \frac{\pi}{Qv}, \tag{4}$$

where Q is the quality factor and v is the velocity of the medium.

With the assumption that the amplitude spectrum follows a Gaussian pattern of distribution, Quan and Harris (1997) after rearranging the equations finally come to the following equation:

$$\int_{\text{ray}} \alpha_0 \text{dl} = \frac{f_s - f_r}{\sigma_s^2}, \tag{5}$$

where f_s is the centroid frequency of the source signal (Figure 2b), f_r is the centroid frequency of the received signal, and σ_s^2 is the variance of the source amplitude spectrum:

$$\sigma_s^2 = \frac{\int_0^\infty (f - f_s)^2 A(f) \text{df}}{\int_0^\infty A(f) \text{df}}, \tag{6}$$

where $A(f)$ is the amplitude spectrum of the source signal, and other parameters are the same as described in the above equation. To account for the increase in the variance of amplitude spectrum σ_s^2 of seismic signal with arrival time, a trend line for σ_s^2 at different arrival times is estimated (Figure 2c). The straight line is fitted to the mean σ_s^2 values.

If the velocity and quality factor Q is assumed constant in a medium, the final expression for the quality factor Q can be written (Talukder, 2013) as

$$Q = \frac{\pi \sigma_s^2 \Delta t}{f_s - f_r}, \tag{7}$$

where Δt is the total traveltime and the rest of the parameters are same as described in the above equations.

Spectral ratio method

The SR method is one of the most commonly used methods to estimate Q in a medium. This method takes into account the differential decay of different frequencies. Higher frequencies tend to decay at a much higher rate as compared with lower frequencies while passing through an attenuating medium (Båth, 1982). The differential decay of different frequencies depends upon the Q of a medium.

Jannsen et al. (1985) discuss the application of the SR method to estimate Q from seismic data. Amplitude spectrums ($A_1(\omega)$ and $A_2(\omega)$) of two reflections from different depths (Z_1 and Z_2), can be written as

$$A_1(\omega) = A_0(\omega) G(Z_1) R_1 e^{-2\alpha_1 Z_1}, \tag{8}$$

$$A_2(\omega) = A_0(\omega) G(Z_2)(1 - R_1^2) R_2 e^{-2\alpha_1 Z_1} e^{-2\alpha_2 (Z_2 - Z_1)}, \tag{9}$$

where $A_0(\omega)$ is the amplitude spectrum of the incident wavelet at $Z = 0$, $G(Z_1)$ and $G(Z_2)$ account for the geo-

metric spreading and other factors leading to decay in amplitudes, R_1 and R_2 are reflection coefficients for different boundaries, and α_1 and α_2 are the attenuation coefficients. The SR of the two spectra can be written as

$$\mathrm{SR}(\omega) = C_1 e^{-2\alpha_2(Z_2 - Z_1)}, \tag{10}$$

$$C_1 = \frac{G(Z_2)(1 - R_1^2)R_2}{G(Z_1)R_1}, \tag{11}$$

where C_1 is the ratio of factors related to the geometric spreading and reflection coefficients. Assuming phase velocity β to be independent of frequency in the SR (Båth, 1982), natural log of the SR can be written as

$$\ln(\mathrm{SR}(\omega)) = \ln(C_1) - \alpha_2 \Delta T \beta, \tag{12}$$

where ΔT is the time difference between two reflections. Substituting the value of α as $\pi f/(Q\beta)$ (Johnston et al., 1979), we get linear relation between ln (SR(ω)) and frequency; i.e.

$$\ln(\mathrm{SR}(\omega)) = \ln(C_1) - \left(\frac{\pi \Delta T}{Q}\right) f. \tag{13}$$

Hence, the slope, i.e., $-\pi\Delta T/Q$, of the SR (in logarithmic scale) versus the frequency plot depends on the Q of a medium, and the intercept is related to the geometric spreading and reflection coefficients, which are independent of the frequency. Using this concept, the Q value can be estimated from the slope of the best-fit line in the SR (in logarithmic scale) versus the frequency plot. In real data, two wavelets can be picked by windowing two reflections (Figure 3a), and then the Fourier transform can be applied to get the amplitude spectrum of these two wavelets (Figure 3b). The SR method can be applied on these two amplitude spectra, and the effective Q of a medium between these reflections can be estimated (Figure 3c).

Analysis using the centroid frequency method

Analysis using centroid frequency plots has been done to study changes in the centroid frequency with depth. An inline has been selected from seismic data in which a BSR is clearly identified by high seismic amplitudes at approximately 1.9 s two-way traveltime in the seismic section (Figure 4a) (Bünz et al., 2012; Smith et al., 2014). The BSR separates hydrate-bearing sediments from an approximately 100-m-thick free-gas zone (Hustoft et al., 2009). Other notable features are the vertical zones of acoustic transparency or chaotic seismic facies. These are interpreted as vertical fluid-flow features, the so-called chimneys. They terminate in seafloor depressions known as *pockmarks* (Figure 4c) (Bünz et al., 2012).

The centroid frequency has been calculated for all of the traces in the seismic section at an interval of 5 ms. Enough samples have been taken to ensure that the lowest frequency in the main seismic bandwidth will have at least one wavelength to sample. The derived centroid frequencies are shown in Figure 4b. The centroid frequency decreases significantly beneath the BSR. Prominent low-centroid frequency anomalies are observed in the free-gas zone especially in the southeastern part of the seismic section (Figure 4b). Gas chimneys are observed in the seismic section. Some gas chimneys also show low centroid frequency anomalies. Some of these anomalies appear to intrude the chimneys from the free-gas zone beneath the BSR. Coincidentally, intrusion happens for gas chimneys that have active gas seepage at the seafloor (Figure 4c) (Bünz et al., 2012).

Q *estimation*

Variance of an amplitude spectrum (σ_s^2) and reference centroid frequency (f_s) were calculated to further estimate Q for different layers using the centroid frequency shift method. To account for an increase in the σ_s^2 with arrival time, σ_s^2 of a seismic signal is plotted with respect to the two-way arrival time. The trend line for σ_s^2 at different arrival times is estimated (Figure 2c). The σ_s^2 to be used in equation 7 is calculated from the linear fit parameters of the best-fit line. The centroid frequency of a seismic signal at the seafloor is used as a reference centroid frequency for estimating a 1D

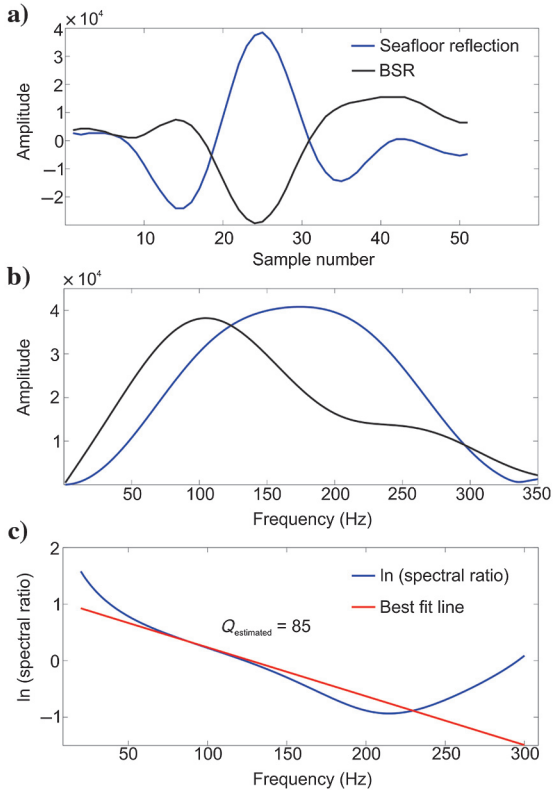

Figure 3. (a) Seafloor reflection and BSR picked from a trace located at the 26th inline and 260th crossline (see Figure 1 for the location). (b) Amplitude spectrum of the picked wavelets. (c) Plot of the SR (in logarithmic scale) versus frequency. The red curve shows the best-fit line (L_1-norm) in this plot. The value Q is derived from the slope of the best-fit line.

Q model for every trace. The centroid frequency of the seismic signal in shallow sediments close to the seafloor (shown in Figure 2b) ranges from 150 to 185 Hz for almost all the traces except for a few located in a pockmark, where there were lower centroid frequency values. The centroid frequency of the seismic signal at the seafloor is expected to be higher than the centroid frequency of a seismic signal in shallow sediments. After neglecting aberrations, we use 182 Hz as a reference centroid frequency (Figure 2b).

Prominent reflections observed in the seismic data have been picked, and Q values for different layers between picked reflections have been estimated (Figures 5a and 6a). A Q model derived from one of the traces in the seismic data is shown in Figure 5a–5d. Centroid frequencies are calculated at a time interval of 5 ms for each trace using a sliding time window along the trace (Figure 5a and 5b). Fluctuations in centroid frequencies make Q estimation difficult. Therefore, to reduce these effects, centroid frequencies of traces falling within the 31.25×31.25 m bin have been stacked to get a centroid frequency trend/curve (Figure 5c). This process also reduces the size of the seismic data set and makes it computationally convenient. Synthetic centroid frequency curves are generated for different

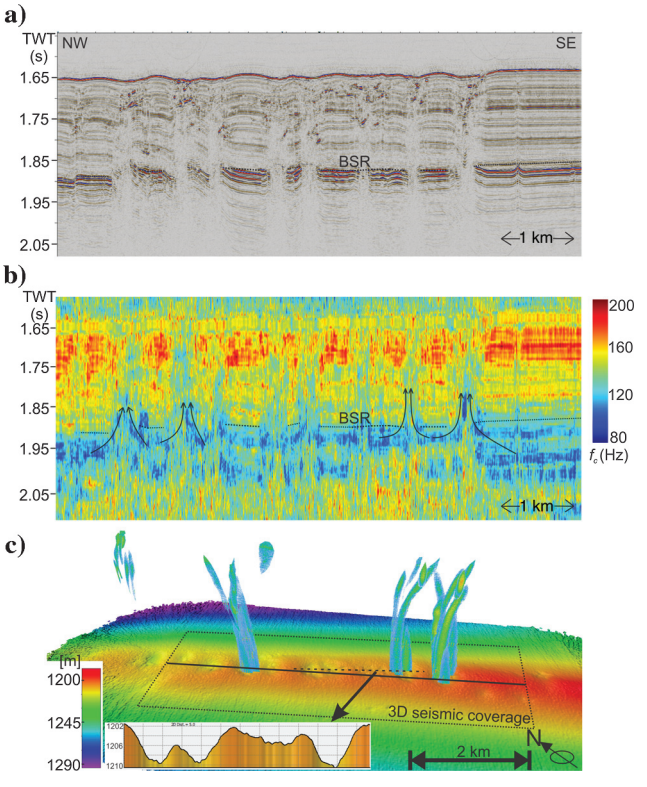

Figure 4. (a) Selected seismic section (inline 115; see Figure 1 for the location) from the 3D seismic data. (b) Centroid frequency plot corresponding to the seismic section. Black arrows indicate the possible subsurface fluid migration through gas chimneys and the subsequent seafloor gas seepage. (c) Acoustic flares documenting active seepage (modified from Bünz et al., 2012). The black line shows the location of the inline shown in panels (a and b).

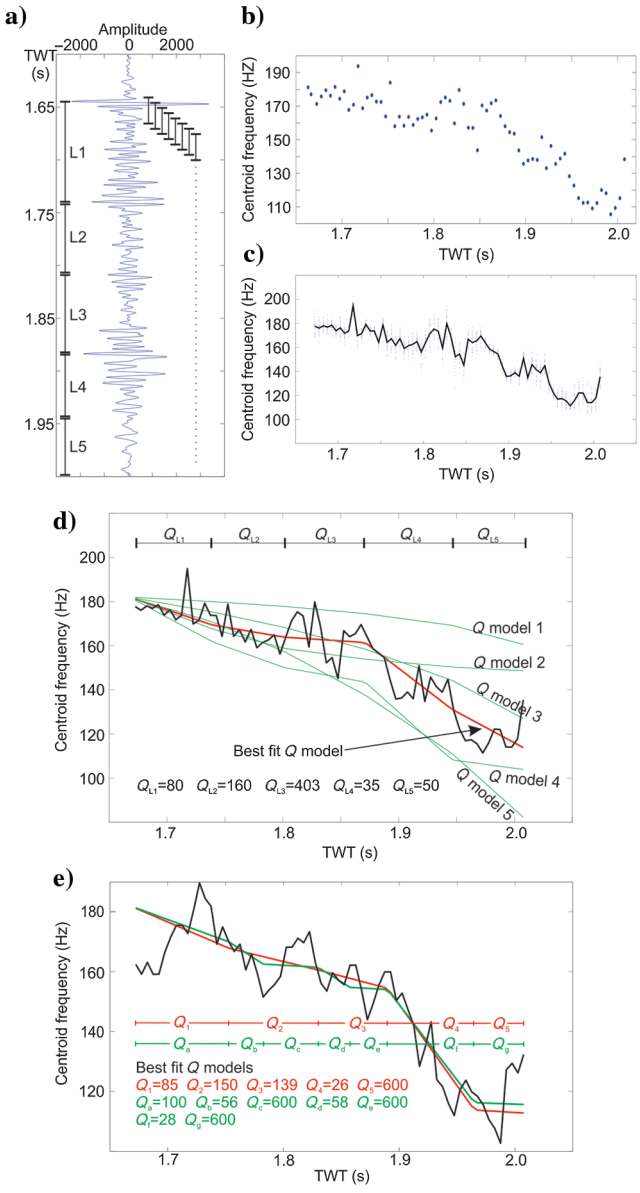

Figure 5. (a) Seismic trace corresponding to 183rd inline and 1093rd crossline (location of the trace lies in the center of B1 as shown in Figure 1). Q has been estimated for the L1, L2, L3, L4, and L5 intervals. (b) Centroid frequencies calculated in the 5-ms sliding time window (Figure 5a). (c) Centroid frequency trend/curve for 25 traces in a 31.25×31.25 m small box B1 (Figure 1). (d) The black curve shows the centroid frequency curve. The green curves show the synthetic centroid frequency curves corresponding to Q model 1 ($Q_{L1} = 500$, $Q_{L2} = 400$, $Q_{L3} = 300$, $Q_{L4} = 200$, and $Q_{L5} = 100$), Q model 2 ($Q_{L1} = 70$, $Q_{L2} = 100$, $Q_{L3} = 200$, $Q_{L4} = 300$, and $Q_{L5} = 500$), Q model 3 ($Q_{L1} = 150$, $Q_{L2} = 125$, $Q_{L3} = 100$, $Q_{L4} = 75$, and $Q_{L5} = 50$), Q model 4 ($Q_{L1} = 50$, $Q_{L2} = 75$, $Q_{L3} = 150$, $Q_{L4} = 30$, and $Q_{L5} = 200$), and Q model 5 ($Q_{L1} = 90$, $Q_{L2} = 65$, $Q_{L3} = 50$, $Q_{L4} = 40$, and $Q_{L5} = 30$). The red curve shows the synthetic centroid frequency curve for the best-fit (L_1-norm) Q model. (b) Five layer best-fit Q model (red) and seven layer best-fit Q model (green) for a centroid frequency curve (location shown by a small box B2 in Figure 1).

possible Q models (Q varying from 1 to 600 in all five layers). Synthetic centroid frequency curves for five Q models out of 600^5 possible Q models are shown in green color in Figure 5d. These synthetic centroid frequency curves are matched with estimated centroid frequency curves (estimated from traces in the 31.25 × 31.25 m bin), and the misfit between the two curves has been computed. The L_1-norm approach (Claerbout and Muir, 1973) has been used to calculate the misfit and to pick the best possible Q model out of the possible range of Q models. The L_1-norm approach has been adopted to reduce the significance of the spiky points in the centroid frequency curves. This process of estimating Q has been repeated on all the traces in the seismic data to generate a Q cube.

Observations

The Q values along one of the inlines (Figure 6a) indicate high Q anomalies in the layer above the BSR and low Q anomalies below the BSR (Figure 6b). The Q slices for different layers give an idea about the lateral variation of Q within a layer. Figure 7 shows Q slices for different layers illustrating the lateral variation of Q anomalies within a layer. The BSR lies between Q slices in Figure 7c and 7d. We observe particularly low Q values in some areas within the first layer (Figure 7a) coinciding with the location of the chimney structures. Q estimates in the second layer follow a normal trend except for few small patches of high Q (Figure 7b). Some of these slightly elevated Q values seem to correspond particularly with the outer rims of the chimney structures (Figure 7b). Just above the BSR, we observe very high Q values, particularly in the southern half of the 3D seismic data (Figure 7c). These anomalies are found to be laterally continuous. On the contrary, Q values in the center part of this slice (Figure 7c) follow the trend of chimneys, and Q values are comparatively lower than those in the slice above (Figure 7b). Extremely low Q values have been observed in the Q slice corresponding to the free gas zone beneath the BSR except for the locations corresponding to that of the chimneys (Figure 7d).

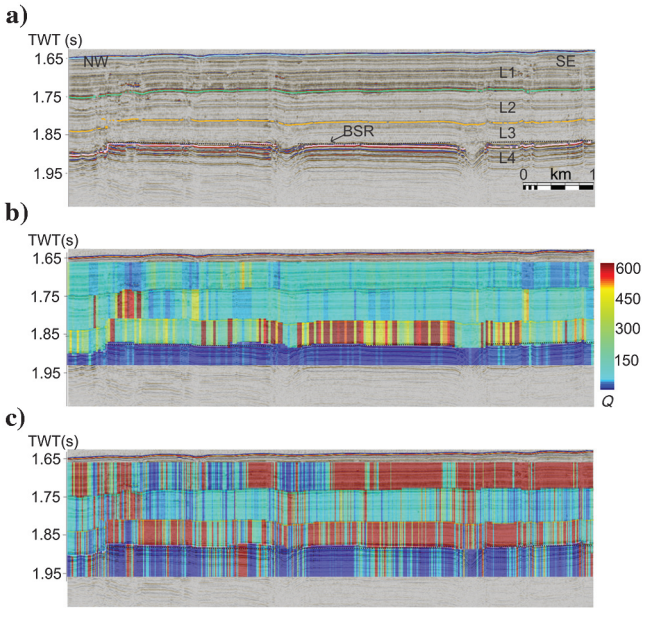

Figure 6. (a) Seismic section of inline 69 (see Figure 1 for location) with picked seafloor and three major subsurface reflections. L1, L2, L3, and L4 show the layers for which Q is estimated. (b) Overlay of seismic section and Q estimates obtained from the centroid frequency shift method. (c) Overlay of the seismic section and Q estimates obtained from the SR method.

Analysis using the spectral ratio method

Q *estimation*

The SR method can be applied to estimate the effective Q of a medium between two prominent reflections (Figure 3). We extend this method to estimate Q for the same four layers between prominent reflections in the seismic data (Figure 6a) as used in the centroid frequency shift method. Picked reflections are windowed, and the SR method is applied on adjacent reflections to estimate a subsurface Q model. Figure 8 shows the different steps involved in the application of the SR method on one of the traces. The same procedure is repeated on all the traces in the seismic volume to generate a Q cube.

Observations

The Q pattern for one of the inlines (Figure 6a) shows high Q values in the layer just above the BSR (Figure 6c). The Q estimates based on the SR method in this layer (Figure 6c) is comparable with the Q estimates from the centroid frequency shift method (Figure 6b). The Q slices for different layers are plotted to further analyze the results (Figure 9). In the plan

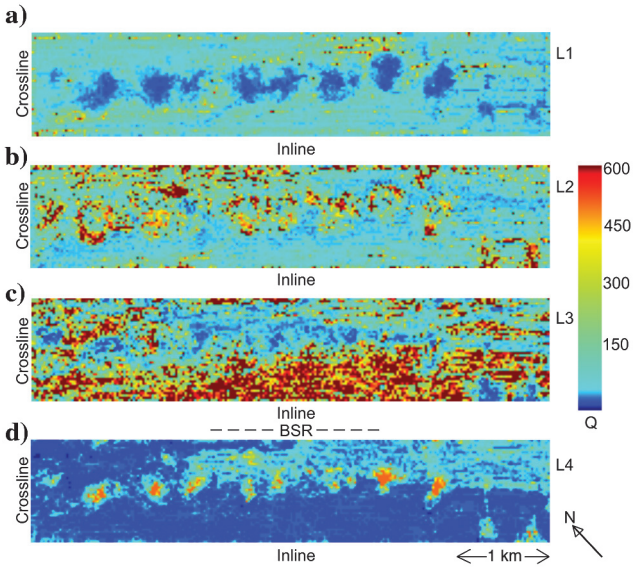

Figure 7. Q slices for different layers estimated using the centroid frequency shift method. (a-d) The Q slices correspond to layers L1, L2, L3, and L4 (Figure 6a), respectively.

view, the Q estimates vary significantly within the first layer (Figure 9a). In the second layer, small patches of high Q values coincide with the chimney features similar to that obtained by the centroid frequency shift method. Also, we observe high Q anomalies in the Q slice corresponding to the layer just above the BSR (Figure 9c). We find that these high Q anomalies are laterally continuous and match well with the anomalies observed in the Q slice obtained from the centroid frequency shift method (Figure 7c). Beneath the BSR, we observe predominantly low Q values (Figure 9d). However, we also observe some regions with high Q anomalies in the fourth layer roughly corresponding to chimney locations (Figure 9d). Here, results obtained through the SR method (Figure 9d) and centroid frequency shift method (Figure 7d) do not agree with each other. At the BSR depth, signal strength is significantly , and Q estimates from SR method are extremely unstable. This may be the reason for the high Q values observed in some areas below the BSR.

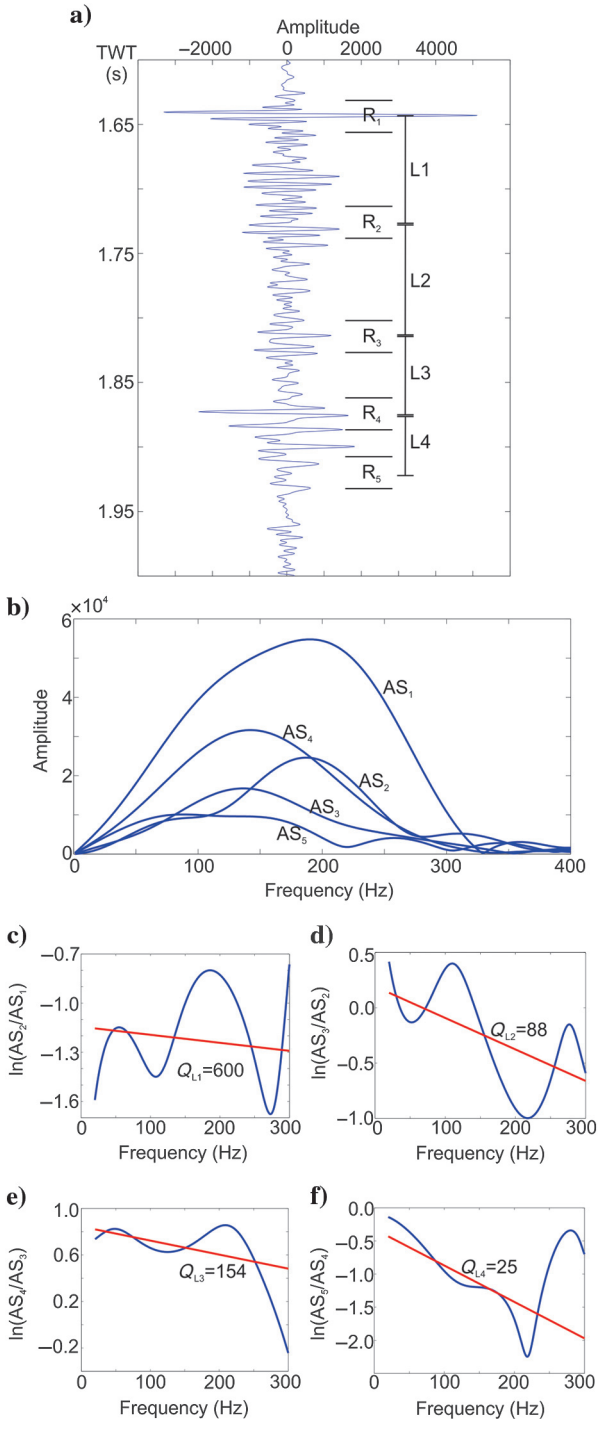

Figure 8. (a) Seismic trace corresponding to the 98th inline and 686th crossline (see Figure 1 for location): L1, L2, L3, and L4 are four layers between five reflections (R_1, R_2, R_3, R_4, and R_5). (b) AS_1, AS_2, AS_3, AS_4, and AS_5 are the amplitude spectra calculated over time windows R_1, R_2, R_3, R_4, and R_5, respectively. (c-f) SR versus frequency plot. The red lines show the best-fit line derived using L_1-norm. Q_{L1}, Q_{L2}, Q_{L3}, and Q_{L4} are the derived Q values for layers L1, L2, L3, and L4, respectively.

Uncertainties and limitations

Estimating Q from seismic data is typically accompanied by some uncertainties and limitations. Contribution of reflectivity sequences in the calculated amplitude spectrum directly affects Q estimates. In case of thin layers with some periodicity, earth's reflectivity function contributes in shaping the spectrum of the effective recorded signals. Weak reflectivity over a time window (Figure 5a) can also create bias in Q estimates if the noise spectrum is not white. Ning and Wen-kai (2010) discuss in detail the effect of reflectivity sequences on Q estimates. The SR method is more sensitive to these effects because Q is estimated from the spectrum of two wavelets. Fluctuations observed in centroid frequency curves are also primarily due to the effect of reflectivity sequences in the recorded signal.

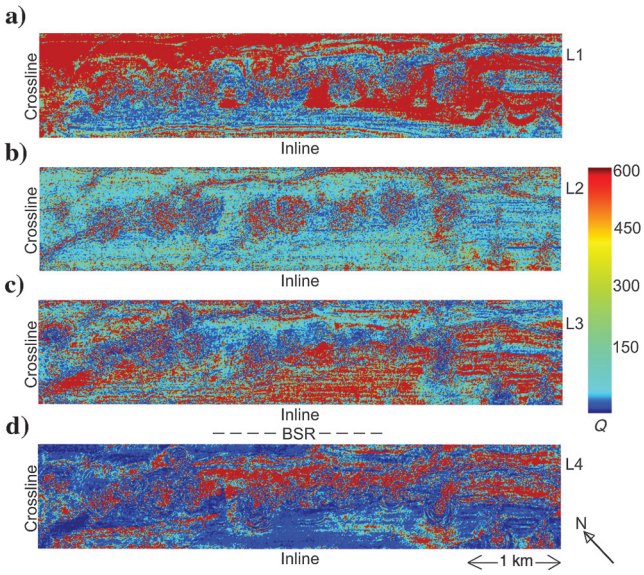

Figure 9. The Q slices for different layers estimated using SR method. (a-d) Q slices correspond to layers L1, L2, L3, and L4 (Figure 6a), respectively.

Scattering is another factor that will lead to reduction in the amplitude of different frequencies. Different types of scattering can occur depending on the size of the particles, which include Rayleigh, Mie, and forward scattering (Mavko et al., 1998). Mie scattering is the type of scattering that will occur when the heterogeneity scale length is of the order of the seismic wavelength. The main difference between scattering and intrinsic attenuation is that scattering redistributes wave energy within the medium but does not remove the energy from the overall wavefield, whereas intrinsic attenuation converts vibration energy into heat energy (Sato and Fehler, 1997). Intrinsic attenuation quantified using different methods also includes the contribution from scattering attenuation (Spencer et al., 1982). This will directly affect the Q estimates from different methods.

Processing of seismic data can be another source of error in Q estimation. Ideally, all the processing steps that can potentially alter the amplitude spectrum of a seismic signal should be avoided. In P-cable data, the potential of this problem is significantly reduced because P-cable data are close to a zero offset (97–143 m), particularly given the water depth in the present study. Frequency distortions due to NMO stretching are negligible for small offsets at deep water depths. Frequency distortions due to Stolt migration are also negligible because the layers in the study area are essentially flat. Apart from these two processing steps, no other step is involved that can potentially influence the analysis.

The traveltime through a picked layer is a very important factor in estimating Q using the centroid frequency shift method. Picking more reflections and using them as layer boundaries increases the number of layers for which an effective Q model will be estimated but decreases the traveltime of the layers. Effect of fluctuations in the centroid frequency curve on Q estimates is more pronounced for thinner layers. Thus, accuracy of the Q estimates in thinner layers is poorer than in thicker layers. Figure 5e shows the best-fit Q models for different numbers of layers. When the number of picked layers is increased from 5 to 7, the instability in the Q estimates can be clearly seen. Therefore, reflections need to be picked properly so that Q can be estimated for different layers with an acceptable accuracy.

A histogram of the Q estimates from the centroid frequency shift method (Figure 10a) and SR method (Figure 10d) in layer 3 (which lies just above the BSR) have been plotted to analyze the statistical distribution of the Q estimates within a layer. The peak at $Q = 600$ observed in the histograms is due to the fact that only Q values up to 600 have been taken into consideration. All Q values greater than 600 will be estimated as 600, and it is extremely difficult to differentiate between different Q values for those higher than approximately 150. The accuracy of the Q estimates decreases for high Q values, whereas it changes very rapidly with a small change in the seismic signal decay. This small amount of decay becomes comparable with the fluctuations caused by other factors, which create a problem in Q estimation. Figure 5d shows the estimated Q for different layers. From layers 2 to 3, estimated Q changes from 160 to 403, but there is a very small change in the tilt of the best-fit curve. This limits the accuracy of Q estimates for high Q values and due to this fact, only Q values up to 600 have been taken into consideration (Figure 10).

Given the two methodological approaches for estimating Q, their inherent limitations and the constraints of the 3D seismic, as earlier reported by Quan and Harris (1997) and Matsushima (2006), we also found that the centroid frequency shift method gave more stable Q estimates. The contribution of reflectivity sequences in the calculated amplitude spectrum and scattering effects limited the vertical resolution of Q estimates. We tried to do high-resolution Q sampling, but the accuracy of the Q estimates decreased when a greater number of layers was used to estimate Q. Reflectivity sequences and scattering effects made the continuous mapping of Q unstable. Q estimates became unreliable for thin-

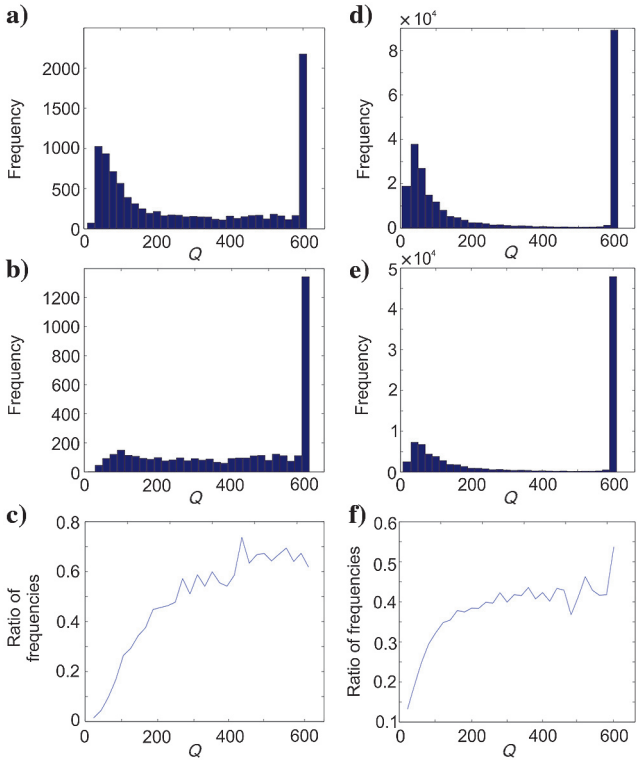

Figure 10. (a) Histogram of Q values obtained using centroid frequency shift method in the layer L3. (b) Histogram of Q values obtained using centroid frequency shift method in the layer L3 with $Q < 30$ (a high concentration of free gas) in the layer L4. (c) Ratio of histograms b and a. (d) Histogram of Q values obtained using SR method in the layer L3. (e) Histogram of Q values obtained using SR method in the layer L3 with $Q < 30$ (a high concentration of free gas) in layer L4. (f) Ratio of histograms e and d. Layers L1, L2, L3, and L4 are shown in Figure 6a.

ner layers. We observed a trade-off between the accuracy and resolution.

Discussion

There are different factors that contribute to intrinsic attenuation of a seismic signal (Toksöz and Johnston, 1981). Major factors that play a crucial role are lithology, fluid type, and structural features (Walsh, 1966; Johnston et al., 1979; Toksöz et al., 1979; Winkler et al., 1979; Spencer, 1979; Toksöz and Johnston, 1981; Winkler and Nur, 1982; Murphy et al., 1986; Pointer et al., 2000; Parra et al., 2002; Prasad and Nur, 2003; Behura, 2009). The exact details of the sedimentary environment of the study area are not well known, but it is believed to be composed of smoothly deposited layers of contourite deposits (Eiken and Hinz, 1993; Howe et al., 2008). Under such geologic settings, the major factors that can prominently change the intrinsic attenuation property of a medium are changes in fluid type and fluid saturation. Changes in the gas hydrate saturation within a gas hydrate stability zone will sharply change the intrinsic attenuation spatially. Several publications explain the relationship between seismic attenuation and fluid saturation (O'Connell and Budiansky, 1977; Mavko and Nur, 1979; Spencer, 1979; Murphy et al., 1986; O'Hara, 1989; Pointer et al., 2000; Prasad and Nur, 2003; Rapoport et al. 2004). In addition, structural features scatter the seismic signal and contribute significantly to the estimated intrinsic attenuation (Hamilton and Mooney, 1990). It is thus challenging to distinguish between scattering attenuation and intrinsic attenuation (Wennerberg, 1993). The Q parameter estimated for quantifying intrinsic attenuation of a medium also includes the effects from scattering attenuation (Spencer et al., 1982). The possible effects of gas hydrates and free gas on Q estimates are studied by estimating Q values for different layers in the gas-hydrate stability zone and free-gas zone. Spatial analysis of the Q estimates from the 3D seismic data then allows us to recognize structures and areas that can be related to the presence of gas hydrates in marine sediments even in the absence of seismic velocity control.

The Q values have been estimated for different layers using the centroid frequency shift method and SR method. The Q values estimated in deeper layers (L2, L3, and L4) using these two methods are found to be in concordance with each other, and Q values in layers just above the BSR (L2 and L3) are in good agreement with the Q values normally observed in gas-hydrate-bearing marine sediments (Wood et al., 2000). The Q estimates in the first layer (L1) do not correspond well. Noisy amplitude spectrum near the seafloor (Dewangan et al. 2014) and fluctuating SR (Figure 8c) can be the possible reason for the unstable Q estimates from the SR method in the first layer. However, in the context of this analysis, it is important to study relative changes in Q particularly along Q slices throughout the whole volume because these might be related to the type of pore fluid and saturation in a given area or structure.

Both Q analysis methods estimate high Q values in a layer just above the BSR (Figures 7c and 9c). Below the BSR, the centroid frequency (Figure 4b) and Q values of both methods drop significantly (Figures 7d and 9d). Very low Q values are observed below the BSR except for the locations below chimneys, where a high Q value is observed (Figures 7d and 9d). A high free-gas concentration can be the reason for rapid attenuation of the seismic signal below the BSR. The strength of the BSR in the seismic data (Figure 4a) also gives some indication about the accumulation of free gas in the region, which is estimated to be as high as 1.5%–2% of the pore space (Hustoft et al., 2009). In gas chimneys, the seismic signal significantly attenuates due to scattering especially in shallow seafloor features such as pockmarks. Low signal strength accompanied with seismic blanking in the gas chimneys make Q estimates in gas chimneys unreliable especially at deeper depths.

By analyzing the distribution of Q values in layer L3 (Figure 10a and 10d), it can be stated that the background Q values in the marine sediments at the BSR depth are in the range of 60–90. If the Q values in layer L3 (the layer above the BSR) above potentially gas-saturated sediments ($Q < 30$ below the BSR in layer L4) are selectively picked (Figure 10b and 10e) and compared with the overall distribution of Q values in the layer (Figure 10c and 10f), relatively higher Q values have been observed above potentially gas-saturated sediments (Figure 10). Particularly, the variable distribution of extended zones of high Q mapped on Q slices of the 3D data (Figure 11b), in comparison with adjacent areas with lower Q, points toward a variable pore fluid type and/or saturation in this strata. There is no indication from the seismic data to expect significant lithologic changes in this rather-homogeneous sedimentary environment. Therefore, we attribute this effect to the presence of gas hydrates in the sediments and suggest that gas-hydrate-saturated sediments exhibit high Q values within the frequency range used in the study. This observation is supported by the fact that both Q analysis methods match well in the distribution of Q above the BSR. In contrast, areas with very low Q below the BSR indicate the presence of free gas (Figure 11c).

It is difficult to estimate accurate Q for high Q value areas as discussed earlier. Therefore, it becomes difficult to state the exact Q value in gas-hydrate-saturated sediments. But from the statistical analysis of the results obtained from both methods (Figure 10), it can be stated that high Q values are observed in gas-hydrate-saturated sediments. Earlier studies on seismic attenuation conducted in the nearby locations also indicated elevated Q values above the BSR (Rossi et al., 2007). Hence, we argue that Q analysis of high-resolution P-cable 3D seismic data with a large bandwidth can detect and outline spatially limited areas of gas hydrate occurrence in marine sediments.

Hustoft et al. (2009) use 135-km east–west-striking MCS profile to derive a velocity model. This profile lies approximately 10 km southward to our study area

(shown in Figure 1) and can be used to interpret the results of the Q analysis. High gas concentrations exist beneath the BSR toward the southwestern half of the Vestnesa Ridge (Hustoft et al., 2009). Similarly, low Q values beneath the BSR in the southwestern half of the 3D seismic data may indicate the presence of elevated gas concentrations at this location (Figures 7d and 9d). The gas chimneys that align at the crest of the Vestnesa Ridge separate this southwestern half from the northeastern half where Q values are generally higher. A similar behavior is observed above the BSR, where high Q values in the southwestern half may indicate higher concentrations of gas hydrates than in the northeastern half. Hustoft et al. (2009) and Bünz et al. (2012) show that the fluid flow system in the Vestnesa Ridge is topographically controlled and that gas migrates to the crest of the ridge beneath the BSR, mostly from the southwestern half. Hence, gas availability may be higher in the southwestern half.

In a more recent study, Plaza-Faverola et al. (2015) show that small-scale fault systems exist at the crest of the Vestnesa Ridge documenting a tectonic control of gas leakage. Fault systems mapped by Plaza-Faverola et al. (2015) at approximately the BSR depth coincide strikingly with the boundaries of abrupt Q changes within layers three and four above and beneath the BSR, respectively (Figure 11a–11c). Changes in the Q within a layer are attributed with a variable pore fluid fill. Hence, the Q analysis indicates that fluid distribution in the region is strongly controlled by fault systems in the Vestnesa Ridge. Fault 1 in Figure 11a delimits the southwestern part indicating higher fluid concentrations in both hydrates above the BSR and free gas below. This area also includes the two most active chimneys on the Vestnesa Ridge (Figure 4c) (Bünz et al., 2012; Smith et al., 2014) corroborating our results that gas is more readily available at this location to either leak to the seafloor or to be bound into gas hydrates. As gas migrates upslope in a northeast direction (Figure 11d; Hustoft et al., 2009), it is trapped by regional fault 1 and uses the fault plane as a migration pathway into the free-gas zone beneath the BSR.

The Q values between faults 1 and 2 indicate lower concentrations of gas hydrates (Figure 11b) and free gas (Figure 11c). Coincidentally, several of the chimneys located in this fault block are inactive. The reduced availability of free gas in this fault block might explain this observation or that most gas has vented through the chimneys. Also, other areas of the 3D seismic volume clearly indicate a relationship between Q values and the mapped fault system, e.g., to the northeast of fault 2 or between faults 2 and 4 (Figure 11a–11c). Together, these results suggest that the availability of free gas is one of the major factors in the accumulation of gas beneath the BSR and the formation of gas hydrates above it and that the availability of free gas clearly seems to be controlled by the structural setting supporting the findings of Plaza-Faverola et al. (2015).

All of the Q slices clearly exhibit the vertical fluid flow features in this area (Figures 7 and 9). However, there are still some interesting subtleties that can be noted from the Q data. When centroid frequencies are plotted for a seismic section, they did not drop rapidly at some places in the northwestern and central parts (Figure 4b) of the seismic section. It is possible that these frequency anomalies might be related to variable concentrations of gas within the free-gas zone beneath the BSR. Lower amounts of free gas might indicate that the fluid flow features such as gas chimneys in nearby locations may lack a gas source. Bünz et al. (2012) document acoustic flares in the water column and shallow high amplitudes in upper 50 m of these fluid flow features. In their study, they show that the chimneys in the central part of the 3D seismic volume and some chimneys in the northwestern part are inactive as compared with chimneys in the southeastern part of the volume (Figure 4c). On the contrary, the active chimneys documented by Bünz et al. (2012) show low-frequency anomalies in the lower part of the chimney just above the BSR (Figure 4b). This might indicate

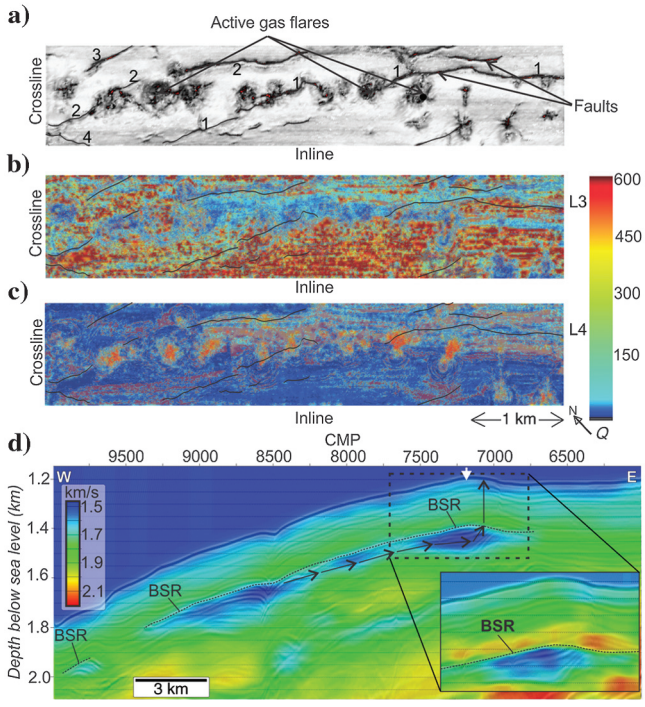

Figure 11. (a) Variance map obtained from a time slice at BSR depth showing several faults (Plaza-Faverola et al., 2015) and gas chimneys (Bünz et al., 2012) piercing through the subsurface. (b) Q slice obtained by overlaying (through 50% transparency) Q slices from the SR method (Figure 9c) and centroid frequency shift method (Figure 7c) in layer L3 (the layer above the BSR). (c) Q slice obtained by overlaying (through 50% transparency) Q slices from the SR method (Figure 9d) and centroid frequency shift method (Figure 7d) in the layer L4 (layer below the BSR). (d) P-wave velocity cross section derived using the MCS profile (see Figure 1 for the location) across the Vestnesa Ridge (modified from Hustoft et al., 2009). Arrows in the figure show upslope gas migration and its leakage from the Vestnesa Ridge.

an active migration of gas from the free-gas zone into the chimney structures supplying the seafloor seep with gas.

Low centroid frequencies have been observed in regions where pockmark features have been observed. This can be due to prominent scattering at pockmarks or attenuation of the seismic energy within 5–10 m of the sediments below the seafloor possibly resulting from the presence of hydrates and/or carbonates. Prominent scattering in pockmarks and within chimneys significantly reduced the signal strength and made it difficult to image Q in gas chimneys at deeper depths. Low signal strength and seismic blanking in gas chimneys reduces the accuracy of Q estimates in gas chimneys. But still, Q values with limited accuracy have been used to study gas chimneys. Both Q estimation methods show small patches of high Q values associated with chimney features at medium depths beneath the seafloor and BSR (Figures 7b and 9b). However, the centroid frequency shift method depicts high Q at the rim of the chimneys possibly indicating that chimneys are lined with hydrates, an interesting though speculative suggestion, although it would fit with theoretical models for chimneys structures (Liu and Flemings, 2007).

Conclusion

We have applied the centroid frequency shift method and SR method to study seismic attenuation in gas-hydrate- and free-gas-saturated sediments using high-resolution P-cable 3D seismic data from the Vestnesa Ridge on the Arctic continental margin of Svalbard. We have estimated Q values for different layers to develop a subsurface 3D Q model. We observed high Q values above the prominent BSR and low Q values ($Q \approx 10 - 30$) below the BSR. Anomalies observed in Q slices obtained from two different methods are found in concordance with each other. But we got relatively more stable Q values from the centroid frequency shift method.

After performing a statistical analysis, we found that an increase in Q values in certain, spatially limited areas above the BSR can probably be associated with the presence of gas hydrates. Under this premise, Q analysis of high-resolution P-cable 3D seismic data is thus an effective method for the detection and mapping of gas-hydrate occurrences in marine sediments. Q values estimated for the strata below the BSR are very low as a consequence of the occurrence of gas trapped in the free-gas zone beneath hydrate-bearing strata.

Faults that exist throughout the Vestnesa Ridge coincide with the Q anomalies in the layers above and below the BSR corroborating recent findings and directly showing that the structural setting and tectonic activity in the region control the availability and spatial distribution of free gas and gas hydrates in the Vestnesa Ridge. The availability of gas in certain spatially limited areas also might explain the present seepage from some of the chimneys on the Vestnesa Ridge, whereas other chimneys are dormant. The low seismic signal strength accompanied by amplitude blanking makes it difficult to accurately image Q in gas chimneys. But still, with limited accuracy, we observed high Q values in gas chimneys in Q slices, hinting toward the presence of gas hydrates in gas chimneys.

Acknowledgments

This work is partly supported by the Research Council of Norway through its Centres of Excellence funding scheme, project no. 223259. We thank the crew of the *R/V Helmer Hanssen* and those who contributed to the P-cable data acquisition. We are also thankful to I. Pecher (associate editor), N. Bangs, G. Rossi, and K. Sain for their constructive comments.

References

Amundsen, L., and R. Mittet, 1994, Estimation of phase velocities and Q-factors from zero-offset, vertical seismic profile data: Geophysics, **59**, 500–517, doi: 10.1190/1.1443612.

Badri, M., and H. M. Mooney, 1987, Q measurements from compressional seismic waves in unconsolidated sediments: Geophysics, **52**, 772–784, doi: 10.1190/1.1442344.

Båth, M., 1982, Spectral analysis in geophysics: Elsevier Science.

Bauer, K., C. Haberland, R. G. Pratt, F. Hou, B. E. Medioli, and M. H. Weber, 2005, Ray based cross-well tomography for P-wave velocity, anisotropy, and attenuation structure around the JAPEX/JNOC/GSC et al. Mallik 5L-38 gas hydrate production research well, *in* S. R. Dallimore, and T. S. Collet, eds., Scientific results from the Mallik 2002 gas hydrate production research well program, Mackenzie Delta, Northwest Territories, Canada: King's Printer and Controller of Stationery, 1–21.

Behura, J., 2009, Estimation and analysis of attenuation anisotropy: Doctoral thesis, Colorado School of Mines.

Bellefleur, G., M. Riedel, T. Brent, F. Wright, and S. R. Dallimore, 2007, Implication of seismic attenuation for gas hydrate resource characterization, Mallik, Mackenzie Delta, Canada: Journal of Geophysical Research, **112**, B10311, doi: 10.1029/2007JB004976.

Best, A. I., J. A. Priest, C. R. I. Clayton, and E. V. L. Rees, 2013, The effect of methane hydrate morphology and water saturation on seismic wave attenuation in sand under shallow sub-seafloor conditions: Earth and Planetary Science Letters, **368**, 78–87, doi: 10.1016/j.epsl.2013.02.033.

Brooks, J. M., H. B. Cox, W. R. Bryant, M. C. Kennicutt, II, R. G. Mann, and T. J. McDonald, 1986, Association of gas hydrates and oil seepage in the Gulf of Mexico: Organic Geochemistry, **10**, 221–234, doi: 10.1016/0146-6380(86)90025-2.

Bünz, S., S. Polyanov, S. Vadakkepuliyambatta, C. Consolaro, and J. Mienert, 2012, Active gas venting through hydrate-bearing sediments on the Vestnesa Ridge, offshore W-Svalbard: Marine Geology, **332–334**, 189–197, doi: 10.1016/j.margeo.2012.09.012.

Chand, S., and T. A. Minshull, 2004, The effect of hydrate content on seismic attenuation: A case study for Malik 2L-38 well data, Mackenzie delta, Canada: Geophysical Research Letters, **31**, L14609, doi: 10.1029/2004GL020292.

Chand, S., T. A. Minshull, D. Gei, and J. M. Carcione, 2004, Elastic velocity models for gas-hydrate bearing sediments: A comparison: Geophysical Journal International, **159**, 573–590, doi: 10.1111/j.1365-246X.2004.02387.x.

Claerbout, J. F., and F. Muir, 1973, Robust modeling with erratic data: Geophysics, **38**, 826–844, doi: 10.1190/1.1440378.

Collet, T. S., R. E. Lewis, S. R. Dallimore, M. W. Lee, T. H. Mroz, and T. Uchida, 1999, Detailed evaluation of gas hydrate reservoir properties using JAPEX/JNOC/GSC Mallik well 2L-38 gas hydrate research well downhole well-log displays, *in* S. R. Dallimore, T. Uchida, and T. S. Collett, eds., Scientific results from JAPEX7J-NOC/GSC Mallik 2L-38 gas hydrate well, Mackenzie Delta, North west Territories, Canada: Geological Survey of Canada Bulletin, 295–312.

Collett, T. S., and J. Ladd, 2000, Detection of gas hydrate with downhole logs and assessment of gas hydrate concentrations (saturations) and gas volumes on the Blake Ridge with electrical resistivity log data, *in* C. K. Paull, R. Matsumoto, P. J. Wallace, and W. P. Dillon, eds., Proceedings of the Ocean Drilling Program, Scientific results: Texas A&M University, 179–191.

Consolaro, C., T. L. Rasmussen, G. Panieri, J. Mienert, S. Bünz, and K. Sztybor, 2014, Carbon isotope ($\delta^{13}C$) excursions suggest times of major methane release during the last 14 ka in Fram Strait, the deep-water gateway to the Arctic: Climate of the Past Discussions, **10**, 4191–4227.

Dewangan, P., R. Mandal, P. Jaiswal, T. Ramprasad, and G. Sriram, 2014, Estimation of seismic attenuation of gas hydrate bearing sediments from multi-channel seismic data: A case study from Krishna–Godavari offshore basin: Marine and Petroleum Geology, **58**, 356–367, doi: 10.1016/j.marpetgeo.2014.05.015.

Ecker, C., J. Dvorkin, and A. Nur, 1998, Sediments with gas hydrates: Internal structure from seismic AVO: Geophysics, **63**, 1659–1669, doi: 10.1190/1.1444462.

Eiken, O., and K. Hinz, 1993, Contourites in the Fram Strait: Sedimentary Geology, **82**, 15–32, doi: 10.1016/0037-0738(93)90110-Q.

Gabor, D., 1946, Theory of communication: Journal of the Institution of Electrical Engineers, **93**, 429–457.

Galperin, E. I., 1985, Vertical seismic profiling and its exploration potential: Springer.

Gei, D., and J. M. Carcione, 2003, Acoustic properties of sediments saturated with gas hydrate, free gas and water: Geophysical Prospecting, **51**, 141–158, doi: 10.1046/j.1365-2478.2003.00359.x.

Gladwin, M. T., and F. D. Stacey, 1974, Anelastic degradation of acoustic pulses in rocks: Physics of the Earth and Planetary Interiors, **8**, 332–336, doi: 10.1016/0031-9201(74)90041-7.

Guerin, G., and D. Goldberg, 2002, Sonic waveform attenuation in gas hydrate-bearing sediments from the Mallik 2L-38 research well, Mackenzie Delta, Canada: Journal of Geophysical Research, **107**, 2088, doi: 10.1029/2001JB000556.

Guerin, G., and D. Goldberg, 2005, Modeling of acoustic wave dissipation in gas hydrate-bearing sediments: Geochemistry, Geophysics, Geosystems, **6**, Q07010, doi: 10.1029/2005GC000918.

Guerin, G., D. Goldberg, and A. Meltser, 1999, Characterization of in situ elastic properties of gas hydrate bearing sediments on the Blake Ridge: Journal of Geophysical Research, **104**, 17781–17795, doi: 10.1029/1999JB900127.

Hamilton, R. M., and W. D. Mooney, 1990, Seismic-wave attenuation associated with crustal faults in the New Madrid seismic zone: Science, **248**, 351–354, doi: 10.1126/science.248.4953.351.

Hatherly, P. J., 1986, Attenuation measurements on shallow seismic refraction data: Geophysics, **51**, 250–254, doi: 10.1190/1.1442084.

Howe, J. A., T. M. Shimmield, and R. Harland, 2008, Late Quaternary contourites and glaciomarine sedimentation in the Fram Strait: Sedimentology, **55**, 179–200, doi: 10.1111/j.1365-3091.2007.00897.x.

Hustedt, B., and R. A. Clark, 1999, Source/receiver array directivity effects on marine seismic attenuation measurements: Geophysical Prospecting, **47**, 1105–1119, doi: 10.1046/j.1365-2478.1999.00169.x.

Hustoft, S., S. Bünz, J. Mienert, and S. Chand, 2009, Gas hydrate reservoir and active methane-venting province in sediments on < 20 Ma young oceanic crust in the Fram Strait, offshore NW-Svalbard: Earth and Planetary Science Letters, **284**, 12–24, doi: 10.1016/j.epsl.2009.03.038.

Jacobson, R. S., G. G. Shor, Jr., and L. M. Dorman, 1981, Linear inversion of body wave data. Part II: Attenuation versus depth using spectral ratios: Geophysics, **46**, 152–162, doi: 10.1190/1.1441185.

Jaiswal, P., P. Dewangan, T. Ramprasad, and C. Zelt, 2012, Seismic characterization of hydrates in faulted, fine-grained sediments of Krishna-Godavari Basin: Full waveform inversion: Journal of Geophysical Research, **117**, B10305, doi: 10.1029/2012JB009201.

Jannsen, D., J. Voss, and F. Theilen, 1985, Comparison of methods to determine Q in shallow marine sediments from vertical reflection seismograms: Geophysical Prospecting, **33**, 479–497, doi: 10.1111/j.1365-2478.1985.tb00762.x.

Johnston, D. H., M. N. Toksöz, and A. Timur, 1979, Attenuation of seismic waves in dry and saturated rocks. II: Mechanisms: Geophysics, **44**, 691–711, doi: 10.1190/1.1440970.

Jung, J.-W., J. C. Santamarina, and K. Soga, 2012, Stress-strain response of hydrate-bearing sands: Numerical

study using discrete element method simulations: Journal of Geophysical Research, **117**, B04202, doi: 10.1029/2011JB009040.

Korenaga, J., W. S. Holbrook, S. C. Singh, and T. A. Minshull, 1997, Natural gas hydrates on the southeast US margins: Constraints from full waveform and traveltime inversions of wide angle seismic data: Journal of Geophysical Research, **102**, 15345–15365, doi: 10.1029/97JB00725.

Lee, M. W., and T. S. Collett, 2001, Elastic properties of gas hydrate-bearing sediments: Geophysics, **66**, 763–771, doi: 10.1190/1.1444966.

Lee, M. W., and T. S. Collett, 2006, Gas hydrate and free gas saturations estimated from velocity logs on hydrate ridge, offshore Oregon, USA, *in* A. M. Tréhu, G. Bohrmann, M. E. Torres, and F. S. Colwell, eds., Proceedings of the Ocean Drilling Program, Scientific Results, 204: Ocean Drilling Program, 1–25.

Liu, B., Q. Yuan, K. H. Su, X. Yang, B. C. Wu, C. Y. Sun, and G. J. Chen, 2012, Experimental simulation of the exploitation of natural gas hydrate: Energies, **5**, 466–493.

Liu, X., and P. B. Flemings, 2007, Dynamic multiphase flow model of hydrate formation in marine sediments: Journal of Geophysical Research, **112**, B03101, doi: 10.1029/2005JB004227.

Matsushima, J., 2005, Attenuation measurements from sonic waveform logs in methane hydrate-bearing sediments at the Nankai Trough exploratory well off Tokai, central Japan: Geophysical Research Letters, **32**, 1–5, doi: 10.1029/2005GL023217.

Matsushima, J., 2006, Seismic wave attenuation in methane hydrate-bearing sediments: Vertical seismic profiling data from the Nankai Trough exploratory well, offshore Tokai, central Japan: Journal of Geophysical Research, **111**, B10101, doi: 10.1029/2005JB004031.

Mavko, G., T. Mukerji, and J. Dvorkin, 1998, The rock physics handbook: Tools for seismic analysis in porous media: Cambridge University Press.

Mavko, G. M., and A. Nur, 1979, Wave attenuation in partially saturated rocks: Geophysics, **44**, 161–178, doi: 10.1190/1.1440958.

Murphy, W. F., K. W. Winkler, and R. L. Kleinberg, 1986, Acoustic relaxation in sedimentary rocks: Dependence on grain contacts and fluid saturation: Geophysics, **51**, 757–766, doi: 10.1190/1.1442128.

Ning, T., and L. Wen-kai, 2010, Improve Q estimates with spectrum correction based on seismic wavelet estimation: Applied Geophysics, **7**, 217–228, doi: 10.1007/s11770-010-0252-2.

Nouzé, H., P. Henry, M. Noble, V. Martin, and G. Pascal, 2004, Large gas hydrate accumulations on the eastern Nankai Trough inferred from new high-resolution 2-D seismic data: Geophysical Research Letters, **31**, L13308, doi: 10.1029/2004GL019848.

O'Connell, R. J., and B. Budiansky, 1977, Viscoelastic properties of fluid-saturated cracked solids: Journal of Geophysical Research, **82**, 5719–5735, doi: 10.1029/JB082i036p05719.

O'Hara, S. G., 1989, Elastic-wave attenuation in fluid-saturated Berea sandstone: Geophysics, **54**, 785–788, doi: 10.1190/1.1442707.

Parra, J. O., C. L. Hackert, and P.-C. Xu, 2002, Characterization of fractured low Q zones at the Buena Vista Hills reservoir, California: Geophysics, **67**, 1061–1070, doi: 10.1190/1.1500366.

Petersen, C. J., S. Bünz, S. Hustoft, J. Mienert, and D. Klaeschen, 2010, High-resolution P-Cable 3D seismic imaging of gas chimney structures in gas hydrated sediments of an Arctic sediment drift: Marine and Petroleum Geology, **27**, 1981–1994, doi: 10.1016/j.marpetgeo.2010.06.006.

Planke, S., F. N. Eriksen, C. Berndt, J. Mienert, and D. Masson, 2009, Spotlight on technology: P-cable high-resolution seismic: Oceanography, **22**, 85, doi: 10.5670/oceanog.2009.09.

Plaza-Faverola, A., S. Bünz, J. E. Johnson, S. Chand, J. Knies, J. Mienert, and P. Franek, 2015, Role of tectonic stress in seepage evolution along the gas hydrate charged Vestnesa Ridge, Fram Strait: Geophysical Research Letters, **42**, 733–742, doi: 10.1002/2014GL062474.

Pointer, T., E. Liu, and J. A. Hudson, 2000, Seismic wave propagation in cracked porous media: Geophysical Journal International, **142**, 199–231, doi: 10.1046/j.1365-246x.2000.00157.x.

Prasad, M., and A. Nur, 2003, Velocity and attenuation anisotropy in reservoir rocks: 83rd Annual International Meeting, SEG, Expanded Abstracts, 1652–1655.

Pratt, R. G., K. Bauer, and M. Weber, 2003, Crosshole waveform tomography velocity and attenuation images of arctic gas hydrates: 83rd Annual International Meeting, SEG, Expanded Abstracts, 2255–2258.

Pratt, R. G., F. Hou, K. Bauer, and M. Weber, 2005, Waveform tomography images of velocity and inelastic attenuation from the Mallik 2002 crosshole seismic surveys, *in* S. R. Dallimore, and T. S. Collet, eds., Scientific results from the Mallik 2002 gas hydrate production research well program, Mackenzie Delta, Northwest Territories, Canada: Geological Survey of Canada, Bulletin, 1–14.

Priest, J. A., A. I. Best, and C. R. I. Clayton, 2006, Attenuation of seismic waves in methane gas hydrate-bearing sand: Geophysical Journal International, **164**, 149–159, doi: 10.1111/j.1365-246X.2005.02831.x.

Quan, Y., and J. M. Harris, 1997, Seismic attenuation tomography using the frequency shift method: Geophysics, **62**, 895–905, doi: 10.1190/1.1444197.

Rapoport, M. B., L. I. Rapoport, and V. I. Ryjkov, 2004, Direct detection of oil and gas fields based on seismic inelasticity effect: The Leading Edge, **23**, 276–278, doi: 10.1190/1.1690901.

Reine, C., M. V. D. Baan, and R. Clark, 2009, The robustness of seismic attenuation measurements using fixed- and

variable-window time-frequency transforms: Geophysics, **74**, no. 2, WA123–WA135, doi: 10.1190/1.3043726.

Riedel, M., T. S. Collett, P. Kumar, A. V. Sathe, and A. Cook, 2010, Seismic imaging of a fractured gas hydrate system in the Krishna-Godavari basin offshore India: Marine and Petroleum Geology, **27**, 1476–1493, doi: 10.1016/j.marpetgeo.2010.06.002.

Ritzmann, O., W. Jokat, W. Czuba, A. Guterch, R. Mjelde, and Y. Nishimura, 2004, A deep seismic transect from Hovgård Ridge to northwestern Svalbard across the continental-ocean transition: A sheared margin study: Geophysical Journal International, **157**, 683–702, doi: 10.1111/j.1365-246X.2004.02204.x.

Rossi, G., D. Gei, G. Böhm, G. Madrussani, and J. M. Carcione, 2007, Attenuation tomography: An application to gas-hydrate and free-gas detection: Geophysical Prospecting, **55**, 655–669, doi: 10.1111/j.1365-2478.2007.00646.x.

Ryu, B.-J., T. S. Collett, M. Riedel, G. Y. Kim, J. H. Chun, J. J. Bahk, J. Y. Lee, J. H. Kim, and D. G. Yoo, 2013, Scientific results of the second gas hydrate drilling expedition in the Ulleung basin (UBGH2): Marine and Petroleum Geology, **47**, 1–20, doi: 10.1016/j.marpetgeo.2013.07.007.

Sain, K., and A. K. Singh, 2011, Seismic quality factors across a bottom simulating reflector in the Makran Accretionary Prism, Arabian Sea: Marine and Petroleum Geology, **28**, 1838–1843, doi: 10.1016/j.marpetgeo.2011.03.013.

Sain, K., A. K. Singh, N. K. Thakur, and R. Khanna, 2009, Seismic quality factor observations for gas-hydrate-bearing sediments on the western margin of India: Marine Geophysical Researches, **30**, 137–145, doi: 10.1007/s11001-009-9073-1.

Sato, H., and M. C. Fehler, 1997, Seismic wave propagation and scattering in the heterogeneous earth: Springer.

Shipley, T. H., M. H. Houston, R. T. Buffler, F. J. Shaub, K. J. McMillen, J. W. Ladd, and J. L. Worzel, 1979, Seismic evidence for widespread possible gas hydrate horizons on Continental slopes and rises: AAPG Bulletin, **63**, 2204–2213.

Sloan, E. D., Jr., 1998, Clathrate hydrates of natural gases, 2nd ed.: Marcel Dekker Inc.

Smith, A. J., J. Mienert, S. Bünz, and J. Greinert, 2014, Thermogenic methane injection via bubble transport into the upper Arctic Ocean from the hydrate-charged Vestnesa Ridge, Svalbard: Geochemistry, Geophysics, Geosystems, **15**, 1945–1959, doi: 10.1002/2013GC005179.

Spencer, J. W., Jr., 1979, Bulk and shear attenuation in Berea Sandstone: The effects of pore fluids: Journal of Geophysical Research, **84**, 7521–7523, doi: 10.1029/JB084iB13p07521.

Spencer, T. W., J. R. Sonnad, and T. M. Butler, 1982, Seismic Q — Stratigraphy or dissipation: Geophysics, **47**, 16–24, doi: 10.1190/1.1441275.

Talukder, M. W., 2013, VSP P-wave attenuation model study in elastic earth: Spectral ratio method vs centroid frequency shift method: Presented at the CSPG CSEG CWLS GeoConvention 2013, Integration: Geoscience Engineering Partnership, AAPG Search and Discovery, Extended Abstracts, Article no. 90187.

Toksöz, M. N., and D. H. Johnston, 1981, Seismic wave attenuation: SEG, Geophysics Reprint Series.

Toksöz, M. N., D. H. Johnston, and A. Timur, 1979, Attenuation of seismic waves in dry and saturated rocks. I: Laboratory measurements: Geophysics, **44**, 681–690, doi: 10.1190/1.1440969.

Tonn, R., 1991, The determination of the seismic quality factor Q from VSP data: A comparison of different computational methods: Geophysical Prospecting, **39**, 1–27, doi: 10.1111/j.1365-2478.1991.tb00298.x.

Vogt, P. R., K. Crane, E. Sundvor, M. D. Max, and S. L. Pfirman, 1994, Methane-generated(?) pockmarks on young, thickly sedimented oceanic crust in the Arctic: Vestnesa ridge, Fram strait: Geology, **22**, 255–258, doi: 10.1130/0091-7613(1994)022<0255:MGPOYT>2.3.CO;2.

Walsh, J. B., 1966, Seismic wave attenuation in rock due to friction: Journal of Geophysical Research, **71**, 2591–2599, doi: 10.1029/JZ071i010p02591.

Wennerberg, L., 1993, Multiple-scattering interpretations of coda-Q measurements: Bulletin of the Seismological Society of America, **83**, 279–290.

Winkler, K., A. Nur, and M. Gladwin, 1979, Friction and seismic attenuation in rocks: Nature, **277**, 528–531, doi: 10.1038/277528a0.

Winkler, K. W., and A. Nur, 1982, Seismic attenuation: Effects of pore fluids and frictional-sliding: Geophysics, **47**, 1–15, doi: 10.1190/1.1441276.

Wood, W. T., W. S. Holbrook, and H. Hoskins, 2000, In situ measurements of P-wave attenuation in methane hydrate and gas bearing sediments on the Blake Ridge, *in* C. K. Paull, R. Matsumoto, P. J. Wallace, and W. P. Dillon, eds., Proceedings of the Ocean Drilling Program, Scientific Results: Ocean Drilling Program, 265–272.

Yoo, D. G., N. K. Kang, B. Y. Yi, G. Y. Kim, B. J. Ryu, K. Lee, G. H. Lee, and M. Riedel, 2013, Occurrence and seismic characteristics of gas hydrate in the Ulleung Basin, East Sea offshore Korea: Marine and Petroleum Geology, **47**, 236–247, doi: 10.1016/j.marpetgeo.2013.07.001.

Zhang, H., S. Yang, N. Wu, X. Su, M. Holland, P. Schultheiss, K. Rose, H. Butler, and G. Humphrey, GMS-1 Science Team, 2007, Successful and surprising results for China's first gas hydrate drilling expedition: Fire in the Ice, **7**, 6–9.

Sunny Singhroha received a B.S. (Hons) and an M.S. (2013) under the five years integrated program in exploration geophysics from the Indian Institute of Technology, Kharagpur. After working as a geophysicist for half a year in Essar Oil Ltd., he started his Ph.D. in marine geophysics from the Centre of Excellence for Arctic

Gas Hydrate, Environment and Climate, based at the University of Tromsø, Norway. The main focus of his Ph.D. work is to study the distribution of gas hydrates in the marine sediments of the Vestnesa and Svyatogor Ridge, offshore W-Svalbard. He is mainly working on high-resolution P-cable seismic data and multicomponent seismic data. His research interests include gas hydrates, seismic attenuation, seismic velocity modeling, full-waveform inversion, rock physics, and EM prospecting.

Stefan Bünz received a master's degree (1997) in geophysics from the Christian-Albrechts University in Kiel, Germany, and a Ph.D. (2003) in geophysics from the University of Tromsø. He is an associate professor at the University of Tromsø, Norway, and a work group leader at the Centre of Excellence on Arctic Gas Hydrates, Environment and Climate. He has extensive experience in the acquisition, processing, and interpretation of 3D and multicomponent seismic data.

Andreia Plaza-Faverola received a B.S. in geophysical engineering from the Simón Bolívar University in Caracas, an M.S. in petroleum geology from French Institute of Petroleum (IFP) in Paris, and a Ph.D. (2010) in marine geophysics from the University of Tromsø. She continued her research career as a postdoctoral fellow at National Geological and Nuclear Science Center (GNS) Science in Wellington. Since 2013, she has worked as a researcher at the Center for Arctic Gas Hydrate, Environment and Climate, based at the University of Tromsø, Norway. She specializes in the implementation of high-resolution geophysical methods for understanding the mechanisms controlling natural gas expulsion from gas hydrates and shallow gas systems in continental margins. Her research focuses on the identification of seismic indicators for paleoseepage events, internal architecture of gas chimneys and quantification of the carbon potential in hydrates and associated free gas systems. She is particularly interested in the processing and interpretation of high-resolution 3D P-cable seismic data and time-lapse studies, integrated seismic tomography and CSEM, implementation of geostatistics for the quantification of gas volumes, prestack depth migration and velocity modeling for identification of deep thermogenic and abiogenic gas sources, modeling of tectonic stress effects on fluid expulsion, and integrated geophysical and seafloor mosaicing analysis of seafloor fluid expulsion features.

Shyam Chand received a B.S. (1992) in physics from the Mahatma Gandhi University, an M.S. (1996) (Tech) in marine geophysics from the Cochin University of Science and Technology, and a Ph.D. in geophysics from the National Geophysical Research Institute affiliated with Osmania University, India. He has extensive experience in seismic processing, interpretation, and basin modeling. He has been working in the field of gas hydrates for more than a decade developing rock-physics models, waveform inversion schemes, and interpretation tools. He has worked as a researcher at Cochin University of Science and Technology, India, a scientist at the National Geophysical Research Institute, India, and a researcher at the National Oceanography Centre Southampton, UK. Currently, he is working as a senior researcher at the Geological Survey of Norway. He is also associated with the Centre for Arctic Gas Hydrate and Environment center in Tromsø, Norway. He is a member of SEG, AGU, and EAGE.

Article II

Singhroha, S., Chand, S., & Bünz, S. (2019). Constraints on gas hydrate distribution and morphology in Vestnesa Ridge, W-Svalbard margin using multicomponent ocean-bottom seismic data. Journal of Geophysical Research – Solid Earth. Doi: 10.1029/2018JB016574

Constraints on gas hydrate distribution and morphology in Vestnesa Ridge, W-Svalbard margin using multicomponent ocean-bottom seismic data

Sunny Singhroha[1], Shyam Chand[2, 1], Stefan Bünz[1],

[1]CAGE — Centre for Arctic Gas Hydrate, Environment and Climate, Department of Geosciences, UiT The Arctic University of Norway, Tromsø, Norway.

[2]Geological Survey of Norway (NGU), Trondheim, Norway.

Corresponding author: Sunny Singhroha (Sunny.Singhroha@uit.no)

Key points:

- Multi component OBS data show variations in gas hydrate distribution in contourite drift sediments of Vestnesa Ridge.
- P and S-wave velocities and 1-D FWI models provide better constraints on gas hydrate and free gas saturation estimates.
- The distribution of gas hydrates and free gas in Vestnesa Ridge are controlled by the presence of shallow faults.

Abstract

Gas hydrates occur within sediments on the western Svalbard continental margin and the Vestnesa Ridge, a large sediment drift that extends in a west-north-west direction from the margin towards the mid-ocean ridge. We acquired multi-component ocean-bottom seismic (OBS) data at ten locations on the crest area of the eastern segment of the Vestnesa Ridge, an area with active gas seepage. P and S-wave velocities are estimated using travel time inversion, and SCA/DEM rock physics modeling is used to estimate gas hydrate and free gas saturation at OBS stations. We apply 1-D Full Waveform Inversion (FWI) at a selected OBS station to study detailed variations of P-wave velocity near the BSR. High interval P-wave velocity (Vp≈1.73-1.82 km/s) and S-wave velocity (>0.35 km/s) are observed in a layer above the BSR and low interval P-wave velocity (Vp≈1.28-1.53 km/s) in a layer below the BSR. We estimate 10-18% gas hydrate and 1.5-4.1% free gas saturation at different OBS stations in a layer above and below the BSR, respectively. We find significant variation in gas hydrate and free gas saturation across faults suggesting a structural control on the distribution of gas hydrate and free gas in the Vestnesa Ridge. Differences in gas hydrate saturation derived from P-wave velocities and earlier estimates obtained from electromagnetic surveys indicate the presence of gas hydrates in faults and fractures. Moreover, beneath some OBS sites, the combined study of P and S-waves, resistivity and seismic quality factor (Q), suggests the co-existence of free gas and gas hydrates.

1. Introduction

Gas hydrate is an ice-like crystalline solid formed under high pressure and low temperature conditions (Brooks et al., 1986; Sloan 1998). Gas hydrates are widely present in continental slope and permafrost environments where temperature and pressure conditions are suitable (Sloan, 1998). The presence of gas hydrate in the sediments is often detected by identifying a bottom simulating reflection (BSR) in seismic data (Hyndman & Spence, 1992; Singh et al.,

1993). A BSR is a strong seismic reflection at the base of the gas hydrate stability zone (GHSZ), which, due to its dependence on pressure and temperature, often parallels the seafloor (Shipley et al., 1979). Free gas is frequently trapped below the GHSZ due to reduced permeability in gas hydrate saturated sediments within the GHSZ. This sudden change in the pore fluid at the base of the GHSZ creates a strong impedance contrast resulting in a sharp, polarity-reversed reflection (BSR) in seismic data. A BSR only provides evidence for the presence of gas hydrates but does not allow for estimation of the amount of gas hydrates trapped in sediments. Gas hydrates fill pore space by forming a sediment-hydrate micro-structure strengthening the matrix of unconsolidated sediments that in turn increases the bulk modulus, thereby resulting in higher P-wave seismic velocities compared to sediments not saturated with gas hydrates (Stoll et al., 1971; Yuan et al., 1996; Lee et al., 1996; Helgerud et al., 1999; Lu & McMechan, 2002; Chand et al., 2004; Bünz et al., 2005; Lee & Collett, 2009; Jaiswal et al., 2012). Hence, high P-wave seismic velocities are observed above the BSR, whereas the presence of free gas in sediments below the BSR reduces the P-wave velocity. S-wave velocities may provide further insights about the distribution of hydrates within the pore space of sediments because it depends on the microstructure of sediment-hydrate composite of gas hydrate bearing sediments. The presence of hydrate increases the shear wave velocity when hydrates form as a part of the frame affecting the shear modulus rather than form as pore filling material with no connection to the sediment frame (Chand et al., 2004; Bünz et al., 2005; Kumar et al., 2007; Westbrook et al., 2008). The presence of free gas does not alter the shear strength of sediments overly, and thus has little effect on the shear velocity (Vs) of the sediments (Dash & Spence, 2011). Thus, saturation of gas hydrates and free gas and their distribution patterns in the host sediments can be estimated by performing velocity analysis of both P and S-waves from seismic data (Song et al., 2018; Bünz et al., 2005; Kumar et al., 2007; Westbrook et al., 2008).

In the present study, seismic velocity analysis is performed using multicomponent, wide-angle ocean-bottom seismic (OBS) data acquired at ten different locations along the eastern segment of the Vestnesa Ridge, offshore W-Svalbard. The widespread presence of a BSR provides evidence for the occurrence of gas hydrate in the Vestnesa Ridge sediments (Hustoft et al., 2009; Petersen et al., 2010; Bünz et al., 2012). Gas hydrates have been directly observed and sampled in several of the pockmarks that occur along the crest of the ridge (Panieri et al., 2017). The BSR is most pronounced at the crest of the ridge where topographically controlled fluid migration leads to the accumulation of free gas beneath the BSR (Petersen et al., 2010; Bünz et al., 2012). Here we focus on the crest area of the eastern segment of the Vestnesa Ridge that is characterized by many active seepages of gas from pockmarks at the seafloor (Smith et al., 2014; Panieri et al., 2017). Different structural features like faults and fractures potentially play an important role in active seepage of methane gas in this area (Plaza-Faverola et al., 2015; Singhroha et al., 2016). It is important to study the overall distribution of hydrocarbons (mainly methane) in the system to better understand fluid flow processes. We derive P-wave and S-wave seismic velocities from the multi-component ocean-bottom seismic data using travel time inversion (Zelt & Smith, 1992). At station OBS5, the P-wave velocity model is further improved using a full-waveform inversion approach (Singh et al., 1993). We use the SCA/DEM approach (Jakobsen et al., 2000; Chand et al., 2006) to calculate gas hydrate saturation from the available velocity models at all ten locations along the ridge. We use this detailed information to study the impact of different structural and stratigraphic factors on the distribution of gas hydrates and free gas in this active fluid flow system in order to better understand fluid flow processes in the Vestnesa Ridge gas hydrate system.

2. Study Area

The Vestnesa Ridge is an approximately 100-km long sediment drift (Figure 1) with a post late-Miocene depocenter filled up with mostly contourite deposits (Eiken & Hinz, 1993; Howe et

al., 2008). It is located on the western Svalbard continental margin, quite close to a mid-ocean spreading ridge and thus is atop a hot (heat flux > 115 mW/m^2) and young oceanic crust (<20 Ma) (Ritzmann et al., 2004; Engen et al., 2008). Sediment thickness in this basin increases from west to east with sediments primarily consisting of glacigenic debris flows, glacimarine and hemipelagic sediments (Vogt et al., 1994; Ottensen et al., 2005). The stratigraphy in the Vestnesa Ridge is divided into three seismostratigraphic units; YP-1 (oldest), YP-2 and YP-3 (youngest) sequences (Eiken & Hinz, 1993). Ocean bottom currents have mainly controlled deposition within the younger sequences (YP-2 and YP-3). The YP-2/YP-3 boundary observed in the seismic data is an unconformity that indicates the onset of Plio-Pleistocene glaciations (Eiken & Hinz, 1993; Knies et al., 2009). The YP-2 sequence is mainly characterized by contourites and YP-1 has sediments with sub-parallel reflection pattern that have been deposited during syn- and post-rift phase of the tectonic activity in the region (Eiken & Hinz, 1993; Hustoft et al., 2009).

Shallow sediments on Vestnesa Ridge are saturated with hydrocarbon gases, mainly methane, locked in the form of gas hydrates with a 30-100 m thick free gas layer beneath (Hustoft et al., 2009; Bünz et al., 2012; Goswami et al., 2015). Fluids coming from depths feeds into the gas hydrate system on Vestnesa Ridge (Knies et al., 2018) and sediments close to the ridge crest show elevated concentrations of gas hydrates compared to surrounding sediments (Hustoft et al., 2009; Goswami et al., 2015; Singhroha et al., 2016). Presence of gas hydrates near the base of the GHSZ and free gas underneath creates a strong BSR along the ridge (Figure 2; Petersen et al., 2010; Bünz et al., 2012). A recent study by Goswami et al. (2015) has predicted that up to 25% gas hydrate saturation might be present in GHSZ away from focused fluid flow features of Vestnesa Ridge.

The crest of Vestnesa Ridge also shows numerous pockmarks with active seepage of gas (Bünz et al., 2012, Smith et al., 2014). Fluid leakage structures, so-called gas chimneys, exist beneath

the pockmarks and provide a pathway for fluids from the free gas zone beneath the BSR to the seafloor (Bünz et al., 2012). Up to 73% gas hydrate saturation might be present within these focused fluid flow features (Goswami et al., 2015).

3. OBS data acquisition and processing

We acquired multicomponent OBS data at ten different stations near the crest of the Vestnesa Ridge (Figure 1 and 2a). The OBS data used in this study has been acquired in multiple years (Table 1). Nine OBS stations are located on the southwestern flank of the ridge and one OBS station is located on the northeastern flank of the ridge (Figure 1). In the present study, we have chosen the location of OBS stations such that they will give a comprehensive overview about the variation of gas hydrate saturation along the ridge and potential impact of subsurface structures on the fluid flow system and gas hydrate saturation.

Earlier studies in the region suggest that faults play a significant role in the distribution of gas hydrates (Singhroha et al., 2016; Plaza-Faverola et al., 2015). Significant changes observed in the seismic Q anomalies across faults suggest substantial changes in hydrate saturation across the fault (Figure 11 in Singhroha et al., 2016). Stations OBS3, OBS4, OBS5 and OBS6 are selected to see the potential difference in seismic velocities across the fault (shown in yellow in Figure 1c) that demarcate seismic Q anomalies (Singhroha et al., 2016). Locations of OBS1, OBS9 and OBS10 help us to get a regional perspective. Station OBS10, which lies on the northeastern flank of the ridge, is used to see the potential changes in seismic velocities across the ridge. This information can be combined with P-wave velocity analysis from one OBS station (Goswami et al., 2015) that lies at deeper depth on the southwestern flank of the Vestnesa Ridge (Figure 1) to get a regional overview about changes in the seismic velocity across the ridge. Earlier studies have predicted differences in the distribution of gas across the ridge due to the upward migration of fluids along the slope towards the ridge (Hustoft et al. 2009; Bünz et al., 2012; Singhroha et al., 2016).

Multi-component OBS records the pressure wave field using a hydrophone and ground acceleration using a three-component seismometer. Vertical components are used to study P-waves and horizontal components are used to study S-waves. We used a Mini GI airgun (Sercel; 15⁄15 in^3) or a GI airgun (Sercel; 45⁄45 in^3) as the active source to acquire high-resolution OBS data, where the two airguns generate seismic energy with frequencies from 20 to 250 Hz (Petersen et al., 2010). The P-cable system (Planke et al., 2009; Petersen et al., 2010) on board *R/V* Helmer Hanssen is used to acquire high-resolution 2D and 3D seismic data (Plaza-Faverola et al., 2015) that is integrated with the OBS analysis (Figure 2). The airgun is fired at an interval of 6 seconds with a firing pressure of 170 bar. Different OBS recorders have different sampling intervals ranging from 0.4 to 1.0 ms (Table 1). We obtain good quality data from the hydrophone component at all OBS stations, which is used for P-wave velocity analysis. We also obtain good quality records from the 3-component seismometer at sites OBS1, OBS2, OBS3, OBS5 and OBS7; however, at other sites, seismometer records are poor quality, probably due to poor coupling between the seismometer and the seafloor.

Processing of OBS data involves some basic steps. The location of an OBS on the seafloor is normally displaced from the location where it was deployed into the water column due to the effect of oceanic currents on the downwards path of the OBS. Knowledge of the precise seafloor location of an OBS is pre-requisite to an accurate velocity model since velocity analysis is very sensitive to the error in the OBS location. Direct arrivals from inline and crossline directions (plotted in black in the Figure 1b) are used to estimate the seafloor location of OBS and seismic velocity in the water column at sites OBS1, OBS7, OBS8 and OBS9. OBS data from sites OBS2, OBS3, OBS4, OBS5, OBS6 and OBS10 is acquired simultaneously with 3D P-cable data acquisition (shown in green in Figure 1b). At these sites, direct arrivals from different shot lines (plotted in green in the Figure 1b) are used to constrain OBS location and water column velocity. A quality check of the relocated positions of an OBS can be done by applying the

travel time correction for the water column. After the correction has been applied, direct arrivals should look flat, as the effect of water column with offset has been removed (Figure 2b). A band pass filter is applied to the dataset to improve the signal quality of the OBS seismic by removing high frequency noise. Corner frequencies in a band pass filter are selected depending upon visual inspection of the noise level in each dataset. Selected frequencies in different OBS stations for low cut and high cut in the band pass filter are between 10-20 Hz and 200-250 Hz respectively. Noise removal makes picking different reflection arrivals relatively easier compared to noisy data (Figure 2c and 3a).

The orientation of horizontal components is different from the inline and crossline directions (Exley et al., 2010). Therefore, for shear wave velocity analysis from the horizontal components of a seismogram, the two components recorded by a seismometer need to be rotated properly (Gaiser, 1999; Brown et al., 2002) so that two horizontal axes of the seismograms will be aligned to inline and crossline directions of the acquisition. This improves the quality of PS sections and makes picking of PS reflection arrivals easier (Bünz et al., 2005; Kumar et al., 2007). We further apply a band pass filter to improve the quality of a PS section. Converted PS waves have significant energy in the lower frequencies as they travel for longer times as compared to reflected PP waves. The S-wave velocity is very low (<0.1 km/s) in the near seafloor unconsolidated sediments and thus we observe ringing in the PS section (Richardson et al., 1991; Figure 4). Applying a low-cut frequency band pass filter (<15 Hz) constitutes a good compromise of removing some of the ringing but preserving useful data in PS sections.

4. Methodology

P-wave velocity model

OBS data has been widely used to study gas hydrates (Katzman et al., 1994; Spence et al., 1995; Hobro et al., 1998; Posewang & Mienert, 1999; Song et al., 2018). Different methods have been

used to derive velocity models using OBS data (Zelt & smith, 1992; Shinohara et al., 1994; Kumar et al., 2007; Zillmer et al., 2005). Most of the methods used for estimating seismic velocities are either ray tracing (Julian & Gubbins, 1977; Virieux and Farra, 1991; Červený, 2001; Wang & Houseman, 1995) or grid based methods (Vidale 1988; Qin et al. 1992; Nakanishi & Yamaguchi; 1986; Rawlinson and Sambridge, 2004). We need good ray coverage to get efficient solutions from most grid-based tomographic or finite difference methods (Rawlinson et al., 2008). Based on ray coverage and separation between OBS stations, we find the ray tracing-based approach by Zelt and Smith (1992) suitable for our dataset. Zelt and Smith (1992) described an efficient numerical solution of the ray tracing equation to estimate travel time for different source-receiver locations under different subsurface velocity models. RayGUI (Song & ten Brink, 2004) provides an interactive graphical user interface that makes it easier to perform velocity analysis using Rayinvr. We use RayGUI to invoke Rayinvr and derive velocity models at different OBS stations.

Different prominent reflection arrivals are picked from OBS data at each site (for example seven picked reflection arrivals at site OBS3; Figure 2c) to derive seismic interval velocities. We tried to pick the maximum possible number of reflection arrivals (seven-eight) at each OBS site keeping in mind the thickness and lateral continuity of individual layers. Velocity estimates for a thin layer derived from travel time inversion is not very reliable as the effect of a thin layer on the curvature of the travel time curve is minimal and layers above this thin layer mainly determine the curvature. Broad combinations of velocity and depth can fit data for thin layers. Hence, we pick reflection arrivals keeping layer thickness greater than 20 m in order to improve accuracy of our results. We also tried to pick the same reflection arrivals at different OBS stations correlated through 2D and 3D seismic data (Figure 2c). In case the same reflection arrival is not strong enough laterally to pick travel times corresponding to far source-receiver offsets at different OBS stations, we picked another nearby strong reflection arrival.

The accuracy of a derived velocity model mainly depends on the accuracy of picked travel times along a reflection arrival and the farthest offset to where the picking can be done (Lines, 1993; Bickel, 1990). Picking at far offset travel times improves the confidence in the estimated velocity model since arrivals have significant move-outs (Dix, 1955; Yilmaz, 2001). However, the picks at far offsets have higher uncertainty as different reflection arrivals converge together and interfere to form a single phase. There is a trade-off between the accuracy of picked arrival times at far-offset and the farthest offset travel times that can improve confidence in the velocity model (Lines, 1993). We do not pick far offset travel times that have high pick uncertainties (> 1 ms).

We invoke Rayinvr using RayGUI (Zelt & Smith, 1992; Song & ten Brink, 2004) to estimate travel times for a given velocity model and the parameters in the velocity model are updated using the results obtained from the inversion (Figure 3 and 4). Velocities in the subsurface layers are assigned in a layer stripping approach starting at the top using travel time inversion of picked reflection arrival times (Figure 3). Different possible velocities and depths are tested in each layer to avoid the convergence of inversion to a local minimum. The process is repeated until we achieve a global minimum misfit between the travel times corresponding to picked and modeled reflection arrivals. For almost all picked reflection arrivals, the RMS misfit between modeled and picked travel times is less than 1 ms.

The resolution of P-wave velocity model obtained using travel time inversion is quite low, depending on the number of reflection arrivals picked in the seismic data. This resolution can be significantly improved by applying full waveform inversion to the OBS data (Singh et al., 1993; Xia et al., 1998; Westbrook et al., 2008). Depending on the type and the quality of the dataset, several 1-D (Pecher er al., 1996; Korenga et al., 1997; Xia et al., 1998; Westbrook et al., 2008) and 2-D full waveform inversion (Delescluse et al., 2011; Jaiswal et al., 2012; Wang et al., 2018) approaches have been used in the past to study the distribution of gas hydrates. In

this study, OBS stations are not spaced closely enough to have overlap of ray-paths in layers below the seafloor; hence, 1-D full waveform inversion is more suitable for this dataset. We apply a downward continuation approach based on a 1-D full waveform inversion method (FWI) (Singh et al., 1993; Westbrook et al., 2008) at station OBS5 in order to estimate the detailed variation of seismic velocities, especially near the BSR (Figure 5). A source wavelet is extracted using primary and multiple reflections from the seafloor (Singh et al., 1993). We use the velocity model obtained from travel time inversion of picked reflection arrivals to estimate the initial reflectivity function (Pecher et al., 1996; Kennett & Kerry, 1979) and assume a fixed relationship between P-wave velocity and density (Hamilton, 1978). Synthetic seismic data is obtained using a convolution operation between a source wavelet and reflectivity function (Kennett & Kerry, 1979). Real data is matched with the synthetic data in frequency slowness domain (Sheriff & Geldart, 1982). We start by matching the seafloor reflection in synthetic and real data and with a downward continuation approach; the P-wave velocity model is updated in successive iterations to reduce the misfit to a minimum (Singh et al., 1993). The RMS misfit for different values of p is in between 0.045-0.07 (Figure 5). The RMS misfit shows a small inconsistent increase with offset (Figure 5). The low RMS misfit between the real and synthetic traces in tau-p domain ensures the accuracy of derived velocity model.

S-wave velocity model

A P-wave velocity model is pre-requisite to derive a S-wave velocity model from converted PS waves (Bünz et al., 2005; Westbrook et al., 2008). In order to constrain S-wave velocity from converted waves, it is necessary to correlate picked reflections in a PP section with reflections in the corresponding PS section (Kumar et al., 2007; Westbrook et al., 2008). Accuracy of the S-wave velocity model depends on the reliability of this correlation (Westbrook et al., 2008). Different methods are used to correlate events in PP and PS sections. An approach to match events in PP and PS by visual correlation of seismic signatures or selection of events from a

limited number of picked events in the absence of OBC data is widely used (Dash & Spence, 2011; Exley et al., 2010; Westbrook et al., 2008; Satyavani et al. 2016). In order to correlate events precisely, a semblance-based approach has been used (Appendix 1). The basic premise behind this approach is the fact that the curvature of PS reflection arrivals in travel time vs offset plot will match with the curvatures of the estimated PS travel time curves for an accurate S-wave velocity model (Appendix 1). Travel times corresponding to these PS reflection arrivals are picked (Figure 4) and uncertainties associated with the velocity model are analyzed using Rayinvr. The resulting S-wave velocity models have less than 3 ms RMS misfit in picked and modelled PS travel times and thus give a good estimate of shear-wave velocities in the subsurface.

Gas hydrate and free gas saturation modeling

A number of empirical relations and rock physics models exist that allow us to estimate gas hydrate saturation from seismic velocity. Models predicting gas hydrate saturation from velocity data range from average travel time models that use simple empirical relations (Wood, 1941; Wyllie et al., 1958) to the more complex, rock physics based models that account for the pore-scale interaction between gas hydrate, fluids and sediment matrix (Ecker et al., 1998; Helgerud et al., 1999; Carcione & Tinivella, 2000; Jakobsen et al., 2000; Chand et al., 2006). The effect of gas hydrates in sediments on seismic velocities is more complex and cannot be precisely estimated using simple empirical models since the behavior of hydrate forming a composite with sediment matrix changes with hydrate saturation and mode of formation (Minshull & Chand, 2009; Chand et al., 2006). The rock physics-based methods incorporate the pore-scale interactions and variations in hydrate-sediment morphology. These methods can effectively account for the hydrate-sediment micro-structure (e.g., whether hydrate forms as a part of sediment matrix, forms in the pore space or forms as filler in fault gaps). Hence, the patterns of velocity variation with hydrate saturation varies between different models of hydrate

formation. Therefore, one has to choose the model based on various parameters such as host sediment type, changes in P and S-wave velocity, presence of faults, etc. to incorporate these effects (Chand et al., 2006; Marín-Moreno et al., 2017). The presence of hydrate in sediments increases the seismic P-wave velocity but may or may not increase S-wave velocity compared to the background velocity, depending on the amount of hydrate present and their form of distribution in the pore spaces. Hence, the difference between the background velocity and the observed velocity changes can be used to find the gas hydrate saturation (Chand et al., 2004).

The self-consistent approximation (SCA) (Willis, 1977) - differential effective medium (DEM) theory (Nishizawa, 1982) predicts the effective stiffnesses of an aggregate of randomly oriented crystals where hydrate is incorporated (Jakobsen et al., 2000). Since DEM preserves the initial connectivity of phases (Sheng, 1990), the combination can produce a composite that is biconnected at any porosity and new components such as hydrates can be introduced to the effective medium. The model can therefore handle the case where gas hydrates are present as an unconnected phase within pore spaces (case 1) or the case where gas hydrates form as a part of the sediment matrix (case 2). In case 1, the effect of increment in gas hydrates saturation is adjusted with equal decrease in water saturation along with an effective change in sediment-water composite stiffness using DEM whereas in case 2, the method is similar but the starting effective medium is a clay-gas hydrate composite representing hydrate as part of the sediment matrix. Since an increase in S velocity is observed above the BSR, hydrate formation as part of sediment-hydrate composite is inferred for a given gas hydrate saturation and we have therefore employed this method to calculate gas hydrate saturations in the present study. This model has been used previously to study gas hydrate saturation from the seismic velocities in nearby locations (Westbrook et al., 2008; Hustoft et al., 2009). The effect of individual fracture properties is not studied here since the seismic data used only gives an estimate of the effective properties of the medium lying in between the source and the receiver, which are several orders

of magnitude larger than the size of the fractures. Existence of pure hydrate filled fractures can therefore result in over prediction of hydrate saturation depending on the porosity of pure hydrate formed but it is partly accounted for in the uncertainty estimates.

Lithology and porosity are very important parameters to estimate seismic velocities in a medium. The porosity parameter becomes even more important in the shallow sub-surface as porosity changes rapidly at these depths. Accurate lithology and porosity parameters are pre-requisite to estimate gas hydrate saturation in marine sediments. We have very limited information available about these parameters in the area. Chemical, XRD and grain size analysis of a gravity core in one of the nearby sites (Hustoft et al., 2009) show 25% clay, 39% mica, 24% quartz, 5% feldspar and 7% calcite as the sediment composition. The sediment composition from this site (Hustoft et al., 2009) is used in the SCA/DEM to derive seismic velocities in a water-saturated medium. As a simple approach, lithology of the near surface sediments is considered the same as the lithology of the deeper sediments as well. We use porosity data obtained from ODP well logging to get a smoothed porosity variation with depth. Differences in lithologies at Vestnesa Ridge and the ODP site should be considered to get a better overview of porosity variation with depth. Hustoft et al. (2009) used a porosity profile in which variations in porosity due to changes in lithologies at the ODP and study sites is considered. The porosity profile used by Hustoft et al. (2009) is also used in this paper as our study area is proximal to the presented in Hustoft et al. (2009). Sediment connectivity and orientation of micro fractures have strong impacts on seismic velocity. We chose the sediment connectivity parameter, which includes the effect of micro fractures that satisfy the range of seismic velocities derived by OBS data.

5. Uncertainty analysis

The uncertainties of the velocity analysis are mostly associated with the accuracy of picking different reflection arrivals from OBS data (Bünz et al., 2005; Plaza-Faverola et al., 2010). Pick

uncertainty depends on the quality of the dataset, as a seismic reflection can be picked with high certainty in a good quality dataset. Datasets with high frequency content, high sampling interval, low signal to noise ratio, etc. will have low pick uncertainty. The quality of source and receiver mainly decide these parameters. Seismic signals generated by seismic sources in this study have high centroid frequencies (>100 Hz) and the OBS data therefore has higher signal to noise ratio than typical seismic sources. However, there is poor signal to noise ratio after a certain depth below the BSR. This can be due to high attenuation in the free gas zone and limited penetration of P-Cable data. Hence, we only model one layer below the BSR. Sampling rate of the recorded data is quite high (Table 1). Certain parameters related to source-receiver geometries like seafloor depth, source-receiver offset, horizontal offset between shot line and OBS location, etc. also affect the pick uncertainty. Pick uncertainty is higher for large source-receiver offsets as reflection arrivals merge at larger offsets thus it is difficult to track a given phase. Reflection arrivals merge at shorter offsets with an increase in depth. Water depth in the study area is around 1.2 km and this allows us to pick a given reflection arrival up to 2-4 km offset depending on the strength of the arrival. Pick uncertainty can be further constrained by picking upper and lower bounds of the picked reflection arrivals thus providing the uncertainty parameter for each travel time pick in Rayinvr. This offset varying pick uncertainty helps in giving a suitable weightage to every travel time pick and thus constrains the derived velocity model well. A fixed constant is typically given as an uncertainty parameter in the input model (Plaza-Faverola et al., 2010). In our case, we have only picked those travel times where our uncertainty about the pick is less than 1 ms.

There are also uncertainties in the estimated velocity model due to the simplistic assumption of a subsurface where layers are isotropic and homogeneous with no horizontal variation along a given layer. Picked travel times along a curvature will not follow the curvature as predicted by the velocity model if there is horizontal variation in seismic velocities (Thomsen, 1986;

Thomsen, 1999). It is hard to study small horizontal velocity variations along a layer with the limited available dataset and there will always be misfit between the picked travel times and estimated travel times due to inherent complexity of the subsurface (Chiţu et al., 2008).

In order to study the sensitivity of the seismic velocity model to all these parameters, we analyze the variation of RMS misfit with change in the velocity model using the approach documented by Katzman et al. (1994). Perturbation of a velocity model increases the RMS misfit between the modelled and picked travel times as estimated seismic velocity models have least RMS misfit. In order to study the uncertainty in a modelled depth or velocity parameter, we perturb either parameter so that the RMS misfit increases and exceeds the pick uncertainty. In some cases, where the modelled travel times fit well with the picked travel times, we need very strong perturbation in order to increase the RMS misfit to 2 ms. On average, we find that we need to perturb the velocity model by approximately 0.06 km/s in order to increase the RMS misfit to 2 ms. Considering the good fit between modelled and picked travel times attained from the layer-stripping approach, uncertainty in the velocity estimates may be less than the uncertainty estimated using the Katzman et al. (1994) approach.

Uncertainties associated with the S-wave velocity model are higher than uncertainties in the P-wave velocity model, because we need very far offset travel time picks to achieve good S-wave velocity estimates. PS waves are reflected at a very low angle (Figure 4c), as S-wave velocities are low compared to P-wave velocities in the near surface sediments. In order to achieve the significant offsets required to perform S-wave velocity modeling, we picked far offset converted PS waves for different seismic reflection arrivals. However, far offset picks are always associated with high uncertainties due to high noise level and interference between different reflection arrivals. Pick uncertainty in picked PS travel times is high (up to 3 ms) leading to high uncertainty in the S-wave velocity model (0.1 km/s).

Uncertainties in velocity models propagate to the uncertainties in gas hydrate and free gas saturation estimates. Uncertainty in gas hydrate saturation estimates also comes from the uncertainties in the lithology, presence of faults/micro fractures and porosity profiles at the study site. We derive porosity and lithology profiles from the limited information available about these parameters in the region. These approximations generate uncertainties in the base velocity profile generated for water-saturated sediments using the SCA/DEM modeling approach. The velocity model in a layer beneath the low velocity zone below the BSR gives us an idea about the accuracy of estimated base velocity profiles and the extent of velocity deviations in layers near the BSR (Bünz et al., 2005; Hustoft et al., 2009). However, due to a limited signal to noise ratio, it is hard to model seismic velocities in this layer. The uncertainties in sediment composition, porosity changes, etc. are calculated using the maximum changes observed in sediment composition and porosity at corresponding depths (Hustoft et al., 2009). This uncertainty is converted to velocity uncertainties and used in the inversion algorithm based on McKenzie & O'Nions (1991) approach (Chand et al., 2006). We calculate uncertainties that arise in gas hydrate and free gas saturation estimates from the SCA/DEM modeling due to uncertainties in the velocity models, porosity and lithology profiles (Chand et al., 2006).

6. Results

Interval P-wave velocity models are estimated in this study for 6-7 layers below the seafloor at 10 OBS locations using travel time inversion (Figures 1, 6 & 7). The P-wave velocity in the water column range from 1.463 km/s to 1.468 km/s at different OBS stations. There are no significant differences in the P-wave velocity beneath all OBS stations in the first 40 m below the seafloor - seismic velocities for this interval are between 1.5-1.537 km/s. There are some differences in P-wave velocities beneath different OBS stations between 40 to 80 m depth below the seafloor. Seismic velocities at OBS3 (1.62 km/s) and OBS5 (1.66 km/s) are higher than seismic velocities (<1.60 km/s) at other OBS stations. P-wave seismic velocities increase by

around 0.1-0.15 km/s beneath almost all stations (Figure 7a) across the ~0.2 Ma discontinuity (shown in the Figure 2c; Plaza-Faverola et al. 2015) around 70-80 m depth below the seafloor. P-wave velocities in the 80 to 130 m depth range below the seafloor vary considerably beneath OBS stations. We find low seismic velocity (1.58 km/s) northeast of a fault (yellow dashed line in Figure 1c) at OBS3 and very high seismic velocity (1.73 km/s) southwest of the fault at OBS5 compared to the seismic velocities (1.62-1.66 km/s) at other OBS sites. In the 130 to 155 m depth range, we find small variations in P-wave velocities (1.65-1.70 km/s) beneath different OBS stations. Significant P-wave velocity differences (1.73-1.82 km/s) are observed in the layer above the BSR. OBS stations southwest of the fault (Figure 1c) i.e. OBS5 and OBS6 show the highest seismic velocities (1.82 km/s) whereas OBS stations northeast of the fault i.e. OBS2, OBS3 sites show the lowest seismic velocities (1.736-1.743 km/s) in this layer. Other sites closer to the ridge crest i.e. OBS1 and OBS4 also show higher seismic velocities (1.80 km/s) compared to seismic velocities (1.74-1.76 km/s) at OBS sites away from the ridge crest i.e. OBS7, OBS8 and OBS9. At site OBS10 on the northeastern flank of the ridge, the seismic velocity (1.757 km/s) does not show any anomalous change in this layer. The depth of the BSR in the study area (Figure 2, 7a & 8) ranges between 190-196 m below the seafloor across all OBS stations. Variations in the P-wave velocities (1.28-1.53 km/s) at different OBS stations are highest in the layer below the BSR. One of the OBS stations southwest of the fault (OBS6) shows the lowest seismic velocity (1.28 km/s). At other OBS stations, seismic velocities are in the 1.35-1.40 km/s range, except at sites OBS2 (1.49 km/s) and OBS9 (1.53 km/s), where higher seismic velocities are observed. P-wave velocities estimated using FWI increase the resolution of P-wave velocity model significantly. At site OBS5, very high P-wave velocities (>1.95 km/s) are observed in a very narrow interval above the BSR.

S-wave velocities have been estimated at sites OBS3 and OBS5 (Figure 6k). Low S-wave velocities (<0.2 km/s) are observed at shallow depths while velocities increase sharply to ~ 0.37

km/s near the BSR depth. S-wave velocities decrease beneath the BSR to 0.272 km/s and 0.252 km/s at OBS3 and OBS5, respectively. There are also significant differences in S-wave reflectivity patterns in the GHSZ for OBS stations on different sides of the fault (yellow dashed line in Figure 1c). There are strong reflections in an interval (~50-60 m) above the BSR in the PS section at site OBS3 (Figure 4a) whereas there are no distinct reflections at site OBS5. PS records in other instruments also show similar differences (Figure 9), which removes the possibility of an instrument related artefact. There are continuous PS reflections at OBS stations southwest of the fault (OBS5 and OBS6) whereas strong distinct PS reflections (Figure 4 and 9) occur in the GHSZ at OBS stations northeast of the fault (OBS1, OBS2 and OBS3).

7. Discussion

Presence of gas hydrates and free gas

We have estimated P-wave velocity profiles at 10 OBS stations (Figure 6 and 7), S-wave velocity profiles at two OBS stations (OBS3 and OBS5) and applied FWI for a detailed investigation of the P-wave velocity at site OBS5. We calculated background seismic velocities assuming water saturated sediments using the SCA/DEM approach (Figure 8a) and compared these with OBS velocity models. There are increases in P-wave velocities (~0.04-0.13 km/s) and S-wave velocities (~0.1 km/s) above the BSR compared to background velocities. A detailed P-wave velocity model derived from FWI at site OBS5 shows an increase (~0.3 km/s) and decrease (~0.2-0.4 km/s) in P-wave velocities above and below the BSR, respectively. These variations in seismic velocities are well above model uncertainties. Considering the contourite depositional setting at the study site where strong changes in seismic velocities due to lithological changes are unexpected, increases and decreases in seismic velocities above and below the BSR, respectively can be attributed to the presence of gas hydrates and free gas in the pore space of the sediments (Hustoft et al., 2009; Goswami et al., 2015).

Gas hydrate and free gas saturation

We estimate gas hydrate and free gas saturations based on difference between estimated and background seismic velocities using the SCA/DEM approach (Figure 8). We further constrain gas hydrate and free gas saturation estimates at sites OBS3 and OBS5 using S-wave velocity analysis. Uncertainties are significantly lower (less than half) in saturation estimates derived from combined analysis of P-wave and S-wave velocities compared to uncertainties in saturation estimates derived from the P-wave velocity alone (shown as error bars in Figure 8b and 8c). We do not find any significant gas hydrate saturation (<0-2%) in the first 50 m of sediments at any OBS site except at OBS3 (0-5%). In the layers between 50 to 100 m below the seafloor, we do not estimate significant gas hydrate saturations at sites OBS1, OBS2 and OBS10 (<0-2%). Beneath the other stations, gas hydrate saturations vary between 3-10%. In the layers approximately 100 to 150 m below the seafloor, gas hydrate saturations vary between 0 to 10% at all OBS stations. It is difficult to study low gas hydrate saturations (<5-10%) from seismic velocity analysis as uncertainties are quite high (shown by error bar in Figure 8). Small variations in seismic velocities may also be due to minor changes in sediment properties rather than the presence of gas hydrates. However, the gas hydrate saturation in a layer close to the base of the GHSZ is high and well above the uncertainty limit. In the layer directly above the BSR, we estimate highest gas hydrate saturations (~18%) at OBS stations that are southwest of the fault (OBS5 and OBS6). We also estimate higher gas hydrate saturations (~16%) at OBS4, which lies on the fault, and at OBS1, which is close to the ridge crest, (Figure 1) compared to other stations where gas hydrate saturations are between 10-13%. At OBS stations northeast of the fault (OBS2 and OBS3) and at station OBS9, we find low gas hydrate saturations (~10%) in this layer. Free gas saturations vary from 1.5% to 4.1% at OBS stations along the ridge. However, OBS stations that are southwest of the fault (OBS5 (3.0%), OBS6 (4.1%) and OBS8

(3.1 %)) have considerably higher free gas saturations compared to the rest of the stations where free gas saturations vary from 1.5% to 2.8%.

Gas hydrates often occur in thin layers of high gas hydrate saturation as observed from drilling at different locations (Collett et al., 2012; Collett et al., 2014). The velocity model from FWI gives finer details about the subsurface velocities (Figure 6e). High P-wave velocities in a narrow zone can potentially be due to high gas hydrate saturation zones in narrow intervals (Figure 8a and 8b). The high P-wave velocity (~2.0 km/s) observed just above the BSR indicates the higher gas hydrate saturation (>20%) near the base of the GHSZ. Combined analysis of the FWI derived P-wave velocity and the S-wave velocity at site OBS5 (Figure 8a and 8b) helps in detecting gas hydrates in thin layers (especially between 125-150 m depth below the seafloor).

Geological controls on gas hydrate and free gas distribution

Gas hydrate and free gas saturation estimates vary along the ridge. The topography of Vestnesa Ridge favors the accumulation of free gas near the ridge crest (Hustoft et al., 2009; Singhroha et al., 2016) and thus, we expect that the gas hydrate saturation will be higher for OBS stations closer to the ridge crest. Velocity models from Goswami et al. (2015) at two locations on Vestnesa Ridge also show that the gas hydrate saturation is higher in the GHSZ just above the BSR for the location closest to the ridge crest. In the present study, we observe higher gas hydrate saturations (>15%) at the OBS stations near the crest of the ridge, except at stations OBS2 and OBS3.

Low gas hydrate saturations derived from P-wave velocity models at OBS2 and OBS3 (around 10%) near the BSR depth has also been predicted by Singhroha et al. (2016) using seismic Q analysis of high-resolution P-cable seismic data (Figure 7). Faults and discontinuities demarcate Q anomalies in the region and the differences in Q can be due to differences in gas hydrate and

free gas saturations across the fault (Figure 7b and 7c). We also find significant differences in P-wave velocities across the fault from OBS3 to OBS5 (Figure 7). Low gas hydrate and free gas saturations near the BSR at sites northeast of the fault (OBS2 and OBS3; Figure 1c) compared to sites southwest of the fault (OBS5 and OBS6) can potentially be due to the presence of fault, which acts as a fluid migration pathway or shuts off the supply of gas-rich fluids to adjacent strata. The ridge topography favors the migration of gases towards the ridge crest; however, faults can play a significant role in controlling the upslope migration of gases. Faults can be permeable and lead to leakage of gases towards permeable layers further up in the stratigraphic section or they can be sealing (due to the displacement of permeable routes by the fault) and block any upslope migration of gases; thus, making the region in the upslope direction gas deprived. Hence, differences observed in estimated gas hydrate and free gas saturations across the fault can be due to differences in the availability of gas.

The distribution of gas hydrates on Vestnesa Ridge is very typical of a deep marine setting, where highest hydrate saturations are found directly above the BSR (Westbrook et al., 1994; Tréhu et al., 2004; Bünz et al., 2005). In these settings, free gas is migrating into the GHSZ right above the BSR where it forms gas hydrate. Ongoing sedimentation and burial moves the deepest gas hydrate accumulations out of the GHSZ, leading to gas hydrate dissociation. Gas released during this process can migrate back into the GHSZ reforming hydrates (Kvenvolden & Barnard, 1983; Minshull & White, 1989; Hyndman & Davis, 1992; Minshull et al., 1994; Nole et al., 2018). This process develops a typical hydrate distribution with depth that we see today (Bhatnagar et al., 2007). Higher gas hydrate saturation estimates obtained using FWI above the BSR (Figure 8b) further supports this theory (Pecher et al., 1996). This type of diffusive flow is the primary mode of gas hydrate formation in regions that are away from permeable faults or fractures (Liu & Flemings, 2011; Daigle & Dugan, 2011; Rempel, 2011). In places close to permeable faults or fractures, advective methane flux can also contribute to

the gas hydrate formation (Rempel and Buffett, 1997; Xu and Ruppel, 1999; Davie and Buffett, 2001; Davie and Buffett, 2003). Faults can act as conduits for fluid flow and the fluid passing through faults can create a series of fracture networks if the fluid pressure exceeds a certain value (Stranne et al., 2017). This process is dominant in fluid flow systems like gas chimneys (Liu & Flemings, 2007). In this study, OBS stations are away from gas chimneys where strong advective fluxes are expected; therefore, we expect gas hydrate saturations derived at OBS stations to be reflective of diffusive fluid flow and slower rates of gas hydrate accumulation. However earlier studies and gas hydrate saturation estimates derived from electromagnetic (EM) data may suggest otherwise (Goswami et al., 2015).

Gas hydrate saturations estimated by velocity analysis of multicomponent seismic data are significantly lower than gas hydrate saturations estimated by the EM method (Figure 10; Goswami et al., 2015). Goswami et al. (2015) predict 30% gas hydrate saturation in 0-100 m depth and 20-30% gas hydrate saturation in 100-200 m depth outside the gas chimney. Higher gas hydrate saturation estimates using resistivity methods compared to gas hydrate saturation estimates using seismic velocity analysis of multicomponent seismic data has been reported in several studies at different sites (Lee & Collett, 2009; Cook et al., 2010; Weitemeyer et al., 2011). The presence of free gas in co-existence with gas hydrates in the GHSZ increases the resistivity of a medium and decreases the P-wave velocity, which may explain the discrepancy in gas hydrate saturation estimates derived from seismic velocity analysis and resistivity analysis. Goswami et al. (2015) investigate this possibility and suggest the presence of co-existing gas hydrates and free gas in gas chimneys and even at sites away from gas chimneys. However, the anisotropic distribution of gas hydrates can also explain the differences in gas hydrate saturations estimated from the P-wave velocity and resistivity analysis. This study and the study by Goswami et al. (2015) assume an isotropic gas hydrate distribution in a medium.

Gas hydrates saturations derived from seismic velocity and resistivity analysis normally overestimate the amount of gas hydrate due to the assumption of isotropic pore filling gas hydrate morphology (Lee & Collett, 2009). Seismic wavelengths used in seismic exploration surveys are long (normally >10 m) and small-scale heterogeneities in the distribution of gas hydrates have a small effect on seismic velocities (Lee & Collett, 2009). The variation in gas hydrate saturation derived from seismic velocity analysis is small (<10-20%) due to changes in the gas hydrate morphology from pore filling to grain displacing (Ghosh et al., 2010). However, this difference can be large (>400%) if the gas hydrate saturation is estimated using resistivity methods with an assumption of an isotropic pore filling gas hydrate distribution in a gas hydrate-filled fracture deposit (Lee & Collett, 2009; Lee & Collett, 2012). Archie's parameters i.e. *a* (cementation exponent), *m* (cementation factor) and *n* (saturation exponent) used in Archie's equation by Goswami et al. (2015) for estimating gas hydrate saturation vary strongly due to anisotropy in a medium (Kennedy et al., 2001; Kennedy & Herrick, 2004; Lee & Collett, 2009). Different anisotropic parameters like the orientation of fractures and inter-connectivity within fractures have a big effect on the resistivity estimates (Kennedy et al., 2001; Kennedy & Herrick, 2004; Lee & Collett, 2009). For example, gas hydrate saturation estimates from resistivity measurements in gas hydrate-filled vertical fractures can be five times higher than the actual gas hydrate concentration (Lee & Collett, 2012). Archie's parameters also vary with changes in the gas hydrate saturation and variations in *n* are bigger than variations in *m* due to anisotropy (Kennedy & Herrick, 2004; Lee & Collett, 2009). The value of *n* can be between 1.25-7, depending on an anisotropy in a medium (Kennedy & Herrick, 2004). Assuming an isotropic gas hydrate distribution, Goswami et al. (2015) use $n = 2$ to estimate gas hydrate saturations. A recent study by Cook and Waite (2018) show that the use of $n = 2$ overestimates the gas hydrate saturation and $n = 2.5$ should be used as a default value for an isotropic gas hydrate distribution if independent estimates are not available. Lee and Collett (2009)

recommend the use of $n > 2.5$ for an anisotropic medium. Earlier studies in the Vestnesa Ridge suggest the presence of faults and fractures in the area (Plaza-Faverola et al., 2015; Singhroha et al., 2016; Bünz et al., 2012). Considering the possibility of a minor fraction of gas hydrates in fractures and faults, we use a value of $n = 3$ in the Archie's equation which fits well for velocity and resistivity analyses to estimate the gas hydrate saturation (Figure 10). The minor presence of gas hydrates (20-30%) in fractures or faults will have a very small effect on gas hydrate saturations derived using seismic velocity analysis and overall change in the gas hydrate saturation will be as small as 1-2% (Ghosh et al., 2010). However, it changes gas hydrate saturation estimates from resistivity analysis by 30%. (Figure 10). The use of $n = 3$ gives the gas hydrate saturation estimate of 13.8-21.1% in 100-200 m depth as opposed to gas hydrate saturation estimates of 20-30% in the same interval for $n = 2$. Gas hydrate saturation estimates for $n = 3$ (13.8-21-1%) match well with the saturation estimates from seismic velocity analysis (10-18%) in a layer above the BSR (Figure 8). There are still differences in gas hydrate saturation estimates from these two methods in the 0-100 m depth interval. These differences could be due to inter-site variability. Significant differences in gas hydrate saturation estimates from EM data and seismic velocity analysis potentially hint towards the presence of gas hydrates in fractures in the region.

It is difficult to differentiate between the possibility of gas hydrates present in fractures and the co-existence of free gas and gas hydrates in the GHSZ using P-wave velocity and resistivity data. Combining the analyses from P-wave velocity models and resistivity data with S-wave velocity models, seismic Q models and PS reflectivity can help us in differentiating between these two possibilities. We do not have resistivity models at all our OBS sites; however, we can analyze our results keeping in mind these two possibilities.

Changes in the PS reflectivity from continuous PS reflections (OBS5 and OBS6) to strong distinct PS reflections (OBS1, OBS2 and OBS3) occur across the fault (Figure 1c, 4 and 9).

These differences in PS reflectivity can be due to differences in the geological settings. Considering that these changes occur across the fault, there is a strong possibility that these differences can be due to changes in the distribution of gas hydrates. The occurrence of free gas or layered gas hydrates in the GHSZ can potentially generate such effects. With the limited geological information in the area, it is difficult to argue in favor of the possibility of gas hydrate as layered deposits at OBS stations northeast of the fault. However, some of our results support the theory that free gas co-exist with gas hydrates in the GHSZ at OBS station northeast of the fault (OBS3 site). The presence of free gas in the GHSZ will decrease the P-wave velocity and Q but will have very little impact on the S-wave velocity. No significant differences in S-wave velocity estimates above the BSR across the fault (OBS3 and OBS5) favor the theory of the presence of free gas in GHSZ (Goswami et al., 2015) at OBS station northeast of the fault (OBS3). The interval P-wave velocity above the BSR is also significantly lower (1.74 km/s) at the OBS station northeast of the fault (OBS3) compared to the interval P-wave velocity (>1.8 km/s) at OBS stations southwest of the fault (OBS5 and OBS6). Q analysis also shows low Q values northeast of the fault compared to high Q values southwest of the fault in a layer above the BSR (Singhroha et al., 2016). The presence of free gas creates high seismic attenuation and thus low Q values are observed in sediments saturated with free gas. Geologically, the presence of free gas in the GHSZ in a contourite setting with good permeability and low gas hydrate saturations (<25%) seems unlikely as we can expect sufficient supply of water to form gas hydrate. Nevertheless, a recent study by Sahoo et al. (2018) shows that hydrate films can envelop free gas in the GHSZ even in sediments with good permeability. Sahoo et al. (2018) attributed differences in gas hydrate saturation estimates from resistivity and seismic observations to the presence of free gas in GHSZ as we observe in our study area (Goswami et al., 2015). Based on this theory and our results, we can hypothesize that gas hydrate saturations can be potentially similar across the fault (Figure 8b and 8c) and there can be differences in the

amount of free gas trapped inside gas hydrate films across the fault leading to differences in P-wave velocities above the BSR in the GHSZ. However, considering the fact that there are low free gas saturations below the BSR at OBS stations northeast of the fault (OBS2 and OBS3), as suggested by Q analysis (Singhroha et al., 2016) and P-wave velocities (Figure 7 and 8), it is difficult to explain higher amounts of free gas trapped in the GHSZ at OBS station northeast of the fault (OBS3) compared to OBS station southwest of the fault (OBS5). Differences in the P-wave velocity and similarities in the S-wave velocity across the fault (OBS3 and OBS5) can also be due to similarity in the load bearing gas hydrate saturation and differences in the pore fill gas hydrate saturation. This is less likely to happen geologically as gas hydrates tend to become load bearing with increase in gas hydrate saturation (Minshull & Chand, 2009). In addition, it will be difficult to explain differences in seismic Q analysis (Singhroha et al., 2016) across the fault. We expect lower S-wave velocity at OBS station northeast of the fault (OBS3) than OBS station southwest of the fault (OBS5). Similar S-wave velocity (~0.37 km/s) observed above the BSR across the fault (OBS3 and OBS5) can potentially also be an artifact due to high uncertainty (~0.1 km/s) in S-wave velocity estimates.

Results from different surveys and methods seem to favor the theory of the co-existence of free gas and gas hydrates northeast of the fault although we cannot rule out the possibility of the presence of gas hydrates in fractures, especially southwest of the fault. Although there are some non-uniqueness interpretation issues, with significant differences in different seismic properties (P and S-wave velocity, Seismic Q and shear wave reflections in PS sections) across the fault (dashed yellow line in Figure 1c), we can say with high confidence that faults play an important role in the distribution of gas hydrates and free gas in the region (Figure 7).

8. Conclusion

We perform seismic velocity modeling at 10 OBS locations along the Vestnesa Ridge to study the gas hydrate saturation. We observe high interval P-wave velocities (1.73-1.82 km/s) in a

layer above the BSR and low interval P-wave velocities (1.28-1.53 km/s) in a layer below the BSR. The depth of the BSR is around 190-196 m at different OBS stations. Results based on FWI suggest that the P-wave seismic velocity can be higher than 1.95 km/s above the BSR at station OBS5. High seismic velocities above the BSR and low seismic velocities below the BSR document the presence of gas hydrate and free gas, respectively along the Vestnesa Ridge. We derive gas hydrate saturations from seismic velocity models using the SCA/DEM approach. Results suggest up to 10%-18% average gas hydrate saturation and 1.5%-4.1% average free gas saturation in layers near the BSR depth. We find high gas hydrate and free gas saturations near the ridge crest, except at few locations potentially shadowed by the fault where gas hydrate and free gas saturations are lower. Hence, we suggest structural and topographical control on the distribution of gas hydrates and free gas along the ridge. Gas hydrate saturations estimated in this study are different from gas hydrate saturations estimated using resistivity data. Gas hydrate-filled fracture deposits or co-existence of gas and gas hydrate in GHSZ can create such differences. Combined analysis from P and S-wave velocity models, seismic Q model and resistivity data suggest the co-existence of free gas and gas hydrates in the GHSZ northeast of the fault.

Acknowledgement

This work is partly supported by the Research Council of Norway through its Centres of Excellence funding scheme, project no. 223259. We thank the crew of the R/V Helmer Hanssen and those who contributed to the OBS and P-cable data acquisition. We thank Andreia Plaza-Faverola, Kate Waghorn and Sunil Vadakkepuliyambatta for their help in this work. We also thank anonymous reviewers and Ingo Pecher (associate editor) for their careful reading of the work and constructive suggestions that improved the manuscript. The data is stored at UiT open research data repository (https://dataverse.no/privateurl.xhtml?token=cc1c7b12-4acf-4d02-a506-f8f6b56f7236).

Appendix 1

Ocean Bottom Seismic (OBS) data is often used to derive subsurface S-wave velocity model in marine settings using reflected converted wave (PS) signals recorded by horizontal components of the seismometer (Bünz et al., 2005; Westbrook et al., 2008; Exley et al., 2010; Dash and Spence, 2011; Satyavani et al., 2016). Converted waves travel downward as P-waves and upon reflection are converted into S-waves, hence, the name PS-waves, or converted waves. A P-wave velocity model is required to derive S-wave velocities from PS reflections. The analysis of the P-wave velocity model constrains the geometry of the subsurface model, i.e. depths of interfaces. Thus, it is necessary to correlate picked reflection arrivals in a PP section with reflection arrivals in the corresponding PS section (Kumar et al., 2007; Westbrook et al., 2008). Seismic signatures in PP and PS sections recorded by OBS data are quite different (Figure 2 and 4) as reflectivity in a PS section depends on several parameters (Aki and Richards, 1980; Connolly 1999; Duffaut et al. 2000) that are different from PP reflectivity. Reflections that are strong in a PP section, for example strong reflections due to the presence of free gas, might not be strong in a PS section (Bünz et al., 2005). Resolution in a PS section is also higher as S-wave velocities are lower than P-wave velocities. This may result in a PS section that has continuous reflections from different reflectors in the subsurface (Figure A1a). All these factors, accompanied by low signal to noise ratio due to poor coupling between seafloor and seismometer in many cases, make it hard to match PP reflection arrivals with their corresponding PS reflection arrivals. Correlation of arrivals in these two sections is a major source of error in the derived S-wave velocities (Westbrook et al., 2008).

In the present study, we have used a semblance approach in a layer stripping fashion to find corresponding reflections in the PP and PS sections. For example, in order to find a reflection arrival in a PS section corresponding to the first picked reflection in a PP section, semblance is calculated for different S-wave velocities in the first layer. Since parameters like P-wave

velocity and depth of a reflector are fixed in a P-wave velocity model, different S-wave velocities will result in different PS reflection arrivals.

$$S_{vs} = \frac{\left[\sum_{j=1}^{N} A_j(t)\right]^2}{N\left[\sum_{j=1}^{N} A_j(t)^2\right]}$$

Here, S_{vs} is the semblance for a given reflection arrival corresponding to a given v_s (S-wave velocity). $A_j(t)$ is the amplitude of j^{th} sample along a reflection arrival corresponding to a given v_s . N is the total number of samples picked along a reflection arrival.

We expect maximum coherence for a PS reflection arrival corresponding to appropriate reflector in the PS section. Figure A1b-g shows the semblance plot for different layers. We, therefore, pick and analyze PS reflection arrivals corresponding to S-wave velocities that lie within the range of possible S-wave velocity values and corresponds to strong semblance values in the semblance plot.

References

Aki, K., & Richards, P. G., (1980). Quantitative Seismology, Theory and Methods. W.H. Freeman and Co., San Francisco, 557 p.

Bhatnagar, G., Chapman, W. G., Dickens, G. R., Dugan, B., & Hirasaki, G. J. (2007). Generalization of gas hydrate distribution and saturation in marine sediments by scaling of thermodynamic and transport processes. American Journal of Science, 307 (6), 861-900.

Bickel, S. (1990). Velocity-depth ambiguity of reflection traveltimes. Geophysics, 55(3), 266-276. doi:10.1190/1.1442834

Brooks, J. M., Cox, H. B., Bryant, W. R., Kennicutt, II, M. C., Mann, R. G., & McDonald, T. J. (1986). Association of gas hydrates and oil seepage in the Gulf of Mexico. Organic Geochemistry, 10, 221–234, doi: 10.1016/0146-6380(86)90025-2.

Brown, R. J., Stewart, R. R., & Lawton, D. C. (2002). A proposed polarity standard for multicomponent seismic data. Geophysics, 67, 1028-1037.

Bünz, S., Mienert, J., Vanneste, M., & Andreassen, K. (2005). Gas hydrates at the Storegga Slide; constraints from an analysis of multicomponent, wide-angle seismic data. Geophysics, 70(5), B19-B34.

Bünz, S., Polyanov, S., Vadakkepuliyambatta, S., Consolaro, C., & Mienert, J. (2012). Active gas venting through hydrate-bearing sediments on the Vestnesa Ridge, offshore W-Svalbard. Marine Geology, 332-334, 189-197. doi:https://doi.org/10.1016/j.margeo.2012.09.012

Carcione, J. M., & Tinivella, U. (2000). Bottom-simulating reflectors: seismic velocities and AVO effects. Geophysics, 65(1), 54–67.

Červený, V. (2001). Seismic ray theory. Cambridge University Press, Cambridge.

Chand, S., Minshull, T. A., Davide, G. & Carcione, J. M. (2004). Elastic velocity models for gas-hydrate-bearing sediments—A comparison. Geophys. J. Int., 159(2), 573–590.

Chand, S., Minshull, T. A., Priest, J. F., Best, A. I., Clayton, C. R. I., & Waite, W. F. (2006). An effective medium inversion algorithm for gas hydrate quantification and its application to laboratory and borehole measurements of gas hydrate-bearing sediments. Geophy J. Int., 166 (2), 543-552.

Chiţu, D., Al-Ali, M., & Verschuur, D. (2008). Assessing estimated velocity-depth models: Finding error bars in tomographic inversion. Geophysics, 73(5), VE223-VE233. doi:10.1190/1.2951469

Collett, T. S., Boswell, R., Cochran, J. R., Kumar, P., Lall, M., Mazumdar, A., et al. (2014). Geologic implications of gas hydrates in the offshore of India: Results of the National Gas Hydrate Program Expedition 01. Marine and Petroleum Geology, 58, 3-28. doi:https://doi.org/10.1016/j.marpetgeo.2014.07.021

Collett, T. S., Lee, M. W., Zyrianova, M. V., Mrozewski, S. A., Guerin, G., Cook, A. E., & Goldberg, D. S. (2012). Gulf of Mexico Gas Hydrate Joint Industry Project Leg II logging-while-drilling data acquisition and analysis. Marine and Petroleum Geology, 34(1), 41-61. doi:https://doi.org/10.1016/j.marpetgeo.2011.08.003

Collett, T. S., Riedel, M., Cochran, J. R., Boswell, R., Presley, J., Kumar, P., et al. (2006). Initial Reports, 4. Directorate General of Hydrocarbons, NOIDA and Ministry of Petroleum & Natural Gas, India.

Connolly, P. (1999). Elastic impedance. The Leading Edge, 18 (4), 438–452.

Cook, A., Anderson, B. I., Malinverno, A., Mrozewski, S. & Goldberg, D. S. (2010). Electrical anisotropy due to gas hydrate-filled fractures. Geophysics 75 (6), F173-F185.

Cook, A. E., & Waite, W. F. (2018). Archie's Saturation Exponent for Natural Gas Hydrate in Coarse-Grained Reservoirs. Journal of Geophysical Research: Solid Earth, 123(3), 2069-2089. doi:10.1002/2017jb015138

Daigle, H., & Dugan, B. (2011). Capillary controls on methane hydrate distribution and fracturing in advective systems. Geochemistry, Geophysics, Geosystems, 12(1). doi:10.1029/2010GC003392

Dash, R., & Spence, G. (2011). P-wave and S-wave velocity structure of northern Cascadia margin gas hydrates. Geophysical Journal International, 187(3), 1363-77.

Davie, M. K., & Buffett, B. A. (2001). A numerical model for the formation of gas hydrate below the seafloor. Journal of Geophysical Research: Solid Earth, 106(B1), 497-514. doi:10.1029/2000JB900363

Davie, M. K., & Buffett, B. A. (2003). A steady state model for marine hydrate formation: Constraints on methane supply from pore water sulfate profiles. Journal of Geophysical Research: Solid Earth, 108(B10). doi:doi:10.1029/2002JB002300

Delescluse, M., Nedimović, M. R., & Louden, K. E. (2011). 2D waveform tomography applied to long-streamer MCS data from the Scotian Slope. Geophysics, 76(4), B151-B163. doi:10.1190/1.3587219

Dix, C. (1955). Seismic velocities from surface measurements. Geophysics, 20(1), 68-86. doi:10.1190/1.1438126

Duffaut, K., Alsos, T., Landroe, M., & Rognoe, H. (2000). Shear-wave elastic impedance. The Leading Edge 19 (11), 1223–1229.

Dvorkin, J., & Nur, A. (1993). Rock physics for characterization of gas hydrates, in The Future of Energy Gases, edited by D. G. Howell, U. S. Geol. Surv. Prof. Pap., 1570, 293–298.

Ecker, C., Dvorkin, J., & Nur, A. (1998). Sediments with gas hydrates: internal structure from seismic AVO. Geophysics, 63, 1659–1669.

Ecker, C., Dvorkin, J., & Nur, A. (2000). Estimating the amount of gas hydrate and free gas from marine seismic data. Geophysics, 65, 565–573.

Eiken, O., & Hinz, K. (1993). Contourites in the Fram Strait. Sedimentary Geology, 82, 15–32, doi: 10.1016/0037-0738 (93)90110-Q.

Engen, Ø., Faleide, J. I., & Dyreng, T. K. (2008). Opening of the Fram Strait gateway: a review of plate tectonic constraints. Tectonophysics, 450, 51–69.

Exley, R. J. K., Westbrook, G. K., Haacke, R. R., & Peacock, S. (2010). Detection of seismic anisotropy using ocean bottom seismometers: a case study from the northern headwall of the Storegga Slide. Geophysical Journal International, 183, 188–210. doi:10.1111/j.1365-246X.2010.04730.x

Gaiser, J. E. (1999). Applications for vector coordinate systems of 3-D converted wave data. The Leading Edge, 18, 1290-1300.

Ghosh, R., K. Sain, and M. Ojha (2010). Effective medium modeling of gas hydrate-filled fractures using the sonic login the Krishna-Godavari basin, offshore eastern India. Journal of Geophysical Research, 115, B06101, doi:10.1029/2009JB006711.

Goswami, B. K., Weitemeyer, K. A., Minshull, T. A., Sinha, M. C., Westbrook, G. K., Chabert, A., Ker, S. (2015). A joint electromagnetic and seismic study of an active pockmark within the hydrate stability field at the Vestnesa Ridge, West Svalbard margin. Journal of Geophysical Research: Solid Earth, 120(10), 6797-6822. doi:doi:10.1002/2015JB012344

Hamilton, E. L. (1978). Sound velocity-density relations in sea-floor sediments and rocks. J. Acoust. Sot. Am., 634, 366-377.

Helgerud, M. B., Dvorkin, J., Nur, A., Sakai, A., & Collett, T. (1999). Effective wave velocity in marine sediments with gas hydrates: Effective medium modeling. Geophys. Res. Lett., 26, 2021–2024.

Hill, R. (1952). The elastic behavior of crystalline aggregate. Proc. Phys.Soc. London, Sect. A, 65, 349–354.

Hobro, J. W. D., Minshull, T. A., Singh, S. C., & Spence, G. D. (1997). Three dimensional seismic studies of the methane hydrate stability zone in the Cascadia margin. Eos Trans. AGU, 78(46), Fall Meet. Suppl.

Hornby, B. E., Schwartz, L. M., & Hudson, J. A. (1994). Anisotropic effective-medium modelling of the elastic properties of shales. Geophysics, 59, 1570–1581.

Howe, J. A., Shimmield, T. M., & Harland, R. (2008). Late Quaternary contourites and glaciomarine sedimentation in the Fram Strait. Sedimentology, 55, 179–200, doi: 10.1111/j.1365-3091.2007.00897.x.

Hustoft, S., Bünz, S., Mienert, J., & Chand, S. (2009). Gas hydrate reservoir and active methane-venting province in sediments on < 20 Ma young oceanic crust in the Fram Strait, offshore NW-Svalbard. Earth and Planetary Science Letters, 284(1), 12-24.

Hyndman, R. D., & Davis, E. E. (1992). A mechanism for the formation of methane hydrate and seafloor bottom simulating reflectors by vertical fluid expulsion. J. Geophys. Res. 97, 7025-7041.

Hyndman, R. D., & Spence, G. D. (1992). A seismic study of methane hydrate marine bottom simulating reflectors. J. Geophys. Res., 97, 6683-6698.

Jaiswal, P., Dewangan, P., Ramprasad, T., & Zelt, C. A. (2012). Seismic characterization of hydrates in faulted, fine-grained sediments of Krishna-Godavari Basin: Full waveform

inversion. Journal of Geophysical Research: Solid Earth, 117(B10), B10305. doi: 10.1029/2012JB009201.

Jakobsen, M., Hudson, J. A., Minshull, T. A., & Singh, S. C. (2000). Elastic properties of hydrate-bearing sediments using effective medium theory. Journal of Geophysical Research-Solid Earth, 105, 561–577.

Julian, B. R., & Gubbins D. (1977). Three-dimensional seismic ray tracing. J. Geophys., 43, 95-114.

Katzman, R., Holbrook, W. S., & Paull, C. K. (1994). Combined vertical-incidence and wide-angle seismic study of a gas hydrate zone, Blake ridge. Journal of Geophysical Research, 99, 17975–17995.

Kemtett, B. L. N., & Kerry, N. J. (1979). Seismic waves in a stratified half space. Geophys. J.R. Astron. Sot., 57, 557-583, 1979.

Kennedy, W. D., and D. C. Herrick (2004), Conductivity anisotropy in shale-free sandstone, Petrophysics, 45, 38–58.

Kennedy, W. D., D. C. Herrick, and T. Yao (2001), Calculating water saturation in electrically anisotropic media, Petrophysics, 42, 118–136.

Knies, J., Daszinnies, M., Plaza-Faverola, A., Chand, S., Sylta, Ø., Bünz, S., Johnson, J. E., Mattingsdal, R., & Mienert, J. (2018). Modelling persistent methane seepage offshore western Svalbard since early Pleistocene. Marine and Petroleum Geology. doi:https://doi.org/10.1016/j.marpetgeo.2018.01.020

Knies, J., Matthiessen, J., Vogt, C., Laberg, J. S., Hjelstuen, B. O., Smelror, M., Larsen, E., Andreassen, K., Eidvin, T., & Vorren T. O. (2009). The Plio-Pleistocene glaciation of the

Barents Sea–Svalbard region: A new model based on revised chronostratigraphy. Quat. Sci. Rev., 28(9), 812–829.

Korenaga, J., Holbrook, W. S., Singh, S. C., & Minshull, T. A. (1997). Natural gas hydrates on the southeast U.S. margin: Constraints from full waveform and travel time inversions of wide-angle seismic data. J. Geophys. Res., 102(B7), 15345–15365. doi:10.1029/97JB00725.

Kumar, D., Sen, M. K., & Bangs, N. L. (2007). Gas hydrate concentration and characteristics within Hydrate Ridge inferred from multicomponent seismic reflection data. Journal of Geophysical Research: Solid Earth, 112(B12), B12306. doi:10.1029/2007JB004993.

Kvenvolden, K. A., & Barnard, L. A. (1983). Hydrates of natural gas in continental margins. Studies in Continental Margin Geology, v. 34, p. 631-640.

Lee, M. W., Hutchinson, D. R., Collett, T. S., & Dillon, W. P. (1996). Seismic velocities for hydrate-bearing sediments using weighted equation. J. Geophys. Res., 101, B9, p 20,347–20,358.

Lee, M. W., & Collett, T.S. (2009). Gas hydrate saturations estimated from fractured reservoir at Site NGHP-01-10, Krishna-Godavari Basin, India. Journal of Geophysical Research, 114, B07102. doi:10.1029/2008JB006237.

Lee, M. W., & Collett, T. S. (2012). Pore- and fracture-filling gas hydrate reservoirs in the Gulf of Mexico Gas Hydrate Joint Industry Project Leg II Green Canyon 955 H well. Marine and Petroleum Geology, Volume 34, Issue 1, 2012, Pages 62-71, ISSN 0264-8172. http://dx.doi.org/10.1016/j.marpetgeo.2011.08.002.

Lines, L. (1993). Ambiguity in analysis of velocity and depth. Geophysics, 58(4), 596-597. doi:10.1190/1.1443443

Liu, X., & Flemings, P. B. (2007). Dynamic multiphase flow model of hydrate formation in marine sediments. Journal of Geophysical Research: Solid Earth, 112(B3). doi:10.1029/2005JB004227

Liu, X., & Flemings, P. B. (2011). Capillary effects on hydrate stability in marine sediments. Journal of Geophysical Research: Solid Earth, 116(B7). doi:10.1029/2010JB008143

Lu, S., & McMechan, G. A. (2002). Estimation of gas hydrate and free gas saturation, concentration, and distribution from seismic data. Geophysics, 67, 582–593.

Marín-Moreno, H., Sahoo, S. K., & Best, A. I. (2017). Theoretical modeling insights into elastic wave attenuation mechanisms in marine sediments with pore-filling methane hydrate. J. Geophys. Res. Solid Earth, 122, 1835–1847. doi:10.1002/2016JB013577.

McKenzie, D. A. N., & O'Nions, R. K. (1991). Partial Melt Distributions from Inversion of Rare Earth Element Concentrations. Journal of Petrology, 32(5), 1021-1091. doi:10.1093/petrology/32.5.1021

Minshull, T. A., & Chand, S. (2009). The pore-scale distribution of sediment-hosted hydrates: evidence from effective medium modelling of laboratory and borehole seismic data. Geological Society, London, Special Publications 319:93-101.

Minshull, T.A., & Singh, S. C. (1993). Shallow structure of oceanic crust in the western North Atlantic from seismic waveform. J. Geophys. Res., 98(B2), 1777–1792. doi:10.1029/92JB02136.

Minshull, T. A., Singh, S. C., & Westbrook G. K. (1994). Seismic velocity structure at a gas hydrate reflector, offshore western Colombia from full waveform inversion, J. Geophys. Res., 99, 4715-4734.

Minshull, T., & White, R. (1989). Sediment Compaction and Fluid Migration in the Makran Accretionary Prism. J. geophys. Res, v. 94, p. 7387–7402.

Nakanishi, N., & Yamaguchi K. (1986). A numerical experiment on nonlinear image reconstruction from first-arrival times for two-dimensional island arc structure. J. Phys. Earth, 34 (1986), pp. 195-201.

Nishizawa, O. (1982). Seismic velocity anisotropy in a medium containing oriented cracks: transversely isotropic case. Jour. Phys. Earth, 30, 331–347.

Nole, M., Daigle, H., Cook, A. E., Malinverno, A., & Flemings, P. B. (2018). Burial-driven methane recycling in marine gas hydrate systems. Earth and Planetary Science Letters, 499, 197-204. doi:https://doi.org/10.1016/j.epsl.2018.07.036

Ottesen, D., Dowdeswell, J. A., & Rise, L. (2005). Submarine landforms and the reconstruction of fast-flowing ice streams within a large Quaternary ice sheet: The 2500-km-long Norwegian-Svalbard margin (57-80N). Geological Society of America Bulletin, 117(7-8), 1033-1050.

Panieri, G., Bünz, S., Fornari, D. J., Escartin J., Serov, P., Jansson, P., et al. (2017). An integrated view of the methane system in the pockmarks at Vestnesa Ridge, 79°N. Marine Geology, 390, 282-300.

Pecher, I. A., Minshull, T. A., Singh, S. C., & Huene R. V. (1996). Velocity structure of a bottom simulating reflector offshore Peru: Results from full waveform inversion. Earth and Planetary Science Letters, 139(3), 459-69.

Petersen, C. J., Bunz, S., Huston, S., Mienert, J., Klaeschen, D. (2010). High-resolution P-Cable 3D seismic imaging of gas chimney structures in gas hydrated sediments of an Arctic sediment drift. Mar Pet Geol., 27(9), 1981-94.

Planke, S., Eriksen, F. N., Berndt, C., Mienert, J., & Masson, D. (2009). Spotlight on technology: P-cable high-resolution seismic. Oceanography, 22, 85. doi: 10.5670/oceanog.2009.09.

Plaza-Faverola, A., Bünz, S., Johnson, J. E., Chand, S., Knies, J., Mienert, J., et al. (2015). Role of tectonic stress in seepage evolution along the gas hydrate-charged Vestnesa Ridge, Fram Strait. Geophysical Research Letters, 42(3), 733-42.

Plaza-Faverola, A., Bünz, S., & Mienert, J. (2010). Fluid distributions inferred from P-wave velocity and reflection seismic amplitude anomalies beneath the Nyegga pockmark field of the mid-Norwegian margin. Marine and Petroleum Geology, 27(1), 46-60. doi:https://doi.org/10.1016/j.marpetgeo.2009.07.007

Posewang, J., & Mienert, J. (1999). The enigma of double BSRs: Indicators for changes in the hydrate stability field. Geo Mar. Lett., 19, 157–163.

Qin, F., Luo, Y., Olsen, K., Cai, W., & Schuster, G. (1992). Finite-difference solution of the eikonal equation along expanding wavefronts. Geophysics, 57(3), 478-487. doi:10.1190/1.1443263

Rawlinson, N., Hauser, J., & Sambridge, M. (2008). Seismic ray tracing and wavefront tracking in laterally heterogeneous media. In R. Dmowska (Ed.), Advances in Geophysics (Vol. 49, pp. 203-273): Elsevier.

Rawlinson, N., & Sambridge, M. (2004). Wave front evolution in strongly heterogeneous layered media using the fast marching method. Geophysical Journal International, 156(3), 631-647. doi:10.1111/j.1365-246X.2004.02153.x

Rempel, A. W. (2011). A model for the diffusive growth of hydrate saturation anomalies in layered sediments. Journal of Geophysical Research, 116, B10105. https://doi.org/10.1029/2011JB008484

Rempel, A. W., & Buffett, B. A. (1997). Formation and accumulation of gas hydrate in porous media. Journal of Geophysical Research: Solid Earth, 102(B5), 10151-10164. doi:doi:10.1029/97JB00392

Richardson, M. D., Muzi, E., Miaschi, B., & Turgutcan, F. (1991). Shear wave velocity gradients in near-surface marine sediments. In J. M. Hovem, M. Richardson, & R. D. Stoll (Eds.), Shear Waves in Marine Sediments (pp. 295-304), Kluwer Academic Publishers.

Ritzmann, O., Jokat, W., Czuba, W., Guterch, A., Mjelde, R., & Nishimura, Y. (2004). A deep seismic transect from Hovgård Ridge to northwestern Svalbard across the continental-ocean transition: A sheared margin study. Geophysical Journal International, 157, 683–702. doi: 10.1111/j.1365-246X.2004.02204.x.

Sahoo, S. K., Marín-Moreno, H., North, L. J., Falcon-Suarez, I., Madhusudhan, B. N., Best, A. I., & Minshull, T. A. (2018). Presence and Consequences of Coexisting Methane Gas With Hydrate Under Two Phase Water-Hydrate Stability Conditions. Journal of Geophysical Research: Solid Earth, 123(5), 3377-3390. doi:10.1029/2018JB015598

Satyavani, N., Sain, K., & Gupta, H. (2016). Ocean bottom seismometer data modeling to infer gas hydrate saturation in Krishna-Godavari (KG) basin. Journal of Natural Gas Science and Engineering, 33, 908-917.

Sheng, P. (1990). Effective-medium theory of sedimentary rocks. Physics Reviews B, 41, 4507–4512.

Sheriff, R. E., & Geldart, L. P. (1982). Exploration Seismology. Vol. I, 106 pp., Cambridge Univ. Press, Cambridge.

Shinohara M., Hirata, N., & Takahashi, N. (1994). High resolution velocity analysis of ocean bottom seismometer data by the τ-p method: Mar. Geophys. Res., 16, pp. 185-199.

Shipley, T. H., Houston, M. H., Buffler, R. T., Shaub, F. J., McMillen, K. J., Ladd, J. W., & Worzel, J. L. (1979). Seismic evidence for widespread possible gas hydrate horizons on Continental slopes and rises. AAPG Bulletin, 63, 2204–2213.

Singh, S.C., Minshull, T.A., & Spence, G.D. (1993). Velocity structure of a gas hydrate reflector. Science, 260, 204-207.

Singhroha, S., Bünz, S., Plaza-Faverola, A., & Chand, S. (2016). Gas hydrate and free gas detection using seismic quality factor estimates from high-resolution P-cable 3D seismic data. Interpretation (Tulsa), 1, SA39-SA54.

Sloan, E. D., Jr. (1998). Clathrate hydrates of natural gases, 2nd ed.: Marcel Dekker Inc.

Smith, A. J., Mienert, J., Bünz, S., & Greinert, J. (2014). Thermogenic methane injection via bubble transport into the upper Arctic Ocean from the hydrate-charged Vestnesa Ridge, Svalbard. Geochem. Geophys. Geosyst., 15, 1945–1959. doi:10.1002/2013GC005179.

Song, J. L., & ten Brink, U. (2004). RayGUI 2.0 - A Graphical User Interface for Interactive Forward and Inversion Ray-Tracing, U.S. Geological Survey Open-File Report 2004-1426.

Song, S., Tinivella, U., Giustiniani, M., Singhroha, S., Bünz, S., & Cassiani, G. (2018). OBS Data Analysis to Quantify Gas Hydrate and Free Gas in the South Shetland Margin (Antarctica). Energies, 11, 3290. doi: 10.3390/en11123290

Spence, G. D., Minshull, T. A., & Fink, C. (1995). Seismic studies of methane gas hydrate, offshore Vancouver Island, Proc. Ocean Drill. Program, Sci. Results 146 (part 1), 163-174.

Stoll, R. D., Ewing, J. I., & Bryan, G. M. (1971). Anomalous wave velocities in sediments containing gas hydrates. J. Geophys. Res., 76, 2090–2094.

Stranne, C., O'Regan, M., & Jakobsson, M. (2017). Modeling fracture propagation and seafloor gas release during seafloor warming-induced hydrate dissociation. Geophysical Research Letters, 44(16), 8510-8519. doi:10.1002/2017GL074349

Thomsen, L. (1986). Weak elastic anisotropy. Geophysics, 51(10), 1954-1966. doi:10.1190/1.1442051

Thomsen, L. (1999). Converted-wave reflection seismology over inhomogeneous, anisotropic media. Geophysics, 64(3), 678-690. doi:10.1190/1.1444577

Tréhu A. M., Long, P. E., Torres, M. E., Bohrmann, G., Rack, F. R., Collett, T. S., et al. (2004). Three-dimensional distribution of gas hydrate beneath southern Hydrate Ridge: constraints from ODP Leg 204. Earth and Planetary Science Letters, v. 222, p. 845–862.

Vidale, J. (1988). Finite-difference calculation of travel times. Bulletin of the Seismological Society of America, 78(6), 2062-2076.

Virieux, J., & Farra, V. (1991). Ray tracing in 3-D complex isotropic media: An analysis of the problem. Geophysics, 56(12), 2057-2069. doi:10.1190/1.1443018

Vogt, P. R., Crane, K., Sundvor, E., Max, M. D., & Pfirman, S. L. (1994). Methane-generated (?) pockmarks on young, thickly sedimented oceanic crust in the Arctic: Vestnesa Ridge, Fram Strait. Geology, 22, 255–258.

Wang, Y., & Houseman, G. A. (1995). Tomographic inversion of reflection seismic amplitude data for velocity variation. Geophysical Journal International, 123(2), 355-372. doi:10.1111/j.1365-246X.1995.tb06859.x

Wang, J., Jaiswal, P., Haines, S. S., Hart, P. E., & Wu, S. (2018). Gas hydrate quantification using full-waveform inversion of sparse ocean-bottom seismic data: A case study from Green Canyon Block 955, Gulf of Mexico. Geophysics, 83(4), B167-B181. doi:10.1190/geo2017-0414.1

Weitemeyer, K. A., Constable, S., & Tréhu, A. M. (2011). A marine electromagnetic survey to detect gas hydrate at Hydrate Ridge, Oregon. Geophysical Journal International, 187, 45–62. doi:10.1111/j.1365-246X.2011.05105.x

Westbrook G. K., Carson, B., Musgrave, R. J., et al. (1994). Proceedings of the Ocean Drilling Program, Initial Reports, v. 146 (Pt. 1).

Westbrook, G. K., Chand, S., Rossi, G., Long, C., Bünz, S., Camerlenghi, A., et al. (2008). Estimation of gas hydrate concentration from multi-component seismic data at sites on the continental margins of NW Svalbard and the Storegga region of Norway. Marine and Petroleum Geology, 25(8), 744-58.

Willis, J. R. (1977). Bounds and self-consistent estimates for the overall properties of anisotropic composites. Journal of the Mechanics and Physics of Solids, 25, 185–202.

Wood, A. B. (1941). A Textbook of Sound. Macmillan, New York.

Wyllie, M. R., Gregory, A. R., & Gardner, G. H. P. (1958). An experimental investigations of factors affecting elastic wave velocities in porous media. Geophysics, 23, 459-493.

Xia, G., Sen, M. K., & Stoffa, P. L. (1998). 1-D elastic waveform inversion: A divide-and-conquer approach. Geophysics, 63, 1670–1684.

Xu, W., & Ruppel, C. (1999). Predicting the occurrence, distribution, and evolution of methane gas hydrate in porous marine sediments. Journal of Geophysical Research: Solid Earth, 104(B3), 5081-5095. doi:10.1029/1998JB900092

Yilmaz, Ö. (2001). Seismic Data Analysis: Society of Exploration Geophysicists.

Yuan, T., Hyndman, R. D., Spence G. D., & Desmons B. (1996). Seismic velocity increase and deep-sea gas hydrate concentration above a bottom simulating reflector on the northern Cascadia continental slope. J. Geophys. Res., 101, 13,655–13,671.

Zelt, C.A., & Smith, R.B. (1992). Seismic travel-time inversion for 2-D crustal velocity structure. Geophys. J. Int., 108, 16-34.

Zillmer M., Flueh, E. R., & Petersen J. (2005). Seismic investigation of a bottom simulating reflector and quantification of gas hydrate in the Black Sea. Geophysical Journal International, Volume 161, Issue 3, Pages 662–678, doi: j.1365-246X.2005.02635.x

Tables and Figures

OBS station number	Year of data acquisition	Sampling rate (ms)	Shot lines	Acquisition gun
OBS1	2012	0.5	Inline and crossline	GI gun
OBS2	2016	1.0	3-D seismic	GI gun
OBS3	2015	1.0	3-D seismic	Mini GI gun
OBS4	2016	0.4	3-D seismic	GI gun
OBS5	2015	0.4	3-D seismic	Mini GI gun
OBS6	2015	1.0	3-D seismic	Mini GI gun
OBS7	2012	1.0	Inline and crossline	GI gun
OBS8	2012	0.4	Inline and crossline	GI gun
OBS9	2012	0.4	Inline and crossline	GI gun
OBS10	2017	0.4	Inline and crossline along with 3-D seismic	Mini GI gun

Table 1. Acquisition details for OBS dataset

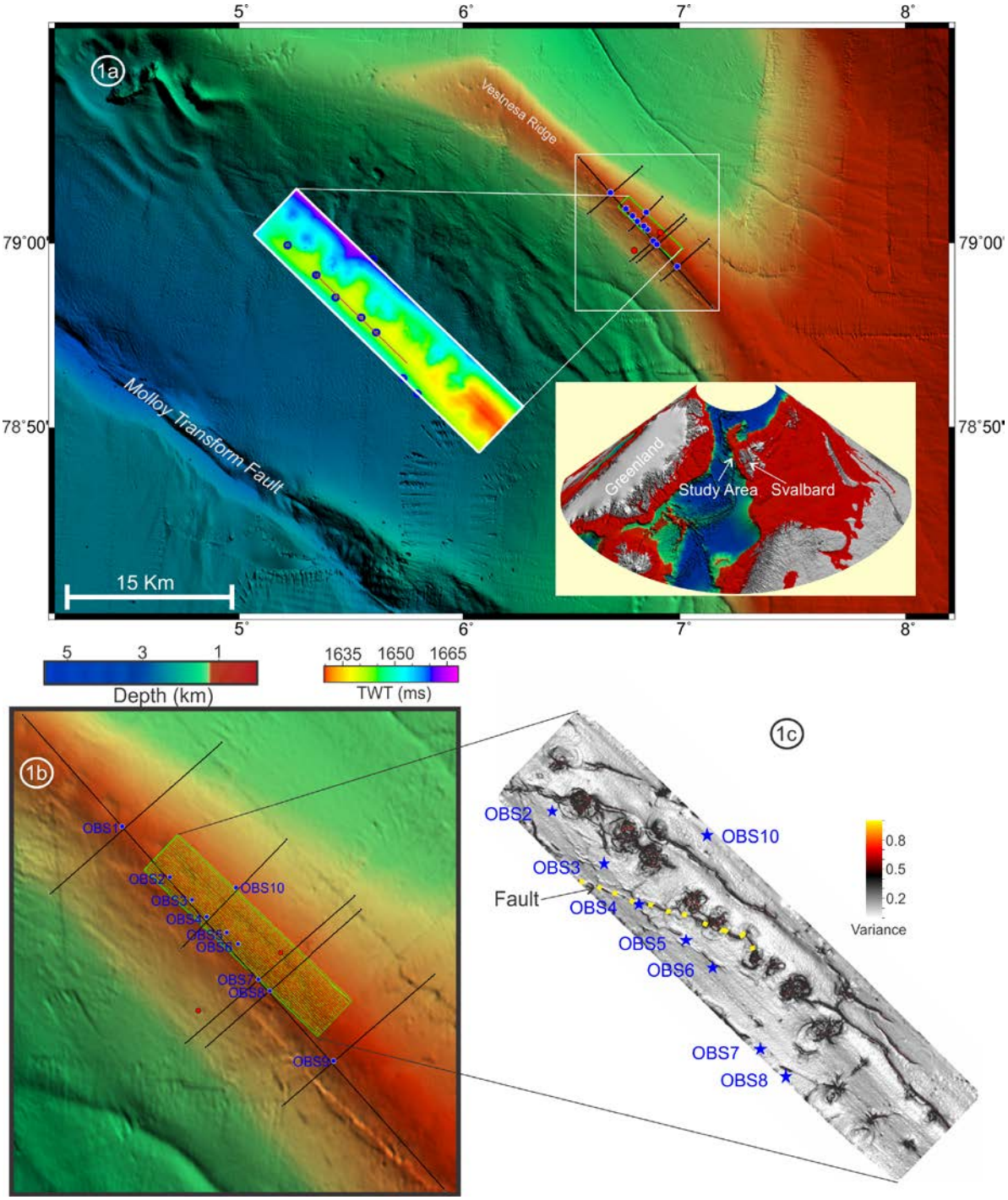

Figure 1. a) Bathymetry map of the study area. Inset figures show the location of the study area and two-way travel time plot for the seafloor. b) Location of different OBS stations. Black lines are shoot lines used to record OBS data. Green lines show shot lines from 3D seismic cube. Red dots show the location of OBS stations from Goswami et al. (2015). c) Location of different OBS stations plotted on variance map illustrating faults (modified from Plaza-Faverola et al. (2015)).

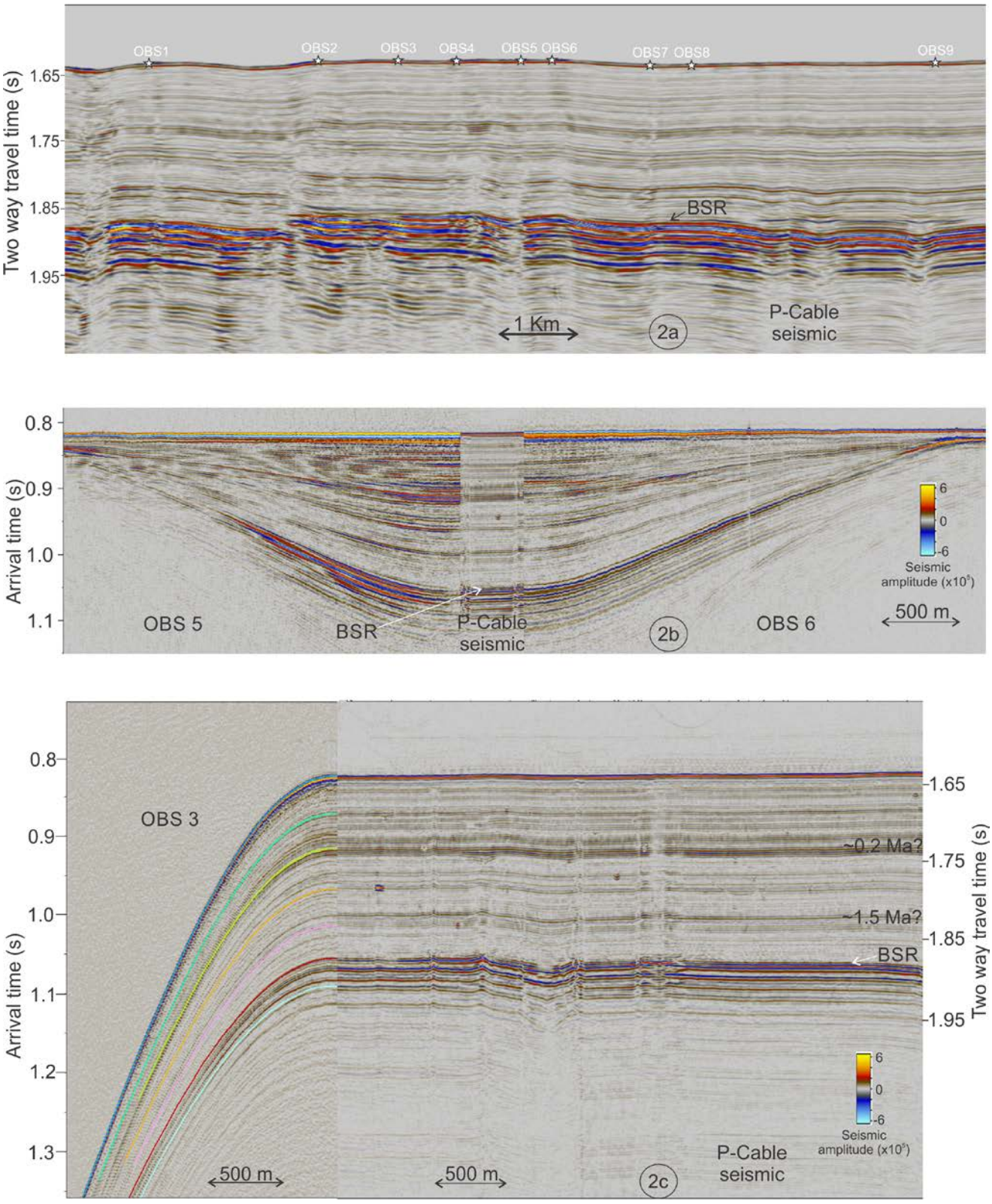

Figure 2. a) 2-D P-Cable seismic data profile passing through 9 OBS stations. b) Offset corrected OBS5 and OBS6 data placed along with P-Cable data. c) OBS3 data along with picked arrivals placed along with P-Cable seismic data.

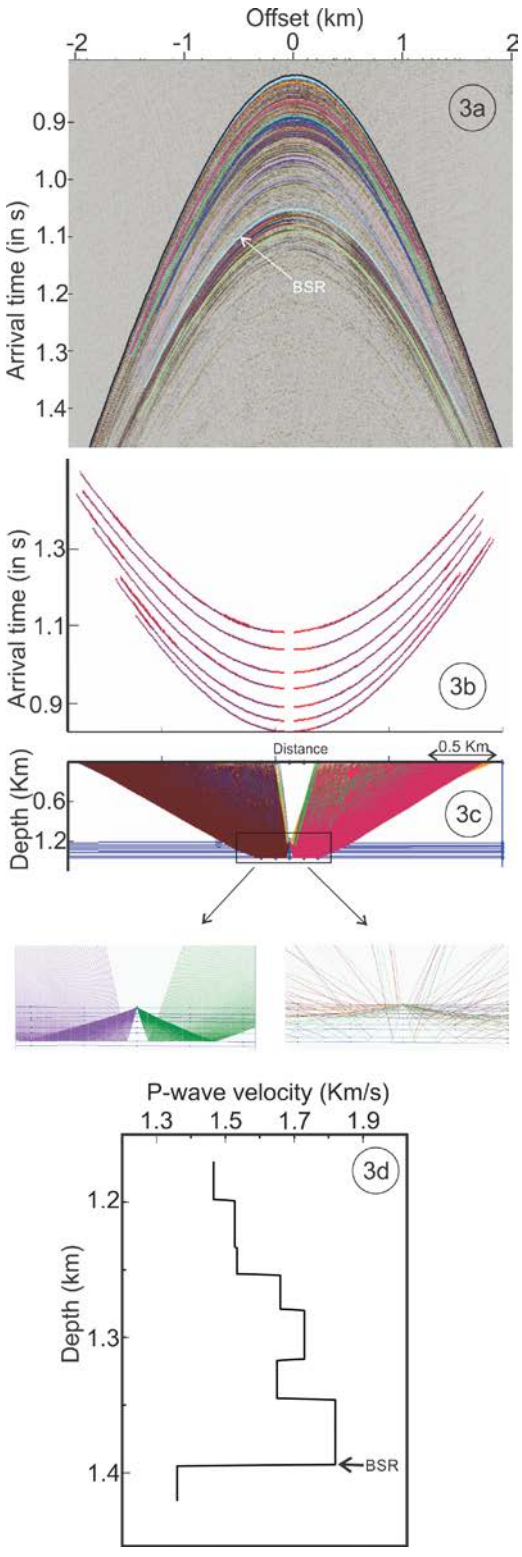

Figure 3. a) P-wave data recorded by hydrophone at site OBS5. Different picked reflection arrivals are shown in different colors. b) Picked reflection arrivals and travel times corresponding to best fit seismic velocity model. c) Ray-paths corresponding to best fit velocity model. d) Best fit inverted P-wave velocity model

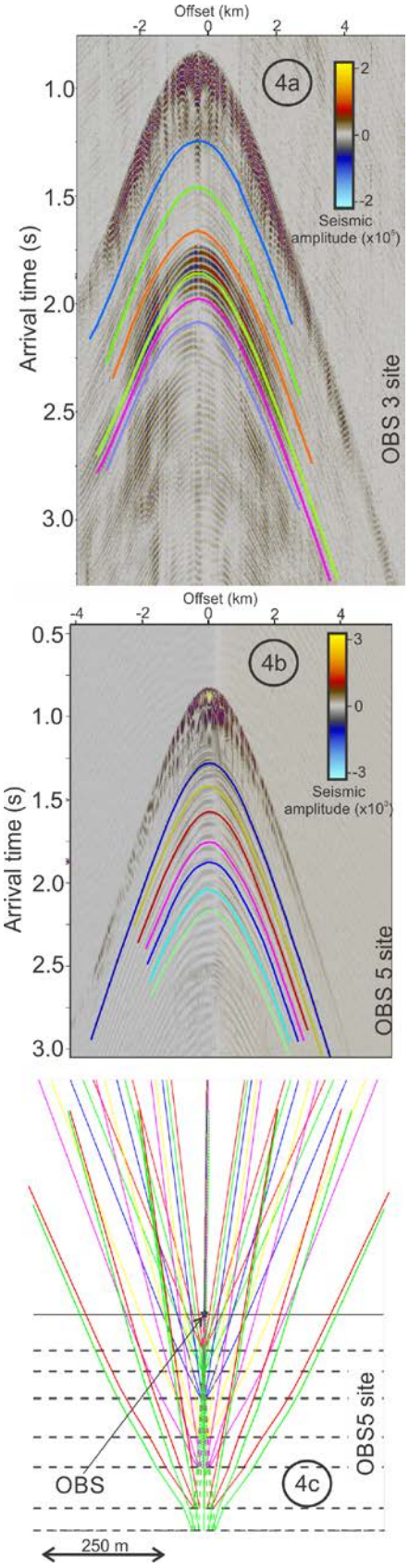

Figure 4. a-b) PS records at sites OBS3 and OBS5 along with picked PS reflection arrivals. c) Ray-paths for S-waves in the inverted model at site OBS5.

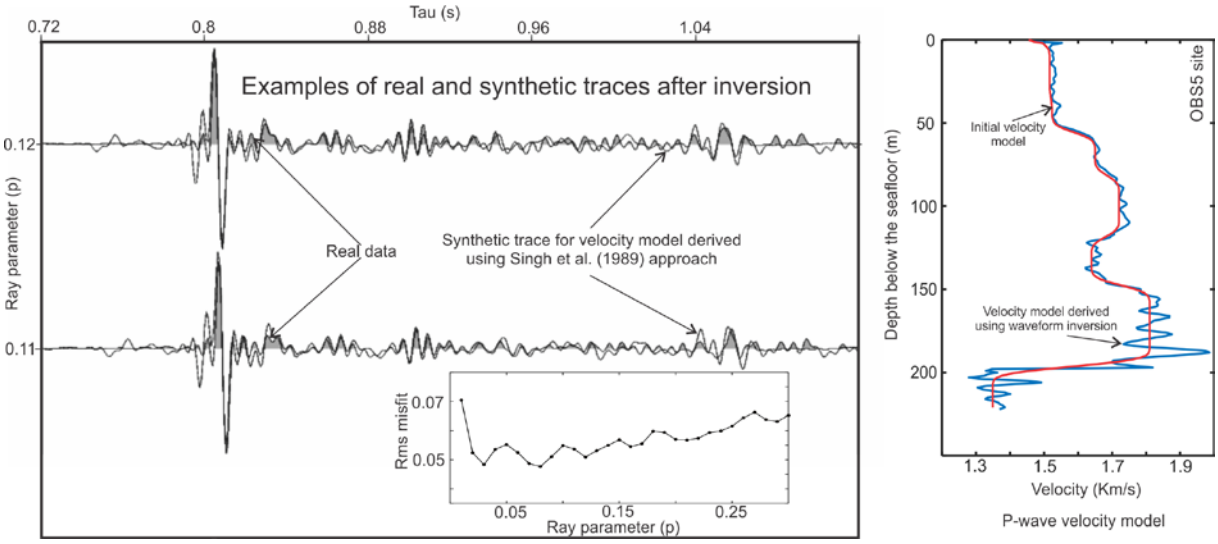

Figure 5. FWI derived P-wave velocity model at station OBS5. Two sample traces (p=0.11 and 0.12) have been shown that shows the match between real and synthetic data derived from inverted velocity model. Inset figure shows the variation of RMS misfit with ray parameter (p).

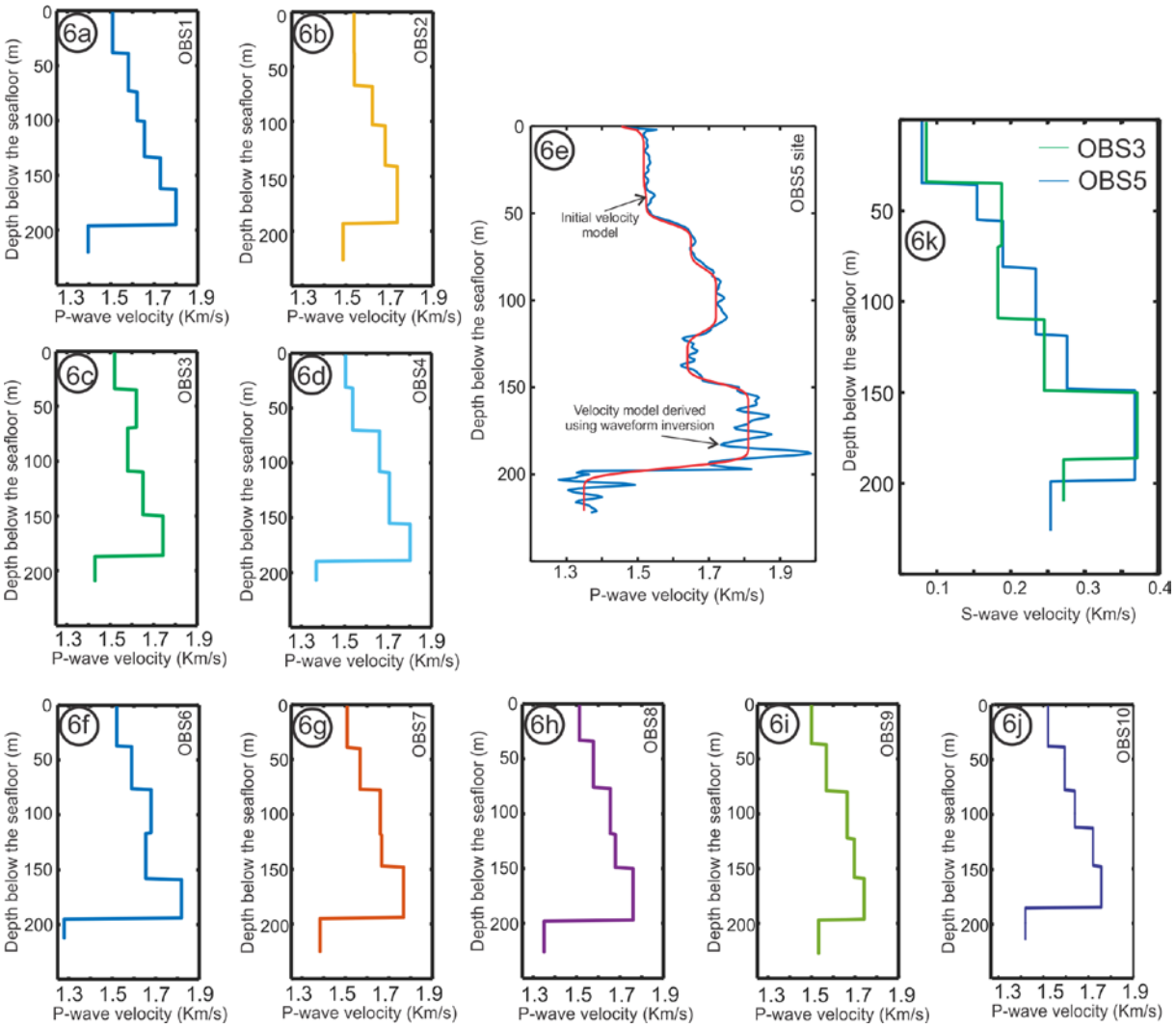

Figure 6. P and S-wave velocity estimates using travel time inversion at different OBS sites. Blue curve in figure 6e shows the velocity model derived using 1-D FWI approach.

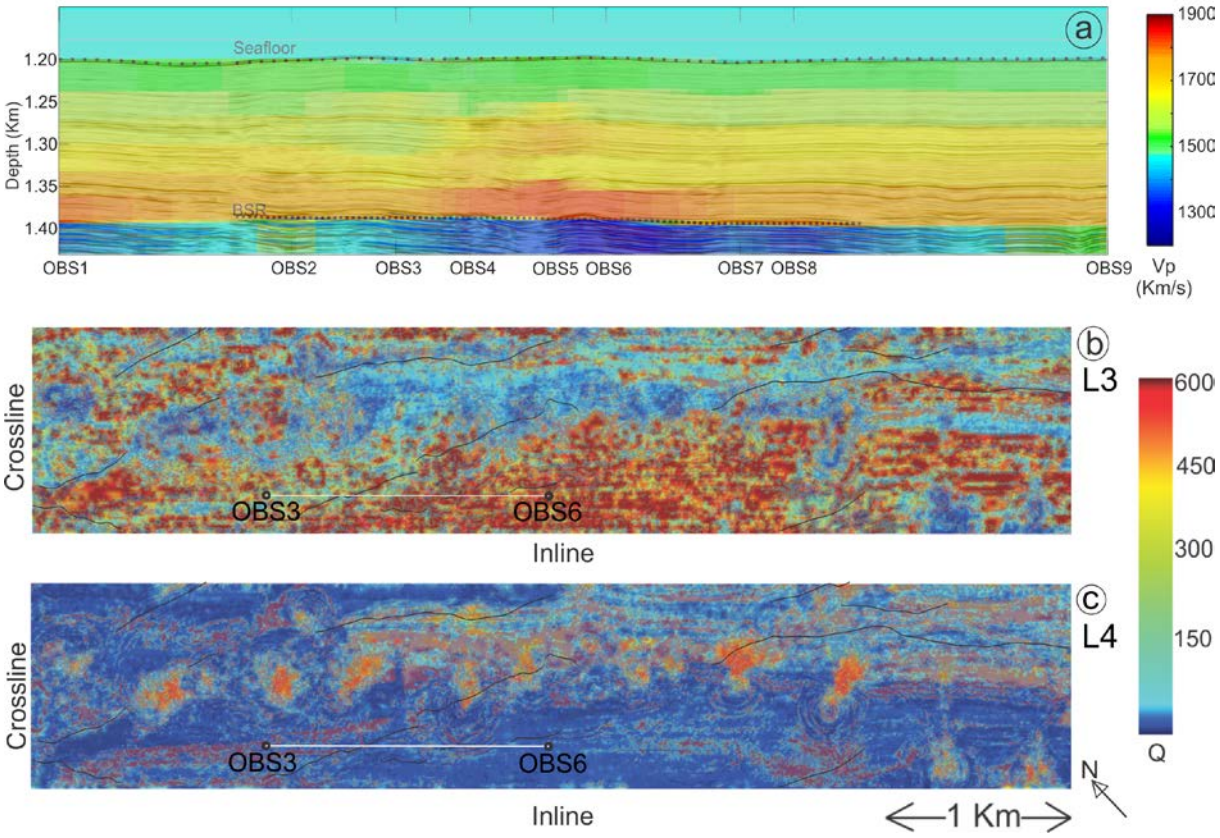

Figure 7. a) overlay of P-Cable seismic data and interpolated P-wave velocity model. Seismic Q map (modified from Singhroha et al., 2016) in a layer above the BSR (b) and below the BSR (c). White line shows the transect from OBS3 to OBS6.

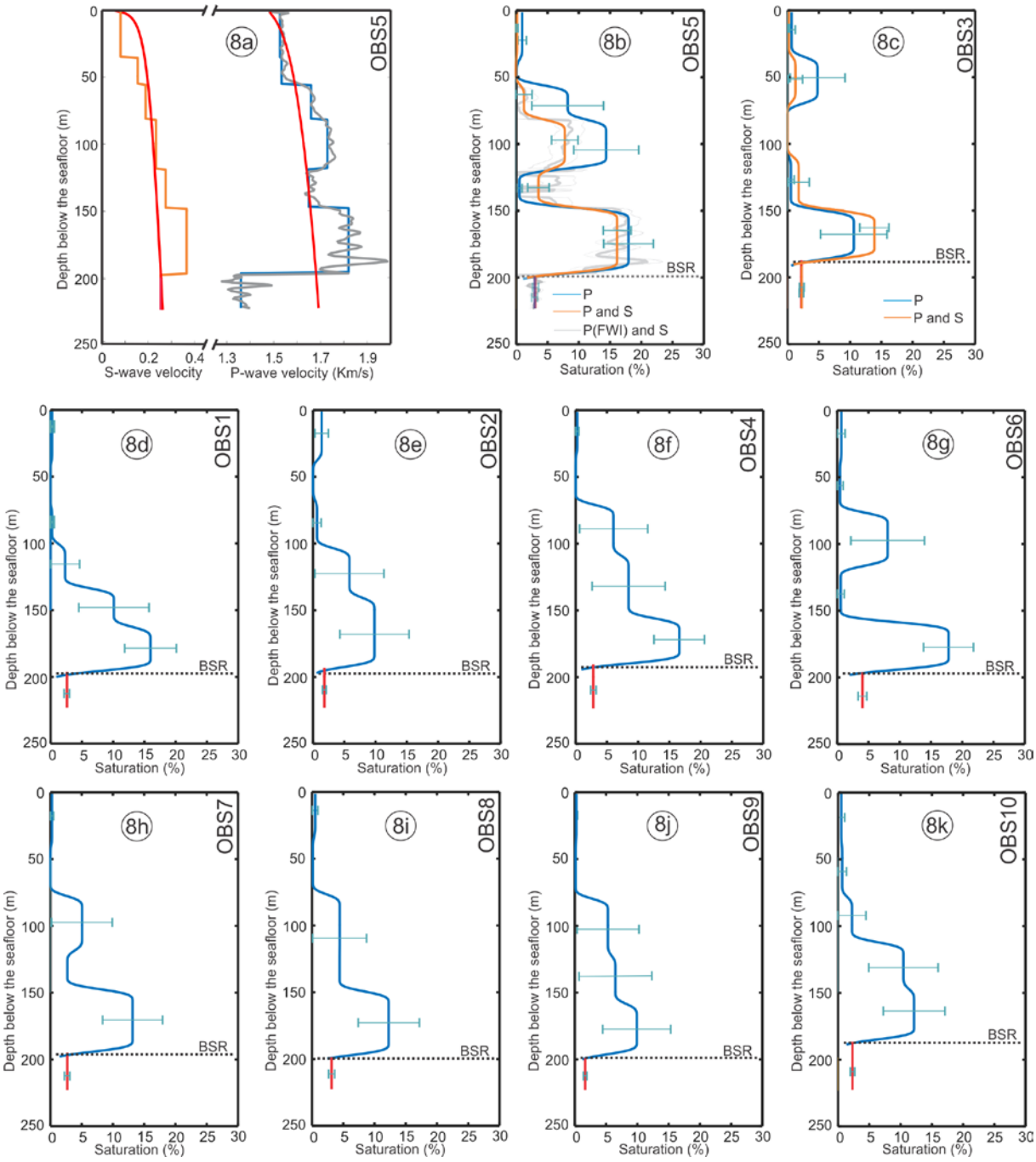

Figure 8. a) Travel time inversion derived (shown in blue) and FWI derived (shown in gray) P-wave and S-wave velocity model at site OBS5 plotted along with background velocity model (shown in red) derived using the SCA/DEM approach. b) Saturation estimated using different possible combination of velocity models at site OBS5. c-k) Saturation estimates at different OBS locations using P-wave velocity model.

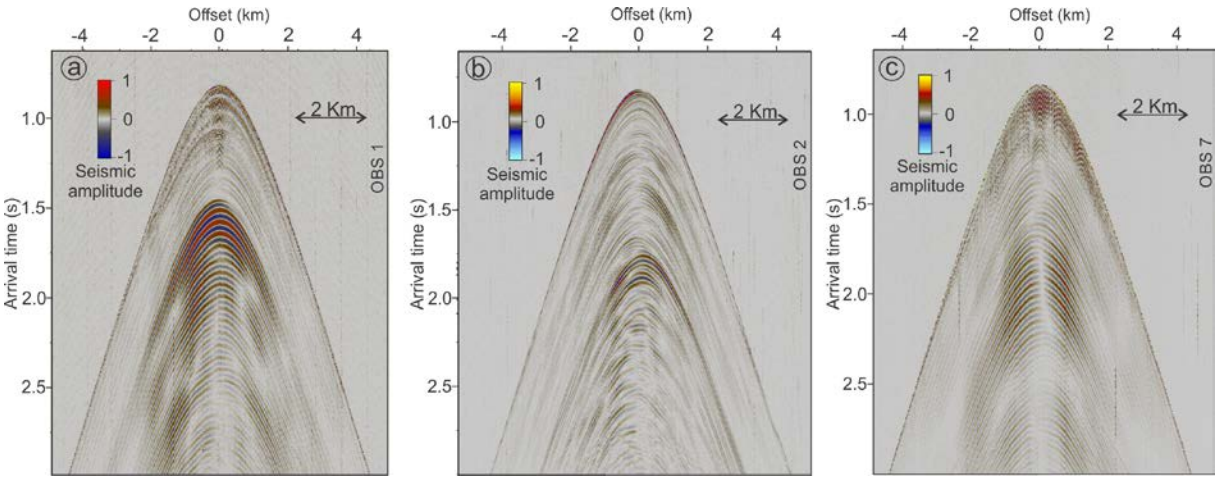

Figure 9. PS data recorded at different OBS stations.

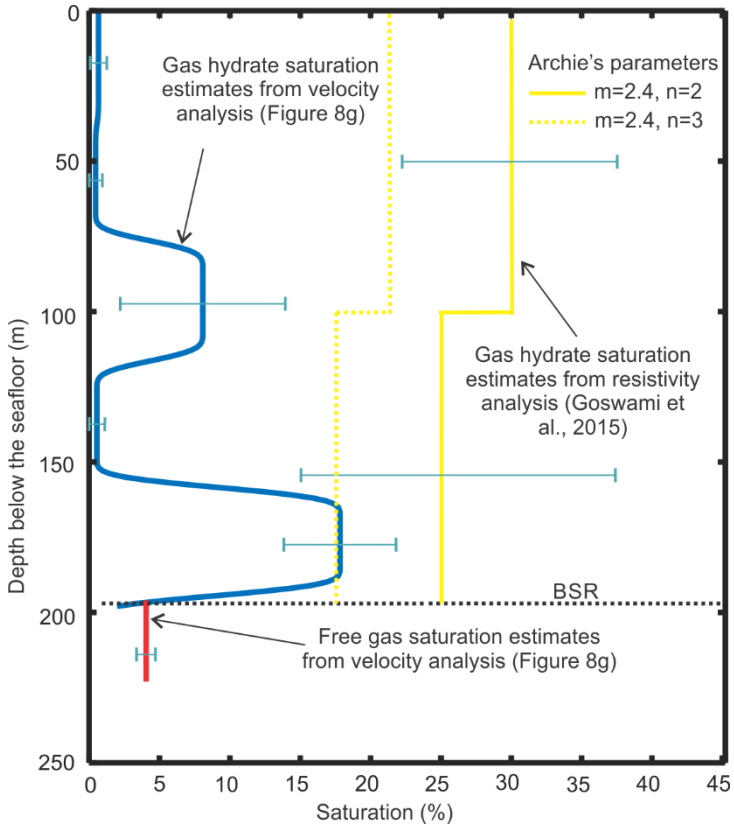

Figure 10. Gas hydrate saturation estimates from velocity analysis of OBS6 and resistivity analysis of CSEM data (Goswami et al., 2015). Yellow line and yellow dashed line show the variation of gas hydrate saturation profile with variation in Archie's parameter *n* (saturation exponent).

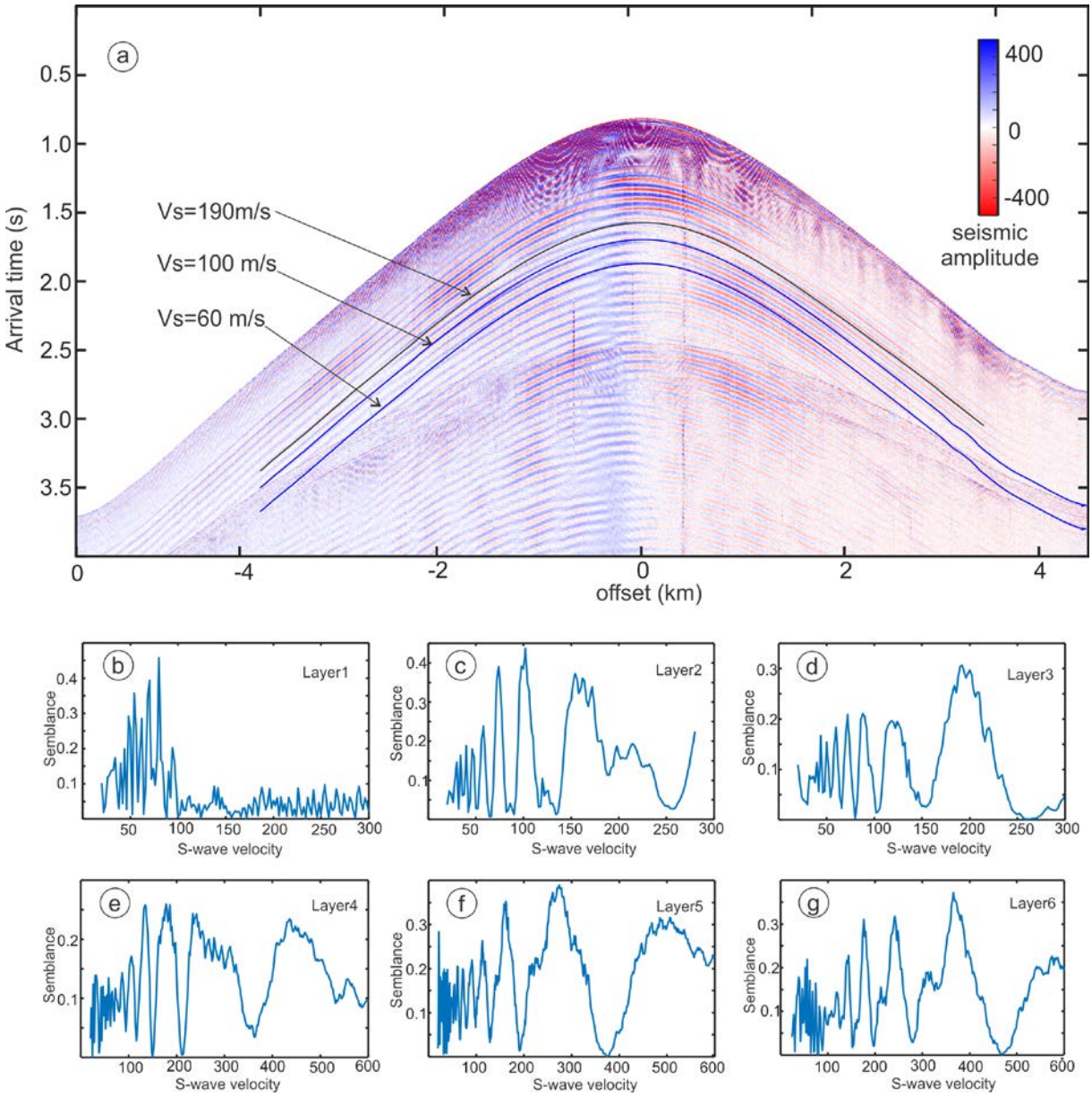

Figure A1. a) S-wave data recorded at site OBS5. Three travel curves show curvature for different possible S-wave interval velocities in the Layer 3. b-g) Semblance plot for different S-wave interval velocities.

List of tables and figures

Table 1. Acquisition details for OBS dataset

Figure 1. a) Bathymetry map of the study area. Inset figures show the location of the study area and two-way travel time plot for the seafloor. b) Location of different OBS stations. Black lines are shoot lines used to record OBS data. Green lines show shot lines from 3D seismic cube. Red dots show the location of OBS stations from Goswami et al. (2015). c) Location of different OBS stations plotted on variance map illustrating faults (modified from Plaza-Faverola et al. (2015)).

Figure 2. a) 2-D P-Cable seismic data profile passing through 9 OBS stations. b) Offset corrected OBS5 and OBS6 data placed along with P-Cable data. c) OBS3 data along with picked arrivals placed along with P-Cable seismic data.

Figure 3. a) P-wave data recorded by hydrophone at site OBS5. Different picked reflection arrivals are shown in different colors. b) Picked reflection arrivals and travel times corresponding to best fit seismic velocity model. c) Ray-paths corresponding to best fit velocity model. d) Best fit inverted P-wave velocity model

Figure 4. a-b) PS records at sites OBS3 and OBS5 along with picked PS reflection arrivals. c) Ray-paths for S-waves in the inverted model at site OBS5.

Figure 5. FWI derived P-wave velocity model at station OBS5. Two sample traces (p=0.11 and 0.12) have been shown that shows the match between real and synthetic data derived from inverted velocity model. Inset figure shows the variation of RMS misfit with ray parameter (p).

Figure 6. P and S-wave velocity estimates using travel time inversion at different OBS sites. Blue curve in figure 6e shows the velocity model derived using 1-D FWI approach.

Figure 7. a) overlay of P-Cable seismic data and interpolated P-wave velocity model. Seismic Q map (modified from Singhroha et al., 2016) in a layer above the BSR (b) and below the BSR (c). White line shows the transect from OBS3 to OBS6.

Figure 8. a) Travel time inversion derived (shown in blue) and FWI derived (shown in gray) P-wave and S-wave velocity model at site OBS5 plotted along with background velocity model (shown in red) derived using the SCA/DEM approach. b) Saturation estimated using different possible combination of velocity models at site OBS5. c-k) Saturation estimates at different OBS locations using P-wave velocity model.

Figure 9. PS data recorded at different OBS stations.

Figure 10. Gas hydrate saturation estimates from velocity analysis of OBS6 and resistivity analysis of CSEM data (Goswami et al., 2015). Yellow line and yellow dashed line show the variation of gas hydrate saturation profile with variation in Archie's parameter *n* (saturation exponent).

Figure A1. a) S-wave data recorded at site OBS5. Three travel curves show curvature for different possible S-wave interval velocities in the Layer 3. b-g) Semblance plot for different S-wave interval velocities.

Article III

Singhroha, S., Bünz, S., Plaza-Faverola, A., & Chand, S. Structural control on the distribution of gas hydrates in the Vestnesa Ridge. Submitted to the Journal of Geophysical Research – Solid Earth.

Structural control on the distribution of gas hydrates in the Vestnesa Ridge

Sunny Singhroha[1], Stefan Bünz[1], Andreia Plaza-Faverola[1], Shyam Chand[2,1]

[1]CAGE — Centre for Arctic Gas Hydrate, Environment and Climate, Department of Geology, UiT The Arctic University of Norway, Tromsø, Norway.

[2]Geological Survey of Norway (NGU), Trondheim, Norway

Abstract

Previous studies show the presence of gas hydrates at shallow depths (up to ~190-195 m below the seafloor) in marine sediments of the Vestnesa Ridge. Temperature and pressure conditions, availability of gases (methane, ethane, propane, CO_2, etc.), salt and pore water affect the formation of gas hydrates. Structural and stratigraphic settings control these factors and thus affect the gas hydrate distribution and morphology. We perform azimuthal seismic velocity analysis using multicomponent ocean-bottom seismic (OBS) data at two sites near the Vestnesa Ridge crest to further study and delineate the gas hydrate distribution and morphology. We study azimuthal seismic velocity anomalies in relation with structural features to understand their impact on the Vestnesa Ridge gas hydrate system. This analysis documents lateral changes in seismic velocities at a small-scale (~10-200 m) along and across faults. Seismic velocity analysis show elevated and reduced seismic velocities in faults in the gas hydrate stability zone (GHSZ) and below the base of the GHSZ, respectively. The association of azimuthal seismic velocity anomalies with faults is stronger at depths close to the bottom-simulating reflector (BSR). This analysis indicate gas hydrate and free gas filled faults above and below the BSR, respectively and changes in the azimuthal seismic velocity across faults suggest spatial changes in the gas hydrate saturation due to faults. These results in relation with the geological setting in the Vestnesa Ridge suggest the presence of advection dominated gas hydrate deposits in faults and the effect of structural features in diffusion dominated settings. This approach demonstrates the potential usage of azimuthal seismic velocity analysis for the study of gas hydrate distribution and morphology in gas hydrate systems.

1. Introduction

Structural and stratigraphic features play a huge role in controlling dynamic fluid flow processes occurring in the subsurface (Bjørlykke, 2015; Spencer, 2012). Low-density fluids, like hydrocarbon gases, have a tendency to move upwards from deeper to shallower depths due to pressure differences unless some impermeable stratum or structural feature traps them. These fluid flow processes can result in seepage of hydrocarbon gases from the seafloor (Bünz et al., 2012) and can also lead to shallow gas accumulations (Vadakkepuliyambatta, 2014). In petroliferous basins, the distribution of fluids depends on fluid migration pathways within a basin and thus these pathways are very important to study (Ligtenberg, 2005; Davies & Handshy, 2003; Caine et al., 1996). Different structural features like the presence of faults, fractures and structural traps determine migration pathways and accumulation zones for fluids (Plaza-Faverola et al., 2015; Vadakkepuliyambatta et al., 2013; Suess et al., 2013; Trehu et al., 2004b).

Faults play a huge role in the fluid migration as these can be sealing or can also act as conduits depending on the material present within a fault plane and the regional stress regime to which they are subjected (e.g., Davies & Handshy, 2003; Ligtenberg, 2005; Caine et al., 1996; Sibson 1994). Hydrocarbons form at different depths depending on the process leading to their formation. Hydrocarbons formed from thermal degradation of organic matter or by abiotic processes generally have deeper origins compared to hydrocarbons formed by microbial degradation of organic matter (Schoell, 1988; Etiope & Lollar, 2013). Hydrocarbon gases migrate from deeper to shallower depths through permeable pathways and in some cases, these migrated gases along with in-situ produced biogenic gases get locked in shallow marine sediments in the form of gas hydrates (Kvenvolden et al., 1993).

Gas hydrates form under low temperature and high-pressure conditions, and have gases trapped inside water molecules in a crystalline structure (Sloan, 1998). Gas hydrates occur

widely in continental margins primarily (99%) as methane hydrates (Ruppel & Kessler, 2017). Gas hydrates are stable only up to a certain depth below the seafloor, as the temperature is too high to be compensated by the pressure after this depth. A bottom-simulating reflection (BSR) often occurs at the base of the gas hydrate stability zone (GHSZ) as free gas is often trapped below gas hydrate-saturated sediments with low permeability (Shipley et al., 1979).

Apart from pressure and temperature requirements, the input of hydrocarbon gas and the presence of sufficient pore water are pre-requisites for the formation of gas hydrates. Migration pathways can control the availability of these fluids; hence, the distribution of gas hydrates is affected by the capacity of structural features to accumulate and transport gas (Taylor et al., 2000; Ben-Avraham et al., 2002; Hennes et al., 2004; Bünz et al., 2012).

The effect of the presence of faults on the distribution of gas hydrates is reported in different geological settings (Lu et al., 2016; Cooper & Hart, 2002; Dewangan et al., 2011; Minshull & White, 1989; Ruppel & Kinoshita, 2000; Ruppel et al., 2005; Madrussani et al., 2010). Northwestern Gulf of Mexico (MacDonald et al., 1994; Milkov & Sassen, 2000, 2001; Sassen et al., 1999, 2001; Chen & Cathles, 2003; Cook et al. 2008), Black Ridge (Rowe & Gettrust, 1993; Paull et al., 1995; Booth et al., 1998, Gorman et al., 2002), Omakere Ridge (Plaza-Faverola et al., 2014), Hydrate Ridge (Suess et al., 1999, 2013; Tréhu et al., 2004a, 2004b; Weinberger & brown, 2006), Krishna-Godavari Basin (Dewangan et al., 2011), and Qilian mountain permafrost (Lu et al., 2016) are examples of geological settings, where structural features play a big role in the distribution of gas hydrates. The effect of faults and fractures on the distribution of gas hydrates is even more pronounced on the fine-grained sediments where secondary porosity plays an important role in the formation of gas hydrates (Collett et al., 2008; Dewangan et al., 2011; Jaiswal et al., 2012a, 2012b). Stratigraphic factors, mainly preferential transportation of gas along permeable layers, control the availability of gas, and

thus control the distribution of gas hydrates (Dallimore et al., 1999; Xu & Ruppel, 1999; Milkov & Sassen, 2001; Matsumoto et al., 2001; Hustoft et al., 2009). Thus, the presence of gas hydrates can be strongly controlled by the structural or stratigraphic setting or both (Milkov & Sassen, 2002).

Pressure cores and well logs are well suited to investigate small-scale heterogeneities in the distribution of gas hydrates (Cook, 2009). These methods are however not suitable for regional studies as they are restricted to individual stations. Seismic velocity analysis provides a mean to study the distribution of gas hydrates (Chand et al., 2004; Kumar et al., 2006; Madrussani et al.; 2010). Seismic velocities estimated using ocean-bottom seismic (OBS) data have been successfully used in different geological settings to estimate gas hydrate saturations in the GHSZ (Bünz et al., 2005; Kumar et al., 2007; Westbrook et al., 2008; Satyavani et al., 2013; Song et al., 2018). Gas hydrate bearing sediments have a higher bulk modulus, and thus exhibit higher seismic velocities ((Ecker et al., 1998; Lee & Collett, 2001; Gei & Carcione, 2003; Chand et al., 2004). Changes in seismic velocities can potentially indicate changes in the pore fill, i.e. the presence of free gas, gas hydrates or potentially, the presence of authigenic carbonates where fluid focusing occurs (Toksöz et al., 1976; Pecher et al., 2003; Kumar et al., 2006). The identification of small-scale (~10-200 m) lateral changes in seismic velocities due to heterogeneities in pore in-fill is challenged by limitations in the seismic resolution (Kumar et al., 2006). Thus, seismic velocity analysis is rarely used to look into small-scale lateral changes in gas hydrate and free gas saturations (Satyavani et al., 2013; Jaiswal et al., 2012b). In the present study, we document results of a high-resolution OBS experiment where we correlate azimuthal P-wave velocity variations with fine-scale structural maps from 3D seismic data. We aim to investigate structural controls, in proximity to fault structures, on the gas hydrate and free gas distribution, and on the focused fluid flow in the Vestnesa Ridge, west-Svalbard margin.

2. Study area

The Vestnesa Ridge is a large sediment drift located at ~79° N on the western Svalbard continental margin (Eiken & Hinz, 1993; Howe et al., 2008; Hustoft et al., 2009) (Figure 1). It bends from SE-NW direction to E-W direction towards the north (Figure 1b). It is bounded by the Knipovich Ridge (KR) in the south, Molloy Ridge (MR) in the Northwest and Molloy Transform Fault (MTF) in the southwest (Figure 1a). Rifting at these mid-ocean ridges (KR and MR) and shear motion at MTF dictate regional stresses and faulting patterns in the region (Plaza-Faverola & Keiding, 2019). Sedimentation on the western Svalbard margin occurred under the influence of bottom-water contourite currents and mainly consist of turbiditic, glaciomarine and hemipelagic sediments (Eiken & Hiz, 1993; Stein et al., 2005; Ottesen et al., 2005).

The presence of a gas hydrate system in the Vestnesa Ridge is well-documented (Goswami et al., 2015; Bünz et al., 2012; Hustoft et al., 2009; Petersen et al., 2010; Singhroha et al., 2019; Smith et al., 2014; Vogt et al., 1994). Seafloor pockmarks and gas chimneys along the ridge are linked to faults and fractures (Plaza-Faverola et al., 2015; Singhroha et al., 2016). Considering the suggested presence of thermogenic gas (Smith et al., 2014; Plaza-Faverola et al., 2017; Panieri et al., 2017) in the study area, the study of fault/fracture systems is even more important as thermogenic gases have deeper origins (often below the GHSZ) and structural features affect the migration pathways of thermogenic gases. Faults at deeper depths in this region can be potential fluid migration pathways for deep sourced warm fluids (Waghorn et al., 2018) whereas faults at the shallower depths in GHSZ can be migration pathways or can also act as seals, as they can potentially be plugged with gas hydrates (Madrussani et al., 2010; Goswami et al., 2017).

Tectonic stresses also play an important role in deciding whether a fault is sealing (blocks the passage of fluids) or non-sealing (allows the passage of fluids). Regional stress variations and

fault mechanics over the geological time control the fluid migration and the episodic seepage along the Vestnesa Ridge (Plaza-Faverola et al., 2015; Plaza-Faverola & Keiding, 2019). Previous studies in this area investigate the potential influence of tectonic stresses and structural features on the evolution of gas hydrate systems (Plaza-Faverola et al., 2015, Singhroha et al., 2016, Singhroha et al., 2019). The eastern segment of the Vestnesa Ridge has several pockmarks, through which methane seeps, compared to the western segment, where pockmarks are inactive (Bünz et al., 2012). Recent studies (Plaza-Faverola et al., 2015; Plaza-Faverola & Keiding, 2019) suggest that these differences can due to differences in the alignment of tectonic stresses that can favor opening and sealing of faults in the eastern and western segment of the Vestnesa Ridge, respectively. P and S-wave velocity analysis (Singhroha et al., 2019) and Q analysis (Singhroha et al., 2016) suggest that faults control the distribution of gas hydrate and free gas in the eastern segment of the Vestnesa Ridge. Hence, these studies suggest that from regional (>30 km) to local scale (1-2 km), structural settings dictate the distribution of fluids within the gas hydrate system.

3. Structural evolution of faults in the Vestnesa Ridge

Vestnesa Ridge has several large and small-scale fault features. Variance attribute maps indicate the presence of fine-scale (a few meters resolution) faults and fractures associated with gas chimneys and seafloor pockmarks (Plaza-Faverola et al., 2015). These maps give a good overview about the evolution of subsurface faults over time (Figure 1e-g). We pick three horizons (Figure 1d) and estimate variance attribute along these three horizons to study the evolution of faults and fractures.

Northeastern flank of the Vestnesa Ridge has large-scale extensive faults typically due to sediment slides (Figure 1g). These faults are continuous even at deeper depths (Figure 1e and 1f). Fault/fracture networks in the southwestern flank of the Vestnesa Ridge are relatively smaller compared to northeastern flank of the ridge (Figure 1e-g). However, faults in the

southwestern flank are more extensive at deeper depths and faults become spatially limited at shallower depths (for example, Fault2 in Figure 1e). At shallower depths, these faults are spatially limited to the close proximity of fluid flow features (Figure 1g). Such changes in the faulting pattern potentially suggest that faulting in this region might be triggered by the high-fluid pressure. At deeper depths, faults can act as potential pathways for fluid migration and fluids tend to migrate towards gas chimneys at shallower depths thus making fault systems spatially limited at shallower depths. Such pattern is not observed on the northeastern flank of the Vestnesa Ridge.

4. Seismic data acquisition

In the present study, our aim is to analyze in detail, on a very small-scale (10-300 m), the role of faults on the distribution of fluids in the eastern segment of the Vestnesa Ridge gas hydrate system. We select our OBS locations on faults to see the relationship between faults and variations in the gas hydrate and free gas saturation (Figure 1c and 1e). One of the OBS was positioned on the fault (shown as Fault2 in Figure 1e); across which seismic velocity analysis (Singhroha et al., 2019) and seismic Q analysis (Singhroha et al., 2016) predicted differences in gas hydrate and free gas saturations. The location of the second OBS station is close to another fault (shown as Fault1 in Figure 1e), as observed and interpreted in time structure variance maps (Plaza-Faverola et al., 2015). We perform seismic velocity analysis to study the detailed variation of seismic velocities with azimuth at these two OBS sites near the ridge crest (Figure 1).

We acquired OBS data in a circular geometry, where we run a seismic source in concentric circular paths around two OBS locations (Figure 1c). We shot in three and four concentric circles in survey one and two, respectively. We did survey one in 2015 and survey two in 2016. Seismic energy was generated by a Mini generator-injector (GI) airgun (15/15 in^3; Sercel) and a GI airgun (45/45 in^3; Sercel) in survey one and survey two, respectively. The

mini GI gun provides higher resolutions compared to the GI gun as the mini GI gun generates a source signal that has broader amplitude spectrum (10-300 Hz) and contains significantly higher energy in high frequencies (peak frequency ~ 150-180 Hz). High frequencies produced by mini GI and GI airguns make reflection arrivals sharp thus allowing us to pick reflections with a low pick uncertainty (<1 ms). Seismic data was sampled at every 0.25 ms. Data processing included standard band pass filtering to improve the signal-to-noise ratio and facilitate picking of seismic horizons.

This acquisition approach has been used earlier for tomographic velocity and anisotropic analysis by qualitatively looking at changes in seismic amplitudes and arrival times in different directions (e.g., Plaza-Faverola et al., 2010; Satyavani et al., 2013; Haacke & Westbrook, 2006; Exley et al., 2010). We use this approach further to estimate azimuthal seismic velocities by picking travel times in different azimuths and then inverting these travel times.

5. Azimuthal seismic velocity analysis

In a circular seismic acquisition geometry, it is easy to pick reflection arrivals at different offsets in different azimuths; thus making it easy to study azimuthal variations in seismic velocities (Figure 2). Travel times from two different offsets corresponding to a reflection from a given flat layer boundary are ideally sufficient to get two unknown parameters in a layer i.e. the thickness and its velocity. Thus, travel times corresponding to three and four different offsets in different azimuths in survey one and two, respectively are theoretically enough to constrain the subsurface velocity model. A simple flat-layered model with five units has been used to test the validity of this approach (Figure 3a). With the layer stripping approach, we will try to constrain the velocity and the thickness of the fourth layer (Figure 3a) using reflection arrival times at different offsets. We will also test the sensitivity of the velocity estimates to the potential uncertainty in the picked reflection arrival times.

Different subsurface velocity models can give the same reflection arrival time at a given offset. Each curve in Figure 3b and 3c shows different possible combinations of velocity and thickness for the fourth layer (Figure 3a) that will have the same reflection arrival time at the given offset. When thickness-velocity pairs have to accommodate travel times for different offsets, the number of possible solutions is significantly reduced; thus increasing the uniqueness of the velocity model. Figure 3b and 3c shows the convergence of curves from different offsets at a single point i.e. at the true velocity and thickness of the layer. Travel times from different offsets, especially far offsets, are needed to increase the confidence in the derived velocity model. For arrival times corresponding to nearby offsets, possible velocity thickness curves are very close; and velocity and thickness values obtained by the intersection of these curves will produce results that will have a very low confidence. Therefore, if few accurate arrival times can be picked at a near, medium and far offset; good velocity models can be derived as curves for different possible velocity and thickness parameters will intersect each other at very high angles that will produce velocity model with high confidence. We also test the accuracy of model considering pick uncertainties. An error of 1 ms in the arrival times corresponds to a maximum possible velocity error of 35 m/s in the final velocity model (Figure 3c).

Seismic velocity modeling

In order to derive azimuthal velocity model, seven prominent reflection arrivals were picked at both investigated sites in a seismic section acquired using circular acquisition geometry (azimuth and offset varies with every trace in the seismic section as shown in Figure 2a). These picked reflection arrival times were sorted by the azimuth and the offset between shot points and the OBS instrument. Seismic velocity model in a given azimuth was calculated using travel times of different reflection arrivals lying along that azimuth (Figure 2b and 2c).

We use high-resolution 3D P-Cable seismic data (Plaza-Faverola et al., 2015) (Figure 1c) and OBS data (Singhroha et al., 2019) acquired in this area to get a starting model for azimuthal velocity analysis. Seismic velocity models estimated using OBS data (Singhroha et al., 2019) are used to depth convert the 3D P-Cable seismic data. We use this depth-converted cube for obtaining initial 2D velocity models in different azimuths. With these 2D models as initial velocity model, we use Rayinvr program based on Zelt and Smith (1992) approach to invert the picked travel times in a layer stripping technique to derive the final velocity model. The travel time inversion for picked travel times along 10° and 190° azimuths is shown in Figure 2b-c. Similar analysis is done in 36 different directions each containing 10° radial azimuths to get an overview of variation of velocities with azimuth around the OBS station. The RMS misfit between the picked arrival times and travel times estimated using Rayinvr in the final velocity model is less than 1 ms therefore indicating a great degree of confidence in the derived velocity models (Figure 2). A low pick uncertainty (<1 ms) and a low RMS misfit (<1 ms) in the best-fit velocity models ensures a low velocity uncertainty in azimuthal velocity estimates (~0.035 km/s as shown in Figure 3c).

6. Results

Results from azimuthal velocity analysis

Azimuthal seismic velocities for each individual layer estimated using travel time inversion are plotted using radial pie charts with different directions representative of different azimuths and the radius of the circle representative of the spread of ray path (Figure 4 and 5). In layer L1 of Survey 1 (layers shown in Figure 2a), the variation in seismic velocity is small (1.506-1.527 km/s) and falls within the uncertainty limits (Figure 4). In layer L2, a velocity change is observed from around 1.57 km/s towards the south-west to around 1.63 km/s within an azimuthal fan of around 60° in ENE region (Figure 4). Small elevations in seismic velocities (15-20 m/s) in 10° azimuthal fans compared to the average velocity (around 1.61 km/s) are

also observed in azimuths corresponding to 300° and 320° (Figure 4). In layers L3 and L4, seismic velocities in one-half side towards the northeast direction are ~30-40 m/s higher compared to the average velocity (~1.62-1.64 km/s) in the other half (Figure 4). In layer L5, high seismic velocities (1.84-1.86 km/s) occur in the north-northeast direction. A patch (20° radial azimuthal fan) of a particularly high seismic velocity (>1.87 km/s) is observed in the northwest direction. Seismic velocities are lower (~1.79-1.80 km/s) towards the southeast (Figure 4). The BSR occurs on the boundary between layers L5 and L6 (Figure 2a). In layer L6, velocities are considerably lower than in the layers above (Figure 4). The average velocity in this layer is 1.343 km/s and it is relatively uniform in different azimuths, except in few orientations where velocities are slightly lower (Figure 4).

Radial pie charts are also used to plot results from survey 2 (Figure 5). In layers LL1 and LL2, high seismic velocities (1.54-1.56 km/s) are observed in the northeast direction compared to the average velocity (~1.5-1.52 km/s). Layer LL3 shows an average seismic velocity of 1.68 km/s, with two azimuthal fans of slightly elevated velocities at 30° (1.74 km/s) and 120° (1.714 km/s). In layer LL4, a patch of relatively higher seismic velocities (1.73-1.745 km/s) lies in the south-southeast direction compared to an average velocity of 1.71 km/s in this layer. In layers above (LL5) and below (LL6) the BSR, very strong variations in seismic velocities can be observed in a number of azimuths (Figure 5b). In layer LL5, seismic velocities on the southwestern side (average velocity around 1.76 km/s) are higher than seismic velocities on the northeastern side (average velocity of 1.73 km/s). Higher seismic velocities are observed along the radial fan of around 40° in the southeast direction with seismic velocities reaching up to 1.823 km/s. The average seismic velocity in layer LL6 (1.41 km/s) is considerably lower. In LL6, particularly low seismic velocities (1.36-1.38 km/s) are observed in a radial fan of 40° in the southeast direction and along 320° azimuth. In

the azimuths corresponding to northwest directions, relatively higher velocities (~1.45-1.50 km/s) are observed.

Correlation between seismic velocity anomalies and structural features

We analyze our velocity results along with variance maps that show structural trends in the study area (Figure 1e-g, 4, 5c, 6 & 7). The overlay of seismic velocities with variance maps allows us to correlate velocity anomalies with faults and fractures in the region. Horizon H30 (Figure 1d) that lies around 30 m below the seafloor is used to analyze anomalies in the shallow layers (Figure 6). Two deeper horizons i.e. H50 and H80 (Figure 8) corresponding to ca. 0.3 Ma and 1.5 Ma respectively (Plaza-Faverola et al., 2015) are used to interpret anomalies for layers that lie in the middle (around 70 m depth below the seafloor; Figure 7) and near the base of the GHSZ (Figure 4-5), respectively. These variance maps are displayed over the velocity anomalies (Figure 4-7) to see the variation in seismic velocities and their relationship with the discontinuities in the sub-surface.

In survey 1 and survey 2, very strong relationship is observed between the distribution of velocity anomalies and faults in the subsurface. Along some azimuths, raypaths pass through faults in the subsurface (as shown in Figure 8c). In the shallow depth (Figure 6), the link between faults in the subsurface and their relationship with anomalies in azimuthal velocity maps is evident (Figure 6). At survey site 1, there is hardly any fault as the variance map is smooth (Figure 6). The azimuthal velocity map also shows hardly any variation and is relatively uniform. This is quite different from survey site 2 where opposite is true. Anomalies in the azimuthal velocity map at survey site 2 seems to be confined by the presence of two discontinuities in the area (Figure 6). There is a small increase in the velocity in south-southeast direction i.e. in the azimuth direction of one of the discontinuities. Anomalies observed in northeast direction also seem to be related with the discontinuity in that direction.

The relation between discontinuities and anomalies is clearer with the correlation of azimuthal velocities with the variance map from H50 horizon (Figure 7). Spikes in azimuthal velocities are concordant with specific azimuths involving discontinuities at the survey site 2. A spike in seismic velocities along fault azimuths and a shadow zone (a zone with lower velocity east of the discontinuity) at the survey site 1 also seem to be related to the fault.

The relationship between faults and velocity changes in azimuthal velocity maps is most evident near the BSR (Figure 4 and Figure 5). In layer L5 (the layer above the BSR), a spike and a decrease in the seismic velocity in the north-northwest direction clearly seem to be related to the presence of a fault (Figure 4). In layer L6, a decrease in seismic velocity occurs along the fault (Figure 4). In survey 2, where OBS is placed near a fault, azimuthal velocity profiles give a very interesting correlation. In layer LL5 (layer above the BSR), velocity spikes can be seen in between two faults shaping an X (Figure 5c). The orientation and alignment of faults also affects the regional distribution of velocities. Velocities in the northeast direction are generally lower than velocities in the southwest direction. In layer LL6 (the layer below the BSR), a decrease in the seismic velocity occurs along the fault in the north-northwest direction (Figure 5c). In the southeast direction, azimuths of low seismic velocities are bounded by faults (Figure 5c).

7. Discussion

Small changes in velocity anomalies (<20-30 m/s) along different azimuths especially in deeper layers can be due to differences in raypaths in shallower layers (Figure 8). However, large changes in seismic velocities (>20-30 m/s) observed along azimuths, where raypaths fall in fault planes (Figure 8), can be certainly associated with discontinuities in the region. From the two surveys, the association of velocity anomalies with faults is clear and the relationship is more prominent at the survey site 2 that has a strong regional fault passing through the OBS location compared to survey site 1 that has a relatively small-scale fault system. The

association of seismic velocity anomalies and faults is also stronger with depth as spikes and decreases in seismic velocities along faults are higher at greater depths.

The presence of different fluids have a big impact on the bulk properties of the medium (Gassmann, 1951; Brown & Korringa, 1975; Batzle & Wang, 1992; Han, 1992; Mavko et al., 1995, 1998; Sengupta & Mavko, 1999; Nolen-Hoeksema, 2000). Secondary porosity in the form of faults and fractures plays an important role in storing and transporting different fluids in the subsurface. Faults and fractures can contain different fluids and different fluids have significant impact on the seismic velocity characteristic of a medium (Hudson, 1981; Brown & Scholz, 1986; Boadu & Long, 1996). Anomalies observed in azimuthal velocity maps need to be studied considering different possible factors that can create velocity anomalies in a medium.

Seismic velocity anomalies that occur along faults can potentially indicate changes in the pore fill and the potential impact of faults on the distribution of pore-fill in the region. These anomalies are observed in a gas hydrate system where different components of the gas hydrate system i.e. methane hydrate and free gas strongly affect the bulk seismic velocity (Singhroha et al., 2019). The presence of gas hydrates increases the P-wave velocity and the presence of free gas in sediments decreases the P-wave velocity (Ecker et al., 1998; Lee & Collett, 2001; Gei & Carcione, 2003; Chand et al., 2004; Song et al., 2018). High seismic velocities anomalies observed in the GHSZ above the BSR in some azimuths can be due to the presence of gas hydrates. Other potential high velocity material like authigenic carbonates can also be present but this possibility is less likely as the OBS sites are far from the active seep sites and there is no evidence of methane seep happening through these faults in the past. Low seismic velocity anomalies observed in the layer below the BSR potentially indicate the presence of free gas. These anomalies can be studied along with the structural and stratigraphic settings to study the evolution of gas hydrates.

In survey one, high velocities obtained in one half towards the east-northeast direction can be due to higher concentration of hydrates towards the ridge crest as reported earlier (Hustoft et al., 2009; Singhroha et al., 2016; Singhroha et al., 2019). High seismic velocities in layer L5 towards the downslope side of the fault and low seismic velocities towards the upslope side of the fault, with raypaths close to the fault in both the cases, show the effect of faults on the distribution of gas hydrates in the region. Low seismic velocities in the free gas zone (Layer L6) along the fault direction further proves the role of fault in the distribution of free gas below the BSR. Earlier works in this region (Plaza-Faverola et al., 2015; Singhroha et al., 2016; Singhroha et al., 2019) also hint towards a greater role of structural features on the distribution of gas hydrates.

In the survey 2, azimuths corresponding to faults show high velocities in the GHSZ. This potentially hints towards the presence of gas hydrates in the faults at this site. Especially, near the BSR depth, spikes in velocities are trapped between two faults. Relative increase in seismic velocities in northeastern half observed in layer L5 in survey 1 is not observed in layer LL5 in survey 2. The fact that faults also determine the variation of seismic velocity anomalies in the GHSZ hints towards a strong control of faults on the distribution of fluids in the GHSZ near the BSR depth. This theory is further concurred by the fact that spikes in seismic velocities are higher at sites where subsurface is more faulted i.e. at the survey 2 site. In survey 2, anomalies in the free gas zone (LL6) suggest lower free gas saturations in the northeastern half. This can be due to the fact that faults seal upward gas migration towards the ridge or gases leak through these fault and thus limited presence of free gas on the other side of the fault. Hence, anomalies observed in the free gas zone can be explained by the sealing nature of faults or the potential leakage of gas through these faults.

In the GHSZ, faults can act as seals due to stress or due to the presence of impermeable gas hydrates. Likelihood of faults being sealed in this segment of the Vestnesa Ridge is relatively

low as methane gas seeps through several pockmarks in this area (Plaza-Faverola et al., 2015; Plaza-Faverola & Keiding, 2019). If a fault is sealing due to the occurrence of gas hydrates in faults, we expect a relatively uniform free gas saturation below the BSR across the fault, as gas hydrate-filled sealed faults cannot affect the free gas distribution below. However, we find higher free gas saturations on the downslope side to the fault. Results from velocity analysis in layers L5, LL5, L6 and LL6 suggest a relatively low gas hydrate (in the GHSZ) and free gas saturation (in free gas zone) in a direction upslope (i.e. northeast) to faults. This is further corroborated by the fact that seismic velocity and seismic Q analysis show differences in free gas saturations across the fault (Singhroha et al., 2016; Singhroha et al., 2019). In addition, we find highest free gas saturations in the faults in the free gas zone (Figure 4 and 5). These observations hint towards a system in which gas migrates upwards through fault networks from the base of the GHSZ. These fault networks spatially shrink at shallower depths and terminate in a gas chimney, which actively seeps methane (discussed in detail in section 3).

Continuous migration of gas through faults can be due to high fluid pressure from below. Gas migrating upwards under the base of the GHSZ seems to be compartmentalized by the presence of faults in the GHSZ (Figure 5c). The fluid pressure southwest of the faults can be very high compared to northeast of the fault as faults can due to difference in free gas saturation. This fluid pressure can create fractures southwest of the fault and gas hydrates can occur in these fractures. Faults and fractures act as conduits, which can lead to the deposition of gas hydrates in faults. The presence of gas hydrates in faults can seal the faults as gas hydrates have low permeability. These sealed faults can lead to accumulation of free gas that may result in an increase in overpressure from the gas below and a reactivation of sealed faults in the GHSZ (Flemings et al., 2003; Hornbach et al., 2004; Kleinberg, 2005; Liu & Flemings, 2007). The overpressure from free gas can also generate fractures and lead to

further deposition of gas hydrates in the fractures generated by free gas (Kumar et al., 2006; Yan et al. 2017).

From the azimuthal seismic velocity analysis, the evidence of spatial variation of gas hydrates due to faults and discontinuities is very strong. This effect seems to be stronger at deeper depths. In shallow depths, small changes in seismic velocities are observed along fault azimuths. This difference can be because of two reasons. Firstly, the subsurface is relatively less faulted near the seafloor. Another reason can be the fact that there is lower gas hydrate concentration at shallow depths and higher concentration of gas hydrates near the base of the GHSZ (Singhroha et al., 2019). Both these factors reduce the likelihood of the presence of gas hydrate-filled faults at shallow depths.

In the Vestnesa Ridge, the effect of faults on the distribution of gas hydrates has been observed at different scales in different studies. Plaza-Faverola et al. (2015) documented the possibility of a link between tectonic stress and seepage at two 3D seismic sites separated by approximately 35 km in the Vestnesa Ridge. The region with active seepage in the Vestnesa Ridge is relatively more faulted compared to other areas where there are pockmarks but there is no gas seepage. Singhroha et al. (2016) and Singhroha et al. (2019) documented the potential impact of faults on the distribution of gas hydrates in an area covered by 3D seismic. This paper documents that even at small scales, faults play a big role in spatial distribution of gas hydrates.

8. Conclusion

This paper documents the application of shooting along circular tracks to study azimuthal velocity variations. Detailed seismic velocity analysis in the Vestnesa Ridge shows that the presence of gas hydrates is strongly affected by fault/fracture systems in the region. We find high velocity patches occurring in the vicinity of inferred fault/fracture systems thus

potentially indicating preferential distribution of gas hydrates along fault/fracture systems in the region. We infer the compartmentalization and preferential alignment of gas hydrates and free gas with the fault systems of the Vestnesa Ridge.

We find that small to large-scale faults have a strong control on the presence and distribution of gas hydrates. Azimuthal variation of velocities document changes in pore fill as we move across faults and discontinuities. Thus, gas hydrate distribution within the GHSZ has a very high spatial variability due to faults and therefore we interpret that the gas hydrate system in the Vestnesa Ridge has a strong structural control. This novel application of derived azimuthal velocities to study the distribution of gas hydrates shows that the circular shooting can be applied to study variations in velocities at a given site and useful geological information can be derived from it.

9. Acknowledgement

This work is partly supported by the Research Council of Norway through its Centres of Excellence funding scheme, project no. 223259. We thank the crew of *R/V* Helmer Hanssen and those who contributed to the OBS and P-cable data acquisition.

10. References

Batzle, M. L., & Wang, Z.-J. (1992). Seismic properties of pore fluids. Geophysics, 57, 1396–1408.

Ben-Avraham, Z., Smith, G., Reshef, M., & Jungslager, E. (2002). Gas hydrate and mud volcanoes on the southwest African continental margin, Geology, 30, 927–930.

Bjørlykke, K. (2015). Petroleum Geoscience From Sedimentary Environment to Rock Physics. Springer-Verlag Berlin Heidelberg, doi: 10.1007/978-3-642-34132-8.

Boadu, F. K., & Long, L. T. (1996). Effects of fractures on seismic-wave velocity and attenuation. Geophysical Journal International, 127(1), 86-110. doi:10.1111/j.1365-246X.1996.tb01537.x

Booth, J. S., Winters, W. J., Dillon, W. P., Clennell, M. B., & Rowe, M. M. (1998). Major occurrences and reservoir concepts of marine clathrate hydrates: implications of field evidence. Geological Society, London, Special Publications, 137(1), 113-127. doi:10.1144/gsl.Sp.1998.137.01.08

Brown, J. S., & Korringa, J. (1975). On the elastic properties of a porous rock on the compressibility of the pore fluid. Geophysics, 40, 608– 616.

Brown, S. R., & Scholz, C. H. (1986). Closure of rock joints. J. geophys. Res., 91, 4939-4948.

Bünz, S., Mienert, J., Vanneste, M., & Andreassen, K. (2005). Gas hydrates at the Storegga Slide: constraints from an analysis of multicomponent, wide-angle seismic data. Geophysics, 70(5), B19-B34.

Bünz, S., Polyanov, S., Vadakkepuliyambatta, S., Consolaro, C., & Mienert, J. (2012). Active gas venting through hydrate-bearing sediments on the Vestnesa Ridge, offshore W-Svalbard. Marine Geology, 332-334, 189-197. doi:https://doi.org/10.1016/j.margeo.2012.09.012

Caine, J. S., Evans, J. P. & Forster, C. B. (1996). Fault zone architecture and permeability structure. Geology, 24(11), 1025–1028.

Chand, S., Minshull, T. A., Gei, D., & Carcione, J. M. (2004). Elastic velocity models for gas-hydrate-bearing sediments—a comparison. Geophysical Journal International, 159(2), 573-590. doi:10.1111/j.1365-246X.2004.02387.x

Chen, D. F., & Cathles III, L. M. (2003). A kinetic model for the pattern and amounts of hydrate precipitated from a gas steam: Application to the Bush Hill vent site, Green Canyon Block 185, Gulf of Mexico. Journal of Geophysical Research: Solid Earth, 108(B1). doi:10.1029/2001jb001597

Collett, T., Riedel, M., Cochran, J. R., Boswell, R., Presley, J., Kumar, P., Sathe, A., Lall, M., Sibal, V., & the NGHP Expedition 01 Scientists (2008). Indian national gas hydrate program, expedition - 01, Initial report, Directorate General of Hydrocarbons, Ministry of Petroleum and Nat-ural gas, India.

Cook, A. E. (2009). Gas Hydrate Filled Fracture Reservoirs on Continental Margins. PhD thesis, Columbia University.

Cook, A. E., Goldberg, D., & Kleinberg, R. L. (2008). Fracture-controlled gas hydrate systems in the northern Gulf of Mexico. Marine and Petroleum Geology, 25(9), 932-941. doi:https://doi.org/10.1016/j.marpetgeo.2008.01.013

Cooper, A. K., & Hart, P. E. (2002). High-resolution seismic-reflection investigation of the northern Gulf of Mexico gas-hydrate-stability zone. Marine and Petroleum Geology, 19(10), 1275-1293. doi:https://doi.org/10.1016/S0264-8172(02)00107-1

Dallimore, S. R., Uchida, T., & Collett, T. S. (1999). Scientific results from JAPEX/JNOC/GSC Mallik 2L-38 gas hydrate research well, Mackenzie Delta, northwest territories, Canada. Geological Survey of Canada Bulletin 544, 403.

Davies, R. K., & Handshy, J. W. (2003). Introduction to AAPG bulletin thematic issue on fault seals. AAPG Bull., 87, 377–380.

Dewangan, P., Sriram, G., Ramprasad, T., Ramana, M. V., & Jaiswal, P. (2011). Fault system and thermal regime in the vicinity of site NGHP-01-10, Krishna–Godavari basin, Bay of Bengal. Marine and Petroleum Geology, 28(10), 1899-1914. doi:10.1016/j.marpetgeo.2011.03.009

Ecker, C., Dvorkin, J., & Nur, A. (1998). Sediments with gas hydrates: Internal structure from seismic AVO. Geophysics, 63, 1659–1669. doi: 10.1190/1.1444462.

Eiken, O., & Hinz, K. (1993). Contourites in the Fram Strait. Sed. Geol., 82, 1–4.

Etiope, G., & Lollar, B. S. (2013). Abiotic Methane on Earth. Reviews of Geophysics, 51(2), 276-299. doi:10.1002/rog.20011

Exley, R. J. K., Westbrook, G. K., Haacke, R. R., & Peacock, S. (2010). Detection of seismic anisotropy using ocean bottom seismometers: a case study from the northern headwall of the Storegga Slide. Geophysical Journal International, 183(1), 188-210. doi:10.1111/j.1365-246X.2010.04730.x

Flemings, P. B., Liu, X.L., & Winters, W. J. (2003). Critical pressure and multiphase flow in Blake Ridge gas hydrates. Geology, 31(12), 1057 – 1060.

Gassmann, F. (1951). Uber die elastizität poröser medien. Vierteljahrsschrift der Naturforschenden Gesellschaft in Zurich, 96, 1–23.

Gei, D., & Carcione, J. M. (2003). Acoustic properties of sediments saturated with gas hydrate, free gas and water. Geophysical prospecting, 51(2), 141-158. doi:10.1046/j.1365-2478.2003.00359.x

Goodman, R. E. (1976). Methods of Geological Engineering. West Publishing, St. Paul, MN.

Gorman, A. R., Hackwith, K. L., Hornbach, M. J., Holbrook, W. S., Lizarralde, D., & Pecher, I. (2002). Migration of methane gas through the hydrate stability zone in a low-flux hydrate province. Geology, 30(4), 327-330.

Goswami, B. K., Weitemeyer, K. A., Bünz, S., Minshull, T. A., Westbrook, G. K., Ker, S., & Sinha, M. C. (2017). Variations in pockmark composition at the Vestnesa Ridge: Insights from marine controlled source electromagnetic and seismic data. Geochemistry, Geophysics, Geosystems, 18(3), 1111-1125. doi:10.1002/2016GC006700

Goswami, B. K., Weitemeyer, K. A., Minshull, T. A., Sinha, M. C., Westbrook, G. K., Chabert, A., . . . Ker, S. (2015). A joint electromagnetic and seismic study of an active pockmark within the hydrate stability field at the Vestnesa Ridge, West Svalbard margin. Journal of Geophysical Research: Solid Earth, 120(10), 6797-6822. doi:10.1002/2015JB012344

Haacke, R. R., & Westbrook, G. K. (2006). A fast, robust method for detecting and characterizing azimuthal anisotropy with marine PS converted waves, and its application to the west Svalbard continental slope. Geophysical Journal International, 167(3), 1402-1412. doi:10.1111/j.1365-246X.2006.03186.x

Han, D. (1992) Fluid saturation effect on rock velocities in seismic frequencies. Presented at SEG Summer Research Workshop, Big Sky, Montana.

Hennes, A. M., Johnson, R. A. & Casavant, R. R. (2004). Seismic characterization of a shallow gas-hydrate-bearing reservoir on the North Slope of Alaska. Proc. AAPG Hedberg Research Conference, September 12–16, Vancouver, BC, Canada.

Hornbach, M. J., Saffer, D. M., & W. S. Holbrook (2004). Critically pressured free-gas reservoirs below gas-hydrate provinces. Nature, 427, 142 – 144.

Howe, J. A., Shimmield, T. M., Harland, R., & Eyles, N. (2008). Late Quaternary contourites and glaciomarine sedimentation in the Fram Strait. Sedimentology, 55(1), 179-200. doi:10.1111/j.1365-3091.2007.00897.x

Hudson, J. A. (1981). Wave speeds and attenuation of elastic waves in material containing cracks. Geophys. J. R. astr. SOC., 64, 133-150.

Hustoft, S., Bünz, S., Mienert, J., & Chand, S. (2009). Gas hydrate reservoir and active methane-venting province in sediments on <20 Ma young oceanic crust in the Fram Strait, offshore NW-Svalbard. Earth and Planetary Science Letters, 284, 12–24.

Jaiswal, P., Dewangan, P., Ramprasad, T., & Zelt C. (2012a). Seismic characterization of hydrates in faulted, fine-grained sediments of Krishna-Godavari basin: Unified imaging. J. Geophys. Res., 117, B04306. doi:10.1029/2011JB009024.

Jaiswal, P., Dewangan, P., Ramprasad, T., & Zelt C. (2012b). Seismic characterization of hydrates in faulted, fine-grained sediments of Krishna-Godavari basin: Full waveform inversion. J. Geophys. Res., 117, B10305. doi:10.1029/2012JB009201.

Kleinberg, R. L. (2005). Mechanical stability of seafloor sediments with application to gas hydrate deposits. Proc 5th Int Conf on Gas Hydrates, 3, 736-748.

Kumar, D., Sen, M. K., & Bangs, N. L. (2007). Gas hydrate concentration and characteristics within Hydrate Ridge inferred from multicomponent seismic reflection data. Journal of Geophysical Research: Solid Earth, 112(B12), B12306. doi:10.1029/2007JB004993.

Kumar, D., Sen, M. K., Bangs, N. L., Wang, C., & Pecher, I. (2006). Seismic anisotropy at Hydrate Ridge. Geophysical Research Letters, 33, L01306.

Kvenvolden, K. A. (1993). Gas hydrates – geological perspective and global change. Reviews of Geophysics, 31 (2), pp. 173-187.

Lee, M. W., & Collett, T. S. (2001). Elastic properties of gas hydrate-bearing sediments. Geophysics, 66(3), 763-771. doi:10.1190/1.1444966

Ligtenberg, J. H. (2005). Detection of fluid migration pathways in seismic data: implications for fault seal analysis. Basin Res., 17, 141–153.

Liu, X., & Flemings, P. B. (2007). Dynamic multiphase flow model of hydrate formation in marine sediments. Journal of Geophysical Research: Solid Earth, 112(B3). doi:10.1029/2005jb004227

Lu, Z., Zhai, G., Zhu, Y., Zhang, Y., Li, Y., Wang, W., . . . Tan, P. (2016). Fault Control of Gas Hydrate Accumulation in Qilian Mountain Permafrost. International Journal of Offshore and Polar Engineering, 26(02), 199-205.

MacDonald, I. R., Guinasso, N. L., Sassen, R., Brooks, J. M., Lee, L., & Scott, K. T. (1994). Gas hydrates that breaches the seafloor on the continental slope of Gulf of Mexico. Geology, 22, 699-702.

Madrussani, G., Rossi, G., & Camerlenghi, A. (2010). Gas hydrates, free gas distribution and fault pattern on the west Svalbard continental margin. Geophysical Journal International, 180(2), 666-684. doi:10.1111/j.1365-246X.2009.04425.x

Matsumoto, R., Takedomi, Y., & Wassada, H. (2001). Exploration of Marine Gas Hydrates in Nankai Trough, Offshore Central Japan. AAPG Annual Convention, Official Program 10, p. A128.

Mavko, G., Chan, C., & Mukerji, T. (1995). Fluid substitution: Estimating changes in Vp without knowing Vs. Geophysics, 60, 1750– 1755.

Mavko, G., Mukerji, T., & Dvorkin, J. (1998). Rock physics handbook: Tools for seismic analysis in porous media. Cambridge University Press

Milkov, A. V., & Sassen, R. (2000). Thickness of gas hydrate stability zone, Gulf of Mexico continental slope. Marine and Petroleum Geology 17, 981-991.

Milkov, A. V., & Sassen, R. (2001). Estimate of gas hydrate resource, northwestern Gulf of Mexico continental slope. Marine Geology 179, 71-83.

Milkov, A., & Sassen, R. (2002). Economic geology of offshore gas hydrate accumulations and provinces. Marine and Petroleum Geology 19 (1), 1-11.

Minshull, T.A., & White, R. (1989). Sediment composition and fluid migration in the Makran accretionary prism. Journal of Geophysical Research 94, 7387-7402.

Nolen-Hoeksema, R. C. (2000), Modulus-porosity relation, Gassmann's equations, and the low frequency elastic-wave response to fluids. Geophysics, 65, 1355–1363.

Ottesen, D., Dowdeswell, J.A., & Rise, L. (2005). Submarine landforms and the reconstruction of fast-flowing ice streams within a large quaternary ice sheet: the 2500-km-long Norwegian-Svalbard margin (57 degrees-80 degrees N). Geological Society of America Bulletin 117, 1033–1050.

Panieri, G., Bünz, S., Fornari, D. J., Escartin, J., Serov, P., Jansson, P., . . . Gracias, N. (2017). An integrated view of the methane system in the pockmarks at Vestnesa Ridge, 79°N. Marine Geology, 390, 282-300. doi:https://doi.org/10.1016/j.margeo.2017.06.006

Paull, C. K., Ussler, W., Borowski, W. S., & Spiess, F. N. (1995). Methane-rich plumes on the Carolina continental rise: Associations with gas hydrates. Geology 23, 89-92.

Pecher, I. A., Holbrook, W. S., Sen, M. K., Lizarralde, D., Wood, W. T., Hutchinson, D. R., . . . Stephen, R. A. (2003). Seismic anisotropy in gas-hydrate- and gas-bearing sediments on the Blake Ridge, from a walkaway vertical seismic profile. Geophysical Research Letters, 30(14). doi:10.1029/2003gl017477

Petersen, C. J., Bünz, S., Hustoft, S., Mienert, J., & Klaeschen, D. (2010). High-resolution P-Cable 3D seismic imaging of gas chimney structures in gas hydrated sediments of an Arctic sediment drift. Marine and Petroleum Geology, 27(9), 1981-1994. doi:10.1016/j.marpetgeo.2010.06.006

Plaza-Faverola, A., Bünz, S., Johnson, J. E., Chand, S., Knies, J., Mienert, J., & Franek P. (2015). Role of tectonic stress in seepage evolution along the gas hydrate-charged Vestnesa Ridge. Fram Strait. Geophysical Research Letters, 42(3), 733-42.

Plaza-Faverola, A., & Keiding, M. (2019). Correlation between tectonic stress regimes and methane seepage on the western Svalbard margin. Solid Earth, 10(1), 79-94. doi:10.5194/se-10-79-2019

Plaza-Faverola, A., Pecher, I., Crutchley, G., Barnes, P. M., Bünz, S., Golding, T., . . . Bialas, J. (2014). Submarine gas seepage in a mixed contractional and shear deformation regime: Cases from the Hikurangi oblique-subduction margin. Geochemistry, Geophysics, Geosystems, 15(2), 416-433. doi:10.1002/2013gc005082

Plaza-Faverola, A., Vadakkepuliyambatta, S., Hong, W. L., Mienert, J., Bünz, S., Chand, S., & Greinert, J. (2017). Bottom-simulating reflector dynamics at Arctic thermogenic gas provinces: An example from Vestnesa Ridge, offshore west Svalbard. Journal of Geophysical Research: Solid Earth, 122(6), 4089-4105. doi:10.1002/2016JB013761

Plaza-Faverola, A., Westbrook, G. K., Ker, S., Exley, R. J. K., Gailler, A., Minshull, T. A., & Broto, K. (2010). Evidence from three-dimensional seismic tomography for a substantial accumulation of gas hydrate in a fluid-escape chimney in the Nyegga pockmark field, offshore Norway. Journal of Geophysical Research: Solid Earth, 115(B8). doi:10.1029/2009jb007078

Rowe, M. M., & Gettrust, J. F. (1993). Fine structure of methane hydrate-bearing sediments on the Blake Outer Ridge as determined from deep-tow multichannel seismic data. Journal of Geophysical Research: Solid Earth, 98(B1), 463-473. doi:10.1029/92jb01706

Ruppel, C., Dickens, G. R., Castellini, D. G., Gilhooly, W., & Lizarralde, D. (2005). Heat and salt inhibition of gas hydrate formation in the northern Gulf of Mexico. Geophysical Research Letters, 32(4). doi:10.1029/2004gl021909

Ruppel, C. D., & Kessler, J. D. (2017). The interaction of climate change and methane hydrates. Reviews of Geophysics, 55(1), 126-168. doi:10.1002/2016RG000534

Ruppel, C., & Kinoshita, M. (2000). Heat, methane, and energy flux in an active margin gas hydrate province, offshore Costa Rica. Earth and Planetary Science Letters 179, 153-165.

Sassen, R., Losh, S., Cathles, L., Roberts, H., Whelan, J. K., Mikov, A. V., Sweet, S. T., & Defretias, D. A. (2001). Massive Vein-filling gas hydrate: Relation to ongoing gas migration from the deep subsurface Gulf of Mexico. Marine and Petroleum Geology 18, 551-560.

Sassen, R., Sweet, S. T., Mikov, A. V., Defretias, D. A., Salata, G. G. & McDade, E. C. (1999). Geology and geochemistry of gas hydrates, central Gulf of Mexico continental slope. Transactions Gulf Coast Association of Geological Societies 49, 462-468.

Satyavani, N., Sen, M. K., Ojha, M., & Sain, K. (2013). Azimuthal anisotropy from OBS observations in Mahanadi offshore, India. Interpretation, 1(2), T187-T198. doi:10.1190/int-2013-0018.1

Schoell, M. (1988). Multiple origins of methane in the earth. Chem. Geol., 78, 1– 10.

Sengupta, M., & Mavko, G. (1999). Sensitivity analysis of seismic fluid detection. 69th Annual International Meeting, Society of Exploration Geophysicists, Expanded Abstracts, Paper BHRP 7.2.

Shipley, T. H., Houston, M. H., Buffler, R. T., Shaub, F. J., McMillen, K. J., Ladd, J. W., & Worzel, J. L. (1979). Seismic evidence for widespread possible gas hydrate horizons on Continental slopes and rises. AAPG Bulletin, 63, 2204–2213.

Sibson, R. H. (1994). Crustal stress, faulting and fluid flow. Geological Society, London, Special Publications, v. 78, no. 1, p. 69-84.

Singhroha, S., Bünz, S., Plaza-Faverola, A., & Chand, S. (2016). Gas hydrate and free gas detection using seismic quality factor estimates from high-resolution P-cable 3D seismic data. Interpretation, 4(1), SA39-SA54. doi:10.1190/INT-2015-0023.1

Singhroha S., Chand, S., & Bünz, S. (2019). Constraints on gas hydrate distribution and morphology in Vestnesa Ridge, W-Svalbard margin using multicomponent ocean-bottom seismic data. Journal of Geophysical Research – Solid Earth. doi: 10.1029/2018JB016574

Sloan, E. D., Jr. (1998). Clathrate hydrates of natural gases, 2nd ed.: Marcel Dekker Inc.

Smith, A. J., Mienert, J., Bünz, S., & Greinert, J. (2014). Thermogenic methane injection via bubble transport into the upper Arctic Ocean from the hydrate-charged Vestnesa Ridge, Svalbard. Geochemistry, Geophysics, Geosystems, 15(5), 1945-1959. doi:10.1002/2013GC005179

Song, S., Tinivella, U., Giustiniani, M., Singhroha, S., Bünz, S., & Cassiani, G. (2018). OBS Data Analysis to Quantify Gas Hydrate and Free Gas in the South Shetland Margin (Antarctica). Energies, 11, 3290. doi: 10.3390/en11123290

Spencer, A. M. (2012). Generation, Accumulation and Production of Europe's Hydrocarbons III: Special Publication of the European Association of Petroleum Geoscientists. Springer Science & Business Media-Science.

Stein, R., Niessen, F., Schoster, F., Bahr, B., Gebhardt, C., Kukina, N., Lensch, N., Nam, S., Noffke, H., Penshorn, D., Puhr, A., Saraswat, R., Schäfer, Chr., Schnieder, J., Thiede, J., Winkleman, D. and Yanina, Y. (2005). Marine geology. In: Scientific Cruise Report of the Arctic Expedition ARK-XX/3 of RV Polarstern in 2004: Fram Strait, Yermak Plateau and East Greenland Continental Margin (ed. R. Stein). Ber. Polarfors., 517, 41–95.

Suess, E., Torres, M.E., Bohrmann, G., Collier, R.W., Grienert, J., Linke, P., Rehder, G., Trehu, A.M., Wallmann, K., Winckler, G., & Zuleger, E. (1999). Gas hydrate destabilization: enhanced dewatering, benthic material turnover and large methane plumes at the Cascadia convergent margin. Earth and Planetary Science Letters, 170, 1-15.

Suess, E., Torres, M., Bohrmann, G., Collier, R., Rickert, D., Goldfinger, C. …. Elver, M. (2013). Sea Floor Methane Hydrates at Hydrate Ridge, Cascadia Margin. In Natural Gas Hydrates: Occurrence, Distribution, and Detection (eds C. K. Paull and W. P. Dillon). doi:10.1029/GM124p0087

Taylor, M. H., Dillon, W. P., & Pecher, I. A. (2000). Trapping and migration of methane associated with the gas hydrate stability zone at the Blake Ridge Diapir: new insights from seismic data. Mar. Geol., 164(1–2), 79–89.

Toksöz, M. N., Cheng, C. H., & Timur, A. (1976). Velocities of seismic waves in porous rocks. Geophysics, 41, 621-645.

Tréhu, A. M., Long, P. E., Torres, M. E., Bohrmann, G., Rack, F. R., Collett, T. S., . . . Weinberger, J. L. (2004a). Three-dimensional distribution of gas hydrate beneath southern Hydrate Ridge: Constraints from ODP Leg 204. Earth and Planetary Science Letters, 222(3-4), 845-862. doi:10.1016/j.epsl.2004.03.035

Tréhu, A. M., Flemings, P. B., Bangs, N. L., Chevallier, J., Gràcia, E., Johnson, J. E., . . . Torres, M. E. (2004b). Feeding methane vents and gas hydrate deposits at south Hydrate Ridge. Geophysical Research Letters, 31(23). doi:10.1029/2004gl021286

Vadakkepuliyambatta, S. (2014). Sub-seabed fluid-flow systems and gas hydrates of the SW Barents Sea and North Sea margins. PhD thesis, UiT The Arctic University of Norway

Vadakkepuliyambatta, S., Bünz, S., Mienert, J., & Chand, S. (2013). Distribution of subsurface fluid-flow systems in the SW Barents Sea. Marine and Petroleum Geology, 43, 208-221. doi:10.1016/j.marpetgeo.2013.02.007

Vogt, P. R., Crane, K., Sundvor, E., Max, M. D., & Pfirman, S. L. (1994). Methane-generated (?) pockmarks on young, thickly sedimented oceaniccrust in the Arctic: Vestnesa ridge, Fram strait. Geology, 22(3), 255–258.

Waghorn, K. A., Bünz, S., Plaza-Faverola, A., & Johnson, J. E. (2018). 3-D Seismic Investigation of a Gas Hydrate and Fluid Flow System on an Active Mid-Ocean Ridge;

Svyatogor Ridge, Fram Strait. Geochemistry, Geophysics, Geosystems, 19(8), 2325-2341. doi:10.1029/2018gc007482

Weinberger, J. L., & Brown, K. M. (2006). Fracture networks and hydrate distribution at Hydrate Ridge, Oregon. Earth and Planetary Science Letters, v. 245, p. 123–136, doi:10.1016/j.epsl.2006.03.012.

Westbrook, G. K., Chand, S., Rossi, G., Long, C., Bünz, S., Camerlenghi, A., . . . Zillmer, M. (2008). Estimation of gas hydrate concentration from multi-component seismic data at sites on the continental margins of NW Svalbard and the Storegga region of Norway. Marine and Petroleum Geology, 25(8), 744-758. doi:10.1016/j.marpetgeo.2008.02.003

Xu, W., & Ruppel, C. (1999). Predicting the occurrence, distribution, and evolution of methane gas hydrate in porous marine sediments. Journal of Geophysical Research 104, 5081-5096.

Yan, C., Cheng, Y., Li, M., Han, Z., Zhang, H., Li, Q., Teng, F., & Ding, J. (2017). Mechanical experiments and constitutive model of natural gas hydrate reservoirs. International Journal of Hydrogen Energy, v. 42, no. 31, p. 19810-19818.

Zelt, C. A., & Smith, R. B. (1992). Seismic travel-time inversion for 2-D crustal velocity structure. Geophys. J. Int., 108, 16-34.

List of illustrations

Figure 1 a) The regional bathymetry map showing the location of the study area along with Knipovich Ridge (KR), Molloy Ridge (MR) and Molloy Transform fault (MTF). b) Detailed bathymetry map of the study area. Survey 1 and Survey 2 are two surveys done to study azimuthal velocity variations around two OBS locations shown as white dots (details shown in Figure 1c). The green rectangle shows the areal bounds of the 3D seismic data acquired along the Vestnesa Ridge. d) A crossline seismic section (passing through the OBS location in survey2) from 3D P-Cable seismic data showing the BSR and other horizons. e-g) Variance maps for different horizons (H30, H50 and H80). These horizons are shown in vertical seismic profiles in Figure 1d.

Figure 2 a) Seismic data acquired from circular shooting at the survey 1 site. Different picked events are shown in different colors. L1, L2, L3, L4, L5, and L6 are the layers for which anisotropic velocity model is estimated. The BSR lies between the layer L5 and L6. b) Picked travel times (shown in red) and best fit travel times curves (shown in blue) along 10° and 190°. Different raypaths for best fit travel times of the inverted velocity model are shown in c).

Figure 3 a) Five layers velocity model and travel times for this model at different offsets. b) Curves corresponding to different offsets showing different possible combinations of the seismic velocity and the layer thickness of the 4th layer that will have same arrival time. c) Effect of the error in the picked travel times on the accuracy of the estimated velocities.

Figure 4 Seismic velocity model in different azimuths for different layers at the survey 1 site (layers shown in Figure 2a). Overlap of the velocity model and the variance map (taken from Plaza-Faverola et al., 2015) is shown for layers L5 and L6.

Figure 5 a) Seismic data acquired from circular shooting at the survey 2 site. Different picked events are shown in different colors. LL1, LL2, LL3, LL4, LL5, and LL6 are the layers for which anisotropic velocity model is estimated. BSR lies between the layer LL5 and LL6. b) Seismic velocity model in different azimuths for different layers at the survey 2 site (layers shown in Figure 5a). c) Overlap of the seismic velocity model and the variance map (taken from Plaza-Faverola et al., 2015) is shown for layers LL5 and LL6.

Figure 6 Overlap of the variance map and azimuthal velocity models for layers L1 and LL1.

Figure 7 Overlap of the variance map for the H50 (Plaza-Faverola et al., 2015) and azimuthal velocity models for layers L2 and LL3.

Figure 8 Schematic of raypaths for the L5 in Inline and crossline directions at the survey site 1 (8a and 8b). Schematic of raypaths for the LL5 in different azimuths along with the variance map at the survey site 2 (8c).

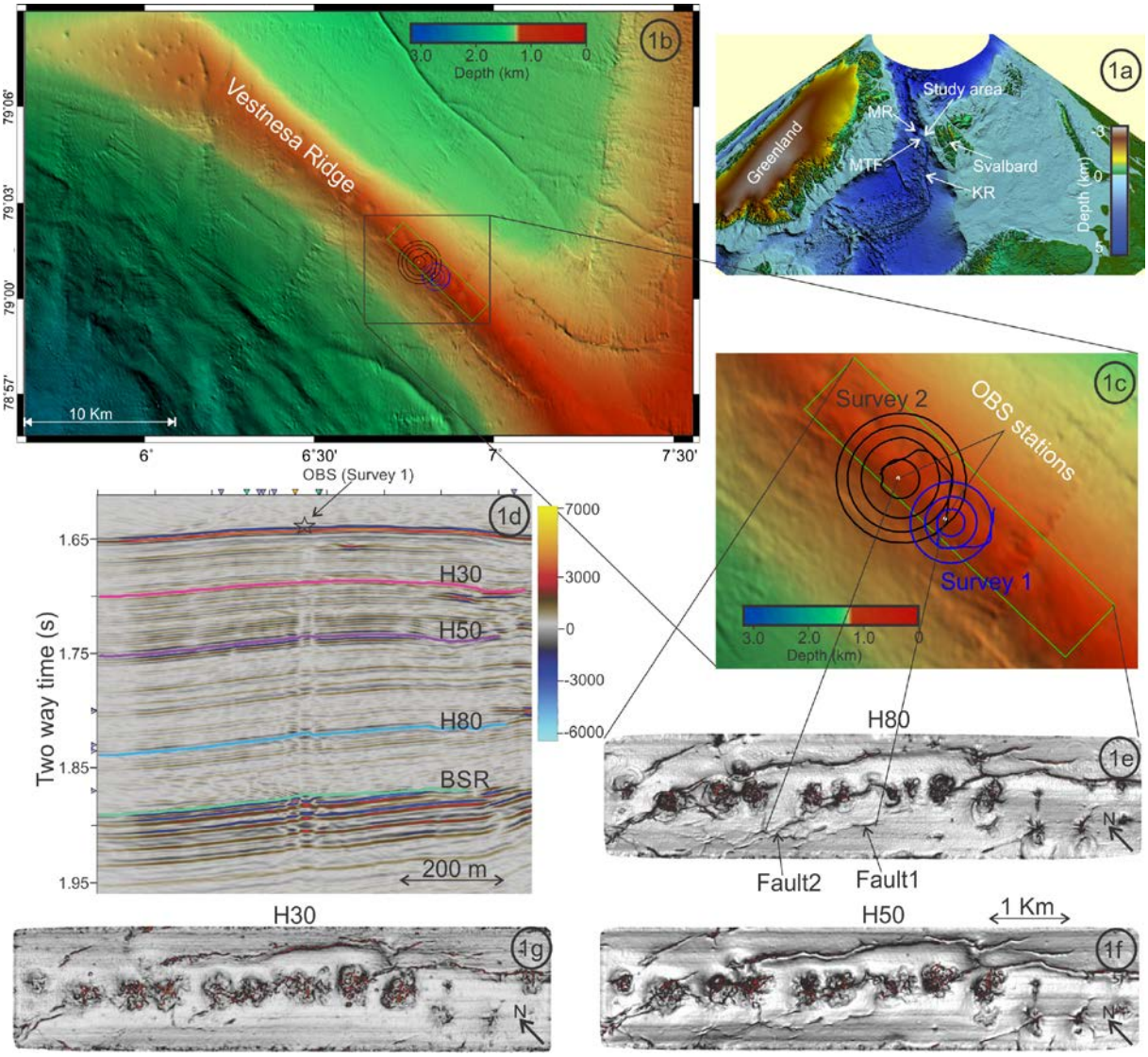

Figure 1 a) The regional bathymetry map showing the location of the study area along with Knipovich Ridge (KR), Molloy Ridge (MR) and Molloy Transform fault (MTF). b) Detailed bathymetry map of the study area. Survey 1 and Survey 2 are two surveys done to study azimuthal velocity variations around two OBS locations shown as white dots (details shown in Figure 1c). The green rectangle shows the areal bounds of the 3D seismic data acquired along the Vestnesa Ridge. d) A crossline seismic section (passing through the OBS location in survey2) from 3D P-Cable seismic data showing the BSR and other horizons. e-g) Variance maps for different horizons (H30, H50 and H80). These horizons are shown in vertical seismic profiles in Figure 1d.

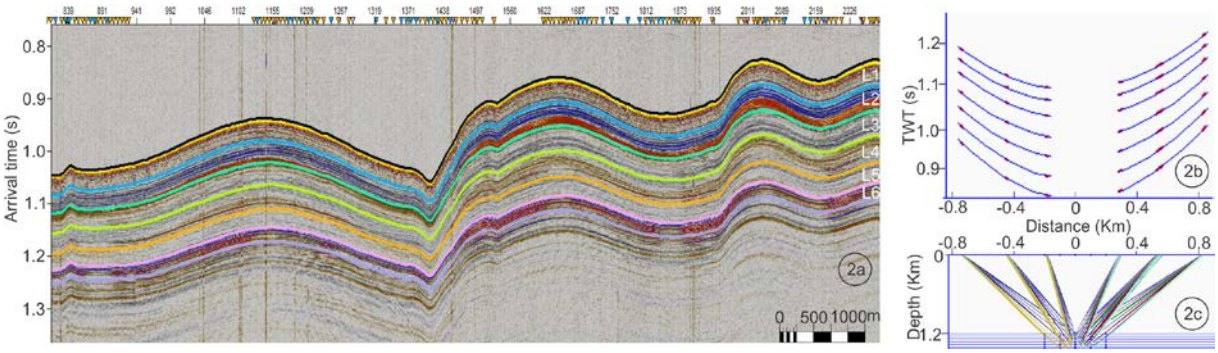

Figure 2 a) Seismic data acquired from circular shooting at the survey 1 site. Different picked events are shown in different colors. L1, L2, L3, L4, L5, and L6 are the layers for which anisotropic velocity model is estimated. The BSR lies between the layer L5 and L6. b) Picked travel times (shown in red) and best fit travel times curves (shown in blue) along 10° and 190°. Different raypaths for best fit travel times of the inverted velocity model are shown in c).

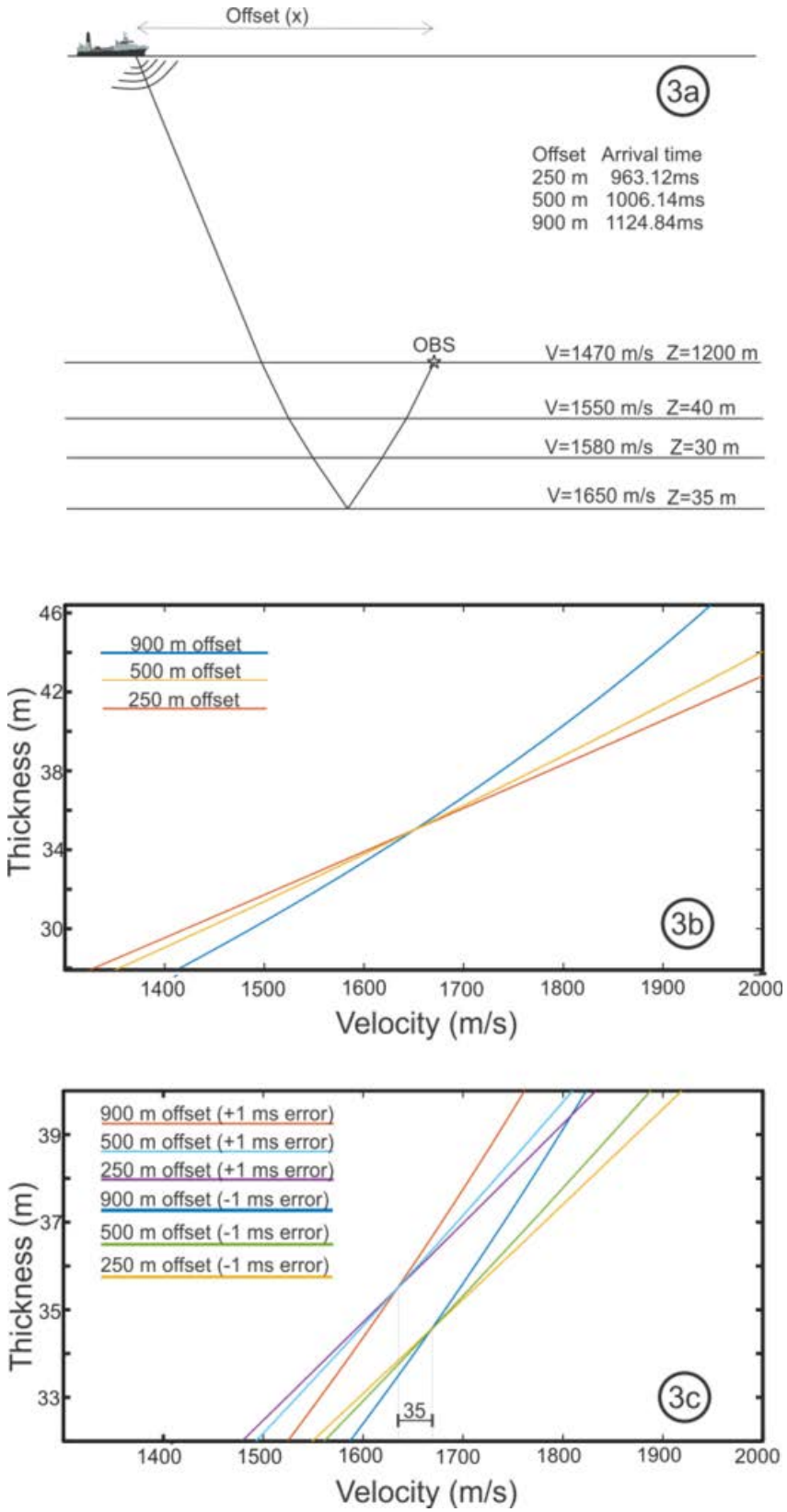

Figure 3 a) Five layers velocity model and travel times for this model at different offsets. b) Curves corresponding to different offsets showing different possible combinations of the seismic velocity and the layer thickness of the 4th layer that will have same arrival time. c) Effect of the error in the picked travel times on the accuracy of the estimated velocities.

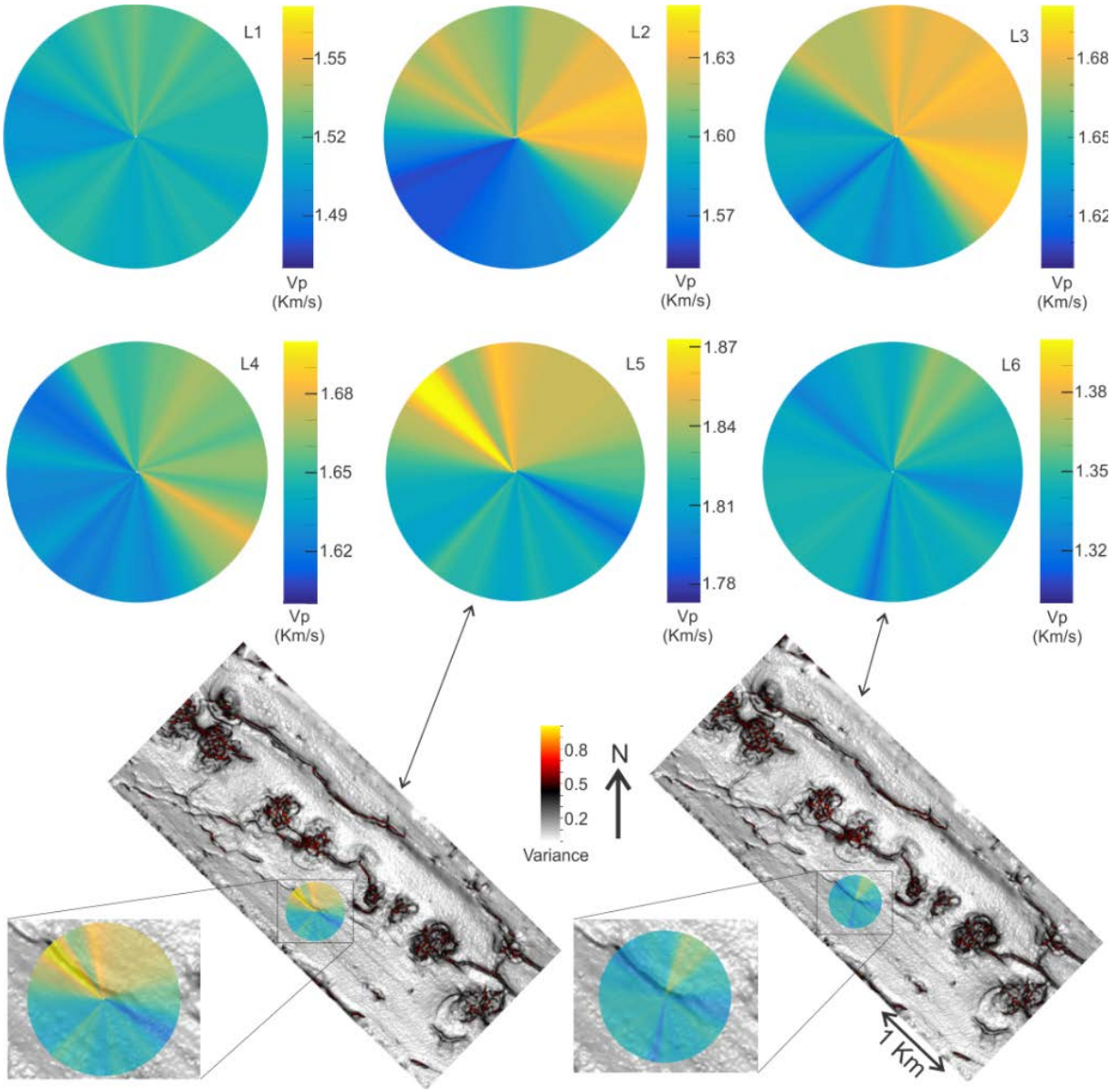

Figure 4 Seismic velocity model in different azimuths for different layers at the survey 1 site (layers shown in Figure 2a). Overlap of the velocity model and the variance map (taken from Plaza-Faverola et al., 2015) is shown for layers L5 and L6.

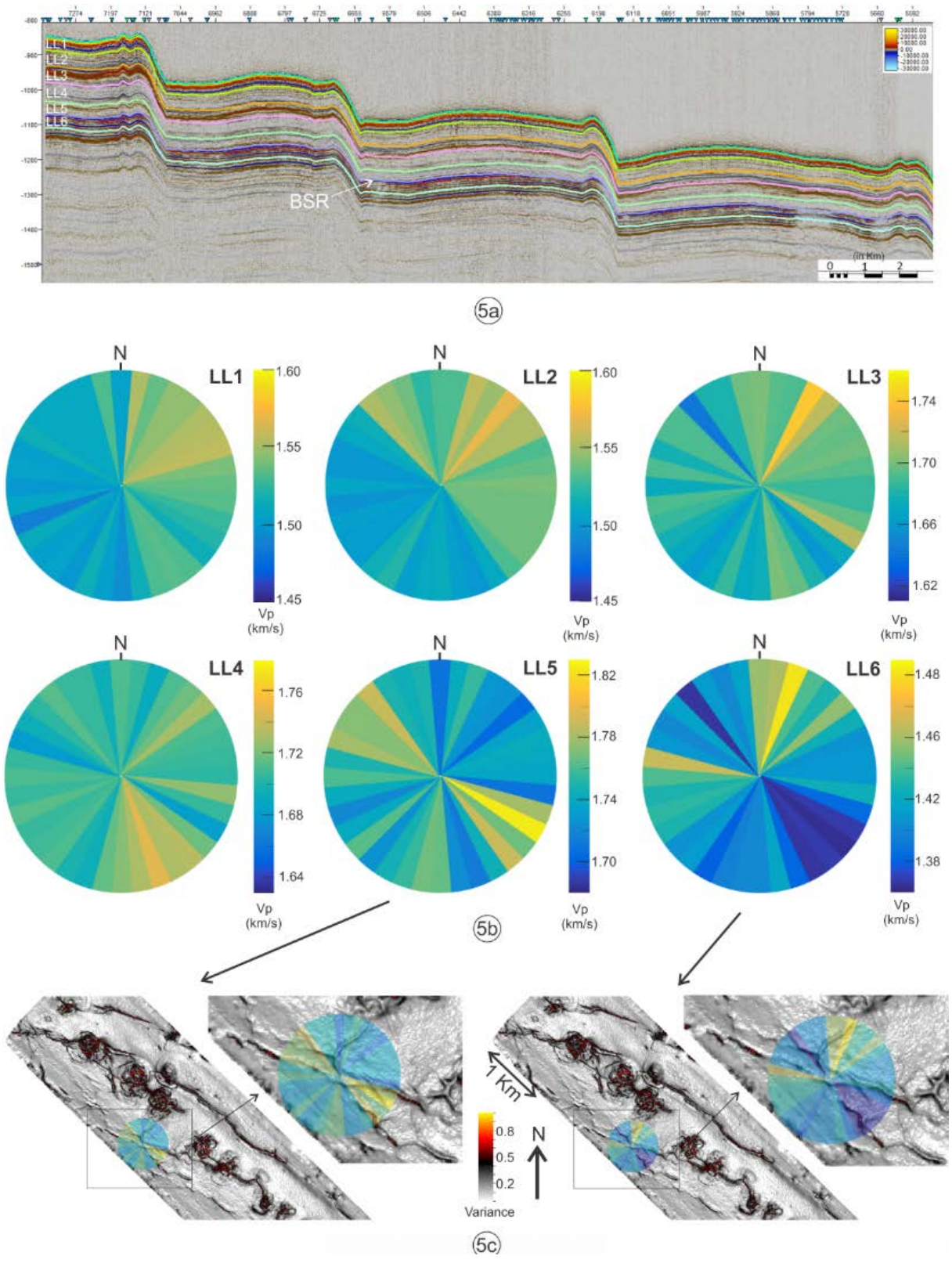

Figure 5 a) Seismic data acquired from circular shooting at the survey 2 site. Different picked events are shown in different colors. LL1, LL2, LL3, LL4, LL5, and LL6 are the layers for which anisotropic velocity model is estimated. BSR lies between the layer LL5 and LL6. b) Seismic velocity model in different azimuths for different layers at the survey 2 site (layers shown in Figure 5a). c) Overlap of the seismic velocity model and the variance map (taken from Plaza-Faverola et al., 2015) is shown for layers LL5 and LL6.

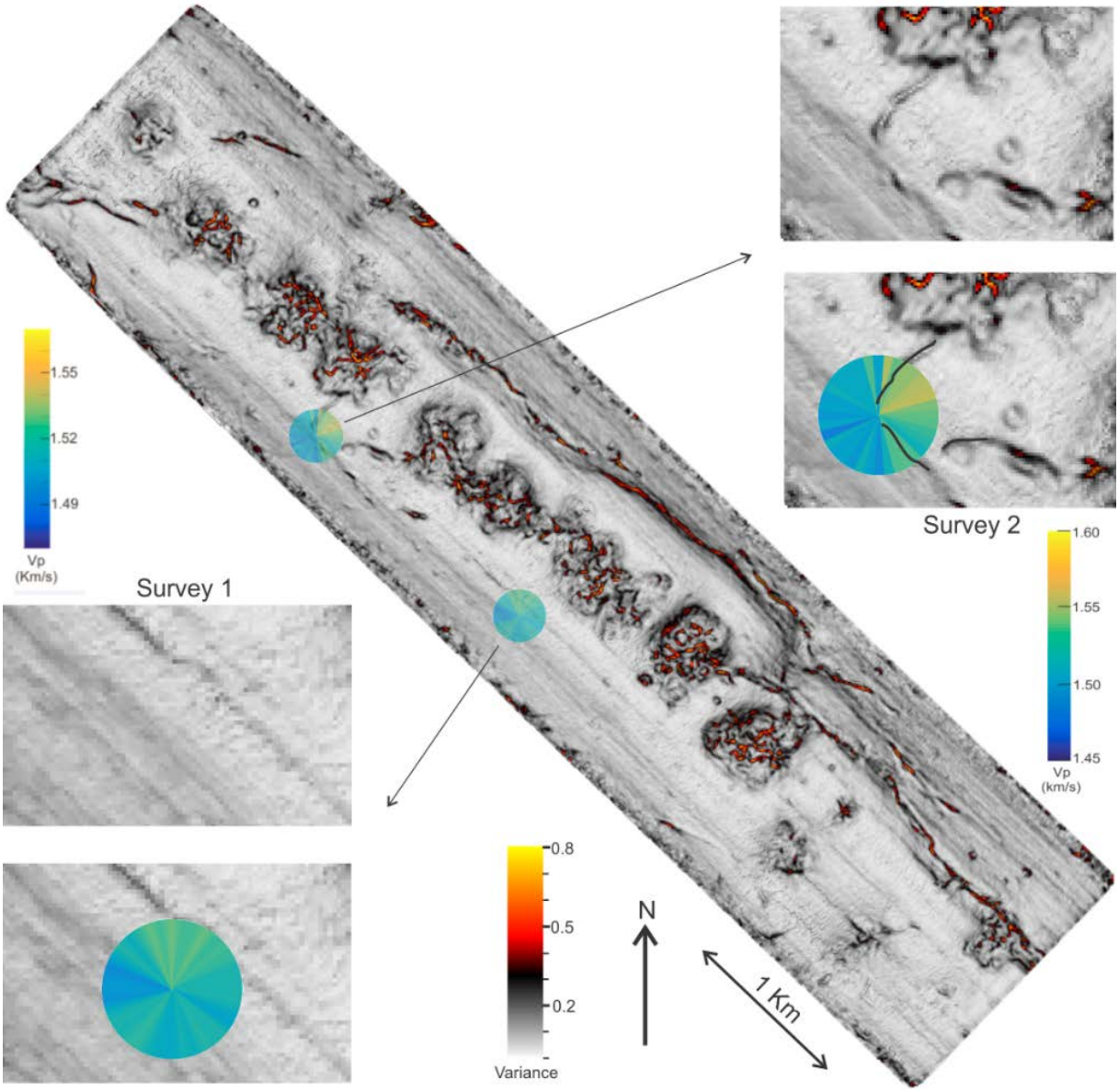

Figure 6 Overlap of the variance map and azimuthal velocity models for layers L1 and LL1.

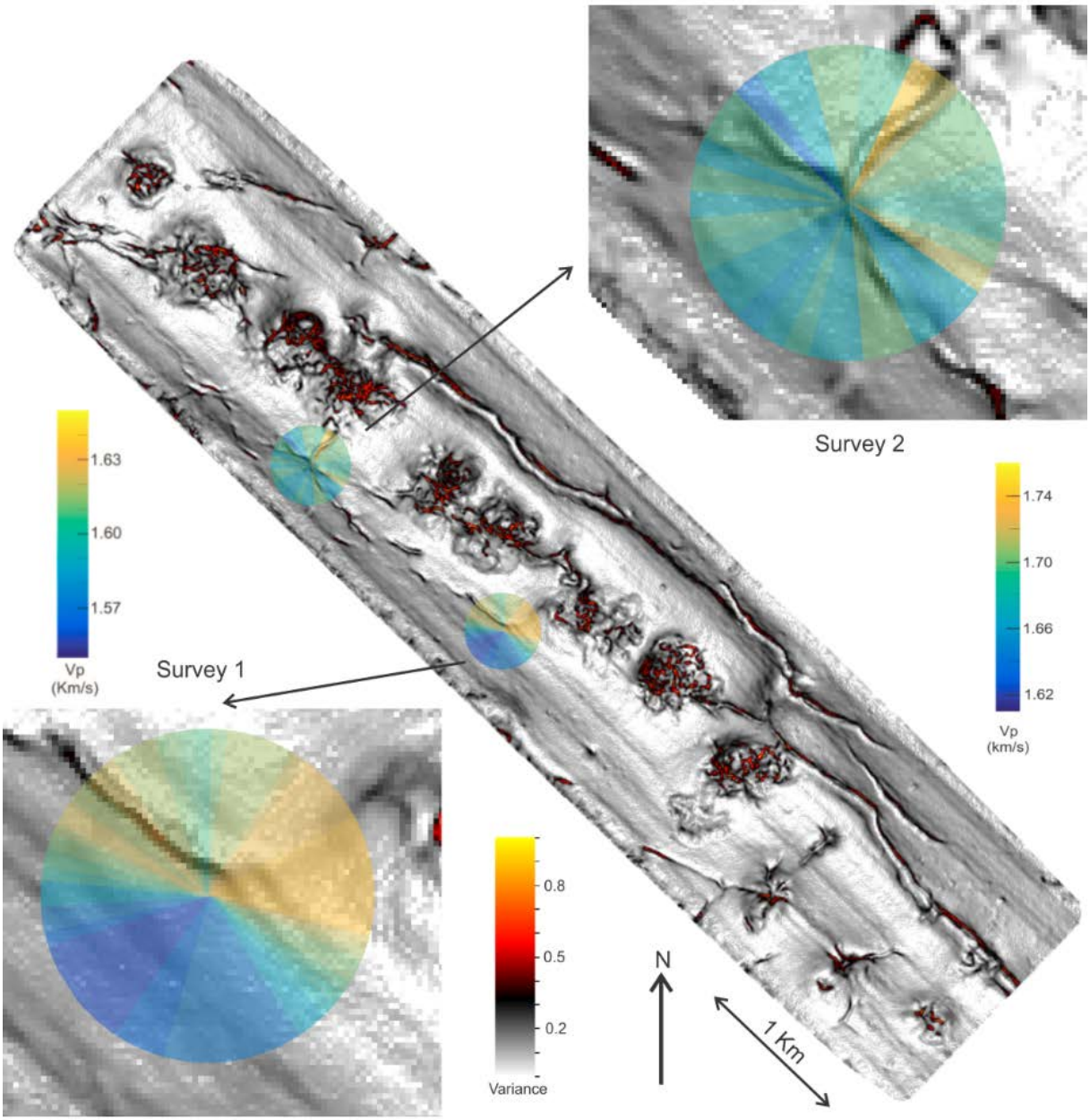

Figure 7 Overlap of the variance map for the H50 (Plaza-Faverola et al., 2015) and azimuthal velocity models for layers L2 and LL3.

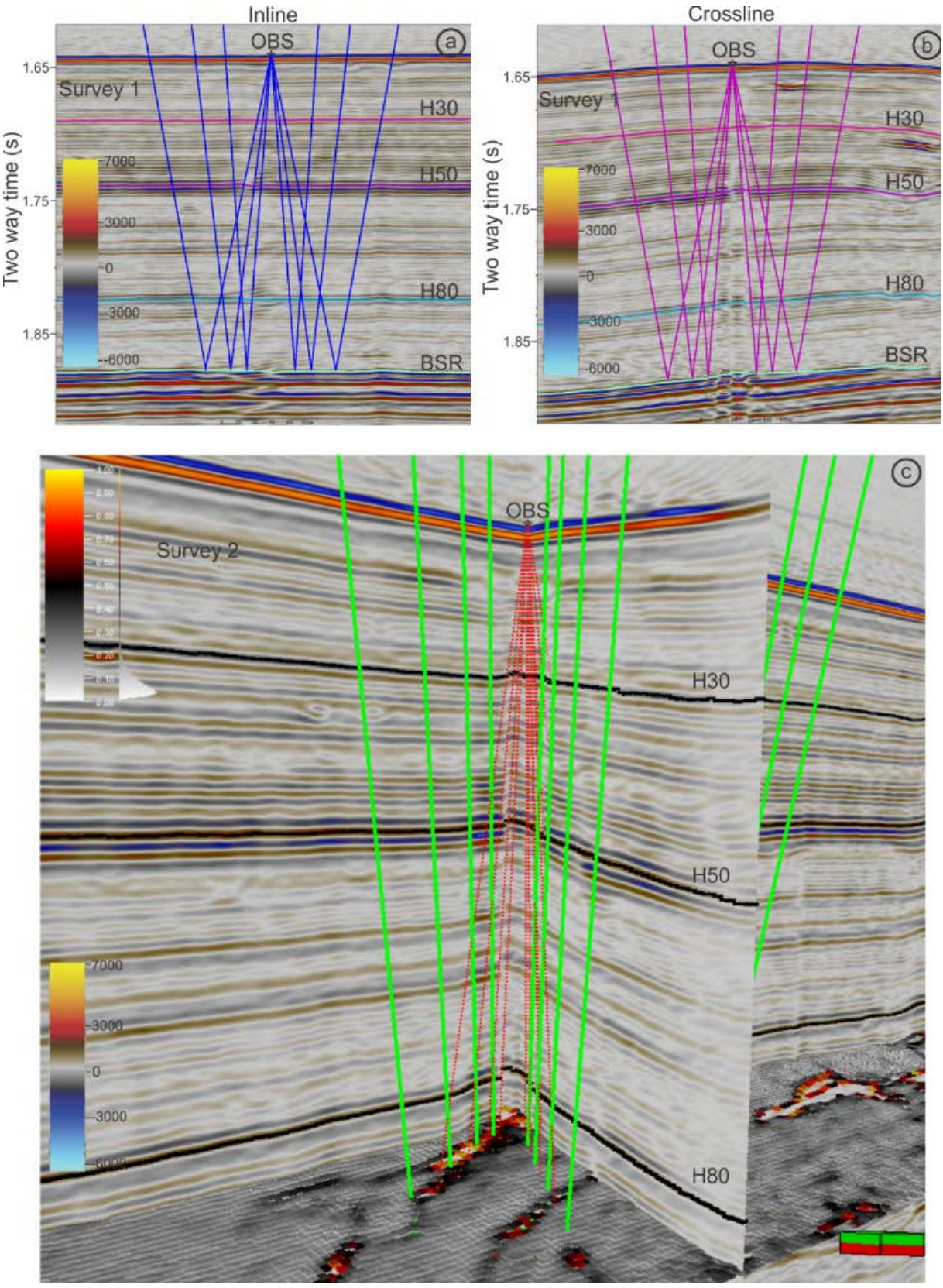

Figure 8 Schematic of raypaths for the L5 in Inline and crossline directions at the survey site 1 (8a and 8b). Schematic of raypaths for the LL5 in different azimuths along with the variance map at the survey site 2 (8c).